

SPECTROSCOPIC INVESTIGATIONS ON METHANE AIR FLAMES CONTAINING COAL DUST

By

JOHN J. HORVATH

A DISSERTATION PRESENTED TO THE GRADUATE SCHOOL  
OF THE UNIVERSITY OF FLORIDA IN  
PARTIAL FULFILLMENT OF THE REQUIREMENTS  
FOR THE DEGREE OF DOCTOR OF PHILOSOPHY

UNIVERSITY OF FLORIDA

1983

#### ACKNOWLEDGEMENTS

In a work such as this there are many people who are partially responsible for its creation due to the assistance and advice rendered by them to its author. This acknowledgement can only begin to thank them for all their efforts.

First and foremost, I must thank Dr. Alex E. S. Green for his constant support, through varied sources, throughout the course of these studies. His constant encouragement and belief in this work helped sustain my motivation throughout periods of thick and thin.

I am also deeply indebted to Dr. Willis B. Person for his untiring efforts on my behalf and the many stimulating and informative discussions on the topic of applied molecular spectroscopy. His constant optimism and friendship turned the darkest night into day.

I am also grateful to the rest of my committee, Dr. Martin Vala, Dr. John Dorsey and Dr. Richard Yost for their advice and attention to details in order to bring this study to a timely conclusion.

My appreciation goes to my typist Joan Raudenbush for a most excellent job of typing under the most adverse circumstances and remaining cheerful throughout.

I wish to thank Dr. D. B. Vaidya for assistance in early studies and on our publication and for the fine Indian dinners I enjoyed at his residence.

The constant stimulation and discussions with Dr. Krishna Pamidimukkala provided impetus for several experiments and provided an excellent sounding board for many of the ideas presented in this study and also for the use of his temperature data.

I would like to thank Jeffery Samuels for his assistance in programming the calculations used in some of these studies and his valuable help in the laboratory.

Enough can not be said about the assistance provided by Millie Neal of the Chemistry Library who always cheerfully renewed books over extended periods of time.

Dorothy Lisca of the Physics Library was also most helpful which is greatly appreciated.

I would like to thank Art Grant, Chester Eastman, and Daily Burch of the Chemistry Department Machine Shop for teaching me about Machine Shop practices and drawing figures and Harvey Nachtrieb and the Physics Department Machine Shop for turning these drawings into useable pieces of apparatus.

Rudy Strohschein of the Chemistry Department Glass Shop made many valuable contributions by constructing all of the glass apparatus used in these studies. Also thanks to Bruce Green for his suggestions on coal dust feeders.

I would also like to thank Dr. James D. Winefordner for loaning some of the equipment used in this study. Finally the independent gas-coal studies of Dr. Alex E. S. Green and Bruce Green provided access to supplies and materials otherwise unattainable.

# TABLE OF CONTENTS

	Page
ACKNOWLEDGEMENTS -----	ii
ABSTRACT -----	vii
CHAPTER	
I. INTRODUCTION -----	1
II. PRE-MIXED LAMINAR METHANE-AIR FLAMES -----	4
Structure and Mechanisms -----	4
General Description -----	4
Structure of Pre-Mixed Laminar Methane-Air Flames --	6
Calculation of Physical Properties of Pre-Mixed Laminar Methane Air Flames -----	13
Thermal and Diffusion Theories of Flame Propagation-	14
Comprehensive Theories of Flame Structure -----	25
Basic equations -----	26
One-dimensional flame equations -----	30
Boundary conditions for flame equations -----	33
Modern theoretical treatments -----	37
Chemical Reactions Occurring in Methane-Air Flames ---	43
Elementary Reaction Mechanism -----	43
Production of Excited State Molecules -----	47
OH -----	48
CH -----	49
C <sub>2</sub> -----	51
CO -----	55
III. CHEMICAL AND PHYSICAL PROPERTIES OF COAL AND ITS COMBUSTION -----	56
Chemical Analysis of Coal -----	56
Coal Petrography -----	66
Molecular Structure of Coal -----	74
Combustion of Pulverized Coal Particles in Laminar Pre-Mixed Flames -----	85



Generation and Combustion of Volatile Matter -----	87
Combustion of Solid Devolatilized Coal Particles (Char) -----	101
Chemical Reaction Mechanisms for Coal Char Combustion -----	114
Mathematical Descriptions of Coal Particle Combustion -----	124
IV. EXPERIMENTAL -----	136
Gas Metering and Flow Control System -----	136
Burner -----	139
Laboratory Coal Delivery Systems -----	140
Spectroscopic Apparatus -----	154
General Considerations -----	160
V. DATA -----	162
Development of a Temperature Measurement Technique and Observations of the Effects of Varying Amounts of Coal on OH Emission -----	162
Survey Spectra of Methane-Air and Methane-Air-Coal Dust Flames -----	170
Measurement of Excited State Populations in Methane- Air and Methane-Air-Coal Dust Flames -----	183
Spatial Temperature Measurements of Methane-Air and Methane-Air Coal Dust Flames -----	212
Investigations for Sulfur and Sulfur Compounds in Methane-Air-Coal Dust Flames -----	212
Effects of Addition of Excess O <sub>2</sub> on Methane-Air-Coal Dust Flames -----	218
Fluorescence Experiments -----	219
Lateral OH Emission Profiles of Methane-Air and Methane-Air-Coal Dust Flames Using an Inversion Technique -----	220
OH, CH and C <sub>2</sub> Emissions from a Single Cone Using an Inversion Technique -----	222
Calculation of Ground State Concentrations Assuming a Thermal Distribution -----	238
VI. DISCUSSION -----	243
Methane-Air Flames -----	243
Effect of $\phi$ Upon Excited State Concentrations -----	243
Spatial Temperature Profiles and Lateral OH Emission Profiles -----	249
Single Cone Data and the Formation of Excited States	253

Methane-Air-Coal Dust Flames -----	257
Stoichiometric ( $\phi = 1$ ) Flame -----	258
Lean ( $\phi = 0.77$ ) and Rich ( $\phi = 1.1$ ) Flames -----	270
Chemical and Physical Processes in Methane-Air- Coal Dust Flames -----	274
Comparison with Computer Kinetic Code Simulation Data -----	282
Conclusions -----	285
Future Work -----	287

#### APPENDIX

COMPUTER PROGRAMS -----	290
REFERENCES -----	297
BIOGRAPHICAL SKETCH -----	311

Abstract of Dissertation Presented to the Graduate School  
of the University of Florida in Partial Fulfillment of the  
Requirements for the Degree of Doctor of Philosophy

SPECTROSCOPIC INVESTIGATIONS ON METHANE AIR FLAMES CONTAINING COAL DUST

By

John J. Horvath

April, 1983

Chairman: Alex E. S. Green  
Cochairman: Willis B. Person  
Major Department: Chemistry

Recently the possibility has been proposed that a natural gas-coal mixture can be used to replace oil in an existing oil boiler. In order to study the physical and chemical effects of combining methane and coal dust in a flame a spectroscopic investigation of methane-air and methane-air-coal dust flames was initiated. A laboratory burner with suitable flow controls, was adapted for the simultaneous combustion of methane-air-coal dust mixtures. Pulverized bituminous coal dust (~200 mesh) was introduced into this burner by means of a fluidized bed device which allowed for a steady and reproducible amount of coal dust to be input to the flame.

Spectral emissions from radical species OH, CH, and C<sub>2</sub> were measured along with CO emissions which were then used to calculate excited state species number densities. Methane-air flames of various equivalence ratios were studied along with stoichiometric, lean and rich methane-air-coal dust flames. Emission intensities were obtained as a function

of height in the various flames and differences between the methane-air and methane-air-coal dust flames are discussed. Spatial temperature measurements of these flames were also obtained.

Spectral emission profiles of the primary reaction zone for the radicals OH, CH and  $C_2$  were obtained and results are discussed in relation to excited state formation mechanisms. Current ideas on the chemical and physical processes occurring in methane-air flames are reviewed along with current knowledge of coal and its combustion. Data from the present study are compared to literature data and chemical and physical mechanisms are proposed to account for these observations.

## CHAPTER I INTRODUCTION

Recently the possibility has been proposed that a natural gas-coal mixture can be used to replace oil in an exciting oil boiler (1). This study pointed out that great monetary savings could be yielded as well as decreasing the country's dependence on foreign sources for a steady and ever increasingly costly supply of oil. This study also pointed out that this idea, the burning of coal in the presence of natural gas, had not been discussed in the literature up to this time. An extensive literature survey revealed that ample literature could be found on the combustion of methane gas and solid coal, but not a single study involving the combined combustion of the two. In advance of the above study, an experimental program had been initiated by Professor Green. The work presented in this thesis represents the first spectroscopic investigation into the physical and chemical properties of combined combustion of methane-coal dust in a laboratory flame.

The chemical and physical process occurring during combustion of methane flames have been well studied, and some basic understandings have been realized (2-5). From spectroscopic observations of methane flames an abundant amount of information can be obtained. For example, chemical species in the flames can be identified by their characteristic spectral emissions and their growth and decay can be followed by

monitoring intensity as a function of position in the flame. The rates of change and the appearance and disappearance of chemical species yield valuable information on the chemical reactions occurring during the combustion process. Spectroscopic measurements are also non-perturbing upon the process being measured which allows measurements to be made in places inaccessible by other means of analysis. For these reasons and the availability of excellent spectroscopic facilities it was decided to study the spectroscopic emission of methane-air and methane-air-coal dust flames to try to understand the processes occurring in a methane-air-coal dust flame.

Questions to be addressed in this study include

1. Dependence of spectral emissions upon flame stoichiometry and their significance on flame chemistry.
2. Do methane spectral emissions change upon addition of coal dust to the flame and are any new emissions produced?
3. How does coal affect the chemistry of the flame?

In Chapter II the general physical and chemical properties of a methane-air flame will be presented. A discussion of flame propagation theory follows and the methods used to theoretically calculate various properties of methane-air flames. Elementary reactions occurring in methane-air flames will also be presented along with a section discussing current ideas of excited state production through chemical reactions for the species investigated in this study.

Chapter III will present chemical and physical properties of coal relevant to this study. Basic chemical composition of coal is discussed as well as techniques used to obtain these values. Different processes occurring during the combustion of coal, i.e. devolatilization,

char combustion, etc., will be presented and discussed along with theoretical approaches to modeling coal combustion systems.

Chapter IV will present the equipment and apparatus used in these studies as well as the experimental methodology used to obtain data. Chapter V will present the results of these scientific investigations and Chapter VI will discuss their significance and conclusions that can be drawn from these studies. The appendix contains the Fortran computer programs used to process data and calculate some of the results presented in this study.

## CHAPTER II PRE-MIXED LAMINAR METHANE-AIR FLAMES

### Structures and Mechanisms

#### General Description

A flame can be said to be a collection of gaseous matter at high temperature, produced by highly exothermic chemical reactions, which results in the emission of light. Two major classes of flames exist, propagating flames characterized by explosions and stationary flames represented by the common Bunsen burner. Both flame types require a fuel (combustible gas or liquid) and an oxidant (usually air or oxygen). Stationary flames can be considered to be of two basic types. In the first case the fuel is burned as it comes into contact with the air. In small flames of this type the combustion processes are mainly determined by the rate of diffusion of the air into the fuel and these types are called diffusion flames. In larger flames of these types, mixing due to turbulence becomes larger than mixing by diffusion, and flame stability and size are mainly governed by aerodynamic effects. These large turbulent flames have been studied in depth by many authors (6).

The second type of stationary flame is that in which the fuel and air or oxygen are pre-mixed before combustion occurs. These are known as pre-mixed flames, and in these flames the combustion processes are mainly determined by the rates of the chemical reactions occurring



in the flame. A Bunsen burner is the simplest type of burner that burns a pre-mixed flame. In this burner the fuel enters from a nozzle shaped orifice about 1 mm in diameter at the base of the burner. The mixing air is then entrained through two adjustable air holes. Even if the air holes are fully open, the amount of air entrained is usually much less than the amount needed for complete combustion (i.e. less than the stoichiometric amount), yielding a highly luminous and unsteady flame. The amount of air entrainment occurring is dependent upon the size of the gas orifice, gas pressure and size of the air holes. Relationships between air entrainment and flow conditions in Bunsen burners have been thoroughly discussed by Lewis and Grumer (7) and Lewis and von Elbe (8, 9). The chief limitations of the Bunsen burner are its inadequate entrainment of air, resulting in a fuel rich flame, the tendency to flash back with large diameter burners, putting an immediate halt to any observations currently in progress and being too unsteady to be suitable for detailed flame studies. One way to designate the fuel to air ratio is by the mixing ratio which is defined as the mole ratio of the oxidant gas (air, oxygen, etc.) to the fuel gas. The stoichiometric mixing ratio will be a function of the fuel and oxidant used in a flame. In the hydrogen-oxygen flame where the overall chemical reaction is  $2\text{H}_2 + \text{O}_2 \rightarrow 2\text{H}_2\text{O}$  the mixing ratio for a stoichiometric flame is 0.5 while for a hydrogen-air flame the stoichiometric mixing ratio is 2.5 (air = 20%  $\text{O}_2$ ). One problem with this type of designation is not being able to specify flame conditions (lean, rich, stoichiometric) without knowing the stoichiometric

mixing ratio, which is dependent on overall flame chemistry. A more convenient and informative term to use is the equivalence ratio which is defined as the actual mixing ratio divided by the stoichiometric mixing ratio. Therefore a stoichiometric flame will have an equivalence ratio of 1.0, a rich flame  $>1.0$  and a lean flame  $<1.0$ . Equivalence ratios will be used throughout this dissertation when discussing fuel/oxidant ratios.

A very steady, homogeneous and laminar flame is obtained when using a grid, or Meker burner with pre-mixed gases. The grid consists of a large number of small circular holes, as opposed to a single large one in a Bunsen burner. The gases are premixed before entering the burner so precise fuel-air ratios can be obtained, from lean through rich conditions, whereas a Bunsen burner can only run rich flames. This is the type burner used in these studies, which is fully described in Chapter IV, using a pre-mixed volume of natural gas and air. Natural gas is predominantly methane ( $\text{CH}_4$ ) with approximately 3 percent occurring as higher hydrocarbon gases. Gas analysis of the natural gas used in these experiments is reported in Chapter VI and in this Chapter methane and natural gas will be used interchangeably, but methane will be used when discussing the chemistry of the flame.

#### Structure of Pre-Mixed Laminar Methane-Air Flames

In the flame used in the present study five distinct regions can be distinguished.

1. The primary reaction zone consisting of cones, a few mm in height, above the holes, a very luminous region where initial combustion occurs.
2. The dark zone, a preheating zone underneath the cones.

3. A secondary reaction zone fed by oxygen from the surrounding room air.
4. An equilibrium zone, which is the most homogeneous part of the flame both in concentrations of species and temperature.
5. A diffusive mixing region where the flame mixes with the room air (mainly  $N_2$ ) and serves as a working flame boundary.

The primary combustion zone is also called the inner cone since it has a conical form when the burner port is round, as in the present case. This combustion zone is where the bulk of the reaction products are formed and is about .05 to 1.5 mm thick at atmospheric pressure with laminar flow and the gas takes about 1-20 ms to pass through this region. The primary reaction zone occurs on a surface of a cone due to the variation of gas velocity through the input ports. The flame gas flow in the input ports assumes a parabolic velocity profile as defined by the Poiseuille equation for laminar flow (10). A typical flow velocity pattern inside a burner port is shown in Figure 1. Figure 2 shows an idealized flame cone, which is assumed to be conical. The dotted line represents the surface inside the cone where the gas temperature rises just above the initial temperature due to conduction from the reaction zone. The solid line is the luminous surface of the flame of area  $a_r$ , which can be visually observed. Assuming the burning velocity is constant over the entire surface and there are no heat losses to the burner, burning velocity can be given by the following equations. Total mass is conserved, yielding

$$\dot{m} = \rho_o v_o a_b = \rho_o v_b a_o$$

and

$$v_b = \frac{\dot{m}}{\rho_o a_o} = \frac{v_o a_b}{a_o}$$

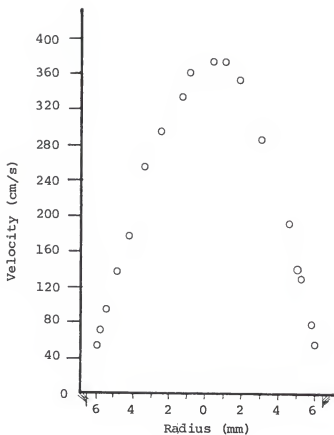


Figure 1. Experimental velocity distribution in a laminar stream of air at the exit of a cylindrical tube of 12.98 mm diameter with a flow of  $241 \text{ cm}^3/\text{s}$  (Adapted from B. Lewis, G. Von Elbe, J. Chem. Phys. 11, 75 (1943)).

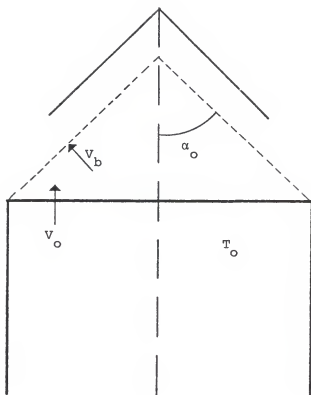


Figure 2. Ideal Flame Cone

where  $\dot{m}$  = rate of mass flow per unit time,  $V_o$  = velocity of unburned flame gases,  $\rho_o$  = unburned gas density at initial conditions,  $a_o$  = area of surface where gas temperature begins to increase,  $a_b$  = cross-sectional area of burner tube and  $V_b$  = burning velocity. In terms of the cone apex angle,  $\alpha_o$ ,

$$V_b = V_o \sin \alpha_o$$

Burning velocity can then be simply calculated by measuring the cone apex angle and measuring the input flow rates and calculating the input flow velocity. The simplicity of these equations in visualizing cone formation and burning velocity is unfortunately negated by the fact that the cone is not perfectly conical and the burning velocity is not constant over the whole cone. Distortion of a perfect cone shape is caused by the pressure inside the cone being greater than ambient, as a consequence of the pressure difference generated by the flame (11, 12). Particle tracking experiments (9, 11) have shown that burning velocity appears to increase at the flame tip and to decrease at the base. The latter is due to the quenching and stabilizing effects (heat loss to burner) of the burner port rim. In the former case, the unburned gas approaching the flame tip is surrounded by hot gas and the burning velocity is increased by heat conduction.

As the unburned flame gases rise, their temperature will increase slowly by conduction until it reaches a point,  $T_i$  the ignition point, where exothermic reactions just begin to be significant. From this point on the reaction proceeds extremely rapidly with an exponential growth in temperature until final maximum flame temperature is reached.

This rapid temperature rise is due to the rapid rate of the chemical chain reactions occurring in the primary reaction zone. In the reaction zone many molecules and radicals are formed with a large percentage in excited states, accounting for the highly luminous nature of the reaction zone. Due to the large release of energy in the reaction zone, the states of the gases are far from equilibrium since the liberated energy has not had a sufficient amount of time to partition equally among all the energy modes of the reaction products. The radiation and composition of the reaction zone have been subjects of intensive study (4, 5).

Above the primary reaction zone is a transition zone which leads to the zone of equilibrium. Many experiments (5) have indicated a narrow zone above the cones where high energy distributions decay to a distribution representative of a thermal distribution at the flame temperature. This decay rate depends on the number of effective collisions per second and how soon the different forms of energy will reach a state of equilibrium. Almost instantly the translational energy is equally distributed among the species present. The populations of the rotational, electronic and vibrational levels follow in that order. Once out of the reaction zone these forms of energy reach equilibrium rapidly and are able to adjust their populations quickly to reflect changes occurring in the flame as other species emit or absorb energy yielding temperature changes. In this way, height dependent phenomena, such as reduction in molecular emission at greater height (lower temperatures) can be explained. Due to the high collisional rates in flames (approximately  $10^9 \text{ sec}^{-1}$ ) and the relatively small number of

collisiona (13) needed to redistribute the nonthermal population into a thermal one, equilibrium conditions are reached soon after leaving the primary combustion zone (14). In this equilibrium region the temperatures determined by translational, electronic, vibrational and rotational population distributions are all the same, as has been demonstrated by many authors (14, 15).

It is possible that some of the flame reactants will not be fully combusted upon exiting the primary combustion zone. This effect is enhanced when the initial gas mixture is deficient in oxygen (fuel rich). Then the burned gases will contain a non-negligible concentration of molecules such as CO which can be further oxidized by the oxygen contained in the surrounding room air. This results in a secondary zone with reactions occurring which are similar to those in the primary reaction. The degree to which this occurs is determined by the initial mixing ratio of fuel gas and oxygen and the availability of oxygen in the surrounding atmosphere. In extreme cases (greatly fuel rich) the outer secondary reaction zone can be hotter than the primary reaction due to this effect. In the fuel lean and stoichiometric flames this effect will be negligible or non-existent.

As the burned flame gases rise their temperature decreases and the upper parts of the flame are less stable than the lower parts. There are several reasons why this occurs. The maximum heat is produced in the primary reaction zone where all of the chemical reactions occur under normal conditions. As these gases rise from the primary reaction zone they are continuously losing heat through radiation, mostly from the infrared bands of  $H_2O$  and  $CO_2$ . The flame gases also mix diffusively



with the surrounding cold room air, mainly nitrogen which cools the flame by absorbing a great amount of heat, and because of the horizontal velocity gradient present turbulence occurs after a short time. These effects cause a flame to "disappear" after a fixed time period, resulting in a finite flame length.

#### Calculation of Physical Properties of Pre-Mixed Laminar Methane Air Flames

During the past years a considerable amount of work has been devoted to measurements of the internal structure of pre-mixed flames. There are many reasons why this has occurred. These investigations help to increase our understanding of the mechanism of flame propagation and the physical processes occurring during combustion. A flame also represents a high temperature, flowing reaction system in which rapid gas phase chemical reactions may be studied. In a flame, the time scale of normal reaction rate studies is replaced by a distance coordinate and flow velocity.

In a pre-mixed flame a cold combustible mixture, upon passing through the flame front (primary reaction zone), is converted into hot combustion products. The analysis of flame structure consists of measuring or calculating

1. The burning velocity, or rate of consumption of gas per unit area of flame front and the thickness of this zone.
2. The variation of the flame temperature as a function of height in the flame.
3. The composition and concentration of all flame species.

Numerous theories have been developed in an attempt to calculate the flame parameters in question, and these can be divided into three major categories:

1. Thermal theories.
2. Diffusion theories.
3. Comprehensive theories, involving hydrodynamic and chemical kinetic equations.

#### Thermal and Diffusion Theories of Flame Propagation

The earliest theoretical approach to flame analysis was the thermal theory of Mallard and Le Chatelier (16) in 1883, who proposed that it is propagation of heat back through layers of gas that is the controlling mechanism in flame propagation. It was assumed that normal heat transfer processes raised the reactants to the spontaneous ignition temperature and that this propagated the flame. They assumed that the flame was divided into two regions, a region of conduction and a region of burning, separated by an ignition point with temperature  $T_i$ . Initial room temperature gases at  $T_o$  are burned to obtain reaction products at a final temperature  $T_f$ . They assumed that the slope of the temperature curve was linear and that it could be approximated by the expression  $[(T_f - T_i)/\delta_r]$  where  $\delta_r$  is the thickness of the reaction zone. The enthalpy balance equation is then given by

$$\dot{m} C_p (T_i - T_o) = \lambda (T_f - T_i) / \delta_r \quad (\text{II-1-1})$$

where  $\lambda$  is the thermal conductivity and  $\dot{m}$  is the mass flow rate, and  $C_p$  is the heat capacity. The mass flow rate is given by

$$\dot{m} = \rho A V_o = \rho V_b A \quad (\text{II-1-2})$$

where  $\rho$  = density,  $A$  = cross sectional area which is set equal to unity,  $V_o$  = velocity of unburned gas, and  $V_b$  = the laminar flame speed. Because unburned gases enter normal to the reaction zone, by definition  $V_o = V_b$ .

The above equation (II-1-1) can be written as

$$\rho V_b C_p (T_i - T_o) = \lambda (T_f - T_i) / \delta_r \quad (\text{II-1-3})$$

or

$$V_b = \frac{\lambda}{\rho C_p} \frac{(T_f - T_i)}{(T_i - T_o)} \frac{1}{\delta_a} \quad (\text{II-1-4})$$

which is the expression for the flame speed obtained by Mallard and Le Chatelier. In this equation the reaction zone thickness,  $\delta_r$ , is not known and would have to be estimated to obtain the burning velocity. This problem was overcome by the work of Nusselt (17) who introduced the velocity of the chemical reaction into the flame velocity equation. Nusselt used a term  $\epsilon$  to represent the concentration of the products, so that the following conditions apply:

$$\text{At } x = x_i, T = T_i, \epsilon = 0$$

$$\text{At } x = x_f, T = T_f, \epsilon = \epsilon_1$$

where  $x$  is linear distance in the flame in the upward direction and  $x_i$  is the height of the ignition point. Assuming that the degree to which the reaction has proceeded is linear in  $x$  we obtain

$$\frac{d\epsilon}{dx} = \frac{\epsilon_1}{(x_f - x_i)} = \frac{\epsilon_1}{\delta_r} \quad (\text{II-1-5})$$

so that

$$\frac{dT}{dx} = \frac{(T_f - T_i)}{\delta_r} = [(T_f - T_i) / \epsilon_1] \frac{d\epsilon}{dx} \quad (\text{II-1-6})$$

In this way the unknown thickness of the reaction zone,  $\delta_r$ , is eliminated but it now becomes necessary to find an expression for the extent of the reaction with respect to  $x$ . Nusselt assumed that the reaction rate,  $\omega$ , is constant and by earlier assumptions the

velocity of the gases in the reaction zone,  $V_b$ , is also constant since

$$\frac{d\epsilon}{dx} = (d\epsilon/dt)(dt/dx) = \omega/V_b \quad (\text{II-1-7})$$

His next assumption was that if the number of moles does not change, the burning velocity can be expressed as a function of temperature as follows:  $V_b = TV_o/T_o$  which contradicts his previous assumption which states that  $V_b$  is constant. Combining equations he obtained his final equation for flame velocity:

$$V_b^2 = \frac{\lambda}{C_p \rho} \frac{(T_f - T_i)}{(T_i - T_o)} \frac{T_o}{T_f} \frac{\omega}{\epsilon_i} \quad (\text{II-1-8})$$

This is similar to expressions derived by Jouguet and Crussard (18) and Daniell (19) also containing false assumptions.

Danköbler (20) derived an equation for flame burning velocity which resembles the equations of Nusselt, Jouguet and Crussard, and Daniell, but modified the assumptions so that the theory is more realistic in representing physical processes. He makes the approximation that the temperature gradient at the ignition point is related to the average temperature gradient across the reaction zone by a constant  $F$ . Then in place of Equation II-1-6, he wrote

$$\left(\frac{dT}{dx}\right)_{x=x_i} = (T_f - T_i)F/\delta_r \quad (\text{II-1-9})$$

Instead of assuming a constant reaction velocity,  $\omega$ , as Nusselt, he defines a mean reaction rate  $\bar{\omega}$  by the equation

$$n_r V_b = \int_0^{\delta_r} \omega dx = \bar{\omega} \delta_r \quad (\text{II-1-10})$$

where  $n_r$  = number of reactant molecules per unit volume initially present. This eliminates the contradiction of constant burning velocity

impose by Nusselt's constant mole assumption. Damkohler's final equation is then written in the form:

$$\lambda (T_f - T_i) F / \delta_r = C_p \rho V_b (T_i - T_o) \quad (\text{II-1-11})$$

or

$$V_b^2 = \frac{F \lambda \bar{\omega} (T_f - T_i)}{C_p \rho n_r (T_i - T_o)} \quad (\text{II-1-12})$$

This equation shows the general feature that the square of the burning velocity will be proportional to the average reaction rate in the reaction zone,  $\bar{\omega}$ . Equation II-1-11 can be solved for  $\delta_r$  which shows that the thickness is inversely proportional to the density (i.e. pressure), burning velocity, and the thermal conductivity.

Later attempts to put the thermal theory of flame propagation into a more quantitative form were made by Zeldovich and Frank-Kamemetsky (21, 22), Zeldovich and Semenov (23, 24), Semenov (25) and Zeldovich (26) who assumed that the reaction only started at a point near the final flame temperature. In this approach it was assumed that there was a temperature  $T_i$  very near to  $T_f$  below which there is practically no reaction;  $T_i$  is basically an ignition point but is much higher than in earlier theories, and is not used as a physically significant constant but as a mathematical device for approximate calculations.  $T_i$  does not appear in the final equations. This theory also assumes a reaction model of form  $nA = B + C$  ....., for which the reaction order may be zero, first or second with respect to A. Intermediate reactions or species are not considered. It is also assumed that the rates of reaction could be described using classical kinetic theory, taking the form  $\omega = k_a e^{-E/RT}$  for a first order reaction or  $\omega = k_a^2 e^{-E/RT}$  for a second

order reaction where  $a_r$  = molecules of reactant/cm<sup>3</sup>,  $k$  = frequency factor,  $E$  is the energy of activation, and  $R$  = gas constant. With a few additional assumptions they were able to derive equations for the burning velocity for first order reactions.

$$v_b^2 = \frac{k_2 \lambda_f C_p^f}{\rho_f L^2} \frac{T_o}{T_f} \frac{\lambda_f}{C_p^f \rho_f^D} \frac{n_r}{n_p} \left[ \frac{RT_f^2}{E} \right] e^{-E/RT_f} \quad (\text{II-1-13})$$

and for second order reactions

$$v_b^2 = \frac{k_2 \lambda_f (C_p^f)^2}{\rho_f L^3} \frac{a_r}{T_f} \left[ \frac{\lambda_f}{C_p^f \rho_f^D} \right]^2 \frac{n_r}{n_p}^2 \left[ \frac{RT_f^2}{E} \right]^2 e^{-E/RT_f} \quad (\text{II-1-14})$$

where  $\lambda_f$ ,  $C_p^f$  and  $\rho_f$  are the thermal conductivity, heat capacity and density at the final flame temperature,  $a_r$  is the concentration of the reactants,  $L$  is the heat of combustion of flame gases,  $D$  is the diffusion coefficient at the final temperature and  $n_r$  and  $n_p$  are the number of molecules of the reactants and products. Semenov (25) considered the conditions for which these equations were valid by calculating the errors incurred by the theories assumptions. He concluded that for bimolecular reactions the solution was valid only for  $RT_f/E \leq 0.1$ . Thus for a bimolecular reaction the application of Equation II-1-14 is only valid for values of  $E$  greater than 40 kcal. at  $T_f = 2000^\circ$ . For unimolecular reactions he found a wider range of applicability.

Belayeu (27) applied the above theory to the calculation of the speed of combustion of the vapor of nitroglycol. The heat of combustion of the vapor phase is conducted to the surface of the liquid and causes it to vaporize. The mass rate of vaporization is measured directly by the rate of lowering of the meniscus of the liquid. and is assumed equal to the mass rate of combustion of the vapor. It is assumed

that the activated molecule of nitroglycol decomposes by itself and the reaction occurs on collision with any other molecule. The equation for unimolecular reactions (Eq. II-1-13) was used, except the the frequency factor  $k$ , instead of having the first order value of about  $10^{13}$ , was replaced by  $Zn_x$ , where  $Z$  is a collision parameter yielding the number of collisions/sec  $\text{cm}^3$ . Belayeu found that the calculated value was in quite good agreement with the experimental value of about  $4 \times 10^{-2} \text{ gm/sec cm}^2$ . These equations were found not to hold for hydrogen and hydrocarbon flames but Zeldovich (26) found reasonably good agreement for carbon monoxide flames.

Bartholomé (28, 29) investigated the combustion of hydrogen, hydrocarbons, alcohols, ethers, nitroparaffins and alkyl nitrates with air, oxygen, nitrous oxide, and their mixtures in order to determine experimentally the variables that have the greatest effect upon flame velocity. Out of these experiments he developed a thermal theory of flame propagation along similar lines and attempted to apply it to hydrocarbon flames with limited success. A later development of the thermal theory by Boys and Corner (30) did not make as many assumptions as previous workers but involved many various constants such as activation energies which were not usually available for use with their explicit equations and made the theory difficult to test. Murray and Hall (31) measured the burning velocity of the decomposition flame of hydrazine ( $\text{N}_2\text{H}_4$ ) and found a value that agreed with the burning velocity predicted by the thermal theory. These experiments showed that the thermal theory could predict burning velocity in a few limited cases and also implied that thermal conduction plays an important role

in flame propagation. Direct experimental evidence is given by the effect of preheating the flame gas mixture, which increases the burning velocity, and the observations by Spalding (32) who used a porous plate burner to abstract heat from the flame and obtain a reduction in burning velocity. However the ignition point is predicted to be at much higher temperatures than those measured by experiments.

During the development of the thermal theories a contrasting school of thought started with the basic idea that the propagation rate depended on the speed of diffusion and on the concentration of active radicals (H, OH, etc.). In a series of papers Tanford and Pease developed the proposition that for certain flame reactions the rate of diffusion of active centers (radicals) into the unburned gas determines the flame velocity. The first paper (33) calculated equilibrium atom and free radical concentrations in moist carbon monoxide flames. The results of this paper indicated that the equilibrium concentration of hydrogen atoms was an important factor in determining the flame velocity. Tanford, in a second paper (34), presented calculations to establish the relative importance of diffusion and heat conduction in creating the hydrogen atoms in the flame zone. The conclusion reached was that diffusion was the controlling process. The third paper (35) developed an equation for flame velocity based on the conclusions of the first two papers. Assumptions used in this development are that the pressure, heat capacity and thermal conductivity are constant. The chemical reaction term is of form  $d\epsilon/dx$ , with the result that  $T$  is the only dependent variable in the development and consists of two limiting cases:



1. All heat is released at the flame front,  $x = 0$ , the flame front being defined as the point where the combustion has reached equilibrium, so that  $d\epsilon/dx = 0$  except at  $x = 0$ .
2. The chemical reaction proceeds evenly across the zone, so that  $d\epsilon/dx$  is a constant.

In order to determine the value of  $d\epsilon/dx$  under assumption one, it becomes necessary to assume a flame zone thickness for calculational purposes. Thicknesses of 0.01 cm for the carbon monoxide flame and of 0.005 cm for the hydrogen flame were used. The combustion zone is assumed to be at a constant mean temperature and the diffusion coefficient has a constant value  $D_m = D_o \left[ \frac{T_f}{T_o} \right]^2$  where  $D_o$  is the diffusion coefficient for hydrogen atoms in unburned gas at room temperature. It is also assumed that the rate of formation of the product at any point can be written as a sum of terms, one for each effective radical or atom, each one being of the first order with respect to the radical and the reactant, and chain branching reactions are assumed not to occur. The general formula derived using these assumptions is

$$V_b^2 = \sum_i \frac{k_i n_i P_i D}{q_p B_i'} \quad (\text{II-1-15})$$

where  $k_i$  = rate constant appropriate to the  $i$ th reaction,  $P_i$  = equilibrium partial pressure at flame front of  $i$ th component,  $q_p$  = mole fraction of potential product and  $B_i'$  is a constant, containing reaction rates, which allows for loss of the active species due to reaction. When flame velocities of carbon monoxide and hydrogen flames were calculated using the above equation, the calculated value of  $V_b$  was never in error by more than 25 percent and in general the error was much smaller. For carbon monoxide flame mixtures the predicted flame velocities varied from 25 to 106 cm/sec which is in good agreement with the stoichiometric burning velocity of approximately 55 cm/sec (15).

Van Tiggelen (36, 37) proposed a theory of flame propagation which emphasized chain branching as the chief reaction mechanism, and derived an expression for the flame velocity by assuming that the velocity is limited by the rate of chemical reaction rather than by heat conduction. Van Tiggelen followed Semenov (38) in stating that the active centers, which propagate the chain reaction, undergo in the course of a molecular collision either

- a. A branching reaction with probability  $\alpha$ .
- b. A chain-breaking reaction with probability  $\beta$ .
- c. A simple elastic collision or a reaction of simple propagation of the chain.

Burning is established when the probability of branching exceeds that of breaking i.e.  $\alpha \geq \beta$ . The total pressure and partial pressure of the reactants are assumed to be known and constant. The temperature in the flame zone  $T_m$  is assumed constant with a mean value between  $T_o$  and  $T_f$ . All molecules are assumed to be equal in size and mass so that  $D = \sigma \bar{v}/3$  where  $\sigma$  is the mean free path and  $\bar{v}$  is the mean velocity of the molecules. If  $d$  is the mean linear distance which a molecule can move in a region then the number of collisions undergone during the displacement is given by (39)

$$Z = 3\pi d^2 / 4\sigma^2 \quad (\text{II-1-16})$$

In order for a chain reaction to be maintained the following condition must be realized

$$3\pi d^2 (\alpha - \beta / 4\sigma^2) = 1 \quad (\text{II-1-17})$$

the displacement  $d$  effected by diffusion in a time  $t$  is given by the approximate expression

$$d^2 = 2Dt = 2\sigma \bar{v}t / 3 \quad (\text{II-1-18})$$

where the mean velocity of the molecules,  $\bar{v}$ , is given by diffusion of the active molecules.

Van Tiggelen then obtains an equation for the velocity of the flame front in a gas at a temperature  $T_m$  which is given by

$$v_b = \frac{4T_o \sqrt{2R(\alpha - \beta)}}{\pi \sqrt{3mT_m}} \quad (\text{II-1-19})$$

For  $\alpha = \beta$  equation 17 gives zero for the flame velocity. Thus the expression anticipates the existence of concentration mixture limits, outside of which combustion is not possible. If one neglects  $\beta$  for mixtures well within the combustion limits, a calculation of  $v_b$  is possible from a knowledge of  $T_m$  and  $\alpha$ . Assuming that the branching reaction involves the radical  $\text{CH}_3$  with  $\text{O}_2$  and the energy of activation of this reaction is taken to be 40 kcal, the probability  $\alpha$  is written as

$$\alpha = [\text{O}_2] \exp (-40,000/RT_m/p) \quad (\text{II-1-20})$$

so that the expression for flame velocity for this reaction becomes

$$v_b = \frac{4T_o \sqrt{2R[\text{O}_2] \exp (-40,000/RT_m)}}{\pi \sqrt{3mT_m}} \quad (\text{II-1-21})$$

Using this equation, flame velocities in mixtures of methane and air have been calculated and the results are in good agreement with the experimental values obtained by Coward and Hartwell (40). Ideas similar to these of Van Tiggelen were also stated in a qualitative form by Spalding (41), who concluded that in branched-chain reactions the reaction rate should be determined by the rate of the branching process,

because of its leading role, and that the reaction mechanism in the simplest case would be identical with that of a simple one-stage reaction.

Similar diffusion theories were presented by Gaydon and Wolfhard (5), Gaydon (42), and Manson (43) with slight variations on previous theories.

These studies proved that there is good evidence in many flames that diffusion of active species, such as free atoms or radicals, is important, but it also became obvious that flame propagation cannot be entirely explained by radical diffusion without also considering heat transfer. If the presence of a free radical alone was sufficient to initiate a reaction, then the fuel/oxidant mixture would be self-igniting. Normally, combustion occurs by a chain mechanism which involves a highly endothermic chain-initiation step, then slightly less endothermic chain-branching reactions and then exothermic chain-propagation reactions. Thermal ignition will normally be limited by the chain-initiation step, and will only occur, for short times, at fairly high temperatures. The role of diffusion may be to overcome this initiation step so that heating to a lower temperature may suffice to provide enough energy for the branching step and cause the reaction to proceed. In dealing with diffusion and thermal theories of flame propagation, it must be remembered that molecular diffusion and heat transfer are governed by similar laws. If we have a propagation mechanism which depends on reactions being started by radical diffusion, but these reactions also require an activation energy, then the flame propagation will depend on both molecular diffusion and heat transfer. In such a case, the less efficient process would tend to be the rate-determining step. For example, if there is

an ample supply of radicals, then the heat transfer required to supply the activation energy will be limiting and factors affecting the heat transfer will have a more important influence than those affecting the supply of radicals. But the fact that heat transfer appears to be important should not mean that radical diffusion does not occur or is not important.

It is evident that any exact solution of laminar flame propagation must take into account both thermal and diffusion theories as well as basic fluid dynamics equations modified to account for the liberation and conduction of heat and for changes of chemical species within the reaction zone due to chemical reactions.

#### Comprehensive Theories of Flame Structure

There seems to be general agreement of workers in the combustion field that the detailed structure of a flame can be determined by solving the equation of state, the equations of conservation of mass, momentum, energy and the hydrodynamical equations of change together with the boundary conditions which are experimentally imposed. The equations of change comprise (44)

1. The equation of continuity of each chemical species.
2. The equation of motion.
3. The equation of energy conservation.

In addition to these principle relations there are the auxiliary relations:

4. The complete set of reaction rate equations in terms of the chemical reaction rate constants.
5. The equations for the diffusion velocities in terms of the usual binary diffusion coefficients and the multicomponent thermal diffusion coefficients.

6. The equation for the pressure tensor in terms of the coefficients of shear and bulk viscosity.
7. The equation for the energy flux in terms of the coefficient of thermal conductivity.
8. The equation for the radiation energy flux in terms of the absorption and emission spectra of the molecules and the radiation emitted or absorbed as a result of the chemical reactions.

These are also the subsidiary relations which determine

9. The coefficient of viscosity for the multi-component mixture.
10. The coefficient of heat conductivity for the multicomponent mixture disregarding the effects due to chemical reactions (which are accounted for in the energy flux equation).

The boundary conditions should include heat transfer from the flame to the flame holder and to the surrounding medium.

The hydrodynamic equations of change, representing the overall conservation of momentum and energy in molecular collisions and the rate of change in molecular species due to chemical reactions and diffusion, can be rigorously derived using kinetic theory beginning with the Liouville equation (45). The same result can also be obtained in a simpler manner from a physical derivation of the Boltzmann equation (46), followed by the identification of the hydrodynamical variables and the development of the equations of change.

Basic equations. The state of a gas mixture may be described by the temperature  $T$ , the velocity  $\vec{V}$  and the molar density of each species  $n_i$  at each point  $\vec{r}$ . In addition, it is convenient to introduce the overall density  $\rho$

$$\rho = \sum_i n_i m_i \quad (\text{II-2-11})$$

where  $m_i$  is the molecular weight of species  $i$ . The equations of change are then

1. The equations of continuity of each chemical species,

$$\left(\frac{\partial}{\partial t}\right) n_i + \left(\frac{\partial}{\partial \vec{r}}\right) \cdot n_i (\vec{v} + \vec{V}_i) = K_i \quad (\text{II-2-2})$$

where  $\vec{V}_i$  is the diffusion velocity and  $K_i$  is the net rate of formation of  $i$  molecules due to chemical reactions. Since chemical reactions neither create or destroy matter as a whole,

$$\sum_i m_i K_i = 0$$

2. The overall equation of continuity (sum of individual equations, each weighted with its corresponding molecular weight) is given by

$$\left(\frac{\partial}{\partial t}\right) \rho + \left(\frac{\partial}{\partial \vec{r}}\right) \cdot \rho \vec{v} = 0 \quad (\text{II-2-3})$$

3. The equation of motion,

$$\left(\frac{\partial}{\partial t}\right) \vec{v} + \vec{v} \cdot \left(\frac{\partial}{\partial \vec{r}}\right) \vec{v} = - (1/\rho) (\partial/\partial \vec{r}) \cdot \hat{p} + (1/\rho) \sum_i n_i X_i \quad (\text{II-2-4})$$

where  $\hat{p}$  is the pressure tensor (including the effects of viscous forces) and  $X_i$  is the external force on a mole of particles of species  $i$

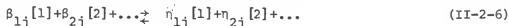
4. The energy balance equation,

$$\begin{aligned} \frac{\partial}{\partial t} \hat{U} + \vec{v} \cdot \left(\frac{\partial}{\partial \vec{r}}\right) \hat{U} = & - (1/\rho) (\partial/\partial \vec{r}) \cdot (\vec{q} + \vec{q}_R) - \\ & (1/\rho) \hat{p} : (\partial/\partial \vec{r}) \vec{v} + (1/\rho) \sum_i n_i \vec{V}_i \cdot \vec{X}_i \end{aligned} \quad (\text{II-2-5})$$

where  $\hat{U}$  is the thermodynamic internal energy of the mixture per unit mass,  $\vec{q}$  is the energy flux due to molecular motions and  $\vec{q}_R$  is the radiation contribution to the energy flux.

These equations are incomplete until expressions for the  $K_i$  and the various fluxes are given. To reduce complexity of calculation these expressions will be given for mixtures of ideal gases. The chemical

kinetics of a reacting mixture may be described in terms of a set of chemical reactions, which may be written symbolically in the form



where the  $\beta_{ij}$  and the  $\eta_{ij}$  are integers and the  $[i]$  indicate the molecular species. Let the rate constant for the  $j$ -th forward reaction be  $k_j$  and that for the reverse reaction be  $k_j'$ . Then in a mixture of ideal gases the rate of the forward reaction is given by

$$k_j n_1^{\beta_{1j}} n_2^{\beta_{2j}} \dots \quad (\text{II-2-7})$$

and a similar expression gives the rate of the reverse reaction. The total rate of formation of  $i$  due to chemical reactions is then

$$k_i = \sum_j (\eta_{ij} - \beta_{ij}) [k_j n_1^{\beta_{1j}} n_2^{\beta_{2j}} \dots - k_j' n_1^{\eta_{1j}} n_2^{\eta_{2j}} \dots] \quad (\text{II-2-8})$$

This is the equation for the  $K_i$  which is used in the equation of continuity of species  $i$ , Equation (II-2-2).

In a mixture of ideal gases, the diffusion velocities are

$$\vec{V}_i = (n^2/n_i \rho) \sum_{mj} D_{ij} \vec{d}_j - (D_i^T/n_i m_i) \partial (\ln T) / \partial \vec{r} \quad (\text{II-2-9})$$

where

$$d_j = \frac{\partial}{\partial \vec{r}} \frac{n_j}{n} + \left[ \frac{n_j}{n} - \frac{n_j m_j}{\rho} \right] \partial \ln p / \partial \vec{r} -$$

$$(n_j m_j / p \rho) \left[ \frac{\rho}{m_j} \vec{x}_j - \sum_k n_k \vec{x}_k \right] \quad (\text{II-2-10})$$

$$\text{and } p = nRT \quad (\text{II-2-11})$$

Here  $n$  is the total number of moles per unit volume and  $R$  is the gas constant. The  $D_{ij}$  are the multicomponent diffusion coefficients and the  $D_i^T$  are the multicomponent thermal diffusion coefficients. Both the  $D_{ij}$  and  $D_i^T$  are complicated functions of the temperature and the



composition. In flames it is usually more convenient to use the implicit expressions for the diffusion velocities given by the diffusion equations obtained by combining Equation (II-2-10) with the equation

$$\vec{d}_i = \sum_j \frac{n_i n_j}{n D_{ij}^B} (\vec{v}_j - \vec{v}_i) + \frac{\partial \ln T}{\partial \vec{r}} \sum_j \frac{n_i n_j}{n D_{ij}^B} (D_j^T / n_j m_j - D_i^T / n_i m_i) \quad (\text{II-2-12})$$

where  $D_{ij}^B$  are the binary diffusion coefficients associated with the interdiffusion of species  $i$  and  $j$ . The binary diffusion coefficients are to a good approximation independent of the composition. The diffusion velocities are defined relative to the mass average velocity  $\vec{v}$  so that

$$\sum_i n_i m_i \vec{v}_i = 0 \quad (\text{II-2-13})$$

In any isotropic, Newtonian fluid, the pressure tensor is

$$\hat{p} = p \hat{U} - 2\eta \hat{S} - K' \left[ \frac{\partial}{\partial \vec{r}} \cdot \vec{v} \right] \hat{U} \quad (\text{II-2-14})$$

where  $\hat{S}$  is the rate of shear tensor

$$\hat{S} = \frac{1}{2} \left[ \frac{\partial}{\partial \vec{r}} \cdot \vec{v} \right] + \frac{1}{2} \left[ \frac{\partial}{\partial \vec{r}} \cdot \vec{v} \right]^\dagger - \frac{1}{3} \left[ \frac{\partial}{\partial \vec{r}} \cdot \vec{v} \right] \hat{U} \quad (\text{II-2-15})$$

the  $\dagger$  indicates the transpose of the vector gradient.  $\hat{U}$  is the unit tensor,  $\eta$  and  $K'$  are the coefficients of shear and bulk viscosity, respectively, and  $p$  is the static pressure, which for an ideal gas is given by Equation (II-2-11).

In a mixture of ideal gases, the contribution of the molecular motions to the energy flux is

$$q = \frac{\lambda \partial T}{\partial x} + \sum_i n_i H_i \vec{V}_i +$$

$$\frac{RT}{n} \sum_{ij} (n_j D_{ij}^T / m_i D_{ij}^B) (\vec{V}_i - \vec{V}_j) \quad (\text{II-2-16})$$

where  $\lambda$  is the coefficient of thermal conductivity and  $H_i$  is the enthalpy per mole of species  $i$ . The energy flux due to radiation processes,  $\vec{q}_R$ , depends in an important way on the exact chemical composition of the mixture and can normally be neglected in laminar pre-mixed flames (45).

When the expressions for the  $K_i$  and the various fluxes are used in the equations of change, Equations (II-2-2,4,5), one obtains a set of nonseparable nonlinear partial differential equations which describe the time and space variation of the variables,  $n_i$ ,  $\vec{v}$ , and  $T$ . These equations involve the rate constants  $k_j(T)$  and  $k_j'(T)$  for the chemical reactions and the transport coefficients  $D_{ij}^B$ ,  $D_{ij}^T$ ,  $n$ ,  $K'$ , and  $\lambda$ .

Equations (II-2-2,3,4 and 5) are the fundamental relations governing the dynamics of any reacting mixture and as written are, for all practical purposes, completely rigorous. Thus they provide a starting point for flame structure calculations but, as is often the case, complete rigor is also accompanied by a complete lack of practical utility. In order to make use of these equations it is necessary to simplify them in several ways, and these simplifications will now be discussed.

One-dimensional flame equations. Normally only one-dimensional flow is considered in combustion models and a reasonable experimental approximation to this can be accomplished by the "flat flame" (41).

The equations of change, described above, can be considered for the special case in which the flow is only in the  $z$  direction (up) and in which all variables are independent of the  $x$  and  $y$  coordinates. At this time it is convenient to define several additional quantities:

1.  $M$  is the total mass flux,  $M = \rho v$ .
2.  $X_i$  is the mole fraction of component  $i$ ,  $X_i = n_i/n$ .
3.  $G_i$  is the fraction of the mass flux due to component  $i$ ,  

$$G_i = \frac{n_i m_i}{(v + V_i)M}.$$

The  $G_i$  are often called the chemical progress variables. It is convenient to consider the  $G_i$ 's as dependent variables and to use the diffusion equation (II-2-12), as part of the hydrodynamic equations.

The expressions for the various fluxes and the above definitions can now be used in the equations reduced to one-dimensional form.

With some rearrangement the following equations are obtained:

1. The equation of continuity of each chemical species,

$$\left(\frac{\partial}{\partial t}\right) (n_i X_i) = - \left(\frac{\partial}{\partial z}\right) (M G_i / m_i) + K_i \quad (\text{II-2-17})$$

2. The overall equation of continuity,

$$\left(\frac{\partial}{\partial t}\right) \rho = - \left(\frac{\partial}{\partial z}\right) M \quad (\text{II-2-18})$$

3. The equation of motion,

$$\frac{\partial M}{\partial t} = - \frac{\partial}{\partial z} \left\{ \rho M v - \left[ \frac{4}{3} \eta + k' \right] \frac{\partial v}{\partial z} \right\} + \sum_i n_i X_i G_i \quad (\text{II-2-19})$$

4. The energy balance equation,

$$\begin{aligned} \frac{\partial}{\partial t} \left[ n_i \sum_i X_i m_i \hat{H}_i - \rho + \frac{1}{2} \rho v^2 \right] = \frac{\partial}{\partial z} \left\{ \lambda \frac{\partial T}{\partial z} - M \sum_i G_i \hat{H}_i - \right. \\ \left. 1/2 M v^2 + \left( \frac{4}{3} \eta + k' \right) v \frac{\partial v}{\partial z} - q_R + \left( \rho M / n^2 \right) \sum_{ij} \left( \frac{D_{ij}^T}{m_i m_j} \right) \left[ G_j - \right. \right. \\ \left. \left. \frac{m_j X_j}{m_i X_i} G_i \right] \right\} + M \sum_i G_i X_i / m_i \quad (\text{II-2-20}) \end{aligned}$$

5. The diffusion equations,

$$\frac{\partial x_i}{\partial z} = \frac{M}{n} \sum_j \frac{(x_{ij} m_{ij} G_j - x_{ji} m_{ji} G_i)}{m_{ij} D_{ij}} - x_i \left( \frac{1 - nm_i}{\rho} \right) \frac{\partial \ln p}{\partial z} + \quad (II-2-21)$$

$$\frac{\partial \ln T}{\partial z} \sum_j \frac{(x_{ij} m_{ij} D_j^T - x_{ji} m_{ji} D_i^T)}{nm_{ij} D_{ij}} + \frac{x_i n}{p} \left[ x_i - \frac{nm_i}{\rho} \sum_j x_j x_j \right]$$

These equations would be used in the study of time dependent phenomena, such as traveling wave combustion, stability questions and the possible transformation of a flame into an explosion.

One-dimensional steady state flames and explosions travel with a constant velocity into the unburned gas. If the unburned gas is stationary, the flame front moves in space with a constant velocity. On the other hand, if the unburned gas moves with the proper constant velocity, the flame front may be maintained at a constant position in space. This occurs when a flame is stabilized on a burner such as the one used in these studies. In this case it is convenient to use a coordinate system fixed with respect to the flame front and consider the stationary state solutions of the equations. This is possible because the hydrodynamic equations apply in any system of coordinates moving with constant velocity.

To obtain the time-independent equations we require that all time derivatives in the hydrodynamic equations, (II-2-17 - 21) be zero. Also we will assume that no external forces act upon the system, so that all the  $X_i = 0$ . Equations (II-2-18, 19 and 20) may then be integrated with respect to  $z$ , with the result that the mass rate of flow,  $M$ , is a constant. The equations are then as follows:

1. The equation of continuity of each chemical species,

$$\frac{dG_i}{dz} = \frac{m_i K_i}{M} \quad (\text{II-2-22})$$

2. The equation of motion,

$$\left( \frac{4}{3} \eta + k' \right) \frac{dv}{dz} = p + Mv + L_i \quad (\text{II-2-23})$$

3. The energy balance equation,

$$\lambda \frac{dT}{dz} + \left( \frac{4}{3} \eta + k' \right) v \frac{dv}{dz} = \sum_i M_i G_i \hat{H}_i + \quad (\text{II-2-24})$$

$$\frac{1}{2} Mv^2 + q_R + L_2 - \frac{PM}{n} \sum_{ij} \frac{D_{ij}^T}{m_i m_j D_{ij}} \left[ G_j - \left( \frac{m_j x_j}{m_i x_i} \right) G_i \right]$$

where  $L_i$  and  $L_2$  are the constants of integration. The diffusion equations are given by Equation (II-2-21) are unchanged (except for omission of the terms due to the external forces,  $x_i$ ).

Boundary conditions for flame equations. In the laminar pre-mixed flame the burnt gases are free to flow undisturbed infinitely far in the positive  $z$  direction. The various properties of the burned gases then asymptotically approach limiting values as  $z$  approaches infinity. These limiting values are called the "hot boundary values and these quantities are indicated by a subscript  $\infty$ . The constants  $L_i$  and  $L_2$  can then be expressed in terms of the hot boundary values of the various quantities by noting that in this limit  $dv/dz$  and  $dT/dz$  are equal to zero. In most flame problems one may neglect radiation effects ( $q_R = 0$ ), neglect thermal diffusion and the Dufour effect ( $D_{ij}^T = 0$ ) and neglect pressure diffusion. When these terms are dropped from the hydrodynamic equations and the constants of integration evaluated in terms of the hot boundary

conditions, one obtains the following "flame equations":

1. The equation of continuity,

$$\frac{dG_i}{dz} = \frac{m_i K_i}{M} \quad (\text{II-2-25})$$

2. The equation of motion,

$$\left( \frac{4}{3} \eta + k^* \right) \frac{dv}{dz} = (p - p_\infty) + M(v - v_\infty) \quad (\text{II-2-26})$$

3. The energy balance equation,

$$\frac{\lambda}{M} \frac{dT}{dz} = \sum_i G_i \hat{H}_i - \sum_i G_{i_\infty} \hat{H}_{i_\infty} - \frac{1}{\rho} (p - p_\infty) - (1/2) (v - v_\infty)^2 \quad (\text{II-2-27})$$

4. The diffusion equations,

$$\frac{dx_i}{dz} = \frac{M}{n} \sum_j \frac{(x_{ij} m_j G_j - x_{ji} m_i G_i)}{m_{ij} D_{ij}} \quad (\text{II-2-28})$$

The problem is then one of solving these equations for specified boundary conditions.

At the hot boundary limit,  $z \rightarrow \infty$ , the various quantities approach finite limits corresponding to complete chemical and thermal equilibrium. Accordingly, the derivatives of all of the quantities approach zero as  $z \rightarrow \infty$ .

The cold boundary conditions are more difficult to specify. First consider the case where all of the  $K_i$  are equal to zero at the cold boundary layer. In this case we can consider an "unattached" flame and let  $z \rightarrow -\infty$ . The boundary conditions at the cold boundary are then completely analogous to those at the hot boundary; the various quantities approach finite limits (properties of unburned gas mixture) as  $z \rightarrow \infty$ , and the derivatives approach zero. Equations relating the values at the two boundaries can be obtained from equations (II-2-26, 27 and 28)

by setting the derivatives equal to zero. Unfortunately this is not a reasonable approximation to actual physical processes occurring. In usual practice Arrhenius type expressions are used for the temperature dependence of the the chemical reaction rate constants. This leads to a small but finite value for the reaction rate even at the cold boundary temperature,  $T_0$ . Other problems involved with the cold boundary condition include back-diffusion of the product gases beneath the burner head, causing the chemical composition of the molecules entering the flame to be ill-defined. Also, unless there is a small amount of heat transferred from the flame to the flame holder, the position of the flame with reference to the flame holder is undetermined.

Hirschfelder and Curtiss (45, 47) eliminated this cold boundary problem by introducing the concept of a flame holder at the cold boundary. This was originally developed as a mathematical concept but it is also physically realistic because all stationary flames use a flame holder (burner) for support and it does heat up due to the flame. Their flame holder had the following two properties:

1. It serves as a porous plug permitting the reactant gases to pass through it freely but preventing the back-diffusion of the product gases.
2. It serves as a heat sink with a small amount of heat transfer taking place from the flame to the flame holder.

The cold boundary conditions at the flame holder, which is taken to be the origin of the  $z$  coordinate system, are:

1. The  $G_i$  are the mass fractions of the various components in the unburned fuel-air mixture.
2. The heat transfer to the heat sink or the value of energy flux at  $z = 0$  is

$$q_0 = -\lambda_0 (dT/dz)_0$$

The concept of the flame holder is apparently necessary if the rate constants are taken to be finite at  $T_0$ . The concept is, however, useful even if the  $K_i$  are equal to zero at  $T_0$  since the heat transfer to the flame holder determines the quenching distance. If the initial temperature, pressure and composition of the fuel-air mixture are specified along with the strength of the heat sink,  $q_0$ , a solution of the equations exists (and satisfies all of the boundary conditions) only for a single value of the mass rate of flow,  $M$ . This value of  $M$  is the product of the flame velocity  $v_0$  (the value of  $v$  at the flame holder,  $Z = 0$  and  $\rho_0$  the gas density at the flame holder. The problem then is an eigenvalue problem for obtaining the proper value of  $M$ .

Hirschfelder et al. (48) studied flames involving the first-order decomposition of azomethane ( $C_2H_6N_2 \rightarrow C_2H_6 + N_2$ ) and the bimolecular decomposition of nitric oxide ( $2NO \xrightarrow{+} N_2 + O_2$ ) in detail. Four cases for the azomethane decomposition were considered: (a) no heat loss to the flame holder, so that  $q_0 = 0$ ; (b) a reasonable amount of heat loss to the holder  $q_0 = 10 \text{ cal/cm}^2\text{s}$ ; (c) 50 percent by volume of inert gases introduced with the fuel, and (d) the decomposition assumed to take place by the autocatalytic mechanism ( $C_2H_6N_2 + C_2H_6 \rightarrow 2C_2H_6 + N_2$ ). For cases a, b and d at one atmosphere pressure the decomposing azomethane has a large flame velocity and a narrow flame zone. For case c, the flame velocity was calculated to be 15cm/sec with flame thickness of 0.019 cm, in good agreement with the measured values.



Modern theoretical treatments. Various other approaches to solve the flame equations have been proposed by several authors. It was shown by Spalding (41) that the steady flame speed could be found conveniently by solving the equations for the unsteady-flame situation. In this paper he calculated the flame speed of a hydrazine decomposition flame using a chain reaction mechanism instead of a unimolecular decomposition. The chain reaction scheme used was proposed by Adams and Stocks (49), as follows:  $A \rightarrow 2B$ , radical production,  $B+A \rightarrow B+2C$ , chain propagation,  $B+B+G \rightarrow 2C+G$ , chain breaking. In this scheme no difference is made between the radicals  $NH_2$ ,  $H$  or other radicals which may be present.  $A$  denotes hydrazine and  $C$  end products. Spalding used for the calculation of the radical concentration and for the burning velocity a numerical integration method which starts from an arbitrary temperature profile through the flame zone and tried to follow the transient process which converges to the stationary state. He used the assumption that the sum of the thermal and chemical enthalpies remains constant throughout the flame so that the mass fraction of the hydrazine is a linear function of the temperature. In this paper he introduced a function defined by the equation

$$d\psi = \rho dz$$

If there were uniform flow in the  $z$  direction,  $\psi$  could be referred to as a stream function. Its definition is such that equal masses of gas are contained between planes where the  $\psi$  values differ by equal amounts. As the density of the gas changes, however, the distances separating these planes vary. The origin of  $\psi$  was chosen in such a way that there is no net mass flow across planes of equal  $\psi$ , although

diffusion may occur. The flame equations were rewritten using this variable and then solved by a finite-difference method (41). Using this method Spalding obtained burning velocities that were in good agreement with published values (49).

In later papers, Spalding and Stephenson (50) and Spalding et al. (51), presented a new procedure for the solution of the differential equations of transient one-dimensional flame propagation employing a coordinate system which moved with the flame. The chief contribution of this paper was the presentation of a series of modified flame equations which reduced the time and storage needed for computation, and which, by suitable implicit formulation of the finite-difference equations, allowed a standard computer program to be used. In earlier work Spalding (41) used the coordinates of time,  $t$ , and 'stream function',  $\psi$ , defined as  $\frac{\partial \psi}{\partial z} = \rho$  and  $\partial \psi / \partial t = -\rho v$ . In this work, time remained as the first coordinate, while the second became the dimensionless stream function,  $w$ , defined as

$$w = (\psi - \psi_H) / (\psi_C - \psi_H) ;$$

where  $\psi_H$  and  $\psi_C$  are the instantaneous values of  $\psi$  at the hot and cold boundaries of the flame, respectively. As the flame develops and spreads into the unburned gas,  $\psi_H$  and  $\psi_C$  change their values; at large times, both  $\psi_H$  and  $\psi_C$  increase linearly with time yielding

$$\frac{d\psi_H}{dt} = \frac{d\psi_C}{dt} = \rho_v S_u$$

where  $S_u$  is the speed of propagation of the flame relative to the unburned gas, and  $\rho_v$  is the density of that gas. Values may be ascribed arbitrarily to the  $\psi_H(t)$  and  $\psi_C(t)$ , but the saving of computer storage

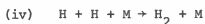
and computational time results from choosing these functions so the hot and cold boundaries lie at the locations at which the gradients of temperature or concentration have just significant values. Therefore the boundary conditions imposed are  $0 \leq w \leq 1$ .

This choice of coordinate system enables the flame equations to be solved by adaptation of a computer program of Patankar and Spalding (52) who developed it to solve the parabolic equations which arise in the theory of the steady two-dimensional boundary layer problem of hydrodynamics. Modifications to this work were presented in Spalding and Stephenson's paper to allow use on the flame equations. Using this program they were able to calculate burning velocity for laminar hydrogen and bromine flames, both for flame propagation into an unlimited expanse of pre-mixed reactants, and for a flame stabilized on a cooled porous plug burner. They were able to obtain quite good agreement with experimental results for both cases, which was attributed to use of a complete chemical kinetic reaction scheme using four reactions. Of course this is still a very simple case.

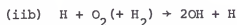
A more complex case was studied by Dixon-Lewis (53, 54) who studied the hydrogen-oxygen flame both theoretically and experimentally. In these papers hydrogen-oxygen burning velocity and concentrations were calculated using different reaction mechanisms and the procedure proposed by Spalding and Stephenson (50), using finite difference methods. Detailed specification of thermodynamic and transport properties were also used in this approach.

The two reaction mechanisms used were as follows:

1. (i)  $\text{OH} + \text{H}_2 \rightleftharpoons \text{H}_2\text{O} + \text{H}$   
 (ii)  $\text{H} + \text{O}_2 \rightarrow \text{OH} + \text{O}$



Assuming reaction (ii) to be the rate controlling step, reactions (i), (ii) and (iii) were combined to give (ia)  $H + O_2 (+ 3H_2) \rightarrow 2H_2O + 3H$ . Reactions (ia) and (iv) provided the complete flame reaction mechanism.



This is a slightly more complex mechanism than before and reaction (v) has been included to observe the effect of the radical recombination reaction on the equilibrium of H and OH by the rapid reaction (i).

In these papers the transport fluxes in the multicomponent flame system due to diffusion and thermal conduction, and to thermal diffusion and its reciprocal effect (dufour effect), are considered from the standpoint of an extension of the Chapman-Enskog kinetic theory of bimolecular gases to polyatomic gases by Wang Chang, Uhlenbeck and de Boer (55) and the subsequent development by Mason, Monchick and co-workers (56-60) to polar-polar molecular interactions. Dixon-Lewis (54) gives equations for the various diffusional, thermal diffusional and thermal fluxes which it is necessary to derive, in order to obtain reaction rates from experimental temperature and composition profiles in flame. Also the organization of computer programs for calculation of the multicomponent diffusion and thermal diffusion coefficients and the thermal conductivity are described. The expressions for the transport fluxes are then used to derive equations for the mole fraction and temperature gradients in the flame where transport processes and

chemical reactions occur side by side. From the mole fraction and temperature at one point in the flame it is then possible to solve the flame equations by a numerical integration method such as the Runge-Kutta procedure to compute the complete composition and temperature profiles. The calculated values for composition profiles were checked experimentally by sampling from the flame in different positions with a quartz microprobe and subsequently analyzed mass spectrometrically using a continuous flow system. Good agreement between theoretical and experimental profile was found except for the hydrogen profile where the computed profile was slightly displaced with respect to the experimental one. This observation was explained by possible diffusion effects in the pressure gradient at the probe tip.

Dixon-Lewis's treatment of flame transport phenomena is the most comprehensive and rigorous discussion currently available that can be used in a computer program for flame calculations(54). This treatment should be included in any flame model that purports to represent actual physical-chemical processes occurring in flames. A complete flame theory would also have to represent the actual chemical reactions occurring and not just a simplified set.

This was partially accomplished in the work of Smoot et al. (61) who studied the kinetics and propagation of laminar methane-air flames using a one-dimensional flame propagation model based upon the equations presented by Spalding et al. (51). This model is based on a numerical, unsteady-state solution of transformed species and energy conservation equations using explicit techniques for diffusion terms (binary diffusion) and linearized, implicit techniques for kinetic terms. A methane-oxygen

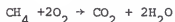
flame kinetic mechanism consisting of 28 elementary reactions and 15 species was postulated and used in this model. Flame velocity, flame thickness, temperature profile and concentration profiles of 13 species were predicted for a series of methane-air flames. In this study the effects of pressure, methane concentration, initial temperature, rate constants and transport coefficients, were investigated. The predictions of the model were compared with experimental data, and agreement was generally quite good. The concentrations of the radicals H, OH and O were found to be of major importance in the propagation of methane-air flames.

The most complete model presented at this time is by Tsatsaronis (62) who solved the transformed species and energy conservation equations using the numerical computer solution proposed by Spalding et al. (51). The diffusion model used was the rigorous and complete one used by Dixon-Lewis (54) based on the modified Chapman-Enskog kinetic theory of Manson, Monchick and co-workers (56-58) for polyatomic gas mixtures containing polar components. He also used a methane-oxygen reaction mechanism containing 29 elementary reactions and 13 species. The effects of equivalence ratio, pressure, initial temperature and transport coefficients on the flame velocity, flame thickness temperature profile and concentration profiles were investigated for a series of methane-air flames. Model predictions were compared with experimental results (63, 64) and were found to be in quite good agreement. It was found that flame characteristics were very sensitive to changes of certain multicomponent diffusion coefficients (eg.  $D_{H,H_2O}$ ,  $D_{H_2,H_2O}$ ) such that an increase of 50% in  $D_{H,H_2O}$  was found to result in a decreasing of the flame thickness

by about 40% and an increase of the flame velocity by more than 100% for a stoichiometric methane-air flame at atmospheric pressure. Neglecting the thermal diffusion ( $D^T$ ) resulted in a decrease of the flame velocity of about 2% and in slight changes in the profiles. It was also found that the concentrations of the radicals H and OH were major factors in determination of flame characteristics and the validity of some chemical rate constants must be questioned.

#### Chemical Reactions Occurring in Methane-Air Flames

In the most simplistic view, the overall chemical reaction occurring in a methane-air flame can be written as



which in fact does describe the reaction, although rather in black box terms, i.e. it accurately describes initial reactants and final products, but gives us no idea of how this overall reaction actually takes place. Fortunately this overall reaction can be broken down into more basic elementary steps which can be studied in greater detail. In fact, the combustion of methane with air has been found to occur through a complex chain reaction scheme with a multitude of individual reactions.

#### Elementary Reactions Mechanism

As is typical in a chain reaction process the methane reaction scheme consists of a chain initiation reaction followed by chain branching and propagation reactions, finally ended by chain termination reactions.

The chain initiation step is now thought to proceed through the following reactions:





Reactions 1 and 3 are most important in lean and stoichiometric flames while reaction 2 becomes important in rich flames. Reaction 4 becomes enhanced with increasing temperature and may become significant at temperatures approaching or greater than 2000 K. In a stoichiometric flame the rate of destruction of  $\text{CH}_4$  by H is about equal to that by OH (65) but H's low concentration precludes it from playing a major role.

The propagation steps involve the consumption of the methyl radicals ( $\text{CH}_3$ ) formed in the initiation reactions. It was first thought (66) that methyl radicals reacted directly with  $\text{O}_2$



Later mechanisms have replaced the above overall reaction by (67)



In addition, methyl radicals can directly oxidize through the following



while at very high temperatures  $\text{CH}_3$  may also dissociate,



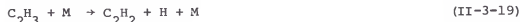
It has also recently been shown that methyl radical recombination (68)



is also responsible for much of the methyl consumption.  $\text{C}_2\text{H}_6$  can be reacted in the following manner (69):







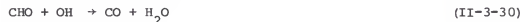
The  $\text{CH}_3\text{O}$  radicals react by means of



with the decomposition reaction providing the major reaction.  $\text{CH}_2\text{O}$  can be removed via the following



with the resultant removal of CHO



Experimental evidence has indicated a large increase in CO as the concentration of  $\text{CH}_4$  decreases (70). It is evident that the CO must be produced from the methyl radicals formed in the initiation step and a possible first step is



followed by



the CO will build up as the  $\text{CH}_3$  is destroyed until the production is overcome by the destruction step



The reactions discussed up to now, which account for the appearance or disappearance of the main species discussed, are all basically of the simple chain type. In addition to these reactions there are the chain branching reactions which lead to the production of the radicals essential for all the other reactions. These branching reactions include



The termination steps of the methane-air flame system would include the following radical recombinations which reduce the contraction of radicals present thereby reducing and ending the reaction.



All of these recombinations are prevalent in methane-air flames with the exception of the H atom recombination which would be much less important in lean flames.

The reactions given in the above section are probably the most important reactions in methane-air flames, with the exception of the  $C_2H_6$  sequence which would only become important in rich flames. Of course this is not a definitive set of equations, as many more combinations of reactions can be thought of, and reaction schemes of up to 100 reactions have been postulated. However it is considered by this author that some intuitive observations can be made on a small reaction set whereas a set of a hundred reactions only tend to cloud the picture unless used in a massive computer code where individual reactions can be varied and the effects observed. Comprehensive compilations of reactions have been obtained for computer calculations and the work of Tsatsaronis (62), Jachimowski and Wilson (69), Smoot et al. (61) and Olson and Gardiner (67) give excellent treatments of large reaction schemes.

#### Production of Excited State Molecules

In emission spectroscopy one observes the light emitted when an excited atom or molecule undergoes a radiative transition to the ground state with the resultant emission of a photon. In a flame there are two basic ways that an excited state molecule can be produced. A molecule can become excited through collisions with other flame gas molecules whereupon the colliding molecules internal molecular energy and translational energy are converted into electronic energy in the other molecule (71, 72). In this case the number of molecules in the excited state is governed by the temperature of the flame and the energy of the excited level involved and is given by Boltzmann's equation.

In the second case an excited state can be produced during a chemical reaction. In most cases the heat of combustion is distributed over the many degrees of freedom of the flame molecules which can then be collisionally transferred to other molecules by inelastic collisions with these molecules resulting in a thermal population. But in certain other cases, a part of the energy released in a particular exothermic chemical reaction is directly converted into excitation energy. In this case the resultant emissions are known as chemiluminescence. This chemiluminescence can be expected to occur in flames because the energy released in many reactions in the flame is of the same order of magnitude as the electronic excitation energy of the molecules (about 2 to 8 eV). In flames both types of excitation mechanisms are present with chemiluminescence processes being more prominent in the primary combustion zone in which the oxidation of the fuel gas takes place. Excellent chemiluminescence studies of non-flame systems have been performed by Polanyi and co-workers (73-75).

OH. In hydrocarbon-air flames the main process for the formation of OH<sup>\*</sup> (excited OH) in the primary reaction zone with high rotational excitation temperature is (5)



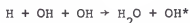
This reaction is exothermic to the extent of about 159 kcal/mole which gives sufficient energy for both electronic and rotational excitation. This reaction was suggested (76) by the observation that high rotational temperatures for OH were only obtained from flames in which CH emission was also strong. It has also been supported by deuterium tracer work (77) and the observation that atomic flames using pure O by titration

did not give strong OH emission but addition of  $O_2$  to these same flames gave strong OH emission (78). The rate constant of this reaction has been measured (79) to be approximately  $1 \times 10^{-3} \text{ cm}^3/\text{molecule sec}$  in low pressure  $C_2H_2$ -air and  $CH_4$ -air flames.

In flames containing hydrogen the inverse predissociation can occur



The strength of this emission depends on the square of the concentration of free atoms (which are in pseudo-equilibrium with each other and ground state OH) and which leads to selective excitation of the  $V' = 2$  and 3 levels. In low temperature flames containing hydrogen the recombination reaction occurs



which results in a normal distribution of rotational and vibrational energy in OH. The rate constant for this reaction has been measured by Belles and Lauver (80) who obtained an average rate constant of  $2 \times 10^5 \text{ liter}^2/\text{mole}^2\text{s}$  for a mixture of 5%  $H_2$  - 95% air in a shock-tube experiment.

Recently (81) the rate constant for the formation of  $OH^*$  by



in a  $H_2/O_2/Ar$  mixture was measured in a shock-tube experiment and was found to be  $1.2 \times 10^{13} \exp(-6940/RT) \text{ cm}^6 \text{ mol}^{-2} \text{ s}^{-1}$ .

CH. For the production of excited CH in flames Gaydon (4) has suggested the following reaction

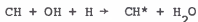


while Hand and Kistiakowsky (82) have given the following reactions

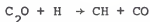


The first reaction is exothermic by 92 Kcal/mole and the last two are exothermic by 62 and 70 Kcal/mole respectively. In a study of  $C_2$ , CH and OH radicals in a low pressure  $C_2H_2/O_2$  flame Bulewicz, Padley and Smith (83) found evidence for the  $C_2$  reaction and obtained an estimated rate constant for this reaction of  $8 \pm 4 \times 10^{-12} \text{ cm}^3/\text{molecules s}$  at a temperature of 2200 K.

Kinbara and Noda (84) studied the time evolution of emission and absorption spectra following flash ignition of a mixture of  $C_2H_2/O^+/NO_2$  and discussed as possible reactions



Another mechanism for formation of ground state CH was given by Becker and Kley (85)



from observations made in a flow-tube system for generation of atomic flames. They suggested that the  $C_2O$  was formed in the reaction



with the HCO formed by hydrogen atom reactions with  $C_3O_2$  and  $CH_2CO$  or by oxygen atoms with  $C_2H_2$ .

A more complicated mechanism for the formation of  $CH^*$  was proposed by Quickert (86) using a two step process

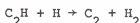


then



He then used this mechanism to explain the experimental results obtained in the room temperature reaction of oxygen atoms with  $C_2H_2$  at low pressure with good correlation to the data.

$C_2$ . The formation of excited molecules in a flame is one of the great unsolved problems in combustion chemistry today. Simple reactions can be written for the formation of  $C_2$  but most are very endothermic and would have difficulty in forming even unexcited  $C_2$ , not to mention the high level of vibrational, rotational, and electronic excitation observed in experiments. Also, isotope studies (87, 88) in  $C_2H_2/O_2$  flames indicate that the two carbon atoms come not from one acetylene molecule but rather from separate carbon fragments. This rules out simple stripping reactions such as



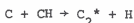
or similar stripping reactions by O atom or OH. At this point in time there is still no generally accepted consensus of how  $C_2^*$  is formed, but there are many proposed mechanisms.

One obvious simple reaction which has been proposed (87)



is indeed sufficiently exothermic (84 kcal/mole) to produce  $C_2$  in an excited state. However quantitative measurements of CH contractions by Bleekrode and Nieuwpoort (89) and Bulewicz, Padley and Smith (83) show such low concentrations of CH that an unconceivably high rate constant ( $2 \times 10^{-9} \text{ cm}^3/\text{molecules s}$ ) is required to explain the observed  $C_2^*$  concentrations.

Another proposed reaction



is also fairly exothermic (61 kcal/mole) but also depends on CH.

The atomic carbon is most likely to be formed by



so that once again the  $\text{C}_2^*$  emission would again tend to depend upon the square of the CH concentration. Fairbairn (88) has discussed the type of reactions forming atomic carbon and proposed for the formation of  $\text{C}_2^*$  the reaction



which is a very endothermic reaction.

A similar type reaction for the formation of  $\text{C}_2^*$  has been proposed by Peeters et al. (90)

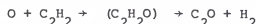


which although exothermic (38 kcal/mole) is probably not energetic enough to form  $\text{C}_2$  in an excited state.

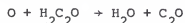
Gaydon and Wolfhard (76) have proposed



to explain the formation of excited  $\text{C}_2$  with the  $\text{C}_2\text{O}$  being formed in a methane-air flame by the following reaction scheme



where  $(\text{C}_2\text{H}_2\text{O})$  is a short lived transition state complex or



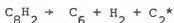
Both of the above reactions involve the atomic carbon species whose formation would not be considered likely on thermochemical grounds, but concentrations of atomic carbon have not yet been measured in flames so these mechanisms remain feasible. These mechanisms, however, have the advantage that the C atoms in the  $\text{C}_2$  are drawn from two different



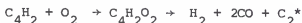
species and would therefore show the randomization of carbon isotopes observed in isotope tracer experiments (87, 88).

Studies of  $C_2$  emission in low pressure hydrocarbon flames have been made by Gaydon and Wolfhard (76) who measured the effect of dilution and also replacement of part of the hydrocarbon fuel by hydrogen or carbon monoxide. In these studies dilution with nitrogen caused a minor decrease in  $C_2$  emission whereas excess oxygen had a strong quenching effect on the emission. When part of the hydrocarbon fuel was replaced with hydrogen or carbon monoxide in the correct amount to remain stoichiometric, it was found that there was a surprisingly rapid fall in the  $C_2$  and CH emissions. This effect was strongest with saturated hydrocarbons, such as  $CH_4$ , and not so strong with unsaturated fuels such as acetylene. Thus in mixed ethane-hydrogen flames the  $C_2$  intensity varied roughly as the square of the ethane concentration whereas in a mixed methane-hydrogen system the  $C_2$  intensity varied with the sixth power of the hydrocarbon concentration. This behavior indicated that the  $C_2^*$  was formed from several hydrocarbon molecules or fragments produced from them.

These observations led Gaydon and Wolfhard to suggest that  $C_2^*$  formation occurred via a polymerization or condensation step in which large polyacetylenes were formed. These large molecules would then decompose exothermically forming  $C_2^*$ , a possible mechanism for  $C_8H_2$  may be

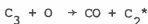


or other reactions might occur such as



Evidence of these large unsaturated molecules occurring in flames has been obtained using mass spectrometry but it still is not a popular mechanism with many researchers in the field.

Savadatti and Broida (91) studied the gas-phase reactions of carbon vapor with a variety of simple gases and their discharge products produced by an electrodeless microwave discharge. The carbon vapor was produced using both arc and resistance heating which provided sufficient carbon vapor to produce bright visible flames. Flames with atomic nitrogen contained only emissions from the CN red and violet systems. Reaction with atomic oxygen gave a brilliant green flame which filled the reaction chamber, indicating a much faster reaction than the case of atomic nitrogen. Spectra of this flame showed very strong  $C_2$  Swan and  $C_3$  (405 nm) bands with weaker CO emissions. When molecular oxygen was used, a green flame, weaker by a factor of 20, was observed which showed all the features of the atomic flame, except  $C_3$  bands. It was proposed that the observed emission of  $C_2$  could be explained by the following reactions:



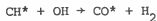
both of these reactions are exothermic with a value of 80.7 Kcal/mole for the first and 87.6 Kcal/mole for the second.

Recently Mann (92) has measured the rate constant for the second reaction in a flow through furnace and obtained a value for the lower bound of  $k > 2 \times 10^{-12} \text{ cm}^3/\text{molecules}$ .

CO. The far ultra-violet bands of the fourth positive bands were observed by Kydd and Foss (93), who observed strong emissions down to 141 nm from low pressure flames of several hydrocarbons including methane. Based upon these observations the reactions



and

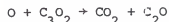
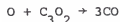


were considered possible.

Becker and Bayes (94) studied CO emission from flames of carbon suboxide ( $\text{C}_3\text{O}_2$ ) and suggested the reaction

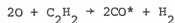


to account for the fourth positive emissions in both the  $\text{C}_3\text{O}_2$  and hydrocarbon flames. It was pointed out in this paper that O atom could react with  $\text{C}_3\text{O}_2$  in the following ways



which results in generation of more than enough  $\text{C}_2\text{O}$  to account for the observed CO emission. The  $\text{C}_2\text{O}$  atomic oxygen mechanism is usually accepted to be the major reaction responsible for the fourth positive emission (4).

Other reactions that have been suggested but not proven include



and the three body recombination



CHAPTER III  
CHEMICAL AND PHYSICAL PROPERTIES OF COAL AND ITS COMBUSTION

Chemical Analysis of Coal

There is general agreement that coal originated through the accumulation of plant debris that was later covered, compacted, and changed into the organic rock that we find today. Due to the differences in plant formations and geological conditions no two coals are identical in nature, composition or origin. The formation of coal from large plant masses via biochemical and geochemical processes is called coalification. The extent of coalification determines the degree to which the original plant material approaches the structure of pure carbon. Most bituminous coal seams were deposited in swamps that were regularly flooded with nutrient-containing water that supported abundant peat forming vegetation. The lower levels of the swamp water were anaerobic and acidic; this environment promoted certain structural and biochemical decompositions of the plant remnants. This microbial and chemical alteration of the cellulose, lignin, and other plant substances, and later depth of burial, resulted in a decrease in the percentage of moisture and a gradual increase in the percentage of carbon content of the mass. This change from peat through the stages of lignite, bituminous, and ultimately to anthracite is characterized physically by decreasing porosity and increasing gelification and

vittrification. Chemically there is a decrease in "volatile matter" content, as well as an increase in the percentage of carbon, a gradual decrease in the percentage of oxygen and as the anthracite stage is approached a marked decrease in the percentage of hydrogen. The progressive changes involved in the coalification process are called an "advance in rank" of coal, and the rank of a coal designates the degree to which the metamorphosis from plant debris to coal has occurred. The highest rank would be pure carbon and the lowest lignite. Table 1 shows the classification of coals by rank (95) showing characteristic properties of each group.

In order to determine the rank of a coal some knowledge of its chemical and physical properties must be known. For practical purposes the chemical composition of coal is always defined in terms of its proximate and ultimate analysis. Neither offers significant information about the molecular structure of coal, but both furnish data that can be correlated with most facets of coal behavior learned from long experience.

Proximate analysis determines 1) moisture contents, 2) volatile matter, (VM), content, 3) ash, inorganic material left behind when all combustible substances have been burned off, and 4) indirectly, the fixed carbon content (FC) which are defined by  $\% \text{ FC} = 100 - (\% \text{ H}_2\text{O} + \% \text{ VM} + \% \text{ ash})$ . Comprehensive reviews of the experimental methods for analysis of coal have been published (96, 97) but in most coal-producing countries national standard techniques are used. In the United States, proximate analysis methods are based on standard methods formulated by the American Society for Testing Materials (ASTM), which are under periodic review.

Table 1  
Coal Classification by Rank

Class	Group	% Carbon (dmmf)	% Oxygen (dmmf)	% Hydrogen (dmmf)	% Volatile matter (daf)	% Moisture (daf)	Btul/lb (daf)
I. Anthracitic	1. Meta-anthracite	>98	1	1.0	<2	<1	>14,000
	2. Anthracite	92-98	2	2.0	2-8	<1	>14,000
	3. Semianthracite	86-92	2	2.5	8-14	<1	>14,000
II. Bituminous	1. Low volatile bituminous	~90	3	3.5	14-22	<1	>14,000
	2. Medium volatile bituminous	~89	3-4	4.5	22-31	<1	>14,000
	3. High volatile A bituminous	80-87	4-10	5.5	31-40	1-2	>14,000
	4. High volatile B bituminous	78-80	10	5.5	31-45	3-5	13,000- 14,000
	5. High volatile C bituminous	76-78	13	5.5	35-45	5-10	10,500- 13,000
III. Subbituminous	1. Subbituminous A	72-76	18	5.0	35-50	10-15	10,500- 11,500
	2. Subbituminous B	72-76	18	5.0	35-50	10-15	9,500- 10,500
	3. Subbituminous C	72-76	18	5.0	35-50	10-15	8,300- 9,500
IV. Lignitic	1. Lignite A	765	30	4.5	40-50	715	6,300- 8,300
	2. Lignite B	765	30	4.5	40-50	715	<6,300

Moisture content (ASTM D 3173-73) is determined by measuring the percentage weight loss of a ground (<60 mesh) 1 gram sample after heating for one hour at  $107 \pm 4^{\circ}\text{C}$  in vacuo or in an inert atmosphere (purified nitrogen). The forms of moisture measured by this method are.

1. Bulk water which is present in large cracks and capillaries and which possesses the normal vapor pressure of water.
2. Physically adsorbed water, which is held in small pores and has a vapor pressure corresponding to its adsorbed state.

Moisture content is determined upon samples that have been allowed to equilibrate under normal laboratory conditions ( $20 \pm 5^{\circ}\text{C}$  and 30 - 60% relative humidity), and this is reported as air-dried moisture content. This differs from natural bed moisture, or capacity moisture, which is the amount of water that a coal will hold when fully saturated at 100% relative humidity (as in an undisturbed coal seam) and thus reflects the total pore volume of the coal accessible to moisture. The usual moisture quantity given is air-dried moisture.

Volatile matter, which varies qualitatively and quantitatively with the rank and composition of the coal, consists of a wide range of low molecular weight hydrocarbons, carbon monoxide, carbon dioxide and chemically reacted water. Except for small amounts of methane and carbon monoxide which may be chemisorbed on the coal, all of these substances form by thermal decomposition of the coal. Table 2 shows typical volatiles released by coal upon heating. Volatile matter is determined (ASTM D 3175-77) by measuring the weight lost when a 1 gram sample (<60 mesh) of coal is heated for 7 minutes at  $950 \pm 20^{\circ}\text{C}$ .

The ash content is determined by measuring the residues left behind when weighed (1 - 2 gm) test samples are completely incinerated in air

Table 2  
Volatile Yields from Bituminous Coal Under Various Conditions<sup>a</sup>

Product	Yield (wt % of coal, as-received)		
	1 atm He	69 atm He	69 atm H <sub>2</sub>
CO	2.4	2.5	-
CO <sub>2</sub>	1.2	1.7	1.3
H <sub>2</sub> O	6.8	9.5	-
CH <sub>4</sub>	2.5	3.2	23.2
C <sub>2</sub> H <sub>4</sub>	0.8	0.5	0.4
C <sub>2</sub> H <sub>6</sub>	0.5	0.9	2.3
C <sub>3</sub> H <sub>6</sub> + C <sub>3</sub> H <sub>8</sub>	1.3	0.7	0.7
Other HC gases	1.3	1.6	2.0
Light HC liquids	2.4	2.0	5.3
Tar	23	12	12
Char	53.0	62.4	40.2

Heating rate, 1000°C/s; average particle diameter, 74µm;

<sup>a</sup>J. B. Howard in "Chem. of Coal Utilization, 2nd Suppl. Volume, M. A. Elliot, Ed. (John Wiley and Sons, New York, 1981).



at  $725 \pm 25^{\circ}\text{C}$  (ASTM D 3174-77). Ash consists of the mineral material in coal which is non-combustible. Table 3 lists minerals found in coal. Typically, mineral matter is randomly distributed in coal as approximately  $2\text{ }\mu\text{m}$  inclusions. In addition to mineral matter, 20-30 trace metals are distributed through the coal. Some metals (boron) are organically bound to the coal molecules; others (zirconium, manganese) form inorganic bonds with mineral matter, while others (copper) occur in both the organic and inorganic forms. Concentrations of 5-500 ppm are typical for trace metals, however some appear at higher levels. Table 4 lists trace metals found in coal and typical concentrations.

The calorific value  $Q$ , which is a complex function of coal elemental composition and rank is usually obtained as part of the proximate analysis of the coal. This is obtained by combusting a weighed sample, usually 1-2 gm, under oxygen (at  $\sim 25\text{ MPa}$ ) in a bomb calorimeter. For adiabatic measurement (ASTM D 2015) the temperature of the calorimeter jacket is continuously adjusted to approximate that of the calorimeter, while in the isothermal procedure (ASTM D 3286) the jacket temperature is held constant and a correction for heat transfer from the calorimeter is applied. In either form of measurement the recorded value of  $Q$  is the gross heat of combustion, since all water generated during the test remains in liquid form. The net value, which is more useful for practical purposes, because water would normally be allowed to evaporate, is obtained by subtracting 1030 Btu/lb of water.

Table 3  
Minerals Found in Coal

Mineral	Formula
<u>Clay minerals (aluminosilicates)</u>	
Kaolinite	$\text{Al}_4\text{Si}_4\text{O}_{10}(\text{OH})_8$
Illite	$\text{KAl}_2(\text{AlSi}_3\text{O}_{10})(\text{OH})_2$
<u>Sulfide and sulfate minerals</u>	
Pyrite	$\text{FeS}_2$
Galena	$\text{PbS}$
Gypsum	$\text{CaSO}_4 \cdot 2\text{H}_2\text{O}$
Kieserite	$\text{MgSO}_4 \cdot \text{H}_2\text{O}$
<u>Carbonate minerals</u>	
Calcite	$\text{CaCO}_3$
Siderite	$\text{FeCO}_3$
<u>Silicate minerals</u>	
Quartz	$\text{SiO}_2$
Zircon	$\text{ZrSiO}_4$
Tourmaline	$\text{Na}(\text{Mg}, \text{Fe})_3\text{Al}_6(\text{BO}_3)_3\text{Si}_6\text{O}_{18}$
<u>Oxide and hydroxide minerals</u>	
Rutile	$\text{TiO}_2$
Hematite	$\text{Fe}_2\text{O}_3$

Table 4  
Trace Metals in Coal

Element	ppm (Avg)
Boron	600
Germanium	500
Bismuth	20
Cobalt	300
Nickel	700
Zinc	200
Lead	100
Silver	2
Tin	200
Molybdenum	200
Cadmium	5
Beryllium	300

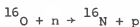
Ultimate or elemental analysis is a quantitative determination of carbon, hydrogen nitrogen, sulfur (organic), and oxygen, which make up the coal substance, and is usually performed using oxidation, decomposition, and/or reduction methods (96, 97). Carbon and hydrogen are usually determined by variations of the conventional Liebig method (98), i.e. by burning a 0.2-0.5 gm sample of coal in pure dry oxygen at 800 to 900°C and completely converting the combustion products to carbon dioxide and water by passing them through heated cupric oxide. The exit stream is then led over hot lead chromate and silver gauze, which removes all oxides of sulfur, and chlorine, and finally sent through absorbers which collect CO<sub>2</sub> and H<sub>2</sub>O. Carbon and hydrogen contents are calculated from the weight increases of the absorbents. Alternative semi-micro methods have been developed which allow for accurate analysis of 50 mg samples in a shorter period of time (99).

Nitrogen is determined using the Kjeldal-Gunning procedure in which the coal (1 gm) is digested with concentrated sulfuric acid and potassium sulfate in the presence of a suitable catalyst (e.g. mercury, a mercury or selenium salt, cobaltic oxide, or perchloric acid). The cooled solution is then made alkaline, and the liberated ammonia distilled into a standard boric or sulfuric acid solution from which nitrogen (as NH<sub>3</sub>) is obtained by back-titration. (100).

Methods for quantitative determination of total (organic and inorganic) sulfur are based on combustion of sulfur containing compounds to sulfate ions, which can be determined gravimetrically or volumetrically. The simplest and most useful (101) is the Eschka procedure (ASTM D 3177) which entails burning the coal sample with a 1:2 mixture of sodium

carbonate and calcined magnesium carbonate in air at  $800 \pm 25^{\circ}\text{C}$ . The resultant sodium sulfate is then extracted with an acid or alkaline solution and precipitated as barium sulfate. In the alternative bomb combustion method (ASTM D 3177) the coal sample is decomposed with sodium peroxide or burned in oxygen at 2-3 MPa. In both cases the proportion of organically bound sulfur in the coal is obtained by separately determining inorganic (sulfate and pyritic) sulfur by the Powell and Parr method and subtracting this from the total sulfur content (102).

Oxygen, the only other element in the organic coal substance is usually reported by difference as  $\% \text{ oxygen} = 100 - (\% \text{ C} + \% \text{ H} + \% \text{ N} + \% \text{ S}_{\text{org}})$  but this value reflects all the errors in previous measurements. Several procedures for direct oxygen analysis have been developed mainly using oxidation or reduction of the coal (103, 104). The most widely used direct method for oxygen is due to Schutze (104) and Unterzaucher (105) and is based on pyrolysis of the coal in nitrogen at  $\sim 1100^{\circ}\text{C}$ . Volatile material released is then passed over carbon at 1100 to  $1200^{\circ}\text{C}$ , and the resultant CO is estimated. Recently it has become practical to determine oxygen content by neutron activation analysis using the reaction



Oxygen concentrations in the coal are then obtained by counting  $\beta$  or  $\gamma$  radiation from the  $^{16}\text{N}$  in the sample and comparing the result with the count for a specimen of known oxygen content (106, 107). This technique has the advantage of being fast and very accurate, but if only organic oxygen is to be determined the sample must be carefully demineralized before being tested.

Since moisture and ash are extraneous to the actual coal substance, analytical data can be expressed on several different bases in order to reflect

- a) the composition of coal as received, air dried, or fully water-saturated coal (at capacity moisture) or
- b) the composition of dry coal: dry, ash-free (daf); or dry, mineral-matter free (dmmf).

To convert data for moist coal to the dry basis, it is necessary to multiply each measured quantity other than moisture by  $100/(100 - \% \text{H}_2\text{O})$  e.g.

$$\% \text{ carbon, dry} = 100 \times \% \text{ C} / (100 - \% \text{H}_2\text{O})$$

Likewise, to convert data for moist coal to the dry, ash-free basis both moisture and ash must be taken into account, such that

$$\% \text{ carbon, daf} = 100 \times \% \text{C} / [(100 - (\% \text{H}_2\text{O} + \% \text{ash}))]$$

However, conversion to the dry, mineral-matter free basis is only possible if the composition of the mineral matter and the actual weight relationship between the original mineral matter and the ash produced from it are known.

### Coal Petrography

Coal is a sedimentary organic rock and is a very complex, heterogeneous mixture of organic compounds and minerals. Rank is thus an oversimplification of the highly heterogeneous nature of the coal substance but is useful to describe gross features. The study of coal as a rock is called coal petrology and the description or classification of coal as a rock is referred to as coal petrography. Coal is not a uniform mixture of carbon, hydrogen, oxygen, sulfur and other elements nor is it a simple uniform polyaromatic polymeric substance. One of the features of coal is that it may be composed of alternating bands of material with

different appearances. It may consist of shiny bands separated by dull bands or layers that are rich in mineral matter (predominantly clays). The nature of these different type bands is dependent upon the various components in the plant material, such as wood, bark, sap leaves, etc., which were used in creation of the coal and the conditions of the coal production.

The basic system of coal petrography used today was developed by M. S. Stopes, a British coal scientist. The nomenclature of Stopes began with a description of the different components of coal visible to the unaided eye, called lithotypes or rock types (108). Vitrain is the most common component of coal and originates from wood or bark. This material forms the uniform, shiny blackbands commonly found in coal and is the main component of bright coals. Clarain is laminated, being composed of shiny and dull bands and has a silky luster. Its origin is variable. Durain is dull, nonreflecting, poorly laminated and of variable composition and origin. It is the hardest component of coal and is a large component of dull coal. Fusain is mineral charcoal, the softest component of coal and is believed to originate from the same material as vitrain. The fate of this material before incorporation into the sediment which became coal is in doubt. Two theories predominate: one that it is the charred remains of wood from forest fires, and the other is that the material was oxidized by bacterial attack near the water line in peat swamps. Fusain is generally found in small amounts in association with other components or lithotypes.

Later Stopes revised her system of nomenclature to include components visible on microscopic examination of polished sections of coal in reflected light (109). The term macerals was suggested for these microscopic components of coal, in analogy to minerals in rocks. Coal could now be thought of as an aggregate of microscopically distinguishable, physically distinctive and chemically different substances called macerals and minerals, with the organic material contained in the macerals and the inorganic in the minerals. Macerals are the smallest subdivision commonly used and are often referred to by their group which can be identified by their -inite endings. Since macerals are derived from different types of substances and often are subjected to different conditions before burial, they were affected to different degrees by the coalification processes that occurred. As rank increases, differences in the properties of macerals become minimized particularly in the anthracitic range.

In bituminous coals there are 3 types of maceral groups which can be broken up into individual types. The vitrinite group originates from plant structural elements, such as wood and bark, which are composed of lignin and cellulose. It is gray in reflected light and the reflectance varies significantly with the rank of the coal. Because most coals contain more than 50% (commonly 75-80%) vitrinite, the gross properties of coals reflect the properties of vitrinite. Three varieties of vitrinite have been recognized to be sufficiently different to warrant their differentiation in a petrographic analysis. The three varieties are vitrinite occurring as bands or lenses (also called telinite,



banded or vitrinite A), vitrinite occurring as a ground mass of attrital coal (collinite, matrix vitrinite, vitrinite B) and pseudo vitrinite. Vitrinite occurring as bands or lenses typically has higher reflectance than associated attrital vitrinite. This band form of vitrinite has less hydrogen and yields less volatile matter than the attrital vitrinite of the same coal (110).

Pseudo vitrinite may occur as either the band or the attrital form. It is recognized in the microscope by its slightly higher reflectance, slitted structure, remnant cell structure, and the presence of serrated edges. First noticed as unfused particles in coke, it was then sought and found in coal (111). It commonly comprises 15-25% of vitrinite in coal and may be as much as 50%. Vitrinite of bituminous rank coals is the fusible component that yields porous coke on pyrolysis, whereas pseudo vitrinite, ranges from fusible to nonfusible (inert). Although it has been shown that some pseudo vitrinite is inert in the coking process (111), it is apparently reactive (converts to liquids) in liquefaction processes (112).

In bituminous coals the exinite or lipinite group are low-reflectance substances of high hydrogen content. Four major categories of exinite have been recognized, and their differentiation is based upon the materials of their origin rather than differences in chemical and physical properties. Sporinite is derived from the exines of spore and pollen grains and is seen under the microscope as thin lenses typically measuring about 2-3 by 5-25  $\mu\text{m}$ . Cutinite is derived from chemically similar material (cuticle) that coats leaves, needles, and some fruiting bodies; it commonly appears in microscopic preparations as elongate strips with serrated edges.

Both sporinite and cutinite have highly polymerized, alicyclic structure, with a significantly higher proportion of hydroaromatic hydrogen than is found in associated vitrinite (113). Resinite is derived from resinous plant materials. Resinites are materials of relatively low reflectance that occur as spherical or ovoid bodies, or as irregularly shaped masses. Resinites originate from hydrogen-rich substances, retain high hydrogen/carbon ratios in coals through the bituminous rank and commonly have a higher hydrogen/carbon ratio than associated sporinites (114). Alginite originates from oil-rich algae. It is relatively rare, being only found in coal layers formed under very wet conditions. The infrared (IR) spectra of alginites are similar to those of resinite, with strong nonaromatic carbon-hydrogen bonds and little evidence of aromaticity (115). Alginite exhibits low reflectance and is distinguished from other exinite macerals by its form, occurring as ovoid bodies with a crenulated border.

The inertinite group, named for its relatively inert behavior on coking, comes from basically the same type of plant components as vitrinite, although this material was strongly affected by oxygen during the early stages of coalification. The reflectance of the inertinite groups is greater than that of the vitrinite group, with a reflectance of about 1-2.5%. The inertinite occurs commonly as discrete particles that except for a small proportion with reflectance near that of the vitrinite, contrast strikingly with the vitrinite. The vitrinite is readily distinguished from the inertinite due to its much larger abundance, its relatively gray appearance, and its form in bands. There are five

classes of inertinite macerals commonly recognized. Sclerotinite is formed from the hard chitinous remains of fungi which were resistant to decay, and relatively reflectant in their natural state. This type maceral is usually found in younger coals. In its most common form sclerotinite occurs as round or ovoid bodies, commonly more than 2  $\mu\text{m}$  in diameter, and more reflectant than associated vitrinite, but seldom exceeding a reflectance of about 1.5%. Often the bodies exhibit an internal cellular structure. Little is known about the properties of sclerotinite, except that its reflectance would indicate that it has a higher carbon content relative to associated vitrinite.

Fusinite or fossil charcoal is believed to have been formed from woody material that was either burned or attacked by bacteria. Semifusinite is similar but differs in the degree of oxidation. Fusinite shows a distinct cellular structure and has a higher reflectivity than semifusinite and the cellular structure is not well defined. Fusinite and semifusinite both have lower hydrogen and higher carbon contents than vitrinite picked from the vitrain bands in the same coal.

Particulate materials with reflectance greater than that of associated vitrinite and which do not exhibit cellular structure have been referred to by a number of different names. According to definitions found in ASTM D 2796 (95) if the maximum dimension of these materials is greater than 10  $\mu\text{m}$ , they are called macrinite; and if less than 10  $\mu\text{m}$  micrinite. Macrinite is a sediment of inert detritus, while micrinite is believed to be a degradation product of protoplasm.

Microlithotypes were introduced to denote typical associations of macerals 50  $\mu\text{m}$  or larger. This has been found to be operationally

useful to recognize certain associations of macerals that occur in particles of crushed coal. Microlithotypes usually contain one to three macerals in varying proportions. The microlithotype concept is predicated on the observations that few coal particles are monomaceralic, and that the reactions of individual coal particles in technological situations are often influenced by the interactions of their constituent macerals and minerals. Where whole particles or portions of particles more than 50  $\mu\text{m}$  thick are uniform in their compositional characteristics, the particle or zone can be classified as a specific type of coal. The classifications of microlithotypes according to the relative proportions of the macerals is given in Table 5.

This identification of the maceral (and mineral) associations in coal particles is potentially useful. Especially in the areas of combustion and liquefaction, the proximity of certain macerals and/or minerals could be as important as the overall maceral composition.

Maceral carbon content (% carbon by weight) increases and the atomic hydrogen to carbon ratio (H/C) decreases in the order: exinite, vitrinite, inertinite (116). Maceral behavior during devolatilization indicates the strong influence of petrography (117). Vitrinite is the plasticizing coke forming portion of the coal structure. Exinite fluidizes and decomposes to tars and gases while inertinite neither plasticizes nor devolatilizes. It has been observed that vitrinite enclosed within relatively inert materials (e.g. mineral matter, inertinite) is not readily liquified because of poor contact with the potential hydrogen-donating solvent. Recently, combustion efficiency has been found to be inversely related to inertinite content,

Table 5  
Common Microlithotypes

<u>Microlithotype</u>	<u>Maceral Groups</u>
Vitrite	Vitrinite
Vitrinertite	Vitrinite + inertinite
Microite	Inertinite, mostly micrinite
Fusite	Inertinite, without micrinite
Sporite	Exinite
Clarite	Vitrinite + exinite
Durite	Inertinite + exinite
Duroclarite	Vitrinite, exinite, inertinite
Clarodurite	Inertinite, exinite, vitrinite

inertinite apparently being responsible for the carbon content of ash particulates (118).

#### Molecular Structure of Coal

In order to understand the complex chemical behavior of coal many researchers have developed various methods (119). Experiments designed to determine the structure and chemistry of coal have been carried on for decades. Much early work consisted of chemical decomposition of coal and solvent extraction to analyze decomposition products in an attempt to understand the basic building blocks of coal structure. A major problem of these techniques was that the coal structure was destroyed and intermediate reactions may have taken place which could modify final products yielding erroneous structures. Since the reaction paths of coal oxidation and reduction were (and for the most part still are) unknown, relationships between reaction products and their precursors were usually speculative. In these circumstances, real progress in understanding the chemical structure of coal became possible with the development of better instrumental techniques, especially non-destructive and modifying techniques such as X-ray diffraction, nuclear magnetic resonance spectroscopy (NMR), reflectance infrared spectroscopy (RIR) and other spectroscopic techniques. These new methods for investigating coal chemistry did not simplify matters, but they offered a means for studying coal without chemically altering it, providing much previously unobtainable information, and for the first time allowed verification of experimental data by cross-checking against data obtained by other

independent methods. Although current ideas of coal molecular structure are still rudimentary and more illustrative than definitive it is at least possible to outline the main features of molecular structure in coal and to identify some significant details at this time.

Much of the work reported in the literature on coal chemistry relates specifically to vitrinite which, while the most abundant component of bituminous coal, is also the most homogeneous maceral. The structural chemistry of exinites and inertinites has been far less studied, and statements about molecular structure in coal must therefore be taken as referring only to a particular constituent. However an analysis of evidence from chemical, spectroscopic and statistical studies leads to the conclusion that coal can be thought of as a natural mixed polymer similar to a complex synthetic copolymer, and that a statistically average coal molecule can be postulated which contains within itself all essential molecular configurations characteristic of the rank of the coal. Individual coal molecules will differ in size and internal organization, so that their diverse components (aromatic, aliphatic, etc.) will not always be present in the same proportions or arranged in the same pattern. And like an incompletely cross-linked three-dimensional copolymer, coal can be separated into fractions that differ from each other in physical properties and, depending on peripheral configurations surrounding the molecular core, may differ in chemical properties also. But in each case the statistically average molecule describes the entire collection,

and to be consistent with the concept of progressive metamorphic development of coal (from lignite to anthracite), the core structure of the average molecule, sub units linked by molecular bridges, changes relatively little upon increasing rank.

Experimental evidence for a polymeric structure for an average coal molecule was given by X-ray diffraction spectra. Coal structures are much too small for single-crystal studies; therefore, all X-ray diffraction interpretation is based upon powder techniques and procedures. The X-ray patterns of coal show diffuse peaks at the positions of the most prominent graphite bands, and the peaks become less diffuse with increasing rank. Although most coals produce patterns with a few diffuse lines, high rank anthracites and meta-anthracites show additional lines identical to those of graphite (120). Exinite and some higher rank coals produce an additional line, which may be quite strong, known as the gamma band. The diffuseness of the X-ray pattern of coal has been attributed to particles in which the arrangement of carbon is that of a graphite crystal, but with extremely small size of the elemental crystallites (121). The similarities to graphite have led to the interpretation that coal consists of very small, graphite like layers packed turbostratically (120). This means that coal contains stacked aromatic layers which are roughly parallel and equi-distant, but with each layer having a completely random orientation in plane and about the layer normals. The gamma band is not related to the graphite structure, and its origin is not understood. Possible explanations are alicyclic structures (122) with parallel stacking or the irregular packing of aromatic layers (123). The gamma band is the most prominent feature



of the exinite pattern. Further X-ray diffraction work (124-126) associated the diffraction maxima with partly ordered aromatic nuclei, the average diameter of these structures in coals with 80-90% carbon is now considered to be no larger than  $7-7.5 \text{ \AA}$  (equivalent to 15-18 carbon atoms or 2-3 condensed benzene rings). On average, only 2-4 nuclei appear to be vertically stacked into crystallites. The generalized average structure then can be deduced from X-ray data and the ultimate elemental composition of coal was one of units of small aromatic nuclei, containing 2-4 rings, linked by hydroaromatic, alicyclic and aliphatic structures and containing various peripheral function groups. Due to their nature X-ray diffraction measurements cannot be used to fill in the remaining chemical structures obtained in a "typical" coal molecule - - only its backbone.

In Table 6 are band assignments in the infrared spectrum of coal showing chemical structures responsible. The following features should be noted:

1. A broad band with maximum near  $3300 \text{ cm}^{-1}$  is due to the OH groups appearing in the organic material since this absorption persists after drying the coal at  $105^{\circ}\text{C}$  for 24 hours (127) or even at these conditions in vacuum. That it consists essentially of phenolic OH seems to be unequivocally proven by the strong decrease in the intensity of this band and by bands which appear at other characteristic positions when the OH groups are acetylated. The position of this band indicates hydrogen bonded OH and must be regarded as an essential feature of the coal structure (128). Strong intramolecular hydrogen bonding cannot be excluded but, as seen from the spectra of model compounds, the

Table 6  
Band Assignments in the IR Spectrum of Coal  
(adapted from ref. 119)

<u>Band Position</u>		Assignment	
cm <sup>-1</sup>	$\mu$		
3300	3	phenolic OH....O -OH str. -OH (Hydroperoxide) -NH str. >NH....N	
3030	3.3	ar. CH str.	
2978 sh.	3.36	CH <sub>3</sub> str.	
2925	3.42	CH <sub>3</sub> str., CH <sub>2</sub> str., al. CH str.	
2860	3.5		
		ar. C=C str.	
1600	6.25		
		C=O....HO-	
1500	6.65	ar. C=C str.	
		CH <sub>3</sub> assym. def.	
1450	6.9	CH <sub>2</sub> scissor ar. C=C str.	
1380	7.25	CH <sub>3</sub> sym. def. C-O str. (phenols) OH def.	
1300	7.7	C <sub>ar</sub> -O-C <sub>ar</sub> str.	
to	to	C-O str. (alcohols)	
1000	10.0	C <sub>ar</sub> -O-C <sub>al</sub> str. C <sub>al</sub> -O-C <sub>al</sub> str.	
900	11.1		
to	to	"aromatic bands"	
700	14.3		

-----  
Continued

Table 6-Continued

$\text{cm}^{-1}$	$\mu$	Assignment
8600	11.6	
820	12.2	ar. HCC rocking (single and
750	13.3	condensed rings)
873	11.5	subst. benzene ring with isolated H
816	12.3	subst. benzene ring with 2 neigh. H
751	13.3	O-subst. benzene ring

ar. = aromatic; al. = aliphatic; str. = stretching; def. = deformation;  
 sh. = shoulder; subst. = substituted.

small intensity and extraordinary band width of the OH absorption in such structures make them generally difficult to detect (129). Hydrogen bonded NH groups may also contribute to the intensity of the band at  $3300\text{ cm}^{-1}$ , but this can be at most a small amount since the total amount of nitrogen in coals is not large.

2. There is no doubt about the assignment of the specific bands occurring in the  $3000$  to  $2800\text{ cm}^{-1}$  region. The very small intensity of the  $3030\text{ cm}^{-1}$  band suggests, on the assumption of high aromaticity in coals, that the aromatic systems present are highly substituted or highly cross linked or both (130). The fact that the band near  $2980\text{ cm}^{-1}$  is only detected as a shoulder led to the conclusion that the  $\text{CH}_3$  content in coals may be small, but  $\text{CH}_3$  groups on aromatic systems absorb mainly at  $2925\text{ cm}^{-1}$  and  $2860\text{ cm}^{-1}$ . Aliphatic  $\text{CH}_3$ ,  $\text{CH}_2$  and  $\text{CH}$  groups all contribute to the intensity of the two bands at  $2925$  and  $2860\text{ cm}^{-1}$  but the dominant contribution may come from  $\text{CH}_2$  groups. At this time it is not possible to determine whether the  $\text{CH}_2$  groups are present in aliphatic chains, in hydroaromatic structures or in cycloparaffins.

3. There is a large very strong band centered at  $1600\text{ cm}^{-1}$  whose assignment remains in doubt. The alternatives for this band are either that the band is due almost solely to the aromatic carbon skeleton (131) or that a significant contribution arises from oxygen containing species in the coal structure (132, 133). The view that this band is due only to aromatic C - C bonds and hence that a high concentration of aromatic carbon is present in coal is based on the following considerations:

- a) A very intense band at  $1600\text{ cm}^{-1}$  occurs also in high molecular weight aromatic petroleum fractions and even in those containing less than 1% oxygen.

- b) The  $1600\text{ cm}^{-1}$  band is not influenced either in intensity or position by acetylation or oxidation of coals which manifests itself in a band near  $1700\text{ cm}^{-1}$ .
- c) The discovery that ether oxygen (as in diphenyl ether) or the oxygen in phenols may produce a marked increase in the intensity of absorption of the aromatic C-C bond (129).
- d) The spectrum of a coal (89%C) has been compared with that of
  - (1) a condensed pitch
  - (2) a high molecular-weight pitch fraction
  - (3) a pitch
  - (4) a mixture of 25 model aromatic substances, and
  - (5) a number of highly condensed aromatic hydrocarbons.

It was found that the optical density of the band at  $1600\text{ cm}^{-1}$  in all of these spectra were about the same with the exception of the pitch. The view that this band is also caused by oxygen containing species is based on the following considerations:

- a) All compounds with strong intramolecular hydrogen bonding in the form of six-membered chelate rings (e.g. hydroxyquinones) or five-membered chelate rings possess very strong absorption at  $1600\text{ cm}^{-1}$ , and the presence of quinone oxygen in coals seems to be proved (134).
- b) Huckel molecular orbital calculations have been used with a bond order concept to show that free carbonyls cannot contribute to the intensity of the band, but show that strongly hydrogen-bonded carbonyls with bond orders of 0.81-0.85 can be expected to absorb in the  $1600\text{ cm}^{-1}$  region (135).

4. The absorption at  $1500\text{ cm}^{-1}$  typical of benzene rings has been clearly established in lignites and subbituminous coals, but could not be observed in bituminous coals (136). This may be explained by the fact that increased substitution on the benzene ring is known generally to weaken this band and the fact that as the degree of condensation increases this band is displaced to smaller wavenumbers and finally disappears in the strong absorption at  $1450\text{ cm}^{-1}$  (137).

5. The strong absorption at  $1450\text{ cm}^{-1}$  may be due in part to  $\text{CH}_2$  groups, but contributions may originate from  $\text{CH}_3$  groups, aromatic C-C bonds, and strongly hydrogen-bonded OH groups.

6. From the rather weak absorption at  $1380\text{ cm}^{-1}$  which can be assigned to  $\text{CH}_3$  groups, it was concluded that the  $\text{CH}_3$  content in coals should be relatively small, but investigations on model compounds have shown that the intensity of this band can vary a great deal. A contribution to this absorption may arise from  $\text{CH}_2$  groups in cyclic structures.

7. The broad and poorly resolved absorption between 1300 and  $1000\text{ cm}^{-1}$  has its origin in the C-O stretching vibration of various ethers but may also contain some aliphatic and aromatic HCC wagging motions.

8. The three bands between 900 and  $700\text{ cm}^{-1}$  which are characteristic of coals of more than 81% carbon are mainly due to aromatic HCC rocking vibrations in benzene and condensed aromatic ring systems. Contributions are also to be expected from the aliphatic HCC rocking motion and may occur from C=C-C in plane deformation vibrations of the carbon skeleton. The bands between 900 and  $700\text{ cm}^{-1}$  have also been interpreted as resulting only from individual benzene rings substituted in various ways (129) as indicated in Table 6.

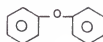
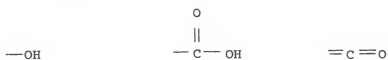
9. From the absence of distinct absorption bands near  $700\text{ cm}^{-1}$ , and the fact that a thin section of a coal studied between 700 and  $900\text{ cm}^{-1}$  showed no infrared active bands, it has been concluded that no long aliphatic chains are present in coal (129).

These observations have been deduced from experimental evidence obtained from many investigations into the infrared spectrum of coals

and an abundance of these spectra have been published in the literature (129, 131-133, 135). Other spectroscopic investigations (138) and wet chemical methods including chemical and electrochemical reduction, catalytic dehydrogenation, reductive alkylation, oxidation, acid-catalyzed depolymerization, alkylation and acylation (139) have been used to obtain a model average molecule of coal. In Figure 3 the basic type molecules and functional groups found in coal are shown. The fundamental carbon backbone structure consists of polynuclear and condensed aromatics such as biphenyl, naphthalene, triphenylene and phenanthrene. A considerable proportion of the potential hydrogen in the condensed aromatic units is substituted. The degree of aromatic substitution varies from about 40% to 70% (140, 141). The substituting hydrocarbon groups are primarily hydroaromatic ring junctions and to a varying extent aliphatic groups. The aliphatic groups include methyl and other alkyl groups as well as methylene, ethylene, and other alkyl bridge structures.

Major oxygen functional groups are the hydroxyl ( $-OH$ ) carboxyl ( $-COOH$ ) and carbonyl ( $-C=O$ ) with lower rank coals containing ether, quinone, methoxyl and heterocyclic oxygen structures. The nitrogen in coal is found in substituted aromatic structures such as ring substituted azines and pyridines also as amine groups attached to aromatic ring clusters. Organic sulfur appears in heterocyclic rings such as thiophenes and occurs as  $-SH$  as a substituent on aromatic rings. Sulfide can also appear as a linking group to connect aromatic clusters.

## Oxygen containing



## Nitrogen containing



## Sulfur containing



Figure 3. Basic Molecular Types in Coal.



A typical bituminous coal (Figure 4) is believed to consist of a series of aromatic/hydroaromatic clusters containing an average of 2-5 rings per cluster and joined by aliphatic structures, such as methylene, ethylene, etc., and also ether and sulfide linkages (142). This arrangement promotes a complex interlocking molecular structure similar to organic polymers. Since the clusters are only loosely connected by aliphatic linkages, clusters will appear on various planes and thus cross linking and development of an extensive pore structure are favored. Pore sizes in coals can range from 200 to 20 Å in diameter. Aliphatic, hydroaromatic and heterocyclic bonds are most susceptible to bond breakage (142); therefore, during heating these structures bear the heaviest responsibility for devolatilization. During carbonization, aromatic carbon is primarily responsible for char formation, while tar comes mainly from hydroaromatic carbon with aliphatic carbon producing CH<sub>4</sub>, CO, CO<sub>2</sub>, H<sub>2</sub>, and higher straight chain hydrocarbons. Chars, the devolatilized portion of the coal, are characterized by highly carbon-rich, polynuclear aromatic structures. In such structures, edge carbons are at least an order of magnitude more reactive than basal carbon due to the availability of unsaturated chemical bonds (143).

#### Combustion of Pulverized Coal Particles in Laminar Pre-mixed Flames

The burning of pulverized coal particles in a flame is a complex mixture of chemical and physical processes. Upon entering the flame a coal particle will heat up until reaching a point where it will undergo devolatilization, the generation of volatile material from the rearrangement of chemical bonds in the coal due to the influence of heating.

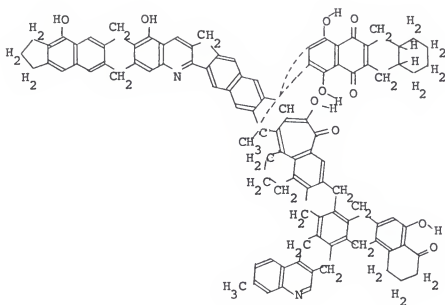


Figure 4. Proposed coal molecule.

Upon forming, the volatiles will leave the coal particle, which is now in a plastic state, causing structural changes to the coal particles. One change is the formation of pores with increased diameters and the formation of cenospheres, hollow spheres formed when coal particles are rapidly heated. Their mass is concentrated in an outer shell, rather than being uniformly distributed throughout the particle, so that internal combustions reactions can occur along with external surface reactions. Once the volatiles have left the coal particle they react homogeneously in the atmosphere surrounding the coal particle to form hot combustion products. Once the volatiles are reacted, or during this process, the remaining solid coal particle, char, undergoes heterogeneous combustion reactions until the carbon is totally consumed and only the non-combustible ash remains.

The nature of these steps and the speed at which they occur are greatly dependent upon the size of the coal particles and its general classification according to rank.

#### Generation and Combustion of Volatile Matter

When coal is heated at a conventional rate ( $0.05^{\circ}\text{C/s}$ ), it appears to decompose, emitting vapors and liquid starting at a temperature around  $350\text{--}400^{\circ}\text{C}$  and the products consist of a carbon-rich residue (char) and a hydrogen-rich volatile fraction. This decomposition continues until a temperature of around  $950^{\circ}\text{C}$  is reached which if maintained for an extended time results in a residue of nearly pure carbon, with a structure resembling that of graphite. The accumulated volatiles are composed of various gases and liquids whose proportions depend on the coal type and the manner of heating.

Given (142) postulated that the volatiles would be created during pyrolysis in the following steps:

- 1) a low temperature (400-500°C) loss of hydroxyl groups
- 2) dehydrogenation of some of the hydroaromatic structures
- 3) scission of the coal molecules at the methylene bridges, and
- 4) rupture of the acyclic rings.

Wiser et al. (143) postulated a sequence of events initiated by the formation of free radical species from a thermal cracking of the linkages forming the aromatic clusters. These free radical species would then stabilize through a rearrangement of atoms within a fragment or by colliding and reacting with another species. The resultant structure, depending on its vapor pressure, would either evolve as volatile material or remain as part of the remaining char. Typical volatiles evolved upon heating coal are listed in Table 2 (119).

In the early 1960's various researchers found that rapid heating ( $1000-10^5$  C/s) techniques for coal permitted substantially more volatiles to be generated than the traditional slow heating methods used in proximate analysis (144-147) and that the liquid and tar fractions were the most strongly influenced. The effective volatile content of a coal must be distinguished from volatile matter (VM), determined by proximate analysis, when the conditions of combustion differ significantly from those of the proximate test. It is incorrect to associate VM with the potential yield of volatiles from pulverized coal particles widely dispersed in a hot gas. The volatiles escaping from particles in the packed bed used in proximate analysis undergo secondary reactions including cracking and carbon deposition on solid surfaces, and the extent of such reactions within the bed is not well established.

Badzoich and Hawksley (147) observed that the yield of volatiles from pulverized coal particles entrained and rapidly heated to 950°C in a preheated inert gas ( $N_2$ ) exceeded the loss of proximate volatile matter found from the difference between the proximate volatile matter of coal and that of char. The results for several different coals were correlated by the empirical relation

$$V^* = Q(1 - VM_C)VM$$

where  $V^*$ , expressed as weight fraction of the original coal, is the ultimate yield of volatiles achieved by heating the coal for an infinite time ( $t = \infty$ ), approximated by measurements at long residence times;  $Q$  is the ratio of total weight loss to loss of proximate volatile matter; and  $VM_C$  is the fraction of the initial proximate volatile matter remaining in the char at  $t = \infty$ . Experimental values of  $Q$  varied from 1.3 to 1.8 depending on coal type, which led to values of  $V^*/VM$  greater than 1. Kimber and Gray (148) extended the measurements to 2000°C and found  $Q$  values from 1.3 to 1.95. The observation of volatile yields exceeding proximate volatile matter is consistent with the results of other investigators who rapidly heated pulverized coal particles dispersed in gas or held in monolayers or thin beds (145, 149).

Earlier work (143, 150) seemed to indicate that the yield of pyrolysis products, for reasonably long experimental times, becomes independent of temperature above about 1000°C. However recent data (148, 151, 152) obtained at higher temperatures suggest that additional devolatilization in relatively short times may be observed by heating the coal to temperatures well beyond 1000°C. This conclusion seems reasonable because the absolute time required for a given degree of

completion of devolatilization is much less for the higher temperatures. For example, the heating of a coal from  $1000^{\circ}$  to  $1900^{\circ}\text{C}$  might produce in fractions of a second an additional weight loss that at  $1000^{\circ}\text{C}$  could only be obtained in times too long to be measured in laboratory experiments. Also the slower rate of volatiles production from the coal particles at the lower temperature might present a larger opportunity for secondary cracking reactions and carbon deposition, which could eliminate the possibility of ever attaining the weight loss achievable at a higher temperature.

The complex molecular decomposition and transport phenomena involved in coal devolatilization and the relatively meager experimental data available on these processes have led to rather inexact theoretical descriptions of the devolatilization mechanism with many various simplifying assumptions called upon. Many authors have approximated the overall process as a first-order decomposition occurring uniformly throughout the particle. The rate of devolatilization is given by:

$$\frac{dV}{dt} = k (V^* - V) \quad (\text{III-1-1})$$

where  $V$  is the cumulative amount of volatiles produced up to time  $t$ , expressed as weight fraction of the initial coal,  $k$  is the rate constant, and  $V$  approaches  $V^*$  as time becomes infinite.  $V^*$  represents the effective volatile content of the coal which should not be confused with the VM content found by proximate analysis. The rate constant is correlated with temperature by an Arrhenius type expression..

$$k = A e^{-E/RT} \quad (\text{III-1-2})$$

where  $A$  is the pre-exponential factor,  $E$  is the apparent activation energy,  $R$  is the gas constant and  $T$  is the absolute temperature.

Most kinetic studies have focused upon the determination of  $k$  and  $V^*$ , finding little agreement on the observed rates of pyrolysis, with several orders of magnitude difference at a given temperature.

Other authors have contended that a simple first order model is inadequate to describe experimental results. Stone et al. (150) improved the utility of Equation (II-1-1) by describing pyrolysis as a series of several first-order processes occurring in different time intervals, which are dependent upon coal type and temperature of volatilization. Wiser et al. (143) used an  $n$ th-order expression to describe devolatilization:

$$\frac{dV}{dt} = k(V^* - V)^n \quad (\text{III-1-3})$$

and found that  $n=2$  gave the best fit to their data over the first 3600 s of weight loss, whereas  $n=1$  was better for longer times. Skylar et al. (153) used the equation of Wiser et al. (143) to fit nonisothermal pyrolysis data for different coals and found that values of  $n$  from 2 to 8 were needed for good correlation. Pitt (154) used an empirical relation

$$\frac{V^* - V}{V^*} = A - B \log(t) \quad (\text{III-1-4})$$

where  $A$  and  $B$  are constants, to correlate his pyrolysis data on different type coals.

One of the serious problems with the above first order approximation is that it fails to describe the experimental result that the apparent value of  $V^*$ , is a function of temperature, a fact that is neither mechanistically correct or mathematically treatable by these equations. As is reflected in the time zone theory of Stone et al. (150) the relatively slow rate of weight loss observed after extended times at a given temperature requires a set of parameter values that differ greatly from those that fit the behavior at short times and higher temperatures.

Since coal devolatilization is not a single step process but rather is a multiplicity of overlapping decompositions, yielding volatiles in different time intervals for isothermal pyrolysis, or in different time and temperature intervals for the usual case of pyrolysis during heat up, any one set of parameter values for these equations cannot be expected to represent data accurately over a wide range of conditions.

It had become evident that a multiple-reaction model was necessary to model the actual conditions occurring during devolatilization and that it should also be applicable to nonisothermal conditions which are representative of actual physical conditions of pulverized coal combustion. Neither Wiser et al. (143) or Badzioch and Hawksley (147) considered the difficult integration involved in nonisothermal cases where heat up is not instantaneous, claiming little decomposition had occurred during their rapid heat up and neglecting any that might have occurred. The problem of how to include, in kinetic studies, the weight lost during heat up had baffled many researchers attempting to evaluate coal devolatilization on an isothermal basis.

Pitt (154) and later Rennhack (155) adapted Vand's (156) treatment of a large number of independent, parallel rate processes to describe the pyrolysis of coal particles in a flame. The thermal decomposition of coal was assumed to consist of a large number of independent chemical reactions representing the rupture of various bonds, forming volatiles, within the coal particle. Differences in the strengths of chemical bonds throughout the coal molecule accounted for the occurrence of different reactions in different temperature intervals. Since the thermal decomposition of a single organic species is usually described as an irreversible reaction that is first-order in the amount of



unreacted material remaining, the rate of volatiles evolution originating from a particular reaction within the coal can be described in a similar manner to Equation (III-1-1) with  $i$  denoting one particular reaction out of many such that.

$$\frac{dV_i}{dt} = k_i (V_i^* - V_i) \quad (\text{III-1-5})$$

if  $k_i$  is of the form of Equation (III-1-2) integration of Equation (III-1-5) for isothermal conditions yields,

$$V_i^* - V_i = V_i^* \exp(-k_i t \exp -E/RT)_i \quad (\text{III-1-6})$$

for the amount of volatiles remaining to be released. Values of  $k_i$ ,  $E_i$  and  $V_i^*$  cannot be predicted and must be estimated from experimental data, which become more complex as more reactions are used. The problem can be simplified if it is assumed that the  $k_i$ 's differ only in activation energy and that the number of reactions is large enough to permit  $E$  to be expressed as a continuous distribution function  $f(E)$  with  $f(E)dE$  representing the fraction of the potential volatile loss  $V^*$  that has an activation energy between  $E$  and  $E+dE$ . Then  $V_i^*$  becomes a differential part of the total  $V_i^*$  and may be written as

$$dV^* = V^* f(E) dE \quad (\text{III-1-7})$$

with

$$\int_0^{\infty} f(E) dE = 1 \quad (\text{III-1-8})$$

The total amount of volatile matter remaining to be released is obtained by summing the contribution from each reaction or by integrating Equation (III-1-6) over all values of  $E$  using Equation (III-1-7) obtaining

$$\frac{V^* - V}{V^*} = \int_0^{\infty} \exp \left[ -k_0 t \exp \left( \frac{-E}{RT} \right) \right] f(E) dE \quad (\text{III-1-9})$$

Equations (III-1-6) and (III-1-9) can be generalized to allow for nonisothermal processes:

$$V_i^* - V_i = V_i^* - \int_0^+ k_i dt \quad (\text{III-1-10})$$

$$\frac{V^* - V}{V^*} = \int_0^\infty \exp \left( - \int_0^+ k dt \right) f(E) dE \quad (\text{III-1-11})$$

Also,  $f(E)$  can be approximated as a Gaussian distribution with mean activation energy  $E_o$  and standard deviation  $\sigma$  obtaining

$$f(E) = \left[ \sigma(2\pi)^{1/2} \right]^{-1} \exp \frac{-(E-E_o)^2}{2\sigma^2} \quad (\text{III-1-12})$$

Assuming that  $k_i = k_{oi} \exp(-E_i/RT)$  with  $k_{oi} = k_o$  for all  $i$ ,

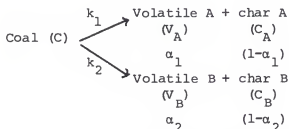
Equations (III-1-11) and (III-1-12) give

$$\frac{V^* - V}{V^*} = \frac{1}{\sigma(2\pi)^{1/2}} \int_0^\infty \exp \left[ -k_o \int_0^\infty \exp \left( \frac{-E}{RT} \right) dT - \frac{(E-E_o)^2}{2\sigma^2} \right] dE \quad (\text{III-1-13})$$

Equation (III-1-13) allows correlation of coal devolatilization data using four parameters ( $V^*$ ,  $E_o$ ,  $\sigma$ ,  $k_o$ ) which is only one more than required by the single step model represented by equations (III-1-1) and (III-1-2). However the use of this slightly more complicated equation eliminates the temperature dependence of  $V^*$  and allows data on a given coal under different sets of experimental conditions to be compared with one set of parameter values. The simple model required a different set of parameter values for each set of experimental conditions, hindering analysis of different sets of data on different coal types.

An alternative approach to modeling coal devolatilization has been to assume the existence of competitive reactions by which the decomposing coal may follow any number of reaction paths depending on the

temperature-time pattern. One model of the devolatilization process developed by Kobayashi et al. (151) considers the coal to degrade into a residue (char) and a volatile component via two competing reactions forming char A and volatile A along with char B and volatile B via the following mechanism:



The  $\alpha_1$  and  $\alpha_2$  are mass stoichiometric coefficients and the pseudo rate constants are given by

$$k_1 = B_1 \exp (-E_1/RT)$$

$$k_2 = B_2 \exp (-E_2/RT)$$

where  $B_1$  and  $B_2$  are pseudo frequency factors and  $E_1$  and  $E_2$  are pseudo activation energies. The A reaction is assumed to dominate at relatively low temperatures and leads to a certain volatiles yield. Reaction pathway B, which has a higher activation energy than path A (60.0 kcal/mole vs 17.6 kcal/mole), becomes more important at higher temperatures ( $> 1200^\circ\text{K}$ ) and also results in more volatiles than reaction A. The overall weight loss is given by

$$\Delta W = \frac{m_{V_A} + m_{V_B}}{m_C} = \int_0^\infty (\alpha_1 k_1 + \alpha_2 k_2) e^{\left[ \int_0^\infty (k_1 + k_2) dt \right]} dt \quad (\text{III-1-14})$$

where  $m_C$  is the d.a.f mass of the raw coal, and  $m_{V_A}$ ,  $m_{V_B}$  the mass of the generated volatiles. Thus this model accounts for the observed increases in volatile yields with increasing temperature and has been shown to accurately represent actual experimental results (151).

The use of multiple independent parallel first-order reactions to describe the evolution of a volatile component was presented by Suuberg et al. (157) who started with equation (III-1-5) and used a series of reactions  $i$ . Assuming that the rate constant for reaction  $i$  was given by  $k_i = k_{oi} \exp(-E_i/RT)$ , the contribution of reaction  $i$  to the rate of evolution of the product evolved up to time  $t$  for isothermal conditions is given by:

$$dV_i/dt = V_i^* k_{oi} \exp\left(\frac{-E_i}{RT}\right) \exp\left(-k_{oi} t \exp\left(\frac{-E_i}{RT}\right)\right) \quad (\text{III-1-15})$$

$$V_i = V_i^* \left[ 1 - \exp\left(-k_{oi} t \exp\left(\frac{-E_i}{RT}\right)\right) \right] \quad (\text{III-1-16})$$

Here  $V_i$  is the amount of volatile product evolved from reaction  $i$  at the time  $t$ , and  $V_i^*$  is the value of  $V_i$  at  $t = \infty$ . The total yield of volatiles, the yield measured experimentally, is given by

$$V_{\text{Total}} = \sum_i V_i \quad (\text{III-1-17})$$

If the coal is heated at a constant rate  $dT/dt = m$  to a temperature  $T$  and maintained for a holding time  $\tau$  at this temperature, the evolution rate and amount of volatiles evolved becomes:

$$\frac{dV_i}{dt} = V_i^* k_{oi} \exp\left[\frac{-E_i}{RT} - k_{oi} \left(\frac{RT^2}{mE_i} + \tau\right) \exp\left(\frac{-E_i}{RT}\right)\right] \quad (\text{III-1-18})$$

$$V_i = V_i^* \left\{ 1 - \exp\left[-k_{oi} \left(\frac{RT^2}{mE_i} + \tau\right) \exp\left(\frac{-E_i}{RT}\right)\right] \right\} \quad (\text{III-1-19})$$

where  $m > 0$ .

It should be noted that the predicted behavior occurring during heating at a constant rate is equivalent to that of an isothermal process of duration  $RT^2/mE$  at the peak temperature attained. Since  $RT/E \ll 1$ , the equivalent isothermal time at the peak temperature is much less

than the time to heat up, which is of the order of  $T/m$ . Also the extent to which most of the reaction occurs at or near the peak temperature increases with decreasing  $RT^2/mE$ .

Derivation of kinetic parameters for the evolution of individual products of coal not only is an effective modeling technique, but offers the potential of helping to identify the decomposition reactions responsible for each product. However progress towards understanding the complete chemical and physical processes occurring is hindered by the large disagreements in parameters determined by different authors (150-157).

One reason for the discrepancy in the kinetic parameters calculated may be caused by secondary reactions occurring during volatile formation (158). Anthony et al. (146) derived a selectivity expression describing assumed competition between diffusional escape and secondary reactions in developing an approximate model for the effect of secondary reactions on the production of volatiles. In this model they defined two types of volatiles, reactive  $V_r$  and nonreactive  $V_{nr}$ . In an inert atmosphere the material balance on the reactive volatile species present in a coal particle is

$$\frac{dV_r'}{dt} - k_c (C - C_\infty) - k_i C = \frac{dC}{dt} \quad (\text{III-1-20})$$

where  $dV_r'/dt$ , the formation rate of reactive volatiles expressed as mass fraction per unit time, represents an irreversible decomposition reaction dependent on temperature and unaffected by the atmosphere containing the decomposing coal particle.  $C$  and  $C_\infty$  are vapor phase concentrations of reactive volatiles in the void volume of the coal

particle and in the ambient gas, respectively, expressed as mass per unit mass of original coal,  $K_c$  is the overall mass transfer coefficient ( $s^{-1}$ ) and  $k_1$  is the overall rate constant ( $s^{-1}$ ) of the deposition reaction, assumed to be first order. In the above equation the coal particle is assumed to possess a fixed internal void space, caused by pores and cracks, of uniform composition and temperature. Reactive species released by thermal decomposition of the coal particle enter this void volume and leave either by mass transfer to the surrounding gas or by solid deposition. Since the mass of the reactive species residing in the vapor phase within the particle is relatively negligible a pseudo-steady state condition exists so that  $dC/dt = 0$ . If  $C \approx 0$ , the above equation becomes

$$\frac{dV_r}{dt} - K_c C - k_1 C = 0 \quad (\text{III-1-21})$$

Since the loss of reactive volatiles from the particle is  $V_r^*$ , then  $dV_r/dt = K_c C$  and from equation (III-1-21)

$$dV_r = \frac{dV_r^*}{(1+k_1/K_c)} \quad (\text{III-1-22})$$

Assuming that  $K_1/K_c$  is independent of the temperature-time history, integration of equation (III-1-22) from  $t = 0$  to  $t = \infty$  gives

$$V_r^* = \frac{V^{**}}{(1+k_1/K_c)} \quad (\text{III-1-23})$$

where  $V_r^*$  is the potential ultimate yield of reactive volatiles with no mass deposition at infinitely long reaction time, likewise  $V_r^*$  is the actual ultimate yield of reactive volatiles at infinitely long reaction time. The mass transfer coefficient is assumed to be proportional to the diffusion coefficient of the volatiles, so that  $K_c = K_c/P$ , where  $P$  is

total pressure. Since  $V^*$  and  $V_{nr}^*$  are the ultimate yields of total volatiles and nonreactive volatiles and  $V^* = V_r^* + V_{nr}^*$ , using equation (III-1-23) one obtains:

$$V^* = V_{nr}^* + V_r^{**} (1 + k_i p/K_c)^{-1} \quad (\text{III-1-24})$$

this relation predicts the approach of  $V^*$  asymptotically to  $(V_{nr}^* + V_r^{**})$  and  $V_{nr}^*$  at low and high pressures, respectively. The variation with pressure of the observed yields of total volatiles obtained experimentally (146) is consistent with this asymptotic behavior.

Although equation (III-1-24) is consistent with the observed effects of pressure, the underlying description of the complex mass transfer and secondary reactions is highly simplified and the mechanistic details are concealed in the ratio  $k_i/K_c$ . The escape of volatiles from a particle is not a simple diffusion process but a complex process involving a time-dependent pore structure and hydrodynamic flow during the period of rapid devolatilization. To account for this behavior, Lewellen (159) developed a bubble transport model for volatiles flow in coal particles. The model describes the nucleation, growth, coalescence, and escape of volatiles-filled bubbles under the influence of viscous forces, pressure, and surface tension. Mass is added to the bubbles by volatile formation and lost through mass deposition accompanying secondary reactions at the bubble surface.

General observations that can be made from devolatilization studies are (143-153).

- 1) A high heating rate will promote the creation of volatiles in excess of the amount found by proximate analysis.

- 2) A high final temperature ( $> 1000$  K) will also increase the volatile production as well as increase the speed of formation with greater yields found at higher temperatures ( $>1500$  K).
- 3) Pyrolysis of coal particles in the presence of hydrogen results in a higher yield of volatiles at a much faster rate than pyrolysis in inert atmospheres (160). The species that react with hydrogen during pyrolysis are not clearly identified and are referred to in the literature as rapid-rate carbon. Evidence suggests that hydrogen interferes with the char forming secondary reactions, presumably by hydrogenating reactive fragments to form light hydrocarbons sufficiently stable to avoid the secondary char-forming reactions.
- 4) The size of the coal particle determines the amount of volatiles produced with small particles ( $< 200 \mu\text{m}$ ) yielding more % by weight loss than large particles ( $> 200 \mu\text{m}$ ). Ubhayaker et al. (152) measured volatiles produced by coal particles of  $20 \mu\text{m}$  and  $100 \mu\text{m}$  in a hot gas at a temperature of  $1700^\circ\text{C}$  and found that the yield of volatiles from the small particles exceeded that from the large by 14 weight % of the coal after 7 ms. Greater differences have been observed for larger particles (161) and this behavior apparently reflects an increased extent of secondary reactions and carbon deposition for larger particles, which is consistent with the idea that larger particles offer more resistance to the escape of volatiles giving more time for secondary reactions to occur.

Once the volatiles have been formed and leave the coal particle in a normal flame environment, they will start to react with the oxidizing atmosphere surrounding the particle and begin to burn. The combustion reaction scheme that occurs is very similar to the reactions present in the methane-air flame presented in Chapter II. Due to the fact that the majority of the volatiles are  $\text{CH}_4$ ,  $\text{H}_2$ , and  $\text{CO}$ , no modifications of this reaction scheme are deemed necessary by this researcher or others (160-163). One consequence of the devolatilization process is that it can not always be considered separately from the heterogeneous reaction of the solid coal particles. The flux of volatiles leaving a coal particle can be large enough to reduce the rate of carbon consumption at the surface.



If the rate of volatiles evolution is slow, then oxygen will readily reach the particle surface to react. On the other hand at high rates of devolatilization, the gaseous volatiles can effectively screen the coal particle from oxygen attack. The volatiles leave the particle surface and subsequently burn in a flame layer which surrounds the particle. As the devolatilization decreases, the flame front recedes towards the surface of the particle and eventually stabilizes there, allowing both heterogeneous and homogeneous reactions to occur simultaneously. For any given type of coal, the rate of volatile production has been found to vary with particle size. For bituminous coal particles, Howard and Essenhigh (164) found that particles larger than about 65  $\mu\text{m}$  did not react heterogeneously during the period of rapid devolatilization.

#### Combustion of Solid Devolatilized Coal Particles (Char)

The combustion of a devolatilized coal particle (char) can be considered to occur in the following steps:

- 1) Diffusion of the oxidant molecules to the surface of the coal particle.
- 2) Transfer of the oxidant molecules from the gaseous phase to the surface of the particle.
- 3) Chemical reaction of the oxidant with the char surface.
- 4) Transfer of the products back to the bulk of the gas.

At any time in the combustion of coal particle the mass rate of consumption of carbon per unit area of external surface of the particle,  $R_T$ , is given by the expression.

$$R_T = 1 / \left( \frac{1}{R_{mt}} + \frac{1}{R_{chem}} \right)$$

where  $R_{mt}$  is the rate which would be observed if the oxidant molecules were to react to form a gaseous product instantly on reaching the

particle surface and  $R_{\text{chem}}$  is the corresponding rate if the oxidant molecules were to encounter negligible resistance in their transfer to the surface but take a finite time to react.  $R_{\text{mt}}$  and  $R_{\text{chem}}$  thus represent the limiting mass-transfer-controlled and chemically-controlled rates respectively.

Early workers such as Nusselt (165), proposed that the oxidation of a coal particle was controlled by diffusion of oxygen through a stationary film to the surface of the particle where it reacts to form CO and/or  $\text{CO}_2$ . A double film model was proposed by Burke and Schuman (166) who postulated that carbon reacts at the surface of the particle with  $\text{CO}_2$  producing CO which is burned in a thin flame front in the boundary layer. No oxygen will reach the particle surface and no CO will reach the boundary layer in this theory and the mass flows are the rate limiting step. These theories also assumed that the coal particle had a solid smooth surface and internal reactions were neglected.

Today, there is now general agreement that reaction control by diffusion is limited to coal particles above about 100  $\mu\text{m}$  in diameter and that the reaction is partially or totally internal (167). Opinions are divided whether the particles burn at constant diameter or with reducing diameter but all agree that the temperature coefficient of the chemically-dominated reaction is high, with activation energies typically quoted in the region of 20 to 60 Kcal. While it has been shown that the rate determining step is a chemical one, the question becomes whether it is the absorption or desorption step that limits the rate of reaction.

An understanding of the overall kinetics of char-gas reactions requires an appreciation for the detailed interactions between gas and solid. These interactions will be discussed in a normal pulverized coal flame where the oxidizing molecules are obtained from air. In early models of gas surface reactions it was common to assume that the surface is more or less uniform, which is far from being the case for combustion of a char particle which contains nearly 25-50% of its volume in pores, dependent upon the coal type (168).

The simple concept of a gas absorbing at a solid surface to form an adsorbed layer which then decomposes after a finite time to yield reaction products has been conceptually elaborated in a number of different ways in the past (169, 170). There are however, only two alternatives for initial adsorption step on coal carbon:

- 1) That the ambient molecules ( $O_2$ ,  $CO_2$ ,  $H_2O$ ,  $H_2$ ,  $CO$ , etc.) present or formed by reactions) adsorb as molecules or,
- 2) That these molecules dissociate as they adsorb.

Investigations during the 1970's have led to the consensus that molecular chemisorption does not occur and that all chemisorption is dissociative, even if mobile. Adsorption of these species is not uniform over the surface of the particle with preferential adsorption occurring on the edge carbons of the coal molecules with basal carbon atoms showing little or no activity for adsorption. When measuring surface area of coal particles it is necessary to distinguish between active and inactive areas. The total surface area (TSA) can be divided into three regions:

- 1) The basal planes, where there is little or no reaction occurring, and no chemisorption film forming.
- 2) The reacting chemically active surface (RASA) where there is again little or no chemisorption film because reaction is so fast that the residence time of the oxygen atoms is negligible.

- 3) The unreacting chemically active surface (UASA), which is covered by adsorbed oxide film, where the reaction initially takes place.

The evidence for the absence of molecular chemisorption is partly direct and partly inferential. Evidence from isotropic tracer studies using  $^{14}\text{C}$  (171-173) and  $^{13}\text{C}$  (174) show that CO is not chemisorbed to any important extent while oxygen isotope studies (175-177) likewise have shown that neither  $\text{O}_2$  nor  $\text{CO}_2$  chemisorbs as molecules. Walker et al. (177) studied nine possible reactions for the formation of  $\text{CO}_2$  using mixtures of oxygen containing  $^{16}\text{O}$ - $^{16}\text{O}$ ,  $^{18}\text{O}$ - $^{18}\text{O}$  and  $^{16}\text{O}$ - $^{18}\text{O}$  in different proportions reacting with carbon. Oxygen with 2.6%  $^{16}\text{O}$ - $^{18}\text{O}$  was found to produce 50-52% of  $\text{C}^{16}\text{O}^{18}\text{O}$ , matching the percentages of the  $^{16}\text{O}$  and  $^{18}\text{O}$  percentages in the original mixture. If molecular chemisorption and reaction had occurred the percentage in the mixed isotope  $\text{CO}_2$  should be 2.6%. Bonnetain et al. (178) found that the volumes of CO and  $\text{CO}_2$  produced varied linearly with each other and also concluded that groups of molecules desorbed together on account of electronic interaction in the graphite surface. The dissociative chemisorption of  $\text{H}_2$  has not been explicitly demonstrated, rather it is implied from the agreement with dissociative adsorption isotherms (179).

The finding that molecular chemisorption does not occur allows one to reduce the large set of multiple equations considered by past reviewers (e.g Walker et al. (180): 14 reactions). Another simplifying assumption that can be made is that the oxide film formed by dissociative adsorption has the same structure whether the O atoms are supplied by  $\text{O}_2$ ,  $\text{CO}_2$ ,  $\text{H}_2\text{O}$  and possible OH. The film formed can thus be represented in each case as  $\text{C}(\text{O})$  with no labeling of where the oxygen originated,

as some writers have done in the past. No matter what its origin the C(O) should decompose in the same way. The net reaction steps for the adsorption and desorption process in oxygen transfer are now considered

to be:



where  $C_F$  indicates a free active site, C(O) represents chemisorbed oxygen atoms and the k's are rate constants. Reaction (III-2-1) represents dual site adsorption, reaction (III-2-6) represents dual site desorption, and reaction (III-2-7) represents a surface migration of an adsorbed oxygen atom to another site. Equation (III-2-1) also

represents irreversible chemisorption of oxygen, with no film decomposition to recover free oxygen.

Although the above reaction scheme is a reasonable explanation of the overall reaction process, reactions such as (III-2-2) and (III-2-3) may be composed of several steps with the reverse action occurring by a different route than the forward reaction. In dissociative adsorption the gas may dissociate as it adsorbs, or before it adsorbs as an intermediate independent step. Thus, for equation (III-2-2) we may write:



the reverse reaction would have great difficulty retracing the same intermediate path and a more likely reverse path may be given by.



which implies that equation (III-2-2) should be written as two independent, irreversible reactions. For equation (III-2-3) it is very likely that the  $H_2O$  will dissociate into  $OH$ , as suggested by Long and Sykes (179) who also postulated that molecular hydrogen would be formed on the surface as a result. In order to describe these occurrences equation (III-2-3) can be written as a reversible reaction sequence:



Molecular dissociation leading to dual site adsorption and single site desorption are probably the most important process occurring in the combustion of coal particles. In active site ( $C_F$ ) theory one usually presumes the following:

- 1) Localized adsorption occurs via collisions with vacant active sites ( $C_F$ );
- 2) One adsorbed molecule or atom per site due to strong valence bonds;
- 3) A constant surface (chemisorptional migration/desorption) mechanism;
- 4) Surface coverage less than a complete monomolecular layer.

Compared to physical adsorption, chemisorption is characterized by a higher heat of adsorption, a slower rate on account of having an activation energy typical of any chemical reaction, and occurrence at much higher temperatures than physical adsorption, which should only occur at temperatures close to the boiling point of the adsorbate due to the weaker forces involved (van der Waal's forces).

The mathematical model used to model the high temperature gas-solid reactions occurring during char combustion was developed by Langmuir (for single site mechanisms), and later extended by Hinshelwood to include dual site mechanisms. The following three assumptions were made in Langmuir's derivation (169, 170).

- 1) The adsorbed entities are attached on the surface of the adsorbent at definite, localized sites, through collision of gas molecules with vacant sites;
- 2) Each site can accommodate one and only one adsorbed entity;
- 3) The energy of the adsorbed entity is the same at all sites on the surface, and is independent of the presence or absence of other adsorbed entities at neighboring sites.

Langmuir assumed a dynamic equilibrium between adsorbate molecules in the gas phase at a pressure  $p$ , and the adsorbed entities in the surface layer; the fraction of sites covered equal to  $\theta$ . The number of molecules colliding with the adsorbent surface per unit area per unit time is proportional to the pressure. The rate of adsorption

is proportional to  $p(1-\theta)$ , and the rate of desorption is proportional to  $\theta$  only. At equilibrium these two rates are equal, such that

$$k_1 p (1-\theta) = k_{-1} \theta \quad (\text{III-2-8})$$

where  $k_1$  is the rate constant for adsorption and  $k_{-1}$  the rate of desorption. Hence,

$$\frac{\theta}{1-\theta} = \frac{k_1}{k_{-1}} p = bp \quad (\text{III-2-9})$$

or

$$\theta = \frac{bp}{1+bp} \quad (\text{III-2-10})$$

Equation (III-2-10) is commonly known as the Langmuir isotherm and is the most common form used, although it conceals the significance of the constant  $b$ .

The full kinetic derivation, given by Langmuir (181), and which is much more enlightening, will now be considered. For the general case of chemisorption at the surface of a solid the velocity of chemisorption will depend upon 1) the pressure, which determines the number of collisions with the surface; 2) the activation energy of chemisorption  $E_a$ , which determines the fraction of the colliding molecules which possess enough energy to be chemisorbed; 3) the fractional coverage of the surface  $f(\theta)$ , which is equal to  $(1-\theta)$  only when single site adsorption occurs, and 4) a steric factor or condensation coefficient  $\sigma$  which may be defined as the fraction of the total number of colliding molecules possessing the necessary activation energy,  $E_a$ , that results in adsorption. The velocity  $V_1$  of chemisorption is therefore given by:

$$V_1 = \frac{\sigma p}{(2\pi mkT)^{1/2}} f(\theta) \exp\left(-\frac{E_a}{RT}\right) \quad (\text{III-2-11})$$



where  $\frac{P}{(2\pi mkT)^{1/2}}$ , obtained from the kinetic theory of gases, is the number of molecules of mass  $m$  striking each unit area of surface in unit time. Likewise the velocity of desorption,  $V_{-1}$ , can be written as

$$V_{-1} = k_{-1} f'(\theta) \exp\left(\frac{-E_d}{RT}\right) \quad (\text{III-2-12})$$

where  $k_{-1}$  is the specific rate constant for desorption,  $f'(\theta)$  represents an appropriate function of the fractional number of sites available for desorption ( $f'(\theta) = \theta$  when the desorption occurs from sites which are occupied by a single adsorbed molecule), and  $E_d$  is the activation energy of desorption.

At equilibrium  $V_1 = V_{-1}$  so that

$$P = (2\pi mkT)^{1/2} \frac{k_{-1}}{\sigma} \exp\left(\frac{-E_d + E_a}{RT}\right) \frac{f'(\theta)}{f(\theta)}$$

Since the difference between the activation energies of desorption and adsorption equals the heat of adsorption,  $Q$ , for the special case when one molecule occupies a single site on the adsorbent surface

( $f'(\theta) = \theta$ ,  $f(\theta) = (1-\theta)$ ) we obtain

$$P = (2\pi mkT)^{1/2} \frac{k_{-1}}{\sigma} \exp\left(\frac{-Q}{RT}\right) \frac{\theta}{1-\theta} \quad (\text{III-2-13})$$

If assumption 3 is valid, that the heat of adsorption  $Q$  is constant for all sites, then equation (III-2-13) can be written as

$$P = \frac{1}{b} \frac{\theta}{(1-\theta)} \quad (\text{III-2-14})$$

where

$$\frac{1}{b} = \frac{k_{-1}}{\sigma} (2\pi mkT)^{1/2} \exp\left(\frac{-Q}{RT}\right) \quad (\text{III-2-15})$$

Equation (III-2-14) is synonymous with the Langmuir equation (III-2-10) previously derived.

Using statistical thermodynamics, the value of the constant  $b$  in the Langmuir equation has been shown to be given by (182, 183):

$$\frac{1}{b} = \frac{(2\pi m)^{3/2} (kT)^{5/2} f_g(T)}{h^3 f_a(T)} \exp\left(\frac{-Q'}{RT}\right) \quad (\text{III-2-16})$$

where  $f_g(T)$  and  $f_a(T)$  are the internal partition functions for a molecule in the gaseous and adsorbed state,  $h$  is Planck's constant and  $Q'$  is the energy required to transfer a molecule from the lowest adsorbed state to the lowest gaseous state, otherwise known as the heat of adsorption at absolute zero. The ratio  $k_{-1}/\sigma$  of the desorption and adsorption constants can be calculated using equations (III-2-15) and III-2-16), provided that the values of  $f_g(T)$  and  $f_a(T)$  can be calculated. Evaluation of  $f_g(T)$  is relatively easy for simple molecules (184) and  $f_a(T)$  is also obtainable, although its value varies according to whether the adsorbed molecule is mobile or immobile (185).

If, on adsorption, each molecule dissociates into two entities and each one occupies one site, the predominant mechanism in coal particle combustion, and is: free to move from site to site (mobile), the Langmuir equation becomes

$$\theta = \frac{(bp)^{1/2}}{1 + (bp)^{1/2}} \quad (\text{III-2-17})$$

under these circumstances,  $f(\theta) = (1-\theta)^2$  and  $f'(\theta) = \theta^2$ . The Langmuir isotherm for two gases adsorbed simultaneously, a condition of high probability during combustion of a coal particle, is given by

$$\theta_A = \frac{b_A p_A}{1 + b_A p_A + b_B p_B} \quad (\text{III-2-18})$$

and

$$\theta_B = \frac{b_B p_B}{1 + b_A p_A + b_B p_B} \quad (\text{III-2-19})$$

where  $\theta_A$  and  $\theta_B$  refer to the fraction of sites covered by molecules of type A and type B, respectively, and  $b_A$  and  $b_B$  are the Langmuir constants for molecules A and B and  $p_A$  and  $p_B$  are their respective partial pressures.

Taking pressures as being proportional to concentration  $C_a$ , and using equations (III-2-11) and (III-2-12) we can write equations for the intrinsic rates of adsorption and desorption as:

$$\hat{R}_a = k_a C_a f(\theta) \quad (\text{III-2-20})$$

and

$$\hat{R}_d = k_d f'(\theta) \quad (\text{III-2-21})$$

where  $k_a$ , the rate constant for adsorption, equals,  $\sigma / (2\pi m_a kT)^{1/2}$ , with  $m_a$  the mass of the adsorbed species and  $k_d$ , the rate constant for desorption equals  $k_{-1} e^{-E_d/RT}$ . The adsorption rate,  $\hat{R}_a$ , can be measured by exposing a clean surface (vacuum heat treatment) to the gas of interest, and the desorption rate  $\hat{R}_d$ , can also be measured by rapidly imposing a vacuum on the sample (169, 170).

For single site adsorption and desorption the rates are given by:

$$\hat{R}_a = k_a C_a (1-\theta) \quad (\text{III-2-22})$$

and

$$\hat{R}_d = k_d \theta \quad (\text{III-2-23})$$

If on adsorption each molecule dissociates and occupies two sites, and the adsorbed layer is mobile the rates of adsorption and desorption are given by

$$R_a = k_a C_a (1-\theta)^2 \quad (\text{III-2-24})$$

and

$$R_d = k_d \theta^2 \quad (\text{III-2-25})$$

Under steady state isothermal conditions,  $R_a = R_d$ , and using equations (III-2-22) and (III-2-23) one obtains

$$\frac{\theta}{1-\theta} = R_k C_a \quad (\text{III-2-26})$$

where  $R_k = k_a/k_d$ . Solving equation (III-2-26) for  $\theta$  one obtains

$$\theta = \frac{R_k C_a}{1 + R_k C_a} \quad (\text{III-2-26a})$$

which is identical to equation (III-2-10) with  $b = R_k$ . Substituting equation (III-2-26a) into equation (III-2-23) we obtain for the overall intrinsic surface rate  $\hat{R}$

$$\hat{R} = \hat{R}_a = \hat{R}_d = \frac{k_d R_k C_a}{1 + R_k C_a} \quad (\text{III-2-27})$$

Where

$$\hat{R} = k C^m \quad (\text{g - carbon/m}^2\text{-s}) \quad (\text{III-2-28})$$

is the overall global rate for the removal of carbon,  $\hat{k}$  is the global intrinsic rate constant,  $C_a$  is the local adsorbant gas concentration and  $m$  is the true overall reaction order. Comparing equations (III-2-27) and (III-2-28), it can be seen that  $R$  will become either first or zeroth order depending upon temperature and concentration (partial pressure). The two limiting cases are given by

$$1. \quad R_K C_a \ll 1 \rightarrow \hat{R} = k_a C_a, \quad m = 1$$

$$2. \quad R_K C_a \gg 1 \rightarrow \hat{R} = k_d, \quad m = 0$$

Thus if a global rate expression is fit to a system controlled by Langmuir kinetics the true order will fall in the range  $0 \leq m \leq 1$  depending upon the concentrations and temperatures of interest. In general, adsorption control (first order kinetics) is promoted by lower reactant concentrations and higher temperatures. It should also be noted at this time that either first or zeroth order kinetics also arise from dual site adsorption with dual site desorption and for the situation of dual site adsorption with single site desorption the possibility of half-order kinetics arises in addition to first and zeroth order kinetics.

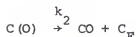
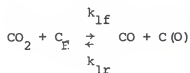
In the case of a multiple component mixture adsorbing on a surface, the isotherm is given in equations (III-2-18) and III-2-19) and the overall rate, for species A, can be found to be

$$\hat{R}^A = \frac{k_d^A R_k^A C_a^A}{1 + R_k^A C_a^A + R_k^B C_a^B} \quad (\text{III-2-29})$$

where the superscripts A and B denote quantities relating to those species. From this equation we see that the second species, which may be an inert, reactant or product gas, inhibits the reaction by taking up active sites.

### Chemical Reaction Mechanisms for Coal Char Combustion

The principle global reactions occurring during coal char combustion are shown in Table 7. The kinetic mechanism of the carbon-carbon dioxide reaction has been studied by many various authors (172, 177, 186-190). The work of Ergun (172, 188) presents convincing evidence for the following oxygen-exchange mechanism:



where the number of free sites is assumed to remain constant with burn off. The global reaction rate for loss of carbon is given by:

$$R = \frac{k_{1f} C_{\text{CO}_2}}{1 + \frac{k_{1r}}{k_2} C_{\text{CO}} + \frac{k_{1f}}{k_2} C_{\text{CO}_2}} \quad (\text{III-2-30})$$

The oxygen exchange mechanism suggests that CO inhibition of the reaction occurs not by adsorption, but rather via reaction between carbon monoxide and chemisorbed oxygen. Previous investigators (186) have thought that inhibition occurs by a simple process of filling active sites with carbon monoxide based on the following reaction mechanism:

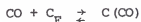
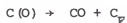
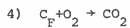
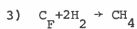
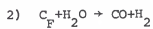
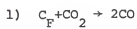


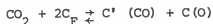
Table 7  
Principal Char Reactions

---



This reaction mechanism also produces a global rate equation consistent with equation (III-2-30), which successfully correlates existing experimental data for the carbon-carbon dioxide reaction (189). However oxygen isotope tracer experiments (171-173) have shown that the absorption of CO can be considered to be negligible, eliminating this mechanism. It is now accepted that the inhibition of the reaction by carbon monoxide is caused by  $\text{CO} + \text{C}(\text{O}) \rightarrow \text{CO}_2 + \text{C}_\text{F}$ .

Inspection of equation (III-2-30) indicates that the Langmuir-Hinshelwood mechanism postulated by Ergun (188), involves single site adsorption and desorption. However it should be recognized that the chemisorption reaction may actually be a dual site mechanism composed of more fundamental steps, such as



If  $\text{C}'(\text{CO})$  is a short lived intermediate, application of the steady state approximation generates the single site adsorption reaction and thus the mechanism remains single site.

The reaction of coal char with steam which can be expressed by the stoichiometric equation,  $\text{C}_\text{F} = \text{H}_2\text{O} \rightarrow \text{H}_2 + \text{CO}$ , has been shown to be similar to the char reaction with  $\text{CO}_2$ , both in mechanism and relative rate. The principle mechanistic studies of the carbon-steam reaction have been reported by Ergun and Mentser (191), Gadsby et al. (192), Blakely and Overholser (193), Strickland-Constable (194), Long and Sykes (179), Johnstone et al. (195) and Ergun (188).

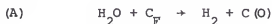
There is general agreement based upon experimental data that the rate of gasification of char by steam is given by an equation of the form:



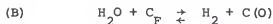
$$\hat{R} = \frac{k_1 C_{H_2O}}{1 + k_2 C_{H_2} + k_3 C_{H_2O}} \quad (\text{III-2-31})$$

where the  $k$ 's are functions of one or more elementary rate constants. The form of this equation is identical to that for the carbon-carbon dioxide reaction and it also predicts that hydrogen will act as an inhibitor in the same way that carbon monoxide does in the char-carbon dioxide reaction. This has been found to be true (179, 192) but does not predict the rate retardation due to carbon monoxide which has been observed by several workers (188, 191, 193, 194).

Two equivalent mechanisms have been postulated for the char-steam reaction:

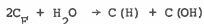


and



Inhibition in the first mechanism is based on hydrogen adsorption (179, 192, 195) and in the second mechanism, on adsorbed oxygen exchange by CO (188, 194). The detailed steps occurring during pathway A have been discussed by Long and Sykes (179) who proposed that the steam molecule decomposes at the carbon surface into a hydrogen atom and hydroxyl radical both of which chemisorb rapidly on adjacent carbon sites. This is followed by the hydrogen atom on the chemisorbed hydroxyl radical joining the hydrogen atom on the adjacent carbon atom which then leaves as a

hydrogen molecule. Therefore the steps in reaction scheme A may be written as:



Evidence for dissociation of the hydroxyl radical has been obtained by Blackwood and McTaggart (196). The inhibition by carbon monoxide was thought to occur in a manner similar to the mechanism in the char-carbon dioxide reaction; i.e.

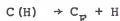


However Gadsby et al. (192) postulated that CO did not by itself inhibit gasification, but by shifting the water-gas equilibrium,



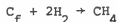
more hydrogen is produced, which does inhibit the char-steam reaction.

Ingles (197) postulated that a carbon surface accelerates the water-gas shift reaction by acting as a chain initiator for the following reactions:



Strickland-Constable (194), observing that hydrogen is not only strongly but very rapidly adsorbed on carbon, supported the view that the hydrogen inhibition in the carbon steam reaction is caused by its chemisorption on active sites.

The reaction of char with hydrogen can be represented by the overall reaction



There are few kinetic studies on the carbon-hydrogen reaction with the main mechanistic studies being reported by Blackwood (198, 199), Zielke and Gorin (200), Moseley and Paterson (201) and Johnson (202). These workers all used high pressure reactors (1-100 atm), but even under these conditions the rates were very slow. Most studies report that the global rate has a simple first order dependence on hydrogen concentration (198, 201-203); i.e.

$$\hat{R} = k_1 C_{H_2} \quad (\text{III-2-32})$$

However, Zielke and Gorin (200) ( $T=925^\circ\text{C}$ ,  $p \sim 30$  atm) find

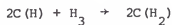
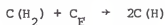
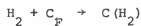
$$\hat{R} = \frac{k_1 C_{H_2}^2}{1 + k_2 C_{H_2}} \quad (\text{III-2-33})$$

while Blackwood (199) ( $T = 650-870^\circ\text{C}$ ,  $p = 4-50$  atm) reports at high  $CH_4$  concentrations

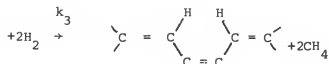
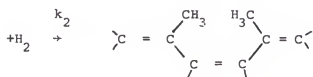
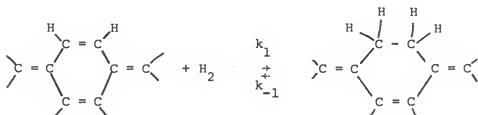
$$\hat{R} = \frac{k_1 C_{H_2}^2 - k_2 C_{CH_4}}{1 + k_3 C_{H_2} + k_4 C_{H_2}^2 + k_5 C_{CH_4}} \quad (\text{III-2-34})$$

where the  $k$ 's are functions of one or more elementary rate constants.

Under appropriate conditions, equation (III-2-34) reduces to either equation (III-2-32) or equation (III-2-33). The following mechanism was postulated to explain the rate behavior of equations (III-2-33 and (III-2-34):



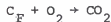
The existence of  $\text{C}(\text{H})$  was postulated since the reaction between carbon and atomic hydrogen also produces methane (196, 203), Zielke and Gorin (200) also postulate that surface methylene ( $-\text{CH}_2-$ ) could replace  $\text{C}(\text{H})_2$  as an active intermediate by the following mechanism:



Blackwood (199) has shown that the global rate  $\hat{R}$  is proportional to the oxygen content of a char sample with purified carbons having  $\hat{R} \approx 0$ . The oxygen content of a char particle remains constant during

gasification, an indication of oxygen-based active sites. Addition of steam also accelerates the rate of the char-hydrogen reaction significantly (202, 204), probably due to C(OH) and C(H) reactions.

Despite the simplicity of the char-oxygen reaction,



the reaction mechanism is not well understood and disagreements still exist among investigators on some aspects of the problem (205). The major question concerning the mechanism of the carbon-oxygen reaction has been whether carbon dioxide is a primary product of the reaction of carbon with oxygen or a secondary product resulting from the gas-phase oxidation of carbon monoxide. The CO/CO<sub>2</sub> question has been studied by many researchers (180, 206-209) with the general consensus being that both carbon monoxide and carbon dioxide are primary products, with the CO/CO<sub>2</sub> ratio increasing substantially at higher temperatures and lower pressures. Experiments using oxygen-activated carbon clearly show that carbon monoxide is favored at higher temperatures (210). A possible explanation for this behavior is that CO is formed at carbon edges while CO<sub>2</sub> is formed at inorganic sites (205, 209). Lower temperatures favor CO<sub>2</sub> due to catalytic activity while higher temperatures promote utilization of carbon edges. The CO/CO<sub>2</sub> ratio can be correlated by (208, 209)

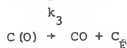
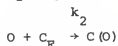
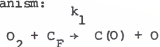
$$CO/CO_2 = Ae^{-E/RT}$$

where  $A \sim 10^{2.5}$ ,  $E \sim 6-9$  kcal/mole for low pressure, and  $A \sim 10^{3.5}$ ,  $E \sim 12-19$  kcal/mole at high pressures. Arthur (208) showed that the ratio could be expressed, for temperatures between 750 and 1690 K, and for two different carbons, as

$$\text{CO}/\text{CO}_2 = 2500 \exp (-240/T)$$

while Rossberg (211) reported similar results for temperatures between 790 and 1690°K for two different carbons.

At ordinary combustion temperatures, the predominant oxidation product still appears to be carbon monoxide which further oxidizes to carbon dioxide in the gas phase. According to von Fredersdorff and Elliott (206) this reaction is very rapid and occurs via the following mechanism:



where the last reaction represents loss of free active sites at high combustion temperatures due to thermal annealing. This oxygen mechanism is consistent with the observed extremely rapid rate of reaction between carbon and oxygen atoms (196) and the blue glow, attributed to  $\text{CO} + \text{O} \rightarrow \text{CO}_2 + h\nu$ , often observed around burning carbon particles.

Neglecting the fourth reaction and assuming a steady state concentration of C(O) we obtain for the global rate:

$$\hat{R} = \frac{k_1 \text{C}_{\text{O}_2}}{1 + \frac{k_1}{k_3} \text{C}_{\text{O}_2}} \quad (\text{III-2-35})$$

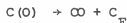
which allows for reaction orders of 0 and 1. However the speed of the reaction cannot be explained unless the active carbon sites are

drastically greater for  $O_2$  compared to  $CO_2$  and  $H_2O$ . A mechanism such as:



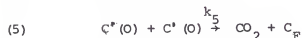
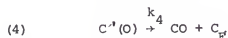
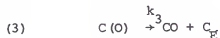
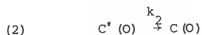
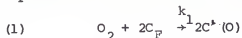
could account for the speed of the reaction but experimental evidence favors a  $C(O)$  mechanism, not  $C(O_2)$ . Experimental evidence has shown that, in the temperature range of 1100-1600 K, the reaction order is one-half (205, 212) and more recent work indicates that for even larger temperature ranges (650-1800 K) a half-order reaction mechanism applies (213, 214). Based upon these results a kinetic mechanism must allow for reaction orders of 0, 1, and 0.5, a mechanism that is indicative of dissociative chemisorption with surface migration.

Blyholder and Eyring (212) have recommended:



where the  $C^+(O)$  represents a mobile ionic bond while  $C(O)$  represents an immobile covalent (carbonyl) bond. This mechanism is also consistent with quantum mechanical calculations which indicate that mobile dissociative two-site chemisorption is more favorable than single site molecular adsorption (215). Unfortunately this mechanism does not account for the rapidity of the  $C/O_2$  reaction at lower temperatures and the reverse of the first reaction cannot occur since experimental evidence has shown that  $O_2$  adsorption is irreversible for temperatures greater than  $-70^\circ C$  (170, 210).

A possible alternative mechanism is.



Reaction 4 is postulated to have a lower activation energy than reaction 3 therefore allowing for faster conversion to CO at lower temperatures than reaction 3. Using oxygen isotopes Walker et al. (177) showed that reaction 5 was the mechanism responsible for primary  $CO_2$  formation and was able to eliminate reactions suggested by others such as



Reaction 5 has also been found to be consistent with experimental results which show that  $CO_2$  is produced during the reaction between carbon and atomic oxygen (196).

#### Mathematical Descriptions of Coal Particle Combustion

The theoretical description of coal combustion had its origin in the work of Faraday and Lydell (216), whose volatiles-ignition theory was generally accepted for most of the 1800's. According to this theory, coals must first devolatilize, partially or completely, before ignition can start. It was assumed that ignition of the solid



residue was in some way conditioned by prior ignition of volatiles. According to the volatiles theory, the inflammability of coals should increase roughly in proportion to the volatile content of the coal. Early work (217-219) appeared to support this theory but by the end of the century there was clear experimental evidence (220, 221) which disputed the volatile theory.

The first mathematical treatment was presented by Nusselt in 1924 (165) who introduced the single film model. In this model it was assumed that the oxidation of carbon is controlled by diffusion of oxygen through a stationary film to the surface of the carbon particle where it reacts to form CO or CO<sub>2</sub>. No other chemical reactions were considered and the flame propagation mechanism was based upon radiation of the burning particles.

Cassal et al. (222, 223) modified the gas-phase Mallard-Le Chatelier burning velocity equation (equation (II-1-4) to include the effects of radiation on coal particles. This approach did not allow for quantitative predictions but it was capable of indicating relative effects of the various parameters. The modified equation is

$$V_B = \frac{\lambda (T_f - T_i)}{\delta} + \frac{\delta z_p \epsilon f \alpha k (T_f^4 - T_o^4)}{\rho_p r_p}$$

$$(\rho_g C_p^g + a_p C_p^p) (T_i - T_o)$$

where  $\epsilon$  = emissivity of the coal particle surface,  $\alpha$  = correction factor  $> 1$ , which accounts for radiation of glowing combustion products (gas and solid,  $F$  = geometrical view factor,  $z_p$  = concentration of dust,  $r_p$  = mass reaction rate of particle,  $\rho_p$ ,  $C_p^p$  and  $p_g$ ,  $C_p^g$  are the

density and heat capacity of the particle and gas respectively,  $k$  is the Boltzmann constant, and  $\lambda$  is the thermal conductivity of the gas. No comparisons of experimental results have been made with this theory.

The radiation theory of coal dust flame propagation was extended further by Essenhigh and Csaba (224) who accounted for temperature differences between particles and gas and added a finite pre-ignition zone. Assumptions included negligible combustion in the pre-ignition zone, a fixed ignition temperature, equal gas and particle velocities and particulate radiation from a grey-body flame at an average temperature,  $T_f$ .

In this model, based upon a thermal theory, the details of the combustion process were neglected. The mixture was assumed to leave the burner at some temperature,  $T_o$ , and in the pre-ignition zone the coal was heated only by radiation. Because of the temperature differences between the gas and solid phases, some of the heat is lost by conduction to the gas. However conduction from the flame to the incoming particles was neglected. At some point in the system the particles were ignited and this ignition temperature was fixed at the coal decomposition temperature ( $\sim 600$  K). This allowed the pre-ignition zone to be decoupled from the flame zone. The radiation intensity decayed exponentially away from the flame front due to absorption by the particles, and emitted and scattered radiation by the coal particles were neglected.

The flame velocity for the case where the gases and particles are in thermal equilibrium is given by

$$V_B = \frac{I_f (1 - e^{-\frac{m t_i}{t_i - T_o}})}{(\rho_p C_p^p + \rho_g C_p^g)}$$

where  $m = 3 \frac{Z_p}{p} \frac{V_B}{4r p_s}$ , and is called the cloud attenuation coefficient and  $t_i$  is the ignition time.  $I_f$  is the intensity of radiation from the flame at the point of ignition, which is evaluated at the mean flame temperature. This model predicted burning velocities varying from 50 to 120 cm/s for stoichiometric mixtures of 50 and 10  $\mu$ m diameter particles, assuming an ignition distance of 10 cm. This theory was compared with experimental work, determining coal flame velocities as a function of temperature, using a coal dust concentration of about 0.3 kg/m<sup>3</sup> (225). Flame temperatures were varied by changing the oxygen percentage, and although the magnitude of the burning velocity was not in good agreement with the theory, the trend of increasing velocity with increasing temperature was found in both cases. It was also concluded from the experimental measurements that thin laminar flames were not likely dominated by radiative heat transfer.

Bhaduri and Bandyopadhyay (226) advanced the radiative approach by incorporating the heat generated due to chemical reactions for the case of equal gas-particle temperatures and for a single coal size. Heat conduction was neglected and only heterogeneous oxidation of carbon in low volatile coal to CO<sub>2</sub> was considered. They obtained a differential equation that required numerical solutions for flame velocity, temperature profile and heat release along the flame:

$$Y I_f \exp[-Y(y_f - y)] - (C_p^g \rho_g + C_p^p \frac{Z_p}{p}) v_B \left( \frac{dT}{dy} \right) + Q = 0$$

where  $Y$ , the radiation coefficient, equals  $3 \frac{Z_p}{p} \frac{V_B}{4r p_s}$ ,  $Q$  is the volumetric heat release due to coal char combustion and  $y$  is the distance in the flame.

Using this equation, Bhaduri and Bandyopadhyay predicted burning velocities for suspensions of anthracite coal and air. For 20% excess air, which yields a flame temperature of 2098 K, the burning velocity was found to decrease from 37 cm/s for 20  $\mu\text{m}$  particles, to 34.6 cm/s for 100  $\mu\text{m}$  particles. For a stoichiometric mixture of 50  $\mu\text{m}$  particles, with a predicted temperature of 2373 K, the predicted burning velocity was 50.0 cm/s. Flame thickness predicted by this equation were about 0.10-0.15 m, which is greatly in excess of the experimental values for laminar coal-air flames.

Marshall et al. (225) developed a simple theory of coal flame propagation which included radiative and conductive effects as well as including an approximate treatment of coal devolatilization. They postulated that the rate limiting steps were diffusional escape of volatiles from the coal, coupled with particulate radiation and gaseous conduction. Their work also indicated that the burning velocity should vary inversely as the square root of the coal particle diameter. Calculated flame velocities were found to be approximately a factor of two larger than experimental values and also predicted a slight increase in flame speed with decreasing particle size and a large increase in speed upon increasing oxygen concentration.

Smoot and co-workers (227-230) have recently described the development of a generalized model for predicting flame propagation in laminar, particle-laden flames. This model specifically takes into account devolatilization and subsequent reactions of gas-phase species. This model has been based upon the numerical technique of Spalding et al. (51), used for laminar methane-air flames, where the steady state

solution for the propagating flame is obtained from the convergence of the unsteady-state conservation equations. Much of this model has been patterned after earlier solutions for propagating methane-air flames (53, 61) but has been generalized to include particle effects.

In this model, basic unsteady-state conservation equations for laminar, multi-component, compressible gas/particle mixtures (231) were used to formulate a one-dimensional, propagating flame model. The coal particles were assumed to be spherical and sufficiently small and numerous enough to be treated as a continuous medium, while particle volume, particle diffusion and collisions among particles were neglected. Pressure was assumed to be uniform while the particle velocities were taken to be equal to the local gas velocity in the flame. Effects of gravity, viscous dissipation, forced diffusion, thermal diffusion, and temperature gradients within particles were neglected. Using Spalding's stream line co-ordinates (50) and earlier work of Smoot et al. (61) the following six equations were derived to describe coal-air laminar flames (230):

1. Gas-species conservation

$$P_g (\partial \omega_{ig} / \partial t) = P_t (\partial / \partial \psi) (P_g P_t D_{ig} / \partial \psi) +$$

$$r_{ig} + \sum (r_{pi})_j - (\sum r_{pj}) \omega_{ig}$$

## 2. Gas phase thermal energy

$$P_g (\partial h_g / \partial t) = P_t (\partial \psi) [ (K_g P_t / C_{pg}) (\partial h_g / \partial \psi) ] +$$

$$\sum_j (Q_{pj}) - Q_{sg} + \sum [r_{pj} (h_{pjg} - h_g) + P_t (\partial \psi) \{$$

$$\sum_i [P_{ig} D_{ig} - (K_g / C_{pg})] h_{ig} \cdot (\partial \omega_{ig} / \partial \psi) \} -$$

$$(P/P_g) \left( \sum_j r_{pj} / P_{pg} \right)$$

## 3. Particle thermal energy

$$P_{pj} (\partial h_{pj} / \partial t) = Q_{pf} - Q_{pj} - Q_{ps} -$$

$$r_{pj} [ (h_{pjg} - h_{pj}) - (P/P_{pg}) ]$$

## 4. Particle mass

$$\partial m_{pj} / \partial t = -r_{pj} / n_{pj}$$

## 5. Particle species conservation

$$P_p (\partial \omega_{pj} / \partial t) = (\omega_{pj} \sum_j r_{pj}) - r_{pj}$$

## 6. Particle number balance

$$P_g \partial n_{pj} / \partial t \sim n_{pj} [\partial P_g / \partial t - \sum_j r_{pj}]$$

where

$$\partial \psi / \partial t = -P_t V, \quad \partial \psi / \partial y = P_t$$

and

$$P_t = P_g + \sum_j P_{pj}$$

for the gas particle mixture. These six equations are a set of  $i + 4j + 1$  equations describing the dependent variables  $w_i$ ,  $h_g$ ,  $h_{pj}$ ,  $w_{pj}$  and  $n_{pj}$  as functions of time ( $t$ ) and position  $\psi(t, y)$ , where  $i$  = the number of

gas phase chemical species and  $j$  = the number of particle phases (discrete sizes or types), with remaining symbols defined in Table 8. These equations reduce to those of Spalding et al. (51) for gas-phase systems such as a normal laminar methane-air flame.

Like the model for the methane-air flame (61) the model equations for coal-air flames also includes variables that must be calculated (i.e. thermal conductivities and binary diffusion coefficients) using auxiliary equations. Gas phase properties were calculated using procedures used by Smoot et al. (61) and described in Chapter II. The heat losses from the gas and the particles to the surroundings ( $Q_{sg}$ ,  $Q_{ps}$ ) were neglected. Coal particles were assumed to be composed of specified amounts of char (carbon) and volatile matter (hydrocarbons, and other gases), whose values were obtained from experimental values (231). The volatiles part of the coal were assumed to react at a rate proportional to the amount of volatile materials remaining:

$$r_{vj} = P_v / [ (d_{pj}^2 / 6 K_v^d) + 1/k_v ]$$

where both activated devolatilization of the coal volatiles  $k_v = A_v \exp(-E_v/RT_{pj})$  and the diffusion of the volatiles products from the surface ( $k_v^d = 2M_v D_{vm} C_v / p_s$ ) determine the net devolatilization rate.

The char part of the coal particle was assumed to react with oxygen as a first order heterogeneous process to produce carbon monoxide

$r_{cj} = \pi M_c d_{pj}^2 C_{og} n_{pj} \phi / [1/k_o + 1/k_c]$  with oxygen diffusion

$k_o = [(D_{cm}/d_{pj}) (2B_j/\exp B_j - 1)]$  and activated surface reactions

$k_c = A_c \exp(E_c/RT_{pj})$  determining the net char reaction rate.

Table 8  
Symbols for Smoot et al. Coal Combustion Model(230)

Nomenclature

A	pre-exponential factor, $\text{cm/sec, sec}^{-1}$
B <sub>j</sub>	particle transpiration parameter
C	molar concentration, $\text{gmol/cm}^3$
C <sub>p</sub>	heat capacity, $\text{cal/g}^{\circ}\text{K}$
d <sub>p</sub>	particle diameter, $\text{cm, } \mu$
D	diffusivity, $\text{cm}^2/\text{sec}$
E	activation energy, $\text{cal/gmol}^{\circ}\text{K}$
h <sub>i</sub>	partial molar enthalpy, $\text{cal/g}$
Δh	heat of reaction, $\text{cal/g}$
k	surface reaction rate coefficient, $\text{cm/sec}$
k <sub>o</sub>	mass transfer coefficient, $\text{cm/sec}$
K <sub>p</sub>	equilibrium constant
K <sub>v</sub>	volatiles diffusion parameter, $\text{cm}^2/\text{sec}$
m <sub>p</sub>	particle mas, g
M	molecular weight, $\text{g/gmol}$
n <sub>p</sub>	particle number density, $\text{cm}^{-3}$
Nu	Nusselt Number
p	static pressure
Q	heat transfer rate, $\text{cal/cm}^3 \text{ sec}$
R	gas constant
r	mass reaction rate, $\text{g/cm}^3 \text{ sec}$
t	time, sec
T	temperature, $^{\circ}\text{K}$
V	velocity, $\text{cm/sec}$
y	distance along foame, cm
ω <sub>1</sub>	mass fraction of i <sup>th</sup> specie
ψ	streamline coordinate, $\text{g/cm}^2$
Ø	surface area factor
ρ	density, $\text{g/cm}^3$

-----  
Continued



Table 8-Continued

## Subscripts

c	char
f	flame
g	gas
hc	hydrocarbon
i	i <sup>th</sup> specie
j	j <sup>th</sup> particle
k	k <sup>th</sup> volatile specie
k	k <sup>th</sup> gas phase reaction
m	product
n	reactant
o	oxygen
p	particle
s	solid
t	total
v	volatiles

Swelling of the coal particles was assumed to be proportional to the extent of devolatilization. Coal or char particles were heated or cooled by conduction from the gas:

$$Q_{pj} = \pi N_u k_{pg} d_{pj} (T_{pj} - T_g) n_{pj} \quad \text{where}$$

$$N_u = 2B_j / (\exp B_j - 1) \quad \text{and}$$

$$B_j = r_{pj} C_{pg} / 2\pi d_{pj} k_{pg} n_{pj}$$

Products of devolatilization were specified as an arbitrary hydrocarbon,  $C_n H_m$ , together with oxygen, nitrogen, etc., and the carbon/hydrogen ratio in the hydrocarbon was obtained from material balance considerations. The rate of oxidation of the hydrocarbon to carbon monoxide and hydrogen was taken from Edelman et al. (232) and is given by

$$(r_{ig})_{hc} = (5.52 \times 10^8 / p^{0.825}) C_{hcg}^2 C_O \exp(-12400/T_g)$$

The coal particle enthalpy was taken to be a weighted average of the enthalpy of the char and volatiles phases, while the enthalpy of the products of particle reaction is:

$$h_{pgj} = [r_{cj}(h_{cj} + \Delta h_c) + r_{vj}(h_{vj} + \Delta h_v)] / (r_{cj} + r_{vj})$$

$$\text{where } r_{pj} = r_{cj} + r_{vj}$$

The model equations were transformed following the approach of Spalding et al. (51) and were solved simultaneously using a numerical finite difference scheme to iterate to the steady state solution.

Predictions were made for a monodisperse suspension of Pittsburgh coal particles which were assumed to contain 50% volatiles initially. For 33  $\mu m$  particles, the predicted burning velocities increased from 14 to 17.5 cm/s as the coal concentration increased from 125 to 625 mg/l.

The predicted flame thicknesses were about 1 cm which agreed well with their experimental values. From these calculations Smoot et al. (228) conclude that coal pyrolysis and subsequent diffusion of the volatiles are the most important mechanism for this type flame, and it should be noted that the radiation propagation theory of Bhaduri and Bandyopadhyay (226) predicted flame thickness on the order of 10 to 20 centimeters.

## CHAPTER IV EXPERIMENTAL

### Gas Metering and Flow Control System

One of the most important parameters to control in any flame diagnostic experiment is that of gas flow rates into the burner undergoing study. The requirements for a gas metering system to obtain accurate results have been discussed by Mavrodineanu and Bolteux (15). Major parameters are accurate control of flow and constant delivery pressure. In order to insure accurate gas flow monitoring and reproducibility the system shown in Figure 5 was designed and constructed.

Pressure regulators used on supply gases were all of 2-stage type (Matheson Corp., Morrow, GA) and were chosen to be compatible with flow rates used during experiments. In order to insure constant delivery pressure, a 2-stage regulator must be used or delivery pressure will be dependent upon remaining tank pressure, which will constantly change as the experiment progresses. The output of the regulators were connected to the main control panel by polyethylene tubing (1/4" od) and Swagelok connectors (1/4"). The main control panel was a free standing aluminum plate (24" x 24" x 3/16") to which the flow control devices were fitted. The control panel was constructed for six different flows in the following arrangement.

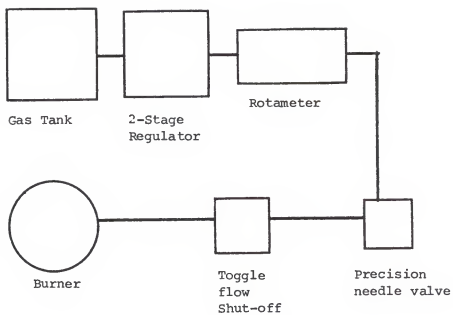


Figure 5. Gas Flow Control System.

Rotameter holders were constructed out of stainless steel and were attached to the plate. Gases entered into the rotameter holders at the bottom through a 1/8" MPT connector, which was screwed into the bottom holder through a hole in the plate. Tapered flute style rotameters (Matheson Corp., Morrow, GA) were used due to their larger linear working range vs a tapered bore style. The rotameters were mounted to maintain a constant inner gas pressure across the tube by placing the pressure regulator prior to the rotameter and the variable restricting orifice (needle valve) after the rotameter (233). Rotameter size (#601-605) as well as needle valve size, (for #601-603 low flow rotameters, fine metering valves (NUPRO, "Series M" Cleveland, OH) were used and for the higher flow 604 and 605 rotameters, forged body regulating valves (Whitey Co., Oakland, CA) were used, chosen so as to give about mid-scale readings of the stainless steel balls (~50 mm) in order to assure a high degree of accuracy and reproducibility. Following the regulating valves were toggle operated forged body shut-off valves (Whitey Co., Oakland, CA) since regulating valves should never be used as a shut-off (may damage valve seat causing irreproducible flow settings) and also to speed flow shut-off in the advent of an accident. From the exits of the toggle valve all flows went directly to the burner.

Delivery pressure gauges on the 2-stage regulators were calibrated against a calibrated absolute pressure gauge (Wallace and Tiernan, Model #FA-233, Belleville, NJ). All delivery pressures were measured in psig (pounds per square inch gauge) and the system was calibrated for 10, 20 and 30 psig. Gas flow rates were calibrated using a linear gas

flow meter (Hastings-Teledyne, #ALK-50K Hampton, VA). Flow rate vs ball height was found to be linear over the entire rotameter range (150 mm) as long as the tube pressure was held constant with the exception of a jump in the #605 rotameter caused by the pyrex and stainless steel ball sticking together. This could be overcome by increasing flow so that the 2 balls separated and then reducing flow to desired rate. Calibration was accomplished using both balls, with the stainless steel ball yielding higher flow rates. Rotameters were operated with both pyrex and stainless balls for a larger range but most flows were referenced vs the stainless steel balls.

#### Burner

The methane-air flame used in these studies was produced by a multi-hole circular burner using the described flow system. The burner design is similar to that used by Horvath et al. (234) in that it consists of an inner and outer flame. The outer flame with the same composition as the inner was used to prevent temperature gradients across the flame and the entrainment of ambient air. This laboratory constructed burner is entirely made of brass with the burner head being 1.25" in diameter. The burner contained 37 holes 0.125" in diameter arranged in three concentric rings around a central hole ( $r_1 = 0.300"$  and 6 holes,  $r_2 = 0.600"$  and 12 holes,  $r_3 = 0.875"$  and 18 holes). Under the burner head is the flame separator, which divides the flame into an inner and outer flame. The inner flame consists of the center hole and the first ring of 6 holes yielding an inner flame diameter of about 0.4375". The outer flame consists of the final 2 rings yielding a total flame diameter of 1.000". The inner flame

gases are introduced through a bottom opening and the outer flame gases are introduced through the upper side openings. The flame separator is seated upon O-rings to make a gas tight seal between the two input flows. Normally a sample is introduced only to the center flame but can be spread throughout the whole flame by removal of the flame separator.

The burner head is screwed down by 8 1/4-20 bolts into the retaining collar, where it makes a gas tight seal on an O-ring. This retaining collar is then screwed into the main body, sealing upon an O-ring. The bottom plate is secured by spring loaded bolts to the main body to allow for expansion in the advent of a flashback. The input tube has two internal O-rings to seal upon the inner feed connector which is usually made of glass. The total length of burner is approximately 5 1/4".

#### Laboratory Coal Delivery Systems

In order to study the combined burning of methane and coal, some method had to be devised to introduce a solid sample (coal) into a standard laboratory burner. In normal spectrochemical methods the sample is usually dissolved in water or some solvent and then introduced using a pneumatic nebulizer. A pneumatic nebulizer uses a high pressure flow of air (approximately 30 psig) to produce a fine spray of droplets which are then easily introduced into the main stream of flame gases (15, 235). The problem in these studies was that coal powder (approximately 200 mesh, 75  $\mu\text{m}$  diameter) was the sample to be studied and is not soluble in water. It was desirable to introduce coal into the flame without modifying it so the possibility of finding a suitable



solvent for coal was eliminated. The only preparation that the coal should undergo is to be ground into the desired mesh size.

Several authors (236-238) have described methods for introducing solid samples to the flame but these were rejected due to their complexity and inaccuracies. An ideal system would deliver a constant and uniform flow of coal at a reproducible rate using relatively simple apparatus. Due to the powdery nature of the coal, when ground to 200 mesh size, it was thought that some type of fluidized bed system might be suitable.

The first model shown in Figure 6 is made from a 350 ml fritted glass funnel. Air to create the fluidized bed is input through the bottom tube (1/4" od) which then travels through the glass plug (10-15  $\mu$ m pores). Coal dust is loaded into the chamber through the 1/2" id tube on the side from a large capacity reservoir. Two tangential 1/4" od tubes serve as auxiliary air input and aerated coal output. Air is input through the lower tube tangentially to the inside wall in an effort to get a swirling air motion inside the chamber, and the output tube is also located tangentially to remove coal dust in the direction of air flow. Both the aspirating air and the auxiliary air could be varied independently to optimize air flow conditions inside the chamber.

This coal nebulization device was tested, as all others, by introducing the coal output into the flame and making visual observations of the coal input rate. This could be easily accomplished by use of a simple glass adapter at the bottom of the burner which was used to mix the main gas flows with that of the coal-air mixture. Input rates could also be easily observed because upon introduction into the flame

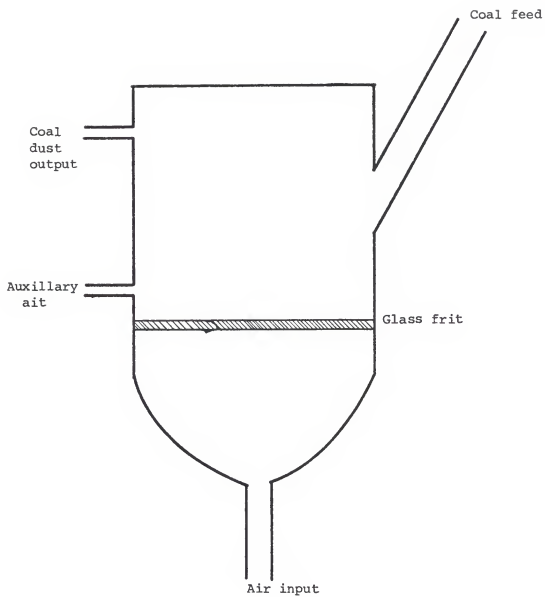


Figure 6. First Coal Feeder

the coal particles burned with a bright orange glow and a considerable light emission. It was then quite easy to see if the flow was uniform and constant by just looking at it. At these early stages this is all that was required to judge success or failure of a system, but later on more precise methods were used to verify uniformity of flow. Upon testing this device the coal input to the burner was found to be very erratic with a pulsating effect being observed. Upon closer observation of the aspirating chamber it appeared that bubbles were bursting at different places on the surface of the coal, causing a small amount of coal to be dispersed throughout the volume of the chamber. Upon raising the flow of fluidizing air, larger bubbles were made but the flow to the burner was still observed to be very erratic. Upon raising input air pressure from 20 psig to 30 psig, more coal was dispersed inside but flow was still very erratic. After approximately five minutes the coal flow dramatically decreased to a very slight level. Upon looking into the chamber, a few clear spots were found on the fritted disk and the coal remained in most other places. It appeared that once the coal was removed from one spot on the disk the air flow took the path of least resistance thereby leaving the rest of the coal unmoved. Reasons for failure of this system were thought to be:

1. Large surface area of glass frit (3" diameter) resulting in a large pressure drop across the frit yielding a small aerating gas velocity.
2. Glass frit pore size (10-15  $\mu\text{m}$ ) was too large to induce a fluidizing action.
3. Volume of chamber was too large to maintain a coal-air dispersion with uniform particle density.

Thinking that in principle it was a good idea, a new coal feeding device was constructed along the lines of the first (Figure 6) with a few modifications. A 60 ml fritted glass funnel was now used with a fine frit pore size (4-5.5  $\mu\text{m}$ ), with all input and output connections as in the larger model. Total length of this model was approximately 3 inches long and frit diameter was approximately 1 1/4". Unfortunately this one did not work any better than the first one by producing an even worse "percolating effect". Fluidizing and auxillary air were adjusted in an attempt to prevent this effect but to no avail. It was decided to pursue a different approach to the problem of asperating coal into the burner.

The fine powdery nature of the coal still gave one hope that some type of air stream method could be used to propel it into the burner. Instead of blowing air up through the coal in an attempt to disperse it another way of accomplishing this was developed. In Figure 7 is shown the second generation coal feeder that was developed. Chamber size was 1 7/8" in diameter and 3" high with a 1/4" id feed tube on top. The input aerating air came in through a nozzle at 45° angle to the bottom of the chamber and the output came out at a right angle to the wall at the top of the chamber. The nozzle ended inside the chamber about 1" from the bottom, with the nozzle hole diameter approximately 1 mm. A magnetic stir bar was placed in the bottom and the apparatus was placed upon a magnet stirrer. A fixed volume of coal was placed inside, enough to fill the chamber approximately 3/4" high. To test this device the stir bar was set on high speed and air was input through the nozzle. A slight amount of air caused a fair amount of

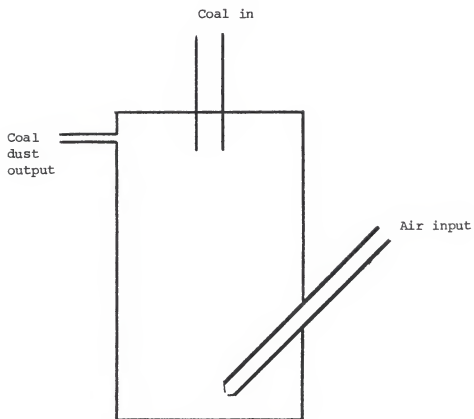


Figure 7. Second Coal Feeder

coal to be introduced into the flame, and upon increasing the air a large amount could be input to the flame. One problem with the glass frit types was the large amount of air that was needed to asperate any coal (about 1 l/min), while with this method it was found that a very small amount of air (< 100 ml/min) would put a visible amount of coal into the flame. Upon increasing the air flow the amount of coal reaching the flame could be varied over a very wide range. On testing for stability over a time period (10 min), it was found that the amount of coal would remain constant for about 2 min, whereupon it started to decrease until hardly any coal was being asperated into the flame after 10 min. This was caused by the sticking nature of the powdered coal. As the air was sent in, it moved all the coal away from one spot forming a crater in the coal contained in the chamber. Even though the stir bar was spinning vigorously, it could not knock down the coal that was sticking to the sides of the chamber. Filling the chamber with coal so it covered the nozzle only added a few more minutes of constant operation to this version of coal feeder.

At the same time two different approaches were being developed for delivering coal into the flame. The first of these, suggested by results obtained in the large combustor development program, is shown in Figure 8. Whereas all the previously discussed coal feeders worked by blowing air into a coal reservoir, this new design worked by sucking the coal out by using an induced partial vacuum. In this design a large amount of coal was placed in a 4" diameter 60° angle funnel which filled the funnel and the straight tube leading from the bottom. At right angles to the bottom tube was another tube which had a room air inlet and a stopcock valve attached. At the end of this tube a

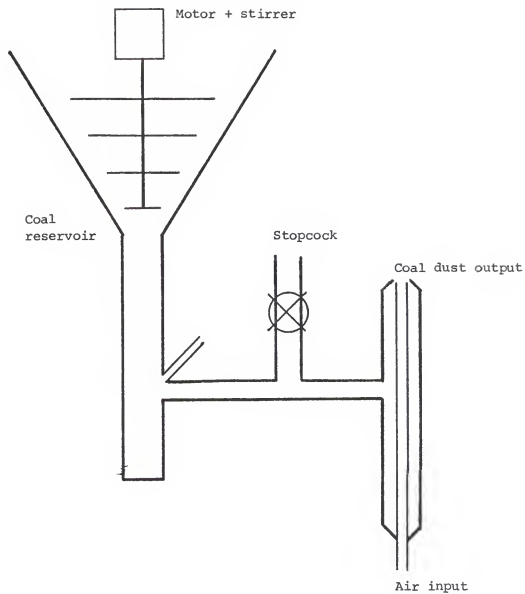


Figure 8. Funnel Feeder

T-tube was connected which contained a nozzle type device. Air was input into the end indicated in Figure 8 and by exiting through the inner nozzle a partial vacuum was sent up through the other tubes due to the Venturi effect (15). This induced vacuum would cause the coal in the funnel to be pulled down through the tubing and exited at the end of the nozzle which was then sent to the burner. The room air inlet had a very narrow opening and served to keep the funnel tube junction agitated in order to obtain a constant flow of coal down from the funnel. The stopcock opening could be used to vary the amount of vacuum produced along with the flow rate of air sent through the nozzle. The position of the nozzle was varied in the T-tube and it was found that the vacuum effect became pronounced at the T junction and was at its greatest at the position shown in Figure 8, at the very end. In this position the coal would be drawn out rapidly causing a crater to be formed in the feed funnel. After the crater was formed no further coal was sucked down due to its sticking properties. This could be prevented by tapping on the funnel causing the sides of the crater to fall down the tube and then into the flame. To prevent this cratering effect from occurring, a 4-vane stir rod was constructed and rotated with a motor as shown in Figure 8. This stirrer was built so that it fit completely inside the funnel and would scrape along the inside walls causing the coal to be moved lower into the funnel. When the coal volume in the funnel became low more coal was dumped in from a supply container (large beaker), this system would allow for a reasonably constant flow rate of coal to be delivered.



The major problem with this system was that low coal feed rates could not be attained. There was a threshold level for the attainment of a vacuum sufficient enough to draw the coal into the system. A small flow rate of air (approximately 200-600 ml/min) would have no effect at all, but once a limiting value was reached (approximately 900 ml/min) the coal would be propelled at a great rate. Further increase of air would only increase the coal feed rate. When full the funnel contained approximately 500 g of coal, when running at a threshold rate of air with regulating stopcock closed the funnel emptied in less than 2 min resulting in a flow rate about 250 g/min. When this large amount entered the burner, it caused the flame to extend into the hood (5 ft above burner) and a large amount of coal was not burned resulting in coal depositing on everything on the laboratory table. This was obviously too much coal to inject into the burner. Upon adjusting the stopcock to vary the amount of vacuum the amount of coal entering the flame decreased (producing only a 4 ft high flame) but there still was a large amount of unburned coal. The only way the coal flow could be reduced was by moving the position of the nozzle behind the T-junction and by opening the stopcock valve. This then allowed a relatively small amount of coal to enter the flame but at very erratic intervals. After much fiddling, not much improvement was realized so this method was abandoned. This would probably work on a much larger burner system which could handle the large output rates of coal that it generated.

After the dismal failures of the previously described methods it was thought that a completely different approach was required. The

earlier methods used air streams to both agitate the coal and deliver it to the burner, and it was found that delivery to the burner was no problem but obtaining a constant flow was. To overcome the constant delivery problem the device shown schematically in Figure 9 was devised and constructed. This method broke the system down into two parts, a constant coal feed part and a burner delivery part. It had been found from earlier experiments that coal could be sent into the flame relatively easily by blowing air over it and sending the air to the burner. The coal particles were light enough so that they were suspended in the air stream and could be transported through plastic tubing without much loss. Coal would be deposited on the insides of the tubing but once a layer was deposited the rest flowed rather easily through the tubing. In the design shown schematically in Figure 9 the coal is contained in a reservoir made from an aluminum funnel and the lower end of it feeds into a chamber containing an auger like rod. This rod had a spiral groove cut into it approximately 1/8" wide and a 1/16" deep. This rod was driven by a variable speed drill through a multi-ratio gearbox. The auger rod was contained in a tube like channel with chambers at both ends. The coal was deposited upon the auger at one end and was then transported by the twisting motion of the auger to another chamber where an air stream was made to pass over the end of the auger. This air, supposedly carrying coal, was then passed to the burner.

Upon testing this device it was found that no coal was transferred into the flame. Upon further observation it was found that the coal dust was sliding in the slots and not being moved down the tube at all.

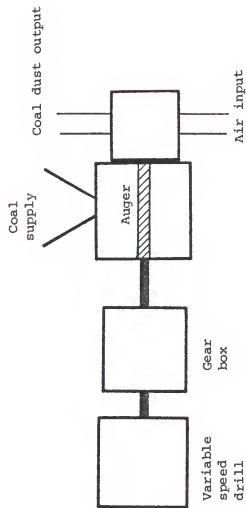


Figure 9. Auger Coal Feeder

The coal particles would stick together and the auger would just twist through the coal without any being deposited in the slots. It was thought that pressure upon the coal would cause it to be transported, but, when pressure was applied by a push plug the only thing accomplished was to compact the powder into a hard mass with no movement of coal down the channel by the auger. Further modifications of the auger (slot width and depth, turning speed, etc.) proved to show little or no improvement in coal delivery.

Based upon the previously stated results it was decided to use an air flow method to asperate coal into the flame. Shown in Figure 10 is the final coal feeder used in the following studies. Several improved features can be seen in this version which lead to improved performance and a useable and reliable coal feeder. The modifications are as follows:

1. Use of a 250 ml round-bottom flask for the coal reservoir.
2. Angling of the input air nozzle so that it pointed down into center and at a tangent to the inside surface to promote a swirling motion inside the flask.
3. Exhaust tube for the coal-air mixture which opened directly straight up and went directly to the burner without any bends in the tubing.
4. Use of a octagonal stirring bar (1/2" x 5/16") in bottom of round bottom flask and positioning of the magnetic stirrer so that the flask was not at the center causing a more vigorous motion to the stir bar.
5. Extremely narrow opening of the nozzle (~0.5 mm) causing the air to enter at a higher velocity.
6. Introduction of an auxillary air inlet at top of flask to dilute the aireated coal if necessary.

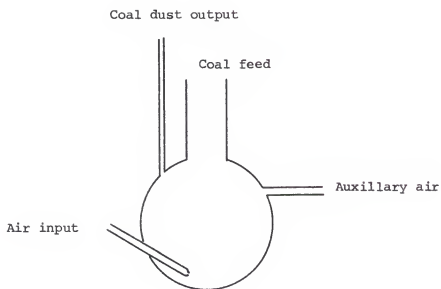


Figure 10. Final Coal Feeder

Upon testing this new coal feeder it was found to give a controllable and steady output of coal into the flame. It was also possible to use a very small amount of air (about 100 ml/min) to get a substantial amount of coal into the flame. It was found that the amount of coal fed into the flame could be varied easily by varying the amount of air input to the flask. Coal input rate was found by weighing the flask containing the coal before and after a test run, timing the length of a run, and then calculating the rate loss of coal per unit time.

One major problem with all the previous coal feeders was in obtaining a constant delivery rate over an extended period of time. This problem could be eliminated with this feeder by having a sufficient amount of coal contained in the flask, approximately 1/3 full. To test reproducibility and steadiness of flow a series of tests were run at the same air flow rate for various times. Results are shown in Table 9, as can be seen the reproducibility of the new system is quite good and the flow appeared constant and uniform to the eye.

#### Spectroscopic Apparatus

A schematic diagram of the gas-coal spectroscopic experimental set up is shown in Figure 11. With this arrangement it was possible to do emission, absorption and fluorescence measurements by only varying the electronic detection components. Table 10 lists the components used in the gas-coal diagnostic system. All of the equipment with the exception of the gas control system and electronic components, was mounted on a 4' x 8' x 12" vibration isolation table (Newport Corp., Fountain Valley, CA) to provide a steady and stable experimental environment.

Table 9  
Reproducibility of Coal Feeder

Air Flow (ml/min)	Time (s)	Wt of Coal (mg)	Feed Rate (mg/min)
30	220	58	15.8
	498	132	15.9
	1003	250	15.0
80	200	126	37.8
	574	368	38.5
	636	398	37.5
110	216	243	67.5
	420	483	69.0
	600	724	72.4

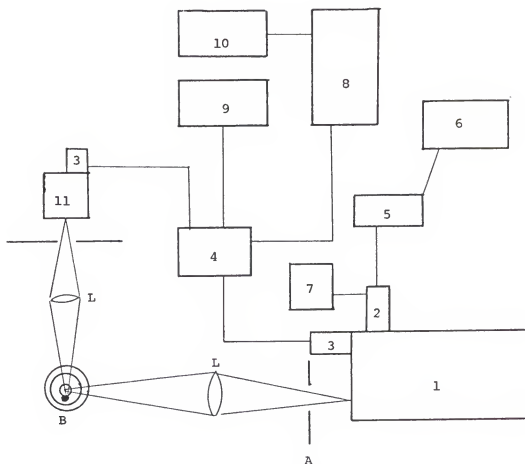


Figure 11. Block diagram of experimental arrangement.

1. 1.26 m, monochromator
2. PMT,
3. diode array
4. TN-1710
5. nanoammeter
6. strip chart recorder
7. PMT high voltage supply
8. PDP 11/34
9. floppy disk drive
10. digital plotter
11. 0.5 m monochromator
- L. lens
- A. aperture
- B. burner



Table 10  
Experimental Components of Gas-Coal Spectrometric Diagnostic System

Component	Model No.	Company
Monochromator	1269	Spex Industries, Inc. Metuchen, New Jersey 08840
Monochromator	82-000	Jarrell-Ash Division Fisher Scientific Co. Waltham, MA 02152
Photomultiplier	9781	EMI Gencom, Inc. Plainview, New York 11803
Power Supply	6515A	Harrison Division Hewlett-Packard Berkeley Hts., New Jersey 07922
Intensified Diode Array/ Multichannel analyzer	TN 1223-21 TN 1710-21 TN 1710-30 TN 1710	Tracor Northern Middleton, WI 53562
Floppy Disk Drive System	TN 1710-24B	Tracor Northern Middleton, WI 53562
Nanoameter	150 A	Keithley Instruments, Inc. Cleveland, Ohio 44139
Recorder	Servo/Riter II	Texas Instruments Co. Houston, Texas 77006
Standard Lamps	DXW FEL 30A/T24/13	Eppley Laboratory, Inc. Newport, RI 02840
Lamp Power Supply	---	Laboratory constructed
Computer	11/34	Digital Equipment Co. Jacksonville, Florida 32205
Digital Plotter	Hi-Plot DMP 7	Houston Instrument Division Bausch & Lomb Austin, Texas 78753

The burner was mounted on a laboratory constructed height riser which was then bolted on a X-Y milling table (Mastercraft tools, #500, Riverside, CA) allowing for accurate positioning of the burner with ability to perform carefully controlled spatial measurements, the Z axis (up-down) had a total travel distance of 10 cm and a variable speed motor (INSCO Corp., Groton, MA) was connected to the X-axis rotation arm allowing for precise scanning of the burner across the entrance slit of the monochromator. Lateral movement scan speed could be varied from 1"/min to 0.02"/min with the X-axis travel being calibrated in .001" steps.

In order to afford a convenient amount of work space under the burner and to allow for observations high in the flame the optical axis for all observations was set at a height of 23" above the top of the table. Supports were designed and constructed to place the optical axis of all spectroscopic instruments and collimating optics at this level. Light emitted from the flame was focused by a quartz lens (dia = 1". focal length = 4") on the slit of a 1.26 m grating spectrometer (ruled area 136 x 116 mm) blazed at 300 nm, with a dispersion of 0.65 nm/mm.. Two exit apparatus allow the use of two different detectors with a rotation of one mirror. Detectors used in these experiments were a side-on photomultiplier and an intensified diode array detector (IDARSS-512 Channels). The photomultiplier was operated at an applied voltage of -700 V, and the IDARSS was operated with an intensifier gain of 10 and variable exposure time and number of exposures depending upon the luminous intensity flux incident upon the IDARSS. For emission measurements at high resolution, the

photomultiplier output was sent to a current to voltage preamplifier and then to a lock-in volt meter for measurement, output was then displayed on the chart recorder. The sources for both absorption and fluorescence measurements were chopped to distinguish them from the background emission and obtain improved signal to noise ratios (239, 240).

Moderate-resolution spectra were obtained using a 0.5 m grating spectrometer (ruled area 52 x 52 mm, dispersion of 1.6 nm/mm) in conjunction with the IDARSS system. Broad band low-resolution spectra were obtained with a 0.2 m holographic grating spectrograph (ruled area 70 mm dia, dispersion of 24 nm/mm) in conjunction with the IDARSS system. Signals from the IDARSS detector are processed by its own signal-processing module contained in a main-frame with other signal-processing devices (i.e. scale calibrator, data smoother, etc.). Data can be stored on a floppy disk for later analysis or transferred to a PDP 11/34 for more processing (i.e., correcting for spectral response). Hard copies of data stored can be plotted by the digital plotter interfaced to the 11/34.

The 1.26 meter spectrophotometric system spectral response characteristics were determined using a calibration standard lamp according to recommended procedures (241). For absorption measurements a secondary light standard source was used and its light was collimated and passed through a quartz diffuser to obtain a uniform beam whose size was determined by blackened apertures. Visual inspection insured that the slit was evenly illuminated. The same light source was used for line reversal temperature measurements (15) by removing the diffuser and focusing the filament of the light source into the flame by a quartz lens. Procedures recommended by Snelleman (242) were used to accomplish

line reversal temperature measurements. For these measurements a 1000 ppm Na solution (from NaCl) was asperated into the flame by a pneumatic nebulizer which used 30 psi air to drive it. Temperatures were also determined using a thermocouple (platinum vs platinum - 10% Rhodium, Omega Engineering Inc., Stamford, CT) oriented vertically so as to provide less perterbation of the flame flow characteristics.

Spatial resolution of  $\pm 1$  mm could be attained and upon movement from one position to another, equilibration of the thermocouple was allowed to take place ( $\sim 1$  min) before reading the next measurement. The fluorescence excitation source was an electrodeless discharge lamp (Hg, Tl, Ga) powered by a microwave generator (Model MPG-4, Opthos Instruments, Ind. Rockville, MD). Electrodeless discharge lamps were run in a  $1/4$  - wave Evenson type cavity and were externally heated according to specifications given by Ball (243). Two quartz lenses were used to focus the light into the flame and a chopper between the two caused an AC fluorescence signal to be generated which could be detected by AC electronics. An He-Cd laser (Model 4050 Liconix, Mountain View, CA) (13 mW) was used as an excitation source for a few experiments.

#### General Considerations

The following general procedures were followed during all experiments performed during this study.

1. All gas flow rates and delivery pressures were checked at the beginning and end of the experiment to insure that desired flame conditions (lean, rich, stoichiometric) remained the same during the entire run.
2. The coal feeder was checked to insure that sufficient coal was present to insure constant delivery rate during the entire experiment; if it was found to be low coal was added. Coal was allowed to enter the flame and run for about 1-2 min to

check if all conditions were right for constant coal delivery (stir motor speed, position of feeder, etc.).

3. In cases where it was needed to know precise coal rate (ex. effect on spectra of increasing coal flow) each and every run was weighed before and after and duration of a run was timed by a stop watch to obtain accurate flow rates. Any run with a visually observable erratic flow was discarded from flow rate studies. On general spectroscopic studies, a known air flow rate was set and periodic weighing and timings were made to check reproducibility of flow settings.
4. For spatial dependent studies all movement occurred in one direction only. To reset for another measurement the height adjuster or length adjuster was returned past reference mark and moved to it from whence measurements began.
5. For all measurements using a light source, the source was allowed to warm up for at least one-half hour at which time it was monitored for stability for a period of 10 minutes. If fluctuations occurred another period of warm-up occurred.

## CHAPTER V

### DATA

The ubiquitous nature of the OH radical in hydrocarbon flames provided a good starting point for these studies. Initial observations indicated that the introduction of small amounts of coal dust ( $< 1 \text{ mg/min}$ ) into a  $\text{CH}_4$ -air flame caused the flame to become highly luminous. As the OH emissions were a useful diagnostic species (i.e. temperature measurements), it was desired to know how the coal dust influenced the OH emissions in the ultraviolet region. Spectroscopic observations of the OH 0-0 band showed variances in the overall band shape, which was further investigated both theoretically and experimentally.

#### Development of a Temperature Measurement Technique and Observations of the Effects of Varying Amounts of Coal on OH Emissions

If the 0-0 vibrational band of OH is viewed in emission under low resolution ( $\Delta\lambda \sim 2 \text{ nm}$ ) it appears as a wide hump starting at 306 nm and extending to around 320 nm with two broad peaks at 307 and 309 nm. The peak at 307 is caused by the heads of the  $R_1$  and  $R_2$  rotational branches and the peak at 309 is caused by the  $Q_1$  and  $Q_2$  branches. Mavrodineanu and Boileux (15) have given fortat parabolas, showing the six main branches of the OH 0-0 band near 306 nm. The intensities of ninety-five lines in 5 branches were calculated by Vaidya et al. (244) who show how the intensity ratio of the two peaks at 307 and 309 can be used to determine the temperature in flames.

The line intensity for emission is given by (4)

$$I = C A \nu^4 \exp(-E_r/kT)$$

where C is an instrumental constant,  $\nu$  is the wave number of the line,  $E_r$  is the rotational energy of the initial level, k is Boltzmann's constant, T is the temperature and A is the transition probability for the line. From the above equation, intensity I can be calculated at different wavelengths for various temperatures provided the values of A and  $E_r$  are known. The numerical values for all the transition probabilities and energy levels of the  $2\Sigma-2\Pi$  transition system in OH have been tabulated by Dieke and Crosswhite (245) and these values were used for the intensity calculations. The line intensities for five branches,  $R_1$ ,  $R_2$ ,  $Q_1$ ,  $Q_2$ , and  $P_1$  were calculated for the temperature range of 600-3500 K. Figure 12 shows intensity vs wavelength data for these branches at temperatures 1500, 2000, and 2500 K. It is seen from Figure 12 that, whereas the shape of the  $Q_1$ ,  $Q_2$  and  $P_1$  branches remains practically unchanged, there is a marked change in the shape of  $R_1$  and  $R_2$  branches with temperature.

For a given resolution  $\Delta\lambda$ , the convolution of line intensities with the triangular slit-function approximation (246, 247) gives the intensity vs wavelength curves which are shown in Figure 13. The equation used for the convolution is

$$I(\lambda) = \sum_{i=1}^K I_i S(\lambda, \lambda_i)$$

where the slit function

$$S(\lambda, \lambda_i) = 0 \quad \text{for } |\lambda - \lambda_i| > \Delta\lambda$$

and

$$S(\lambda, \lambda_i) = 1 - \frac{|\lambda - \lambda_i|}{\Delta\lambda} \quad \text{for } |\lambda - \lambda_i| \leq \Delta\lambda$$

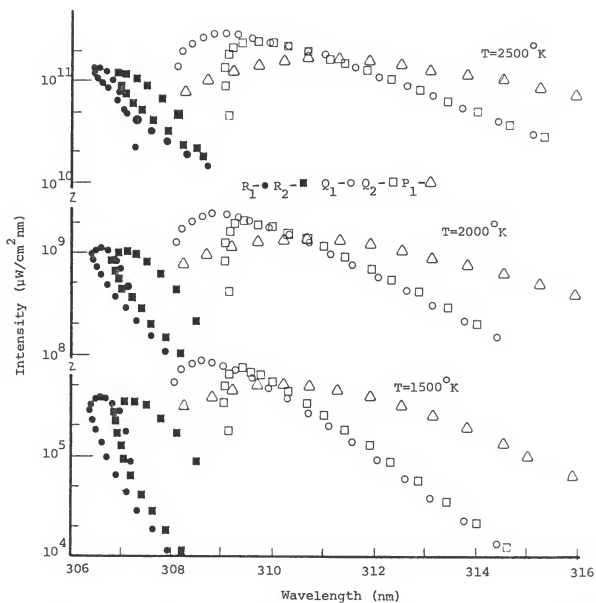


Figure 12. Calculated intensities of 5 branches of OH 0-0 band at 1500, 2000 and 2500  $^\circ\text{K}$ .



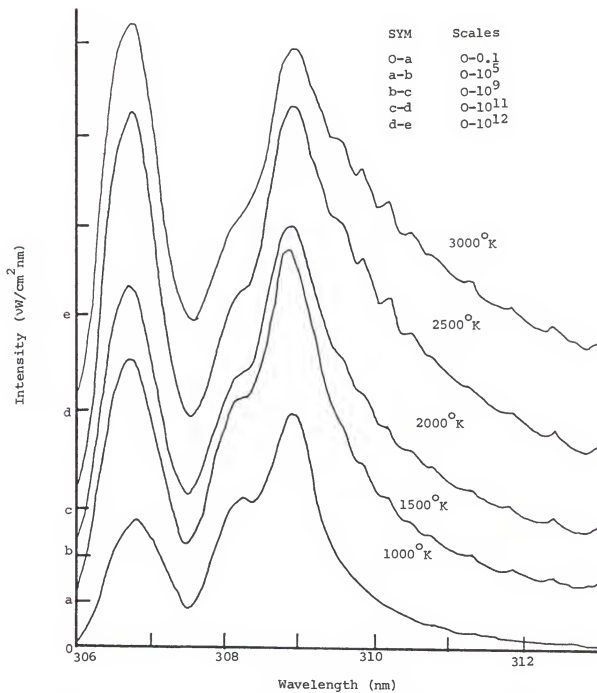


Figure 13. Spectral profiles of OH 0-0 band at different temperatures for a resolution  $\Delta\lambda = 0.5 \text{ nm}$ .

Here  $\Delta\lambda$  is the resolution,  $I_i$  is the intensity of the line,  $\lambda_i$  is the wavelength of the line,  $\lambda$  is the wavelength of the bandpass center, and  $I(\lambda)$  is the convoluted intensity. The instrumental profile necessary to determine the shape of the slit function was obtained with a He-Cd laser at 325 nm.

The following features can be observed in Figure 13. 1. All the curves show two prominent peaks, one near 307 nm and the other near 309 nm. 2. The intensity ratio of these two peaks changes with the temperature. 3. The minor feature observed near 308 nm diminishes with an increase in temperature. 4. The features observed at wavelength above 310 nm become prominent at higher temperatures. Plots of the ratio  $I(309)/I(307)$  vs temperature are shown in Figure 14. Thus, at a given resolution  $\Delta\lambda$ , for a known ratio of  $I(309)/I(307)$  the temperature in a flame can be determined from the corresponding curve.

In the  $600 \leq T \leq 2000$  K temperature range the ratio  $I(309)/I(307)$  may be fit with very good precision (1%) with the empirical equation (244)

$$R(t, \Delta\lambda) = \frac{I(309)}{I(307)} = \frac{A}{B + (T/T_O)^P}$$

where  $T_O = 1000$  K,  $A = 2.825$  and  $P = 1.145 \exp(-0.5076 \Delta\lambda)$ ,  $B = 1.927 \Delta\lambda - 0.1216 - 1.378 \lambda^2$ . By inverting the above equation a convenient interpolation formula can be obtained

$$T = T_O [(A/R) - B]^{1/P}$$

for calculating the temperature from an experimental ratio measurement. Figure 14 illustrates the temperature vs intensity ratio relationship for three values of  $\Delta\lambda$ . The points represent the theoretical data and the lines represent the analytic expression. As is seen, the fits are

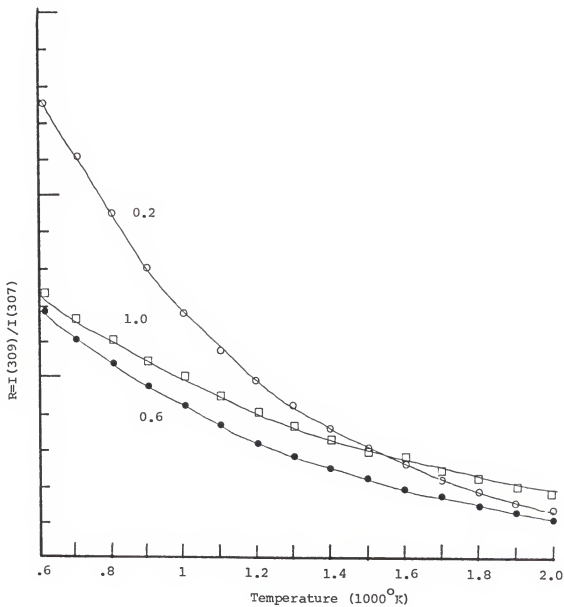


Figure 14. Intensity ratios vs. temperature for spectral resolutions  $\Delta\lambda = 0.2 \text{ nm}$ ,  $\Delta\lambda = 0.6 \text{ nm}$  and  $\Delta\lambda = 1.0 \text{ nm}$ .

very good. Since slit functions usually depart from triangular shape, it would be wise in actual applications to use test experimental data to determine the parameters A, P, and B.

At this point in time many OH spectra were obtained from a methane-air flame, but the effects of coal upon these emissions were still unknown. To investigate this question an experiment was conducted where various amounts of coal (200 mesh, 5-400 mg/min) were added to a CH<sub>4</sub>/air flame, and the OH emissions were observed. The total air flow was held constant and the coal dust was only introduced into the center section of the burner. All spectroscopic observations were made at a height of 4 cm (measured from the burner head) and the IDARSS system was used with both 0.5 m and 1.26 m grating monochromators.

The coal used (Virginia bituminous) had a calorific value of 13,000 Btu/lb. Assuming complete combustion, the percentage of energy produced by the coal was calculated as a function of coal flow rate. These percentages are shown in Table 11. As increasing amounts of coal are added, the total luminous output of the flame increased dramatically. At low flows an orangish glow is seen, and the particles of coal leave luminous trails as they rise in the flame. The larger coal particles continue their incandescence for longer periods of time than smaller ones, which stop before reaching very high in the flame. As the particles first enter the flame they appear to emit a burst of luminescence which rapidly decays to a lower level of light emission which continues until the particle is completely combusted. Larger particles seemed to emit larger bursts for a slightly longer period

Table 11  
Coal Flow Rates Used in Experiment and Heat Production Ratios

Spectrum #	Coal Flow (mg/min)	Released Heat <sup>1</sup> from Coal $\Delta H_C^C$ (kcal/min)	Total <sup>2</sup> Flame $\Delta H_C^C / \Delta H_C^G$	Inner <sup>3</sup> Flame $\Delta H_C^C / \Delta H_C^G$
1	-	20.73, 3.41 <sup>4</sup>	0.0000	0.0000
2	5.5	0.0397	0.0020	0.0116
3	7.5	0.0542	0.0026	0.0159
4	9.5	0.0686	0.0033	0.0201
5	16.0	0.1156	0.0056	0.0339
6	42.0	0.3033	0.0146	0.0889
7	63.0	0.4550	0.0218	0.1334
8	66.0	0.4767	0.0230	0.1398
9	145.0	1.0472	0.0505	0.3071
10	202.0	1.4589	0.0704	0.4278
11	305.0	2.2028	0.1063	0.6460

<sup>1</sup>Calculated assuming complete combustion of 13,000 Btu/lb coal.

<sup>2</sup>Ratio of heat energy produced by coal combustion to that produced by methane/air flame.

<sup>3</sup>Above ratio for inner flame region where coal is injected and observations are made.

<sup>4</sup>Heat released by gas flame only, total flow 1.56 l/m (1.11 g/min) inner flow only 0.36 l/min (0.257 g/min).

of time than small particles. High-resolution spectra ( $\Delta\lambda = 0.06 \text{ nm}$ ) showed no gross structural changes in relative rotational line structure intensities, but a slight increase was seen in total overall intensity. Figure 15 shows a high-resolution spectra of the laboratory methane-air flame, and Figure 16 shows the same flame with the addition of  $\sim 305 \text{ mg/min}$  of coal dust.

The intensity ratio ( $I(309)/I(307)$ ) temperature method was used to determine the temperature of the laboratory methane-air flame, as well as for the gas flame of a large experimental burner designed in connection with a gas coal burning project by other workers in this laboratory. Figure 17 shows a moderate resolution spectrum ( $\Delta\lambda = 0.6 \text{ nm}$ ) obtained by a 0.5 m monochromator of the laboratory gas flame in the 279-324 nm spectral region. From this spectrum the intensity ratio of the two peaks is found to be 1.206 which gives a temperature of 2025 K from the interpolation formula given previously. This value of the temperature is close to the 2050 K temperature obtained with the sodium line-reversed method. Temperature determined from the rotational structure of the  $R_2$  branch of the 0,0 band (245) was found to be 2020 K.

Figure 18 shows the spectrum of an after-burning flame from the large experimental combustor taken with this laboratory's mobile spectroscopic facility (248, 249). The temperature derived from the spectrum is  $\sim 1500 \text{ K}$ , which was expected due to the nature of the after-burning flame and is in good agreement with thermocouple temperature measurements of 1550 K (250).

#### Survey Spectra of Methane-Air and Methane-Air-Coal Dust Flames

A series of survey spectra were obtained with the 1.26 m spectrometer in conjunction with a high gain photomultiplier with enhanced

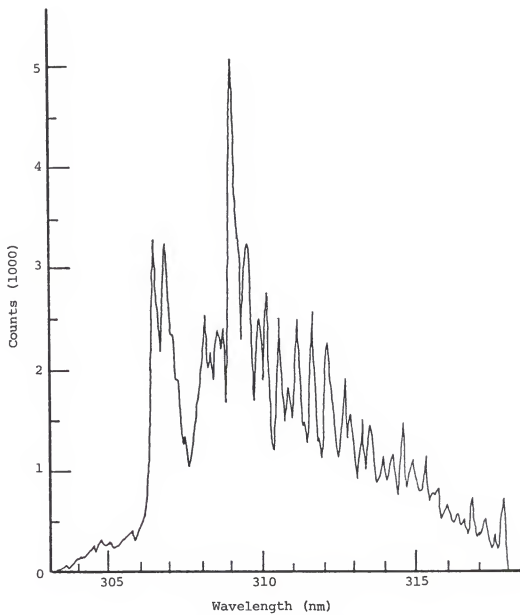


Figure 15. 1.26 m spectrum of CH<sub>4</sub>/Air flame in 0-0 band.

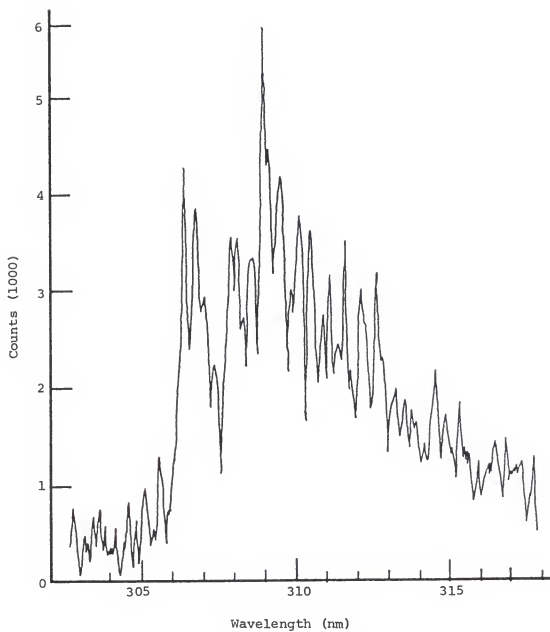


Figure 16. 1.26 m spectrum of  $\text{CH}_4/\text{Air}$  flame with addition of 30 mg/min of 200 mesh pulverized coal.



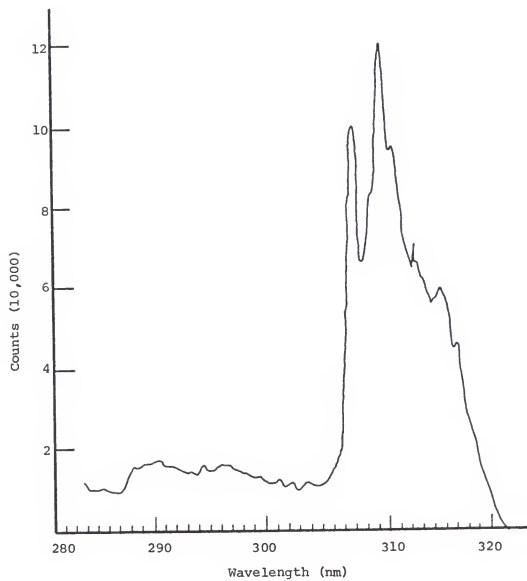


Figure 17. 0.5 m spectrum of CH<sub>4</sub>/Air flame 0-0 band.

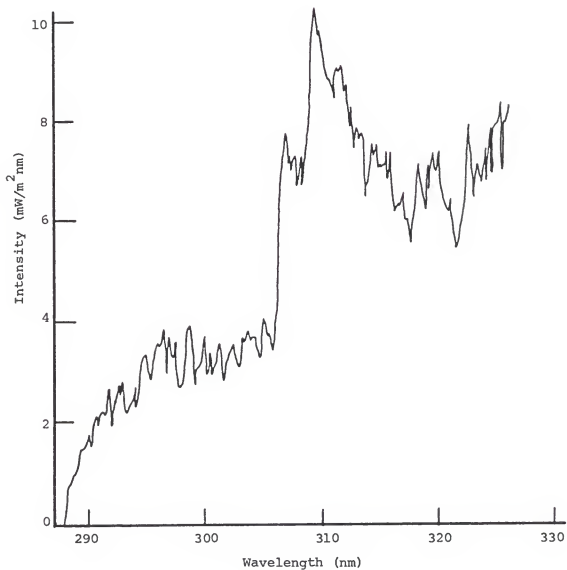


Figure 18. Spectrum of afterburning flame taken with mobile laboratory using 0.5 m spectrograph through periscope..

ultraviolet response (EMI-9781vEFL) The spectral region covered was from 180 nm to 600 nm and a 100  $\mu$ m slit, 1 cm high was used to obtain reasonable resolution and adequate light gathering ability. All spectra were run with room lights off to avoid mercury lines emitted by the fluorescent overhead lights, which were observed during preliminary observations. Spectral emitters positively identified (251) and observed in a stoichiometric  $\text{CH}_4/\text{air}$  flame in this region were:

1. CO - fourth positive system:  $\text{A}^1\Pi - \text{X}^1\Sigma^+$  from  $\sim 192$  to 235 nm, many different vibrational bands.
2. OH - a.  $\text{B}^2\Sigma^+ - \text{A}^2\Sigma^+$  (1,9) vibrational band at 254-260 nm  
b.  $\text{A}^2\Sigma^+ - \text{X}^2\Pi$ ; vibrational bands, (3,0) at 242-252 nm; (2,0) at 262-272 nm; (1,0) at 281-300 nm; (0,0) at 305-325 nm listed in order of increasing intensity.
3. CH - a.  $\text{B}^2\Sigma^- - \text{X}^2\Pi$  (0,0) and (1,1) vibrational bands from  $\sim 387$ -404 nm. b.  $\text{A}^2\Delta - \text{X}^2\Pi$  (0,0) and (1,1) and (2,2) vibrational bands from 417-440 nm.
4.  $\text{C}_2$  Swan bands:  $\text{d}^3\Pi_g - \text{a}^3\Pi_u$  vibrational bands: (5,4), (6,5), (4,3), (3,2), (2,1) and (1,0) from 466-474 nm; (3,3), (2,2), (1,1) and (0,0) from 504-516.5 nm; (2,3), (1,2) and (0,1) from 552-564 nm.

Molecular energy level symbols were given as upper level first to be consistent with the usual molecular spectroscopic conventions as discussed by Herzberg (252). These spectra are also shown in Figures 19 to 24. Spectra of CO, CH and  $\text{C}_2$  were only observed low in the flame (0-10 mm) while OH emissions (0,0) were visible higher up in the flame ( $\sim 7$  cm) but with diminishing intensity with increasing height.

Upon introducing coal into the flame slight changes were seen in the spectra of CO and OH with larger changes in the spectra of CH and  $\text{C}_2$ , mainly intensity changes. New emissions were observed in the region between 402 and 412 nm which can be assigned to the  $\text{C}_3$  radical

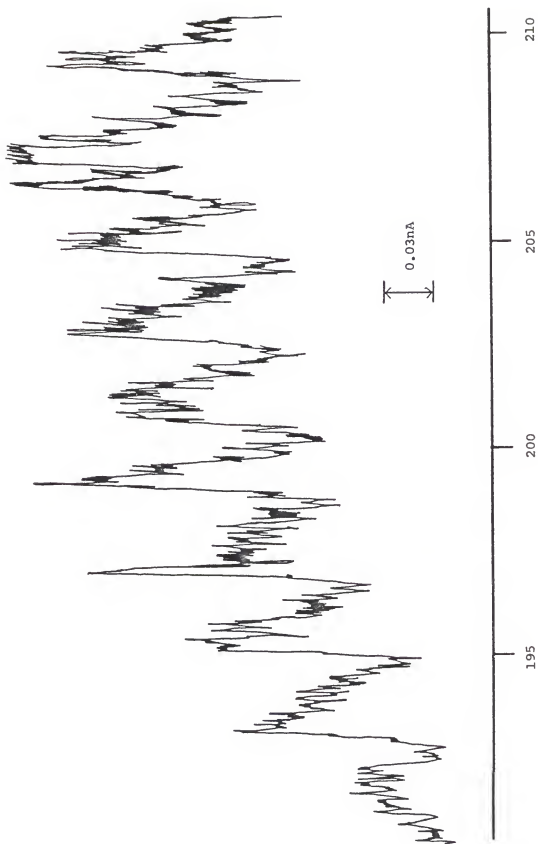


Figure 19. CO fourth positive (slit=100 $\mu$ , 1 cm high, chart 2"/min, 5 $\times 10^{-2}$  nm/s).

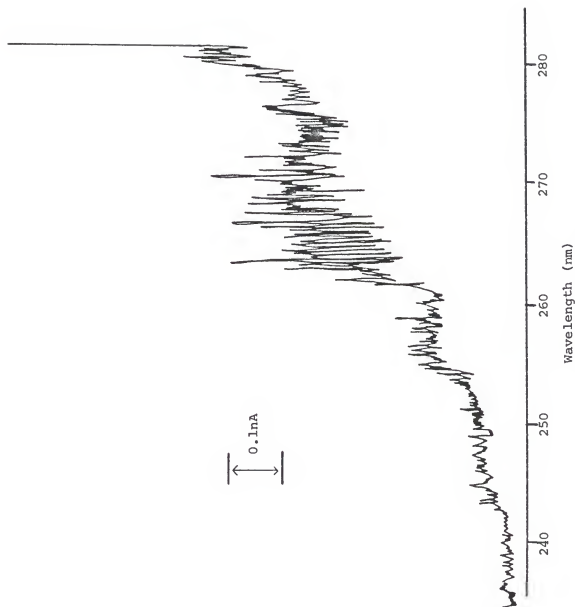


Figure 20. OH spectra 240-280

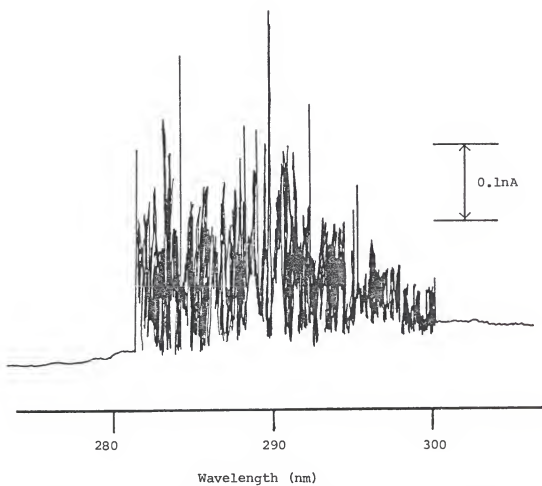


Figure 21. OH (1,0) band (slit  $100\mu$ , 1cm high chart 1"/min mono  $5 \times 10^{-1}$  nm/s).

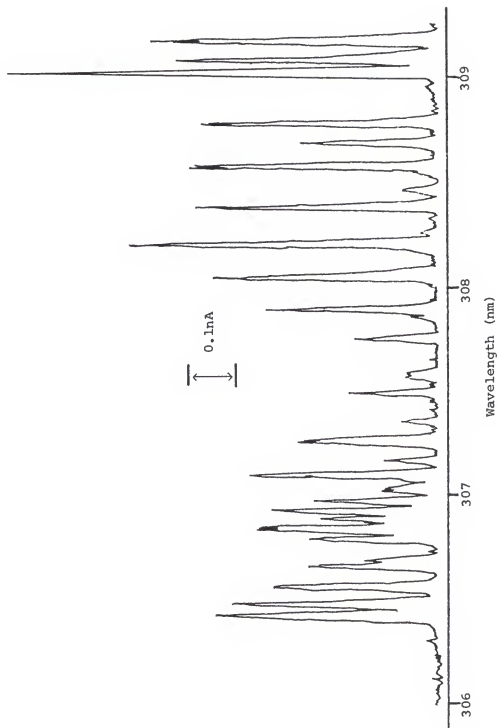


Figure 22. High resolution spectra of (0,0) OH (slit =  $20\mu$ , 2mm high chart  $1''/\text{min}$ ,  $5 \times 10^{-4}$  nm/s).

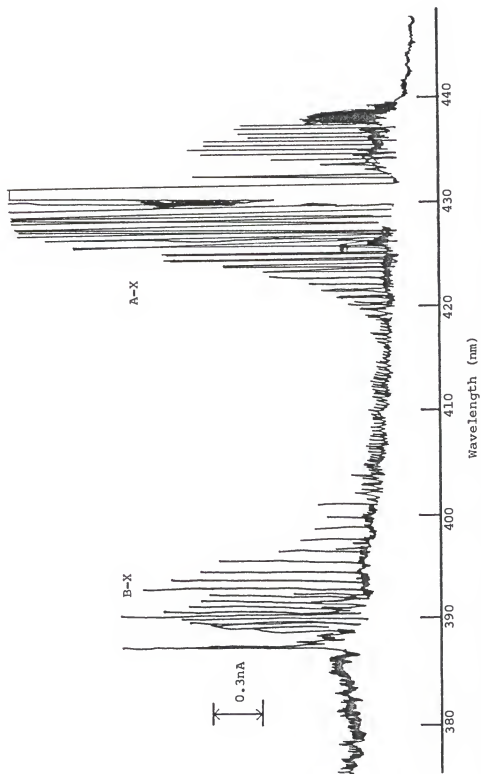


Figure 23. CH bands, B-X, A-X (slit=100 $\mu$ , 1 cm high chart 1"/min, mono  $1 \times 10^{-1}$  nm/s).



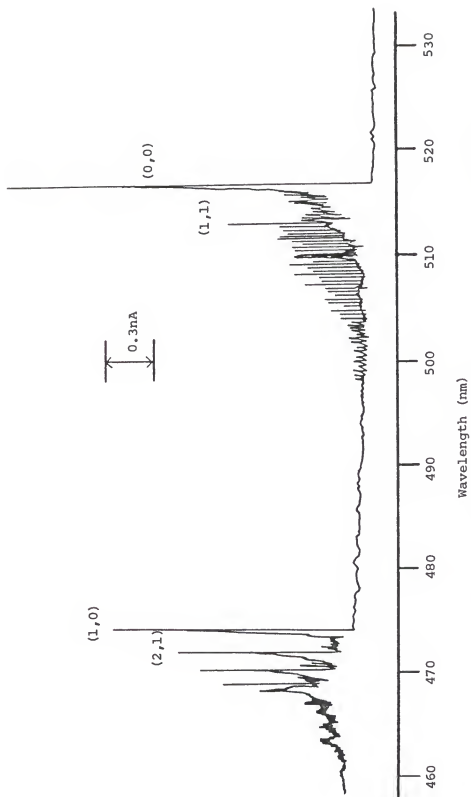


Figure 24. C<sub>2</sub> bands A-X (slit=100μ, 1 cm high, chart 1"/min, mono 1x10<sup>-1</sup> nm/s)

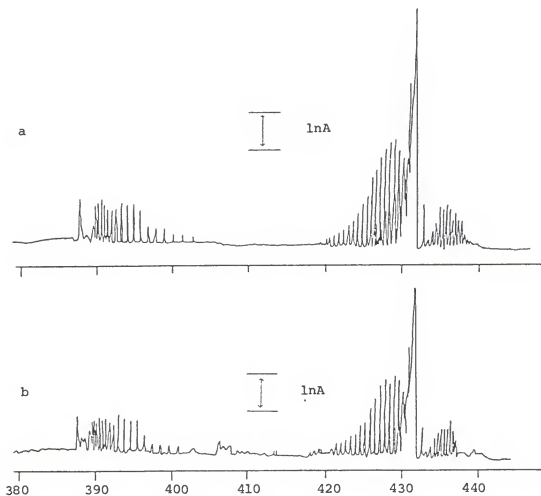


Figure 25. Spectra of CH Region

a) CH<sub>4</sub>/Air Flame

b) CH<sub>4</sub>/Air + 100 mg/min Coal

(slit=100μ 1 cm high,  
chart 1"min 2x10<sup>-3</sup>nm/s)

${}^1\Pi_u - {}^1\Sigma_g^+$  transition. Figure 25 shows the region of 386 to 440 nm of a methane-air flame and methane-air flame with approximately 100 mg/min coal dust showing the decrease in the CH emissions and the appearance of  $C_3$  emissions in the coal dust flame.

Measurement of Excited State Populations in Methane-Air and Methane-Air-Coal Dust Flames

In this set of experiments the spectral emissions of OH, CH,  $C_2$  and CO were measured as a function of height in the flame. In a methane-air flame fuel/air ratios ( $\phi$ ) of 0.66, 0.77, 0.90, 1.00, 1.10, 1.30, 1.50, 1.70, 1.80, 1.90 and a diffusion flame were measured while in a methane-air-coal dust flame ratios of 0.77, 1.00 and 1.10 were measured using a coal flow rate of approximately 30 mg/min. Total gas flow rates were held constant, with fuel and air being adjusted to obtain desired  $\phi$ . In this experiment the flame separator was not used and the coal was dispersed through the total flame volume. For the  $\phi = 1.00$  flame methane flow was 1.614 l/min with an air flow of 16.9 l/min for a total flow rate of 18.514 l/min, which was held constant for all gas flames and flames with coal. Table 12 gives volume flow rates and mass flow rates for the flames studied.

All measurements were made using the 1.26 m monochromator with the same photomultiplier detector as was used for the survey spectra. Two millimeter high slits were used for all measurements while 100  $\mu$ m wide slits were used for OH, CH and  $C_2$  while a 350  $\mu$  wide slit was used for CO measurements due to the low intensity of these bands.

The intensity of a spectral line in emission,  $I$ , is defined as the energy emitted by the source per second (252). In an optically thin gas this is equal to  $1/4\pi$  times the product of four factors:

Table 12  
Volume and Mass Flow Rates for Experimental Flames

$\phi$	liters/min $\text{CH}_4/\text{air}$	grams/min $\text{CH}_4/\text{air}$
0.66	1.108/17.406	0.796/20.626
0.77	1.267/17.247	0.909/20.438
1.00	1.614/16.90	1.159/20.027
1.10	1.76/16.754	1.263/19.853
1.30	2.045/16.468	1.468/19.515
1.40	2.183/16.330	1.568/19.351
1.70	2.586/15.927	1.856/18.874
1.90	2.843/15.669	2.042/18.568
$\infty$	1.614/0	1.159/0

1. The number of molecules in the upper level per unit area in the line of sight. If  $n_2$  is the number per unit volume of these molecules, and  $l$  is the thickness of the emitting layer then the number of molecules is given by  $n_2 l$ .
2. The transition probability  $A_{21}$  of the line being observed.
3. The energy  $h\nu$  of the line, where  $h$  is Planck's constant and  $\nu$  is the frequency ( $s^{-1}$ ) of the line.
4.  $\Omega$  the solid angle of collection observed.

This yields for the intensity of a line, the equation

$$I = \frac{1}{4\pi} \Omega n_2 A_{21} h\nu$$

which can be solved for  $n_2$  yielding

$$n_2 = \frac{I}{l} \frac{4\pi}{A_{21} h\nu \Omega}$$

The intensity of a line was measured experimentally in the following manner. First the survey spectra were studied to find lines that were relatively intense and free from overlap by other lines. Unfortunately no lines could be found of sufficient intensity which were completely isolated from other spectral lines. A compromise was made between the need for an individual line and the need for adequate signal strength to perform the measurements.

The absolute spectral response of the photometric system was determined using a calibrated standard of spectral irradiance. By also measuring the bandpass of the monochromator, by scanning across a suitable narrow line source (He-Cd laser), the photometric system was calibrated for absolute intensity measurements. In order to measure the intensity of a line the monochromator was slowly scanned ( $1 \times 10^{-2}$  nm/s) across the line of interest and the photomultiplier output was displayed on a strip chart recorder (2"/min). The lines were selected such that a baseline

could be established after the line was scanned to obtain a value for the background signal. The intensity of this line was taken to be the peak value as the line was scanned. The bandwidth of the monochromator (0.065 nm) insured that the line was totally within the bandpass of the monochromator due to its small line width ( $<0.005$  nm) (245), therefore yielding an integrated value for the intensity of this line. This peak intensity, measured in nanoamperes, could then be converted into  $\text{W}/\text{cm}^2 \text{Sr}$  using the calibration scale at that wavelength.

The line observed was identified by comparison to reference spectra and by the wavelength dial of the monochromator which was sufficiently accurate ( $+0.1 \text{ \AA}$ ) so that the reading could be used for line identification. An example would be the Q<sub>9</sub> line of OH (0-0) which is given by Dieke and Crosswhite (245) to be 306.372 nm was found to be 306.383 by the monochromator dial.

For all species except CO, where an entire vibrational band was measured, there was more than one line contained in the monochromator's bandpass when centered on the primary line. To calculate a number density, the transition probabilities of the lines within the bandpass of the monochromator were summed together to obtain an effective transition probability for the observed intensity. This summation of transition probabilities induces a systematic error into the number density calculations by yielding an effective value larger than the "true" value. This error would cause the calculated number densities to appear smaller than the "true" value. In order to accurately estimate this error one must know the fraction of the total measured intensity caused by each individual line within the observed bandpass. The actual error might be

calculated by convoluting the slit function with the expected line profile which can be determined using the Voigt' profile equation assuming the same broadening mechanism for all lines observed. This systematic error would at most cause a factor of two difference between the measured values and the "true" absolute number densities, but the relative numbers should be as accurate as the transition probabilities  $\sim \pm 20\%$ .

For the calculations involving OH the rotational line transition probabilities were obtained from the work of Dimpel and Kinsey (253) who observed the radiative lifetimes of individual rotational states which were then used to calculate Einstein A and B coefficients for the (0-0) band of the A-X transition. Rotational lines observed within the spectral bandpass (0.065 nm) were identified using the tabulations of Dieke and Crosswhite (245) and the spectrophotometric atlas of the A-X transition by Bass and Broida (254). The transition probabilities of the lines found to lie within the bandpass were summed to obtain an effective transition probability (255). The frequency used for calculations was the center frequency of the bandpass.

For the calculations involving CH and C<sub>2</sub> no compilations of individual rotational transition probabilities were found to exist in the literature so rotational transition probabilities were calculated in the following manner. This discussion follows the nomenclature and notation of Tatum (256) and the recommended conventions for defining transition moments and intensity factors in diatomic

molecular spectra by Whiting et al. (255) as well as the conventional notations of molecular spectroscopy (i.e. ' = upper state, " = lower state, etc.) (252).

The strength of a rotational line ( $S_{J',J''}$ ) can be given by the expression (256)

$$S_{J',J''} = \frac{S(N'J', N''J'') \left| R_e^{v'v''} \right| (n'v', n''v'')|^2}{(2-\delta_{O,\Lambda}) (2S+1) (2J'+1)}$$

where  $\left| R_e^{v'v''} \right| (n'v', n''v'')|^2$  is the band strength, which is the square of the transition moment of the band and is a function of the electronic and vibrational levels involved in the transition. The  $n', n''$  define the two molecular states and the  $v', v''$  the vibrational levels. The  $S(N'J', N''J'')$  are the line strength factors, also known as the Honl-London factors, which determine the relative intensities of the branches within a band and the relative intensities of a line in a branch. The Honl-London factors are dimensionless while the line strength has the same dimensions as the band strength which is  $[\text{dipole moment}]^2$  for electric dipole radiation. The original formula of Honl and London (257) only applied to transitions between singlet states, however formulae which apply to transitions between states of higher multiplicity have been given by many other workers such as Mulliken (258), Kovacs (259) and Schadee (260).



For calculation of rotational line strengths the Honl-London factors must obey the following sum rule. The sum of the Honl-London factors for all those transitions that have a common upper level is  $2J'+1$ . This implies that the sum of the Honl-London factors for all the branches in a band is  $(2-\delta_{O,\Lambda})(2S+1)(2J'+1)$  when the factors are expressed in terms of  $J$ . This accounts for the denominator in the line strength equation where  $(2-\delta_{O,\Lambda})$  is the electronic statistical weight which equals  $2S+1$  for  $\Sigma$  states and  $2(2S+1)$  for other electronic states and  $2S+1$  is the spin multiplicity which is given as a left hand superscript in the molecular term symbol.  $J'$  refers to the rotational level of the upper state.

Honl-London factors for  $CH A^2\Delta-X^2\Pi$  and  $C_2 d^3\Pi-a^3\Pi$  were calculated using the formula of Schadee (260). For the rotational levels involved in  $CH$  (258) and  $C_2$  (260) both molecular levels involved in the transitions were considered to belong to Hund's case b. Once individual rotational line strengths ( $S_{J,J'}$ ) were calculated the transition probabilities were obtained by using the following equation (256);

$$A_{21} = \frac{16\pi^3}{3hc} \nu^3 \frac{S_{J,J'}}{2J'+1} (8.47842 \times 10^{-30})^2$$

where  $\epsilon_0$  is the permittivity of vacuum and the numerical term converts line strength in atomic units to SI units.

Band strengths for  $CH$  were obtained from the work of Hinze, Lie and Liu (261) who obtained a value of 0.3785 a.u. for the (0,0) band of the  $A^2\Delta-X^2\Pi$  transition and a value of 0.3361 a.u. for the 1-1 band.

These values were obtained from an ab initio calculation of the dipole transition matrix elements using extended configuration interaction (CI) electronic wavefunctions as reported by Lie, Hinze and Liu (262). From the calculated transition matrix elements, band strength and band oscillator strength were calculated. The authors reported an accuracy of  $\pm 15$  percent for their calculated results of band strengths. Calculated radiative lifetimes were in good agreement with experimental values. Rotational lines observed within the spectral bandpass were identified using the tabulations of Moore and Broida (263) and the spectrophotometric atlas of CH from 300 to 500 nm by Bass and Broida (264).

The band strength for  $C_2$  was obtained from the work of Cooper (265) who obtained a value of 4.10 a.u. for the (0,0) band of the  ${}^3\Pi-{}^3\Pi$  transition which is in good agreement with the value of 4.12 a.u. obtained by Arnold and Langhoff (266). Cooper calculated potential energy curves and spectroscopic constants for the triplet states of  $C_2$  using self-consistent-field plus configuration interaction techniques. The variation of the electronic transition moment with internuclear separation was calculated for the Swan, Ballik-Ramsay and Fox-Herzberg band systems and was found to be in good agreement with existing experimental and theoretical data. Rotational lines observed within the bandpass were identified using the tabulations of Phillips and Davis (267) on the Swan system of the  $C_2$  molecule.

For the CO calculations the vibration band at 208.9nm(5,12) was used and the transition probability of this band was given as  $0.221 \times 10^7 s^{-1}$  by Mumma, Stone and Zipf (268). They used electron

impact on CO to generate emission from the fourth positive bands and used relative intensity measurements on 28 bands to determine the dependence of  $R_e$  (electronic transition moment) on the  $r$  centroid. which is  $R_e = 1.9(1.0 - 0.6 \bar{r}_{v',v''})$ . Absolute transition probabilities were computed using the above functional form for  $R_e$  and normalizing the total transition probability of the  $v'=2$  level to published experimental results. The vibrational level observed was identified using the tabulations of Krupenie (269) and the published CO fourth positive spectra of Hornbeck and Herman (270) and Headrich and Fox (271).

Transitions observed and the transition probabilities used are given in Table 13 and the calculated concentrations as a function of height for all the different flames are shown in Figure 26 to 39. The solid angle of collection ( $\Omega$ ) was the same for all measurements with a value of 0.0123 Sr. Because the flame is not a perfect cylinder and various fuel/air ratios led to different size flames the individual flame widths were measured as a function of height and these values are used for the path length for the respective flames. Table 14 gives the values of path length used for the different flames at different heights.

In Figures 40, 41 and 42 the differences between the 3 flames with coal dust and the identical flames without coal dust are shown. A number less than one indicates a decrease in excited state population upon the introduction of coal while a number greater than one indicates an increase in excited state population upon the introduction of coal dust. These ratios also indicate present changes which will be used when discussing the data. For example, a ratio of 1.10 means a ten percent increase.

Table 13  
Lines Observed-Transition Probabilities vs Excited State Calculations

Species and lines	Wavelength (nm)	$\lambda(s^{-1})$
<hr/>		
OH(0-0)		
$Q_1^7$	308.9734	6.403 E5
$Q_2^3$	308.9861	5.448 E5
$Q_2^2$	308.9861	4.964 E5
CH(0-0)		
$Q_{1d}^7$	431.1306	4.357 E4
$Q_{2c}^7$	431.1306	3.870 E4
$Q_{2d}^7$	431.0908	3.871 E4
CH(1-1)		
$Q_{1c}^8$	431.1110	3.412 E4
$Q_{1d}^7$	431.1425	3.869 E4
$Q_{2c}^7$	431.1425	3.436 E4
C <sub>2</sub> (0,0)		
$P_1^{15}$	516.5026	5.536 E4
$P_1^{14}$	516.5026	5.925 E4
$P_1^{16}$	516.5026	5.194 E4
$P_2^{13}$	516.5026	6.361 E4
$P_2^{14}$	516.5026	5.916 E4
$P_3^{12}$	516.5026	6.879 E4

-----  
Continued

Table 13-Continued

Species and lines	Wavelength (nm)	$A(s^{-1})$
$P_2^{15}$	516.5026	5.528 E4
$P_3^{13}$	516.5242	6.382 E4
$P_3^{12}$	516.5242	6.905 E4
$P_3^{14}$	516.5242	5.932 E4
$P_3^{11}$	516.5026	7.511 E4
$P_3^{15}$	516.5026	5.542 E4
CO(5,12)	208.99	2.21 E6

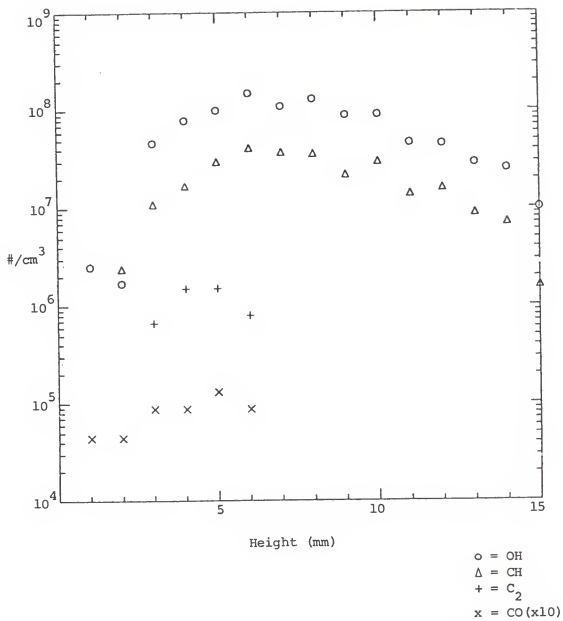


Figure 26. Excited state concentrations for  $\phi = 0.66$ .

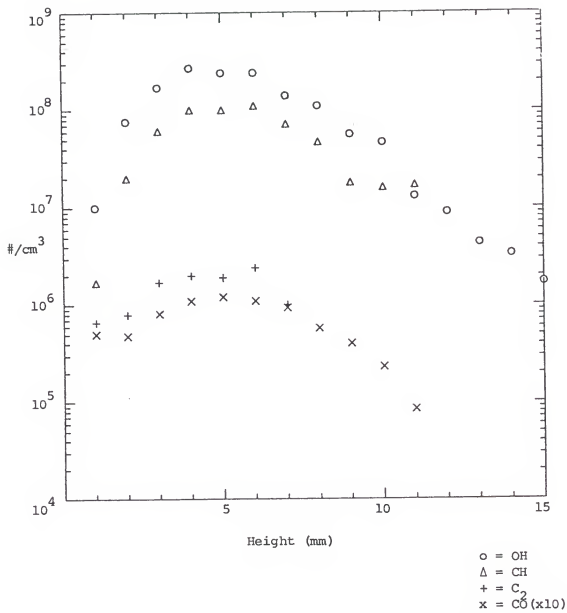


Figure 27. Excited state concentrations for  $\phi = 0.77$

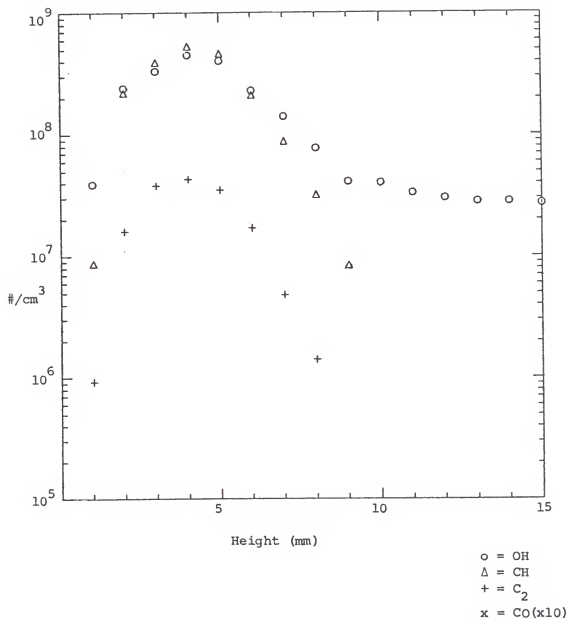


Figure 28. Excited state concentrations for  $\phi = 0.90$



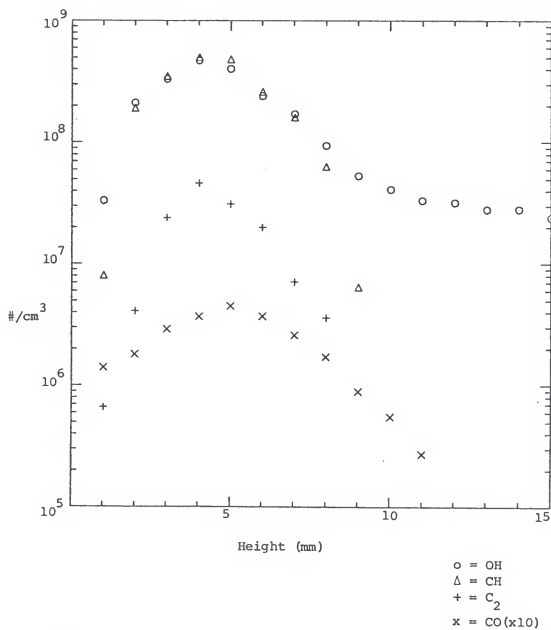


Figure 29. Excited state concentrations for  $\phi = 1.00$

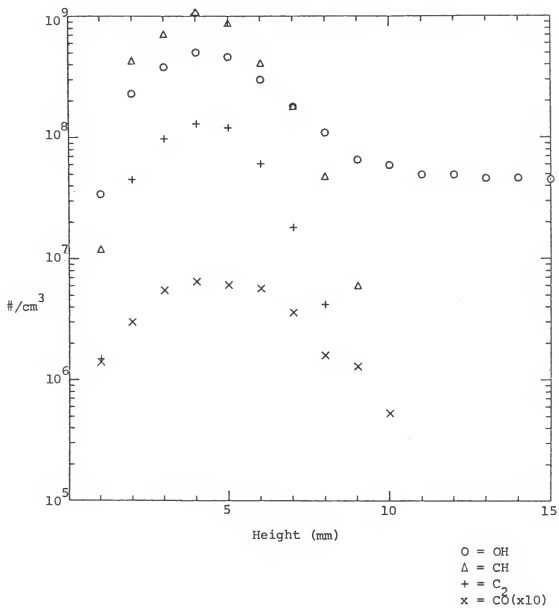


Figure 30. Calculated Excited State Concentrations for  $\phi = 1.1$

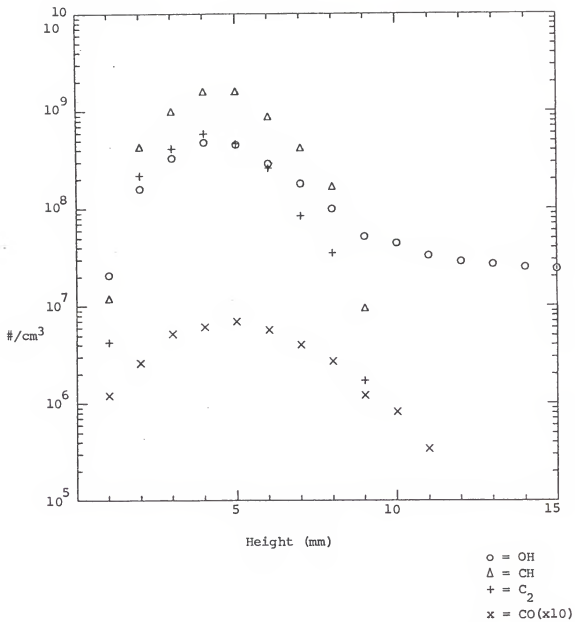


Figure 31. Excited state concentrations for  $\phi = 1.3$ .

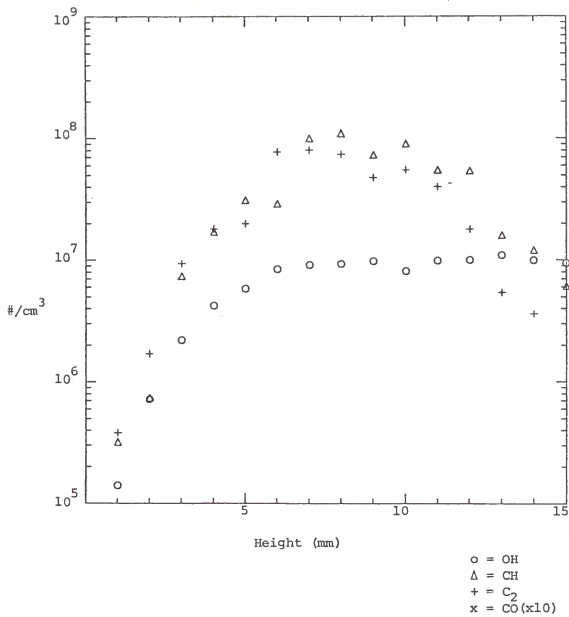


Figure 32. Excited state concentrations for  $\phi = 1.5$ .

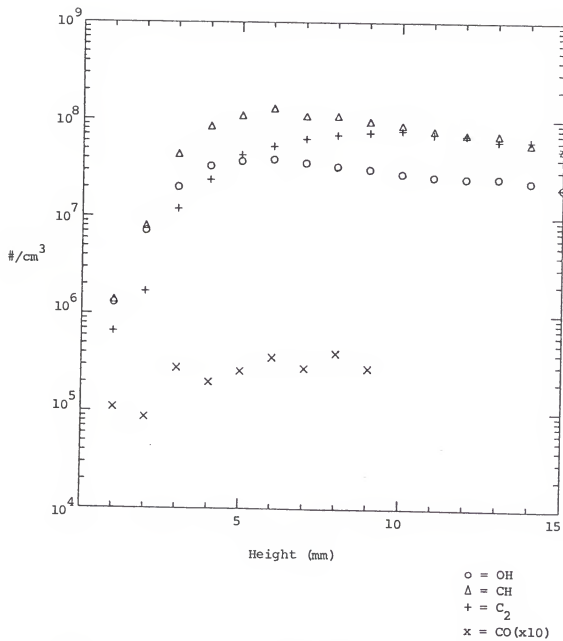


Figure 33. Excited state concentrations for  $\phi = 1.70$ .

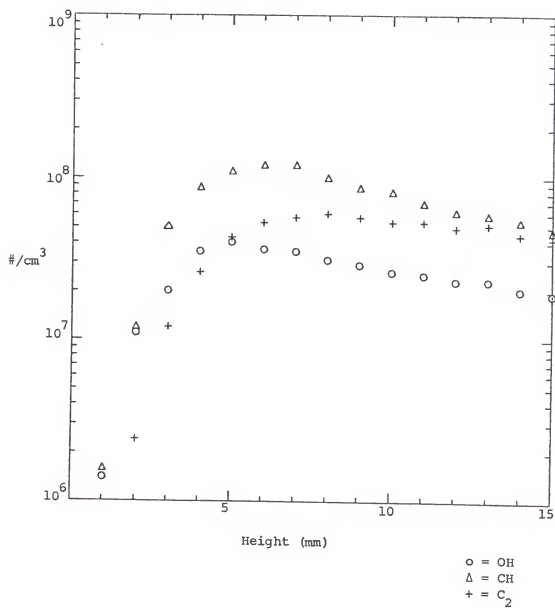


Figure 34. Excited state concentrations for  $\phi = 1.8$

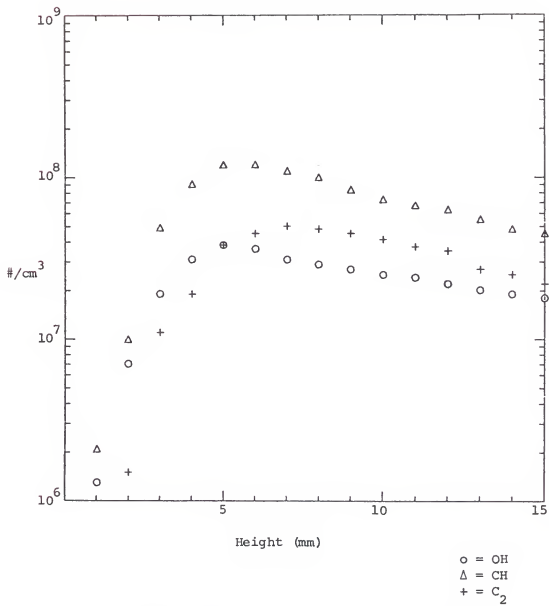
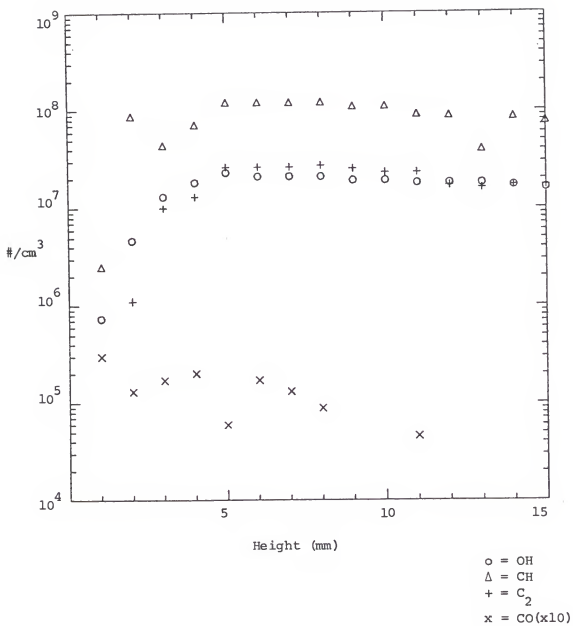


Figure 35. Excited state concentrations for  $\phi = 1.90$ .

Figure 36. Excited state concentrations for  $\phi = \infty$



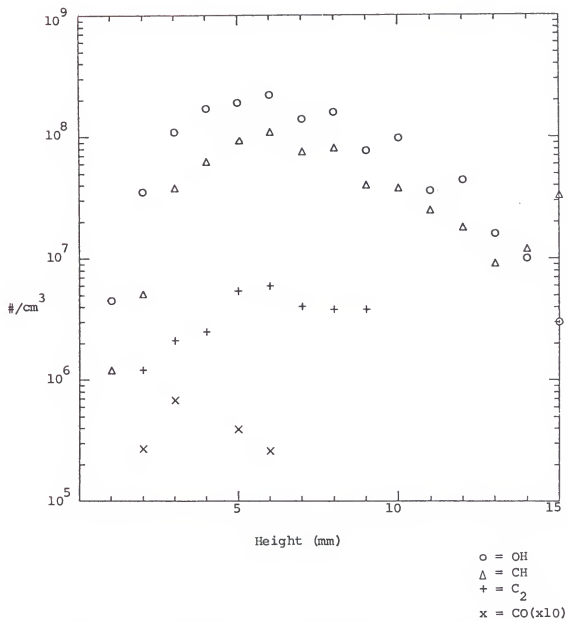


Figure 37. Excited state concentrations for  $\phi = 0.77 + 30$  mg/min coal.

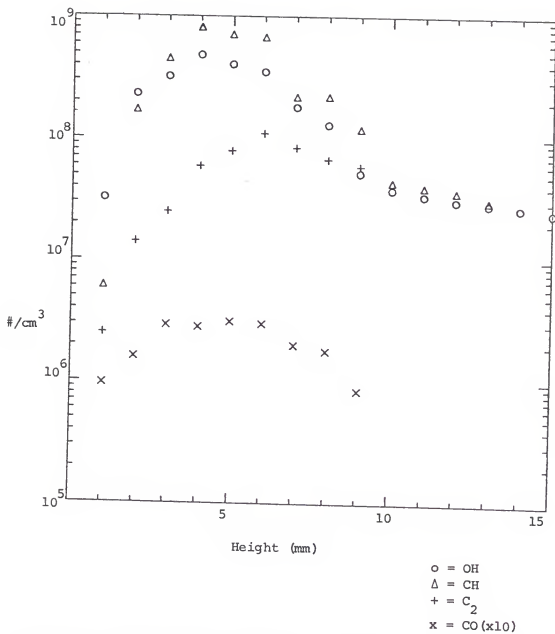


Figure 38. Excited state concentrations for  $\phi = 1.00 + 30$  mg/min coal.

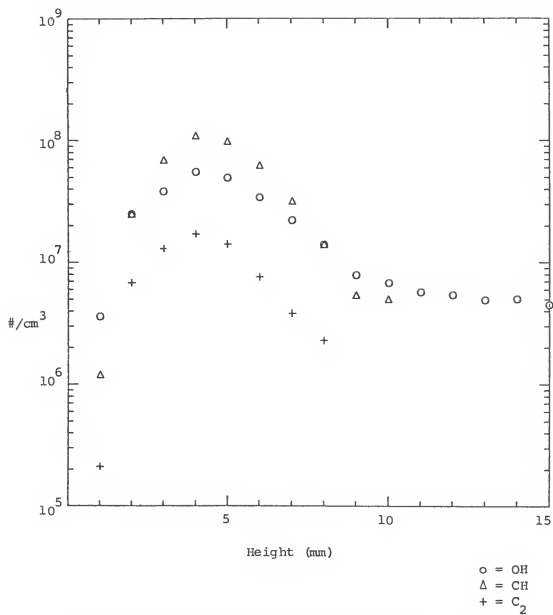


Figure 39. Excited state concentrations for  $\phi = 1.10 + 30 \text{ mg/min coal}$ .

Table 14  
Flame Widths (cm) vs Height (mm)

$\phi$	Height									
	2	4	6	8	10	12	14	16	18	20
0.66	2.9	2.9	2.9	3.0	3.0	3.0	3.2	3.5	3.5	3.6
0.77	2.9	3.0	3.0	3.0	3.0	3.0	3.0	3.0	3.0	3.0
0.90	2.9	3.0	3.0	3.0	3.0	3.1	3.1	3.1	3.1	3.1
1.0	2.9	2.9	3.0	3.0	3.1	3.1	3.1	3.1	3.1	3.0
1.1	3.0	3.0	3.0	3.2	3.3	3.3	3.2	3.2	3.2	3.2
1.3	3.1	3.1	3.3	3.3	3.4	3.5	3.5	3.5	3.5	3.4
1.5	3.0	3.0	3.1	3.1	3.2	3.2	3.3	3.3	3.3	3.3
1.7	2.9	2.9	3.0	3.0	3.0	3.0	3.2	3.2	3.2	3.3
1.8	2.9	2.9	3.0	3.0	3.0	3.0	3.2	3.2	3.2	3.2
1.9	2.9	2.9	3.0	3.0	3.0	3.0	3.2	3.2	3.2	3.2
$\infty$	3.0	3/0	3/0	2.9	2.8	2.8	2.6	2.6	2.6	
1.0+Coal	2.9	2.9	2.9	2.9	2.9	2.9	3.0	3.1	2.9	2.8
1.1+Coal	2.9	2.9	3.0	3.0	3.0	3.1	3.1	3.0	3.0	3.0
0.77+Coal	2.5	2.9	2.9	3.0	3.0	3.1	3.3	3.4	3.4	3.3

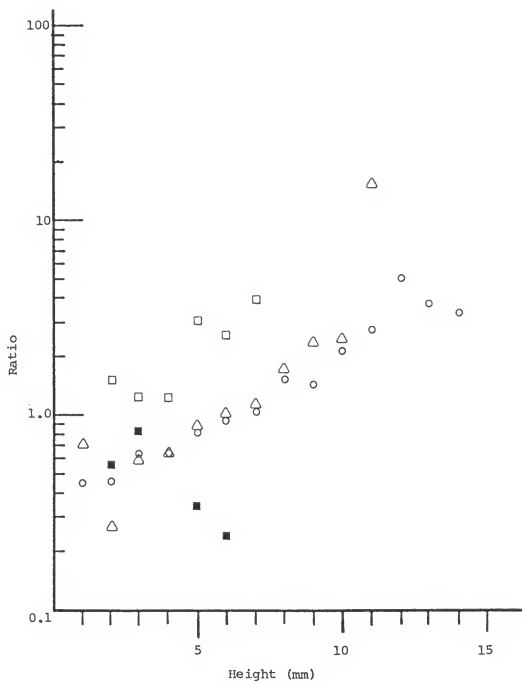
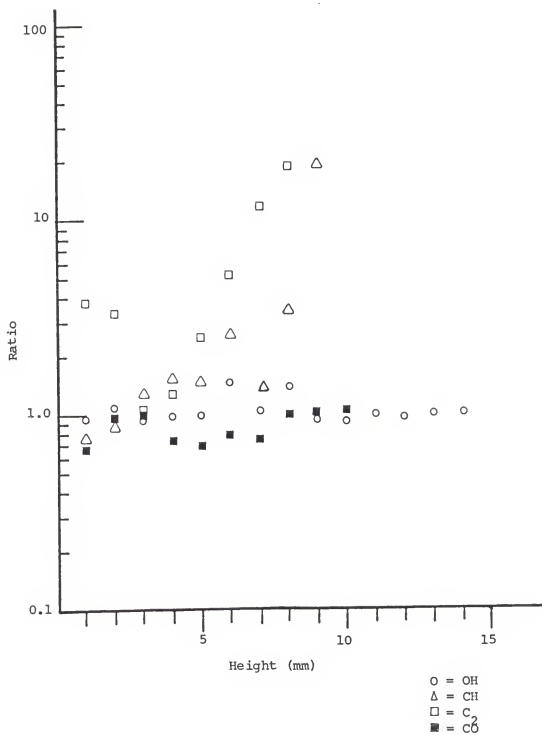


Figure 40. Ratio of change for flame  $\phi=0.77$ .

Figure 41. Ratio of change for  $\phi=1.0$ .

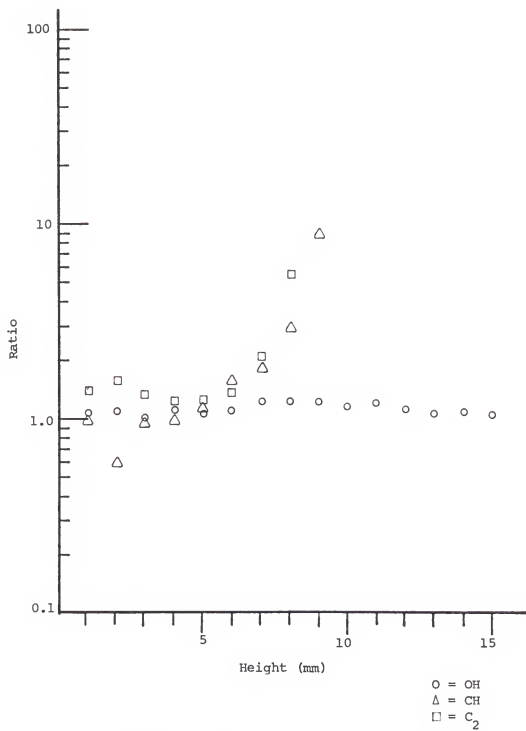


Figure 42. Ratio of change for flame  $\phi=1.1$ .

### Spatial Temperature Measurements of Methane-Air and Methane-Air-Coal Dust Flames

Spatial temperature profiles were obtained by Dr. K. M. Pamidimukkala in concurrence with another gas-coal study (272) who graciously made these data available to aid in the present study. Illustrative temperatures for two flames studied in emission are given in Tables 15 and 16. These temperatures have been measured and calculated to include heat losses due to radiation according to equations given by Fristrom and Westenberg (273). This heat loss was calculated to be 400 K for the thermocouple used. Due to the radial symmetry present in the round burner all temperature measurements were made in one horizontal plane outward from the center in one direction parallel to the burner head. Measurements within 1 cm of the center are accurate to  $\pm 10$  K while measurements further out from the center would be accurate to  $\pm 50$  K due to fluctuations and disturbances in the outer edges due to room air mixing. Table 17 shows percentage differences between the 3 flames with coal dust and the identical flames without coal dust for the temperatures at 0 radius. A negative percentage shows a cooler flame upon addition of coal dust while a positive percentage indicates a hotter flame with coal dust.

### Investigations for Sulfur and Sulfur Compounds in Methane-Air-Coal Dust Flames

A series of experiments were undertaken to observe any sulfur containing species that might be present in a methane-air-coal dust flame. The coal flows in this series were varied from 30 mg/min to 150 mg/min in a stoichiometric flame. Species searched for were (251)

1.  $S_2 - B^3\Sigma^- - X^3\Sigma^-$  from 470-503 nm with most intense bands at 479.06 (3,18)<sup>g</sup>, 484.21 (4,19), 489.36 (2,18), 493.70 (3,19), 498.95 (4,20) 503.62 (5,21), 509.02 (6,22) 519.42 (5,22), and 524.97 (6,23). Bands also investigated between 370 and 420 nm



Table 15  
Experimental Spatial Flame Temperatures for a  $\phi=1.00$  Flame

Height (mm)	Radial axis (mm)							
	0	2	4	6	8	10	12	13
1	1940	1864	1931	1900	1939	1780	1730	1470
2	1987	1931	1964	1960	1960	1956	1790	1507
3	2000	1975	1925	1975	1960	1923	1823	1544
4	2000	1987	1975	1964	1960	1923	1831	1553
5	1987	1975	1975	1964	1948	1910	1802	1565
6	1975	1964	1960	1960	1940	1900	1790	1565
7	1964	1960	1960	1948	1931	1890	1790	1553
8	1964	1960	1960	1948	1931	1890	1790	1544
10	1960	1948	1948	1940	1923	1872	1755	1526
14	1948	1948	1940	1931	1906	1839	1703	1498
20	1948	1940	1931	1923	1881	1814	1659	1452
30	1931	1923	1910	1898	1898	1729	1507	1348

Table 16  
Experimental Spatial Flame Temperatures for a  $\phi=1.70$  Flame

Height (mm)	Radial axis (m)						
	0	2	3	6	8	10	12
2	728	728	728	787	912	1129	1508
4	728	728	744	787	924	1230	1651
6	744	744	744	814	969	1386	1720
10	744	744	744	840	1087	1616	1780
15	744	744	773	876	1250	1668	1789
20	759	759	801	958	1461	1712	1797
25	759	759	827	1034	1571	1746	1797
35	757	801	888	1309	1633	1755	1797
45	801	840	1034	1526	1695	1763	1797
55	888	969	1280	1651	1729	1772	1789
65	1118	1240	1544	1695	1746	1772	1772

Table 17  
Percent Change in Temperature Upon Addition of Coal (30 mg/min)

Height (mm)	$\phi=1.0$	$\phi=1.1$	$\phi=.77$
1	-13	-9	-13
2	-10	-9	
3	-5	-6	-19
4	-3	-4	
5	-2	-3	-19
6	-1	0	
7	-	-	-24
8	-	-	
9	-	-	
10	-2	0	-26
15	-2	0	-22
20	-3	0	-10
30	-2	0	-3

were 373.98 (0,7), 383.71 (0,8), 393.89 (0,9), 404.56 (0,10) and 419.36 (1,12).

2.  $\text{SH} - \text{A}^2\Sigma^+ - \text{X}^2\Pi$  the most intense band was investigated (251) which is the (0,0) with heads at 323.66 ( $\text{R}_1$ ), 324.07 ( $\text{Q}_1$ ) and 327.91 ( $\text{Q}_2$ ).

3.  $\text{SO} - \text{B}^3\Sigma^- - \text{X}^3\Sigma^-$  strong bands at 327.10 (0,10), 316.48 (0,9), 306.41 (0,8) and 282.74 (1,6) due to interference of strong lines of OH the following region was also investigated.

$\text{A}^3\Pi - \text{X}^3\Sigma^-$  strong bands at 254.17 (3,0  $\text{R}_{21}$ ), 255.85 (2,0  $\text{R}_{32}$ ), 256.80 (2,0  $\text{R}_{21}$ ) and 257.81 (2,0  $\text{R}_{11}$ ).

4.  $\text{SO}_2 - {}^1\text{B}_2 - {}^1\text{A}_1$  observed in the region of 280-309 nm with band heads at 283.23, 285.20, 286.89, 288.77, 290.65, 292.31, 292.48, 293.77, 294.38, 296.12, 298.00, 300.10, and 302.21.

${}^1\text{B}_2 - {}^1\text{A}_1$  system was looked for in absorption between 220 and 235 nm.

5.  $\text{CS} - \text{A}^1\Pi - \text{X}^1\Sigma$  observations were made in the region of 250-270 nm where the following bands were located, 252.32 (2,1), 253.87 (3,2), 257.56 (0,0), 260.59 (2,2), 262.16 (3,3), 266.26 (0,1) and 269.32 (2,3).

6. S - atomic lines at 469.625, 469.545 and 469.413 nm.

All the above regions yielded negative results when observed in emission with low and high amounts of coal at the heights of 4,20 and 50 mm. The only changes that occurred in these spectral regions when coal was added to the flame were 3 lines found in the wavelength region of 325-332 nm. These lines are shown in Figure 43. It was first thought that these lines might belong to SH but the narrowness of these lines seemed more indicative of atomic rather than molecular spectra. Higher resolution spectra with a slower scan rate were made of these lines but no visible structure could be seen. Upon checking atomic wavelength tables the lines at 324.8 and 327.5 nm were assigned to Cu and the line at 330 was assigned to Na. Verification was accomplished

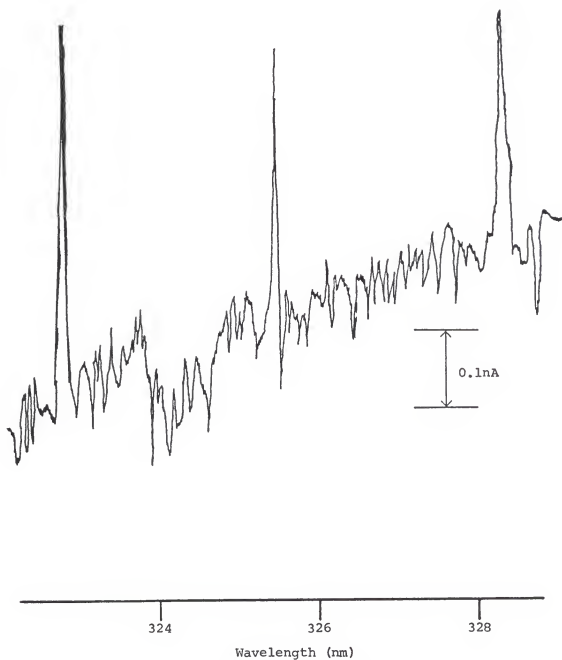


Figure 43. Ultraviolet line spectra (slit=50 $\mu$ , 2mm high, chart 1"/min  $5 \times 10^{-3}$  nm/s).

by aspirating a 1000 ppm solution of  $\text{CuSO}_4$  and observing the emission which appeared at the position of the first two lines tentatively assigned to Cu. The line at 330 was confirmed by aspirating a 1000 ppm solution of NaCl and observing a line at the same place.

Upon review of the literature it was found that  $\text{SO}_2$  is a better absorber than emitter so an attempt was made to observe  $\text{SO}_2$  in absorption with resultant negative results. To check the technique used for absorption measurements an attempt was made to observe OH in absorption. The absorption of OH was seen in the first attempt so technique was assumed to be correct. The absorbance was not large ( $\leq 1\%$ ), but amplification scale was expanded to enable positive identification of OH.

As the coal used in these experiments contained a low percentage of sulfur  $\leq 2\%$  it might not be surprising that no sulfur containing compounds were seen. Samples of coal were then made which contained 1, 2, 4, 8, 15, and 30% by weight sulfur, which was made from powdered flowers of sulfur. Once again all the studies proved to be negative.

#### Effects of Addition of Excess $\text{O}_2$ on Methane-Air-Coal Dust Flames

In this experiment the coal was introduced to only the center section of the flame and the oxygen was only introduced into this region also. The flame was set up as stoichiometric and a coal flow rate of 30 mg/min was used. Oxygen was introduced into the inner flame gas lines and its flow was varied from 0.075 to 0.25 l/min. Upon introduction of oxygen to the methane-air-coal dust flame the visible character of the flame changed from an orange color to a whitish color

with the white emission coming from a round area approximately 3-6 mm above the burner head. Spectra were obtained from this region but no new emissions were observed but a slight increase was seen in the intensity of the OH, CH, and C<sub>2</sub> emissions.

#### Fluorescence Experiments

Two excitation sources were used for these experiments, a He-Cd laser and a mercury electrodeless discharge lamp. The He-Cd laser was a continuous type which gave lines at 325 and 442 nm with powers of 13 and 35 mW respectively. The Hg discharge emitted all the normal mercury lines with the majority of power in the 254 nm line. Both sources were chopped by a mechanical chopper and the resultant fluorescence, if any, was detected by the 1.26 m monochromator/photo-multiplier combination in conjunction with a lock-in voltmeter.

Two experimental runs were made using each source, first a run on just a methane-air flame to observe any background fluorescence that might occur and then a run with the introduction of coal into the flame. The spectral region scanned was from 180-600 nm at a height of 2 cm and the coal flow rate was ~50 mg/min with a stoichiometric flame used for all cases. For both sources no background fluorescence was seen in the methane-air flame and no fluorescence was seen when coal was added also. In order to check optical alignment, a critical variable in fluorescence measurements, the flame was run without being ignited and water was aspirated into the flame gases using a pneumatic nebulizer. The water droplets in the gas flow scattered the excitation light source, which was clearly seen by the detection apparatus.

Lateral OH Emission Profiles of Methane-Air and Methane-Air-Coal Dust Flames Using an Inversion Technique

In this set of experiments OH (0,0) emission profiles were taken of a series of flames at different heights. The methane air-flames had  $\phi$ 's of 0.66, 0.77, 1.00, 1.10, 1.30, 1.70 and  $\infty$  while the methane air-coal dust flames had  $\phi$ 's, of 0.66, 1.00, 1.10. The burner was moved across the slit of the monochromator by a motor driven X-Y milling table at a rate of 0.5"/min, the emissions were monitored with the 1.26 m monochromator/PMT system and the resultant signal was recorded on a strip chart recorder run at a speed of 2"/min. This resulted in 4 mm of chart paper for every millimeter in the flame for an approximate flame spatial resolution of 0.25 mm. The slit used was 100  $\mu$ m wide and 2 mm high. These spatial scans of OH emission intensity were digitized and stored on a PDP 11/34 computer for later calculations.

In the spectroscopic study of cylindrically symmetric emitters, such as the flame in the present study, measurements are usually carried out on a small cross-section of the light source in a direction perpendicular to its axis. A "side-on" measurement such as this includes contributions from the outer regions of the flame along with emissions from the center of the flame giving an integrated average of a small strip in the flame. In order to separate the contributions of the different radial zones and to obtain the true radial characteristics of the source, one of the many graphical or numerical procedures for solving Abel's integral equation must be used (274). Upon solving Abel's equation one obtains the true radial intensity distribution. Computer programs were written and are given in the Appendix for data manipulation.



The following programs were used:

1. SETJEF. This program accepted the raw data and was used to convert chart paper units into intensities in nanoamperes and flame distance in millimeters. As some scans were made in both directions this program could also flip the data so all measurements would be from the same reference direction.
2. SMOO5J. This program accepted data sets from the SETJEF program and performed a five point least squares smoothing of the data. This program was taken from the work of Savitzky and Golay (275) with modification necessary to function on our computer system.
3. INVERA. This program accepted data sets from the SMOO5 program and performed an Abel inversion upon the data to obtain the distribution of emitters from the observed projected intensity profile. The procedure used to calculate the inversion is that of Barr (276) who used an analytic form for the observed emission which could then be solved numerically to obtain the inversion. In this method, if the horizontal slice is taken at a distance  $y$  from the center of the flame axis and is of height  $\delta y$  (slit height) and width  $\ell$  (slit width) then the total light flux falling on the detector is given by

$$I(y)\ell\delta y = \ell\delta y \int_{-x}^x f(r)dx,$$

where  $f(r)\ell dx\delta y$  is that part of the flux which originates in the volume element  $\ell\delta y dx$  located at radial distance  $r$  from the axis. In this expression the integral is taken along a strip at constant  $y$ ,  $x^2 + y^2 = r^2$ ,  $x^2 = R^2 - y^2$ , and  $R$  is the radius beyond which  $f(r)$  is negligible. Therefore the equation can also be written as

$$I(y) = 2 \int_y^R \frac{f(r)rdr}{(r^2 - y^2)^{1/2}}$$

which is one form of Abel's equation with  $I(y)$  the measured intensity.

If  $f(r)$  is zero for all  $r > R$  then the above equation inverts analytically (277) into

$$f(r) = -\frac{1}{\pi} \int_r^R \frac{(dI/dy)dy}{(y^2 - r^2)^{1/2}}$$

In most experiments  $I(y)$  is obtained as a set of numerical data rather than as an analytic function. Several different methods (278, 279) have been developed for performing the above integral numerically, but they all necessarily suffer from the fact that when the derivative of  $I(y)$  is evaluated, noise on the data is amplified. In the method of Barr the integration is performed before the final differentiation with a smoothing technique applied between the two. This method showed good response to noisy data and was of suitable form for computer calculation. Once the inversion was obtained it was formatted to allowing direct plotting by a digital plotter.

Figure 44 to 54 show the observed intensity and the inverted profile for a typical height in the flames studied.

OH, CH and  $C_2$  Emissions from a Single Cone Using an Inversion  
Technique

In these experiments the spectral emissions from a single cone were studied. A single cone was obtained by plugging all the cones except the center one with clay from underneath the burner head. The clay was scraped off the top of the burner to insure a flat surface to avoid any disturbing aerodynamic effects due to the clay. In these experiments the burner was moved at the rate of 0.2"/min with a chart speed of 2"/min yielding 10 mm of chart for every 1 mm in the flame for an approximate resolution of 0.05 mm in the flame. The 1.26 m monochromator/PMT system was used with a slit width of 100  $\mu$ m and a height of 2mm. Measurements were taken at 1 mm intervals up to a height where the cone no longer existed ( $\sim 5$  mm).

In Figure 55 to 57 are emission profiles and inversion profiles for OH, CH and  $C_2$  at a height of 3 mm. In Figure 58 is a diagram of an idealized cone defining cone width,  $C_w$ , which is measured from one intensity maximum on one side of the cone to the other intensity maximum on the other side of the cone, and reaction zone thickness,  $R_w$ ,

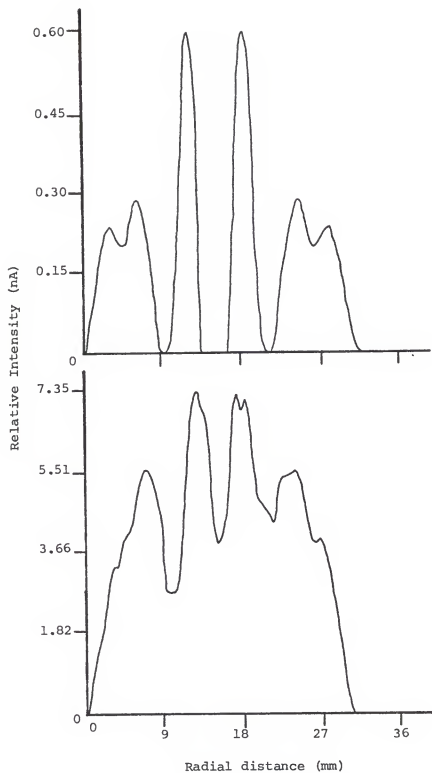


Figure 44. OH emission flame profile (bottom) and inversion profile (top) for a flame with  $\phi = 0.66$  at a height of 10 mm.

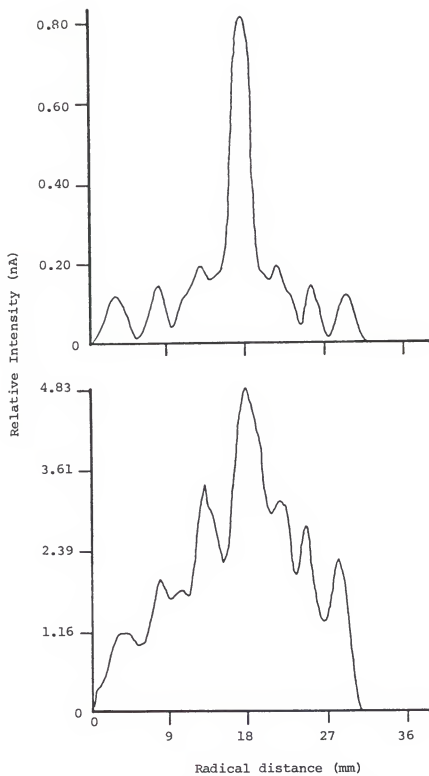


Figure 45. OH emission flame profile (bottom) and inversion profile (top) for a flame with  $\phi = 0.77$  at a height of 10 mm.

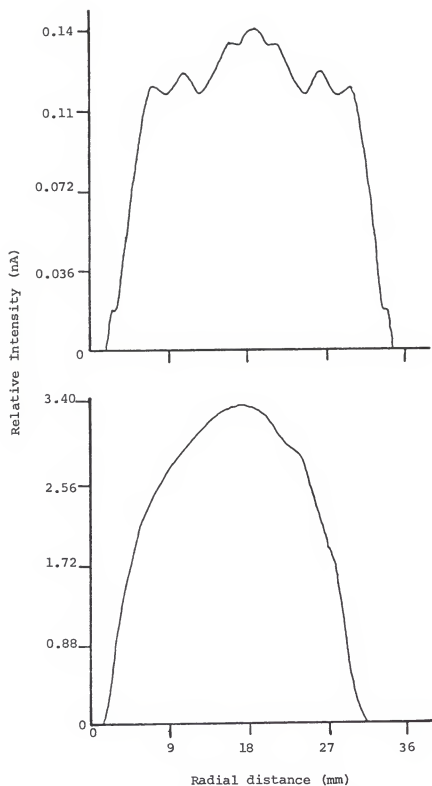


Figure 46. OH emission flame profile (bottom) and inversion profile (top) for a flame with  $\phi = 1.00$  at a height of 10 mm.

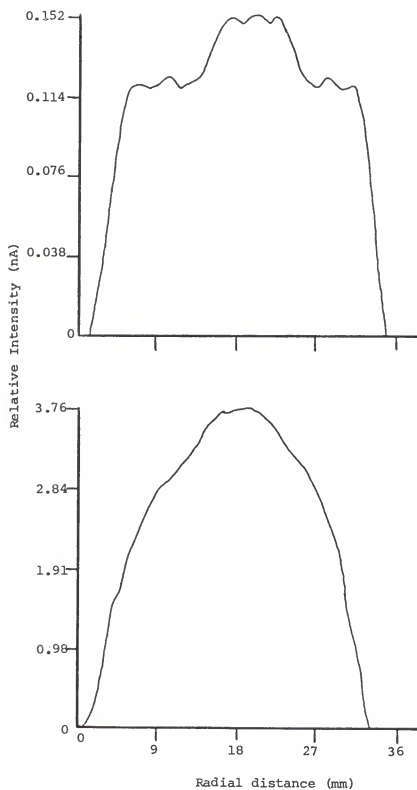


Figure 47. OH emission flame profile (bottom) and inversion profile (top) for a flame with  $\varnothing = 1.10$  at a height of 10 mm.

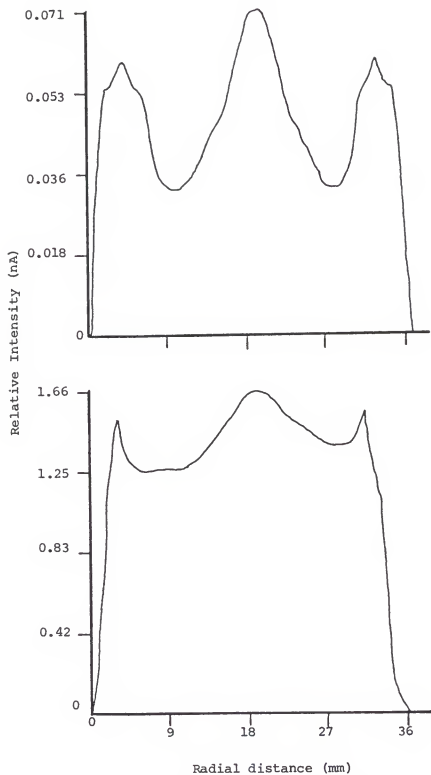


Figure 48. OH emission flame profile (bottom) and inversion profile (top) for a flame with  $\phi = 1.30$  at a height of 10 mm.

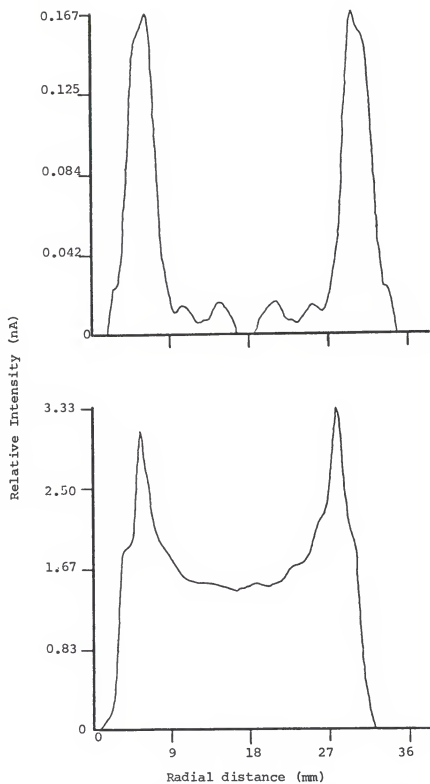


Figure 49. OH emission flame profile (bottom) and inversion profile (top) for a flame with  $\phi=1.70$  at a height of 10 mm.



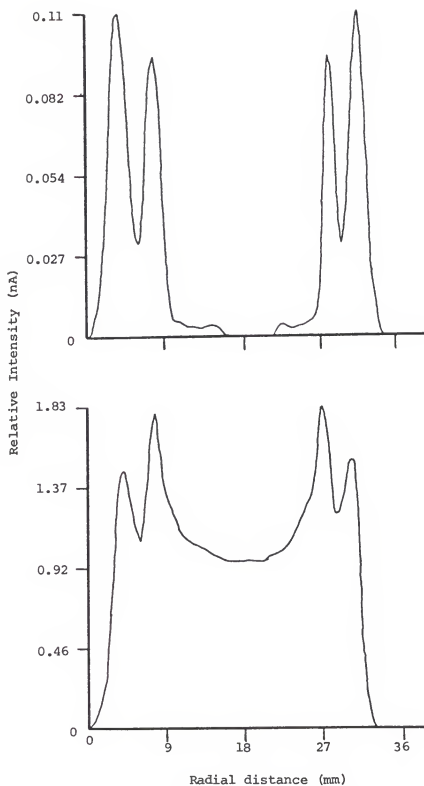


Figure 50. OH emission flame profile (bottom) and inversion profile (top) for a flame with  $\phi = 1.70$  at a height of 18 mm.

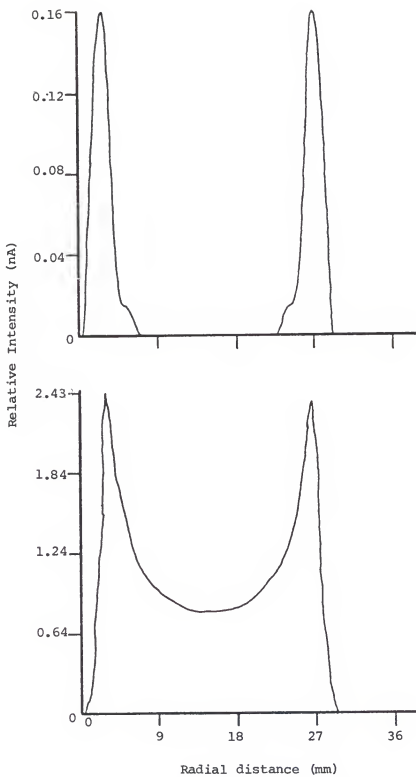


Figure 51. OH emission flame profile (bottom) and inversion profile (top) for a flame with  $\phi = \infty$  at a height of 10 mm.

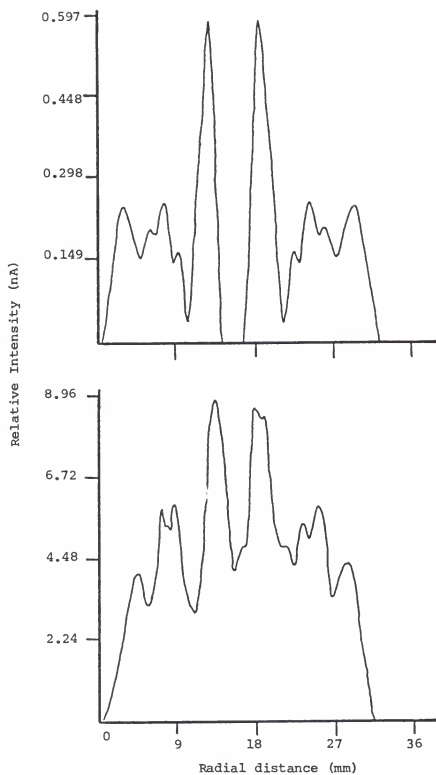


Figure 52. OH emission flame profile (bottom) and inversion profile (top) for a flame with  $\phi = 0.77$ +Coal (30 mg/min)

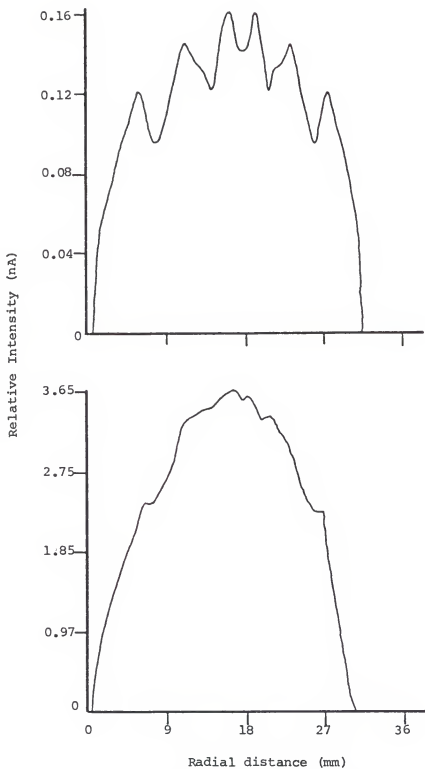


Figure 53. OH emission flame profile (bottom) and inversion profile (top) for a flame with  $\phi = 1.00 + 30$  mg/min coal at a height of 10 mm.

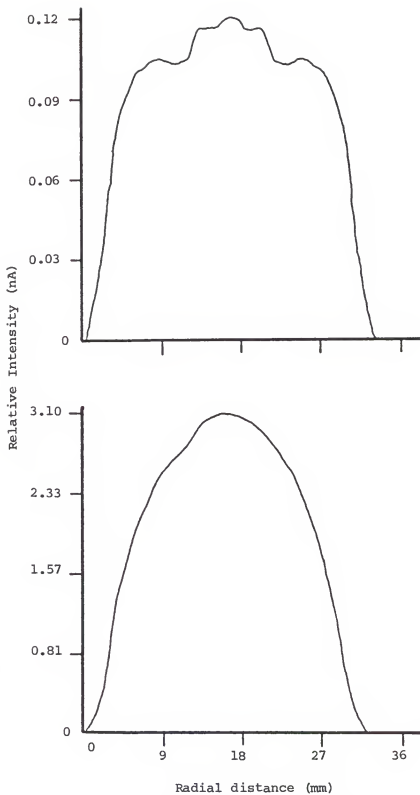


Figure 54. OH emission flame profile (bottom) and inversion profile (top) for a flame with  $\phi = 1.10 + 30$  mg/min coal at a height of 10 mm.

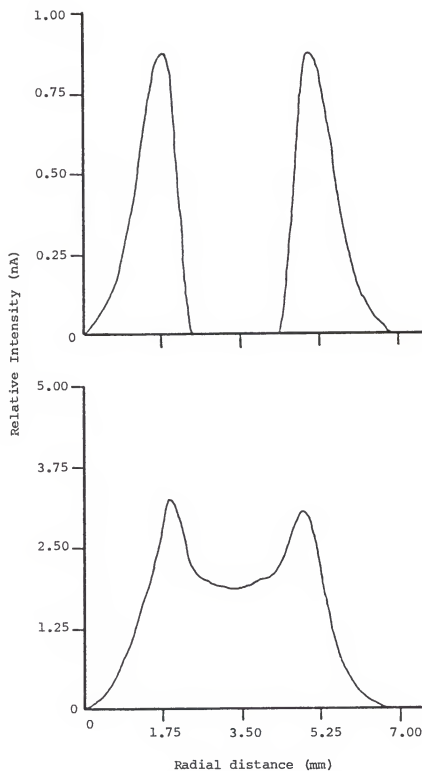


Figure 55. OH emission flame profile (bottom) and inversion profile (top) from a single cone with  $\phi = 1.00$  at a height of 3 mm.

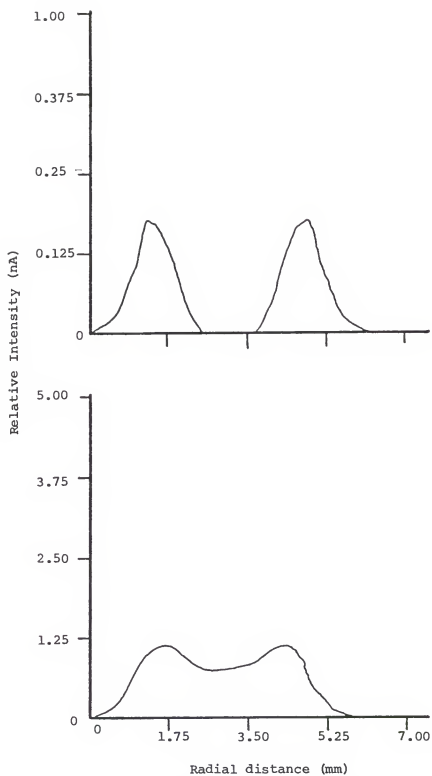


Figure 56. CH emission flame profile (bottom) and inversion profile (top) from a single cone with  $\phi = 1.00$  at a height of 3 mm.

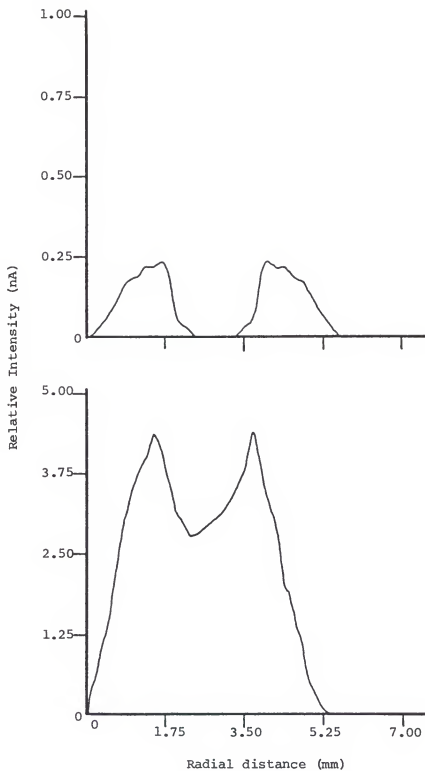


Figure 57. C<sub>2</sub> emission flame profile (bottom) and inversion profile (top) from a single cone with  $\phi = 1.00$  at a height of 3 mm.



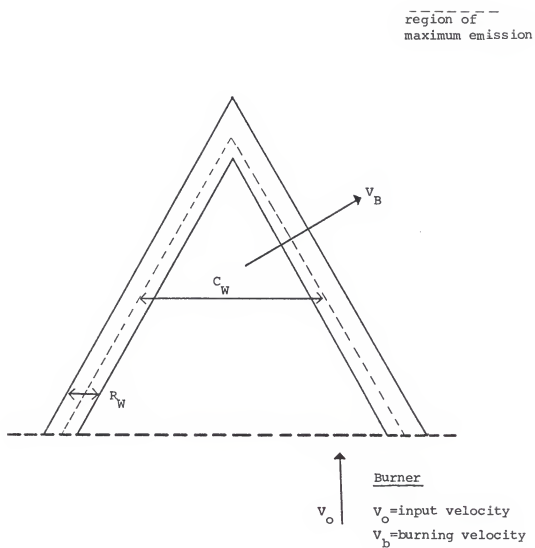


Figure 58. Ideal Cone Defining  $C_W$ ,  $R_W$

which is the width of the cone wall as determined by spectroscopic emissions.  $C_w$  can be measured from both raw emission data and inverted data while  $R_w$  is best determined from inversion data. Table 18 shows  $C_w$  values obtained from both emission and inversion data while Table 19 shows  $R_w$  values obtained from inversion data.

#### Calculation of Ground State Concentrations Assuming a Thermal Distribution

The population in an upper state,  $n_u$ , thermally populated from a lower ground population,  $n_T$ , can be expressed as (252).

$$\frac{n_u}{n_T} = \frac{e^{-\Delta E/kT}}{Q_{int}}$$

where  $\Delta E$  is the energy difference between the upper and lower levels and  $Q_{int}$  is the internal partition function which is a product of the internal rotational, vibrational and electronic partition functions. The internal partition function is both a function of temperature and molecular properties and has been discussed in great detail by Tatum (280).

Assuming the flame to be in thermal equilibrium, which is not valid in the primary reaction zone, we can calculate a ground state population for the molecules.

Table 20 shows ground state concentrations calculated using temperatures measured using a thermocouple (272) and excited state concentrations calculated earlier. Values of partition functions were obtained from the calculations of Tatum (280). These calculated ground state values are significantly greater than experimentally measured values (79, 83) indicating a non-thermal excited state population due to chemiluminescent reactions. The maximum temperatures measured in these flames are given in Table 21.

Table 18  
 $C_W$  (mm) Values from Emission and Abel Inverted Data

H (mm)	OH		CH		$C_2$	
	emission	inversion	emission	inversion	emission	inversion
1	3.90	3.82	3.50	3.59	3.10	3.11
2	3.55	2.91	3.20	3.21	2.90	2.86
3	2.85	2.68	2.50	2.42	2.10	2.14
4	2.40	2.00	2.00	2.00	1.80	1.88
5	1.50	1.67	1.10	1.08	0.65	0.69
6	1.20	1.19	-	1.07	-	0.15
7	-	0.97	-	0.78	-	-

Table 19  
 $R_w$  (mm) Values for Single Cone Emissions

H (mm)	OH	CH	C <sub>2</sub>
1	1.14	1.18	1.31
2	1.25	0.95	0.97
3	1.69	1.15	1.48
4	1.80	1.63	1.15
5	2.15	0.87	1.52
6	2.06	-	-
Avg	1.68	1.15	1.36
$\sigma$	0.41	0.29	0.23

Table 20  
Ground State Concentrations ( $\#/\text{cm}^3$ ) Assuming a Thermal Distribution

Height (mm)	$\phi=1.0$	$\phi=1.0+\text{Coal}$	$\phi=0.77$	$\phi=0.77+\text{Coal}$	$\phi=1.10$	$\phi=1.10+\text{Coal}$
<u>OH</u>						
2	1.02E21	1.33E22	1.36E27	3.84E30	1.92E21	2.26E22
6	1.41E21	2.76E21	4.01E26	2.13E30	2.05E21	2.52E21
10	2.79E20	4.31E20	2.28E23	1.32E28	4.86E20	5.58E20
14	2.06E20	3.41E20	8.71E20	6.00E24	4.39E20	4.56E20
<u>CH</u>						
2	1.77E18	8.60E18	7.31E21	9.18E23	5.47E18	1.70E19
6	2.57E18	8.66E18	4.13E21	2.86E24	4.52E18	7.56E18
9	7.32E16	2.14E18	2.04E19	6.14E22	7.71E16	6.90E17
<u>C<sub>2</sub></u>						
2	1.51E16	1.95E17	1.33E19	3.05E21	2.11E17	1.17E18
6	8.18E16	5.33E17	1.72E18	1.07E21	2.76E17	3.41E17
8	1.55E16	3.85E17	1.69E17	1.93E20	1.98E16	1.08E17
<u>CO</u>						
2	2.07E23	7.03E24	3.55E32	9.48E37	7.85E23	-
6	5.37E23	6.73E24	1.93E29	3.10E35	1.37E24	-
10	9.72E22	2.43E23	9.12E26	-	1.49E23	-

Table 21  
Maximum Temperatures vs  $\phi$  for  $\text{CH}_4$ /Air Flames

$\phi$	$T_{\text{max}}$ (K)
0.66	1694
0.77	1738
1.00	2000
1.10	1956
1.30	1931
1.40	1856
1.70	1789
1.90	1797
$\infty$	1660

## CHAPTER VI DISCUSSION

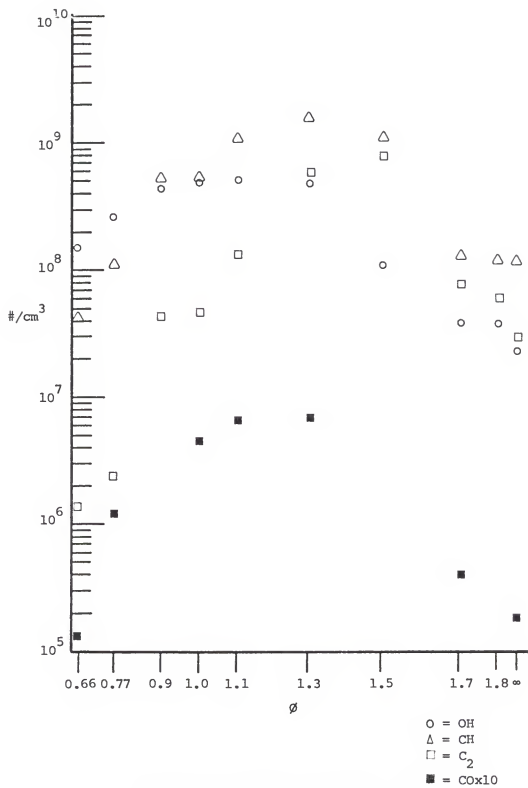
### Methane-Air Flames

#### Effect of $\phi$ Upon Excited State Concentrations

Figure 59 shows the maximum population of  $\text{OH}^*$ ,  $\text{CH}^*$ ,  $\text{C}_2^*$  and  $\text{CO}^*$  as a function of  $\phi$  and Figures 26 to 36 show concentrations as a function of height in the flame for the different  $\phi$  values studied. From Figure 59 we can see that  $\text{OH}^*$  has a maximum population at  $\phi = 1.1$  with a relatively flat distribution around this value from  $\phi = 0.90$  to 1.3.  $\text{CH}^*$  is found to have a maximum value at  $\phi = 1.3$  along with  $\text{CO}^*$  while  $\text{C}_2^*$  is maximum at  $\phi = 1.5$ .

Number densities at these  $\phi$  values are  $\text{OH}^* = 5 \times 10^8/\text{cm}^3$ ,  $\text{CH}^* = 1.6 \times 10^9/\text{cm}^3$ ,  $\text{C}_2^* = 8.0 \times 10^8/\text{cm}^3$  and  $6.9 \times 10^5/\text{cm}^3$  for  $\text{CO}^*$ . These can be compared with the values obtained by Porter et al. (79) who obtained concentration values of  $\text{OH}$ ,  $\text{CH}$  and  $\text{C}_2$  in both ground and electronically excited states in low pressure  $\text{C}_2\text{H}_2$  and  $\text{CH}_4$  flames. Concentration values obtained for excited species in a fuel rich flame ( $\phi = 1.58$ ,  $p = 18$  torr) were  $\text{OH}^* = 1.8 \times 10^7/\text{cm}^3$ ,  $\text{CH}^* = 1.9 \times 10^7/\text{cm}^3$  and  $\text{C}_2^* = 5 \times 10^7/\text{cm}^3$ .

The values of Porter et al. can be converted to atmospheric pressure values assuming ideal gas behavior, in order to compare values. In the flame of Porter et al. a pressure of 18 torr was used and a

Figure 59. Maximum populations vs  $\phi$



temperature of 1600 K was obtained for this flame. Using  $PV = nRT$  and converting torr into pascals we can solve for total number density at this pressure,

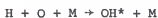
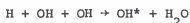
$$\frac{n}{V} = \frac{2394}{(8.3144)(1600)} = 1.80 \times 10^{-1} \text{ moles/m}^3$$

Likewise, for an atmospheric pressure flame (101325 Pa) at 1900 K we obtain a number density of  $6.41 \text{ moles/m}^3$ . Taking the atmospheric value and dividing by the low pressure value we obtain 35.6 so to convert number densities at low pressure to atmospheric values we must multiply by 35.6. We therefore obtain values of  $6.4 \times 10^8/\text{cm}^3$  for  $\text{OH}^*$ ,  $6.8 \times 10^8/\text{cm}^3$  for  $\text{CH}^*$  and  $1.8 \times 10^9/\text{cm}^3$  for  $\text{C}_2$ , from Porter's values which are in quite good agreement with the experimentally obtained atmospheric pressure flame values obtained in the present study.

Ground state populations measured by this group (76) were  $\text{OH} = 2.8 \times 10^{14}/\text{cm}^3$ ,  $\text{CH} = 4.4 \times 10^{12}/\text{cm}^3$  and  $\text{C}_2 = 7.6 \times 10^{11}/\text{cm}^3$  in the rich flame and in the lean flame ( $\phi = 0.43$ )  $\text{OH} = 3.21 \times 10^{14}/\text{cm}^3$ , and  $\text{CH} = 1.5 \times 10^{12}/\text{cm}^3$  with  $\text{C}_2$  undetectable. Bulewicz, Padley and Smith (83) obtained ground state values in 665 Pa flame of  $1.1 \times 10^{14}/\text{cm}^3$  for  $\text{OH}$ ,  $1 \times 10^{12}/\text{cm}^3$  for  $\text{CH}$  and  $3 \times 10^{11}/\text{cm}^3$  for  $\text{C}_2$  in a flame with  $\phi = 1.0$ . As the flame was made rich ( $\phi = 1.5$ ) the  $\text{OH}$  concentration dropped to  $6 \times 10^{13}/\text{cm}^3$  with both  $\text{CH}$  and  $\text{C}_2$  increasing to  $1.5 \times 10^{13}/\text{cm}^3$  and  $1.2 \times 10^{13}/\text{cm}^3$  respectively. Maximum concentrations were obtained at equivalence ratios of 1.0 for  $\text{OH}$ , 1.4 for  $\text{CH}$  and 1.5 for  $\text{C}_2$ . Only relative excited state populations were measured in this study with arbitrary units of 90 for  $\text{OH}^*$ , 6.5 for  $\text{CH}^*$  and 0.8 for  $\text{C}_2$  at  $\phi = 1.0$ . Cattolica (281) has obtained similar ground state concentration values

in an atmospheric methane-air flame while Heffington et al. (282) have obtained excited state concentrations in good agreement with the present study in a shock-tube study of  $\text{CH}_4/\text{O}_2/\text{Ar}$  mixtures. No previous studies of excited state absolute concentrations in atmospheric methane-air flames were found in the literature to obtain a direct comparison with the present study.

On comparing Figure 59 with Table 21 we see that the maximum temperature of 2000 K is found at  $\phi = 1.0$ , while maximum OH concentration is found at  $\phi = 1.1$  with a relatively small change from  $\phi = 0.9$  to 1.3. In Figure 29 for  $\phi = 1.00$  we see that initially the  $\text{OH}^*$  concentration is greater than the  $\text{CH}^*$  but after a height of 2 mm the  $\text{CH}^*$  is greater until after 7 mm, when the  $\text{OH}^*$  is once again greater. The  $\text{CH}^*$  emissions are no longer visible after a height of 9 mm whereas the  $\text{OH}^*$  is visible to a much greater height. This extended OH emission is caused by radical recombination reactions of the type



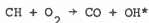
Experimental evidence (281) has shown that atomic oxygen has its peak concentration in lean flames with a maximum value at  $\phi = 0.9$ , while hydrogen atom reaches a maximum in rich flames at  $\phi = 1.2$ . Therefore in lean and stoichiometric flames the primary  $\text{CH}_4$  destruction step is



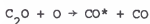
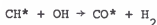
which accounts for the high concentrations of OH radicals in these flames.

As the amount of methane in the flame is reduced (increasingly lean) it is obvious that less carbon is available for molecule formation so that as  $\phi$  approaches zero, carbon containing molecules should decrease. This is the effect seen in Figure 59 with the molecular species containing more carbon,  $C_2^*$ , declining much faster than  $CH^*$ . The production of  $C_2^*$  involves at least 2 or more carbon fragments coming together which is less likely as  $\phi$  decreases. This same effect causes a drop in  $CH^*$  and  $CO^*$  emissions which are both dependent on multi-carbon containing molecules for their production.

Also in this figure one can see evidence for the reaction

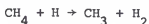


because the decrease in  $OH^*$  appears to speed up once the  $CH^*$  population begins to decline rapidly at  $\phi \leq 0.90$ . Another interesting feature in the figure is the way the  $CO$  decreases as the  $OH$  and  $O$  atom concentrations become smaller, possibly indicating that reactions



may play a role in  $CO^*$  formation.

As the flame is made more fuel rich we see a substantial increase in carbon containing species and a slight increase in  $OH^*$  at  $\phi = 1.1$  with a constant reduction at larger  $\phi$ 's. The  $CO^*$ ,  $CH^*$ , and  $C_2^*$  reach maxima at successively larger equivalence ratios. In these rich flames we now have more hydrogen atoms than oxygen atoms and the predominant methane destruction reaction is

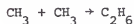


with



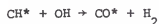
also occurring in the region near  $\phi = 1.00$ . At large values of

$\phi$  ( $> 1.3$ ) the reactions



become more probable. Warnatz (283) has calculated that for lean or stoichiometric conditions about 30% of the methyl radicals are consumed by recombination, with the percentage increasing to 80% for rich flames.

As the equivalence ratio is increased the maximum temperature drops from a value of 1956 K at  $\phi = 1.1$  to 1789 K at  $\phi = 1.7$ . This decrease in temperature is due to incomplete combustion occurring due to a lack of oxygen. This is also the reason for the decrease in  $\text{CO}^*$  because all the discussed mechanisms partially depended upon the O or  $\text{O}_2$  concentration with the exception of



which depends upon OH which is also decreasing rapidly in these rich flames.

A possible explanation for the behavior of  $\text{CH}^*$  is that even though the oxygen concentration is decreasing, the OH concentration stays at a sufficient level, due to the slow nature of the radical recombination reactions, in order to combine with the  $\text{C}_2$  which is increasing until  $\phi = 1.5$  is reached. The  $\text{C}_2$  concentration should increase with larger  $\phi$ 's if Gaydon and Wolfhald's polymerization mechanism is responsible

for the formation of  $C_2^*$ . Formation of ground state  $C_2$  is also favored by higher  $\phi$  by possibly being formed from  $C_2H_6$  as discussed previously. As the equivalence ratio increases further the  $C_2^*$  and  $CH^*$  concentrations drop possibly due to the decrease in temperature or due to larger polymeric molecules forming in the excess hydrocarbon environment, which are less likely to decompose into  $C_2^*$  and  $CH^*$ .

Methane-air flames with large equivalence ratios appear very luminous to the eye due to the formation of soot particles in the flame (284, 285). These soot particles are thought to be made out of polycyclic aromatic hydrocarbons and long chain hydrocarbons which have condensed into larger particles. Soot in flames is what appears as smoke and can be observed in most any fuel rich flame. When the soot is formed it may possibly attract small hydrocarbons which may be precursors to  $C_2^*$  and  $CH^*$  therefore lowering the amounts of these species produced. Flames observed in these studies evidenced signs of soot formation (luminous character) at a  $\phi$  of  $\sim 1.5$  with increasing luminosity at higher  $\phi$  values.

#### Spatial Temperature Profiles and Lateral OH Emission Profiles

A flame is not a uniform hot collection of gases but has different temperatures at different spatial positions depending upon the equivalence ratio (9). Tables 15 and 16 show spatial temperatures vs height for two methane-air flames with different  $\phi$  values. Figures 44 to 54 show integrated lateral intensities of OH emission along with the Abel inverted plots to show spatial emission intensities. From the above figures it becomes evident that the temperature distribution and emission profiles are highly dependent upon the value of  $\phi$ .

In these studies the total flow volume was kept constant so we would only observe the effects of varying  $\phi$  without worrying about a change due to aerodynamic effects. In the normal stoichiometric case the cones were well defined with a height of approximately 4 mm. The flame ran without any visible fluctuations and appeared to have a well defined shape. The overall color of the flame at this  $\phi$  value was a bluish-green color in the cones with less green color higher up in the flame when observed in the dark. When room lights were on the cones still retained their color but the remainder of the flame appeared colorless. Also at this equivalence ratio the flame had a total height of about 10 cm. Above the cones at a height of 10 mm the flame appeared to be uniform and homogeneous to the eye.

As the flame was made lean ( $\phi < 1.0$ ) several noticeable changes occurred with the first observable one being a change in the color of the cones to a much bluer color with a slight touch of green at a  $\phi$  of 0.90. Also the flame decreased in height to about 8 cm at this equivalence ratio. The cones also appeared to change shape now having a height of about 3 mm and appearing much more squat. The flame still appeared uniform but seemed to be more transparent than the stoichiometric flame. At an equivalence ratio of 0.77 there was a visible change in the appearance of the flame. First there was a great reduction in height down to approximately 5 cm with an extremely transparent bluish color. The outer cones on the burner consisted of only the inner edge and the flame gave the appearance of being blown upward. There were some small gaps between the cones and the flame consisted more of streamers than of a uniform flame. These inhomogeneities can be seen

in the emission profile, Figure 45, and are clearly evident in the inverted profile above the emission.

At a  $\phi$  Of 0.66 no cones were visible with the flame assuming a very distorted shape. The flame had decreased greatly in height down to approximately 3 cm and seemed to consist of disjointed pieces. In this flame there was a great amount of movement and turbulence and the flame had the shape of a large V. In this flame there was only a faint trace of bluish color, and the flame was very transparent. Temperature profiles of this flame show a low temperature in the center which increases outward which is in direct contrast with the stoichiometric flame which is hotter at the center.

A completely different series of changes occurs when the flame is made slightly rich ( $\phi = 1.10$ ). The major observable change is in the color of the cones. Overall flame shape and size is identical to the stoichiometric flame but the cones now have more of a greenish color as opposed to a blue-green color in a stoichiometric flame. The cone height and shape are identical and the OH emission profile is basically identical to the stoichiometric flame with the inversion showing a slight increase in emissions at the flame center. As the equivalence ratio becomes larger the cones become greener and gradually increase in height until at  $\phi = 1.3$  they all coalesce into one large cone with an approximate height of 2 cm. As the fuel is increased the cone increases in height until at  $\phi = 1.5$  the cone is no longer visible and the flame becomes luminous, giving off an orangeish-yellow light similar in appearance to that emitted by a candle. At this point the total flame length has increased, reaching a height of 15 cm with the upper 5 cm of the flame not well defined due to its turbulent, flickering appearance.

At  $\phi = 1.7$  the flame has the same dimensions as at  $\phi = 1.5$  with the exception of more luminosity and a little more of a flickering upper area. An OH emission profile at a height of 10 mm (Figure 49) shows a maximum intensity at the edges with less in the middle while the inversion shows that the edge emission comes from what appears to be 2 zones at the edge. This effect is more pronounced at a height of 18 mm (Figure 50) where these two zones are seen clearly in both the emission and inversion plots. Referring to the temperature profile for this flame (Table 16) we also see that the hottest region of the flame is out at the edges where the maximum emission occurs.

The reason for these two emission zones is as follows. In such a rich flame as this there is not enough oxygen present to completely combust all the fuel. Even though it is not visible in this luminous flame the primary reaction zone is where the combustion occurs and in this case it is near the edge of the flame which we observe as the inner peak. The outer emission zone is another region similar to the primary reaction zone but in this case the room air diffusing inward towards the flame allows combustion to occur in this region at an effective equivalence ratio smaller than the inner combustion zone, therefore resulting in a greater intensity of OH emissions which would be indicated by Figure 59.

In a diffusion flame, which has no premixed air, the inner primary reaction zone should not exist and all combustion will only take place at the outer edges. As can be seen in Figure 51 in the diffusion flame only one region of combustion occurs on the boundary layer between the fuel and the room air. The maximum temperature in



a diffusion flame is also lower due to the inefficient transfer of oxygen into the flame as opposed to a pre-mixed flame.

#### Single Cone Data and the Formation of Excited States

The spectral emissions from a single cone were studied in order to gain some understanding of the sequence of processes occurring in the primary reaction zone. Figure 58 shows an ideal cone and defines the cone width,  $C_w$ , and the reaction zone thickness,  $R_w$ . The emissions of  $OH^*$ ,  $CH^*$ , and  $C_2^*$  were measured spatially and the cone width and reaction zone thickness were obtained from emission plots and inversion plots. The direction of the burning velocity is also indicated in Figure 55 which can also be used as a reaction coordinate with events in the inner edge of the cone occurring before events on the outer edge. Measured values for  $C_w$  and  $R_w$  are given in Tables 18 and 19 and emission and inversion profiles at a height of 3 mm are shown in Figures 55 to 57.

In these series of measurements the single cone appeared to be a slight bit larger (~ 5 mm high) and wider than the cones in a full flame which can be attributed to a neighbor effect in the full flame, whereby the cones were not able to spread out due to the influence of a nearby cone. In a full flame the cone base was about the size of a burner hole (0.125") while with a single cone the base extended approximately 1.5 mm out from the edge of the hole. The fuel and air flow rates were adjusted to obtain a steady and well shaped cone and the ratio of the two flows were adjusted to obtain a stoichiometric flame.

From Table 18 it can be seen that  $C_2^*$  reaches a maximum value first followed by  $CH^*$  and then the  $OH^*$ . The average separation between the

$C_2^*$  maximum and  $CH^*$  is 0.39 mm with a standard deviation of 0.06 and the average separation between the  $CH^*$  maximum and the  $OH^*$  maximum is 0.38 mm with a standard deviation of 0.03. Using a value for the burning velocity of a stoichiometric methane-air flame of 45 cm/s, obtained from Andrews and Bradley (286), we convert distances in the flame into time. Upon making this conversion we find that the  $CH^*$  emission peaks 0.87 ms after the  $C_2^*$  maximum with the  $OH^*$  maximum occurring 0.84 ms after the  $CH^*$  maximum and 1.71 ms after the  $C_2^*$  maximum.

The reaction zone width,  $R_w$ , of each species is such that there is a considerable overlap between the 3 zones, with  $C_2^*$  emission reaching past the center of the  $OH^*$  reaction zone. From the first appearance of  $C_2^*$  it is 0.15 mm or 0.33 ms to the first appearance of  $CH^*$  and 0.4 mm or 0.88 ms to the first appearance of  $OH^*$  emission, while the first appearance of  $OH^*$  occurs 0.28 mm or 0.56 ms after the first appearance of  $CH^*$ , as observed at a height of 1 mm. The region of  $C_2^*$  emission persists until 0.25 mm (0.55 ms) before the end of  $CH^*$  emission and until 0.44 mm (0.97 ms) before the end of  $OH^*$  emission yielding a total reaction zone width of 1.52 mm, as measured by optical emissions from  $C_2^*$ ,  $CH^*$  and  $OH^*$ .

These data shows that in the primary combustion zone the excited species are formed in the following order  $C_2^*$ ,  $CH^*$  and  $OH^*$ . Porter et al. (79) in a study on low pressure  $C_2H_2/O_2/N_2$  flames found that in a rich flame ground state  $C_2$  and  $CH$  reached a maximum before excited  $C_2^*$  and  $CH^*$  with both ground state maxima at a height of 12 mm with  $C_2^*$  at 16 mm and  $CH^*$  at 17 mm.  $OH^*$  reached a maximum value at 11 mm while

OH ground state was maximum at 20 mm in this flame. However in a lean flame all three excited species, OH\*, CH\* and C<sub>2</sub>\* reached a maximum value at 5 mm with maxima for both ground state CH and OH at 9mm, with ground state C<sub>2</sub> undetectable in this flame. These results indicate different pathways for the production of ground states and excited states.

In the present study the pattern of emissions can be explained by the following mechanism. Assuming for now that the C<sub>2</sub>\* is formed in some unknown step, we observe that the onset of CH\* emission occurs 0.33 ms after the beginning of C<sub>2</sub>\* emission. Due to the short radiative lifetime of C<sub>2</sub>\*, 160 ns (287), a ground state population of C<sub>2</sub> will build up via the reaction



which has a rate of  $6.27 \times 10^6$  transitions s<sup>-1</sup>. In a stoichiometric flame the predominant initiation mechanisms are



which imply a reasonable concentration of OH radicals in the primary combustion zone under stoichiometric conditions. Therefore CH\* can be produced by the following reaction



with the C<sub>2</sub> being produced by the radiative decay of C<sub>2</sub>\*.

Once the CH\* is formed it too will undergo radiative transitions,



resulting in a buildup of ground state molecules. In the case of CH\* the radiative lifetime is longer than the lifetime of C<sub>2</sub>\* with a value

of 508 ns (286), resulting in a decay rate of  $1.96 \times 10^6$  transitions  $s^{-1}$ , thereby resulting in a slower buildup of ground state molecules than the  $C_2$  case. We observe that the onset of  $OH^*$  emission occurs 0.56 ms after the beginning of  $CH^*$  emission. This indicates the production of  $OH^*$  is due to



where the CH is produced through radiative decay of  $CH^*$ . Due to the longer lifetime of  $CH^*$  one would expect the production of  $OH^*$  to take longer than the production of  $CH^*$  from  $C_2$  which is observed in this study.

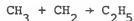
As for the formation of  $C_2^*$ , this study indicates that it should be a relatively fast process and precursor for the radicals  $OH^*$  and  $CH^*$  in a stoichiometric methane-air flame. A possible mechanism would involve a scheme such as



followed by formation of  $CH_2$  by



then



which forms a molecule containing two carbons which can be reduced to  $C_2$  by hydrogen atom abstraction.

Another possible reaction scheme is



followed by



Although it may result in a faster overall reaction process, it is not very likely to form  $\text{C}_2^*$  due to the endothermic nature of the final two reactions with values of +32.79 and +18.00 kcal/mole respectively.

The only other possible mechanisms for the formation of  $\text{C}_2^*$  would have to involve  $\text{C}_3$ . Possible endothermic reactions for the production of  $\text{C}_2^*$  from  $\text{C}_3$  include



with the former more likely than the latter to form  $\text{C}_2^*$ .

#### Methane-Air-Coal Dust Flames

To determine the chemical and physical processes occurring when an amount of coal dust is added to a methane air flame we must examine the nature of the changes which occur upon the addition of coal. Figures 37, 38 and 39 show excited state concentrations as a function of height for a methane-air-coal dust flame with equivalence ratios of 1.0, 1.1 and 0.77 with a coal flow rate of 30 mg/min. Figures 27, 29 and 30 show the respective flames without coal. Figures 40, 41, and 42

show the change in emissions when coal is added to a flame.

This is defined as

$$\frac{[A]_{CH_4 + coal}}{[A]_{CH_4}} = \text{ratio of change}$$

where  $[A]_{CH_4 + coal}$  is the number density of a species in the methane-air-coal dust flame and  $[A]_{CH_4}$  is the number density of the same species in a methane-air flame of the same equivalence ratio. Therefore a number less than one indicates less of a certain species in a methane-air-coal dust flame than in a methane-air flame while a number greater than one indicates an increase upon the addition of coal.

Table 17 shows the percentage change in temperature upon the addition of coal, which is calculated for the flame center in a similar way as the concentration percentages. Table 22 shows flame center temperatures for two methane-air-coal dust flames and four methane-air flames showing measured temperatures from 2 mm above the burner head to 4 mm below the head. These beneath the burner head temperatures were obtained by inserting the thermocouple down the center hole. Temperatures obtained at negative values were not corrected for radiation losses as was the case for the above head measurements.

#### Stoichiometric ( $\phi = 1.0$ ) Flame

One change that occurs in a flame with  $\phi = 1.0$  which can be seen from Figures 29 and 38 is that the  $C_2^*$  and  $CH^*$  emissions are visible at greater heights in a flame containing coal than one without coal. In the methane air flame the signals from  $C_2^*$  and  $CH^*$  became undetectable at heights of 8 and 9 mm respectively while in a flame containing coal dust they were detectable to heights of 9 and 13 mm respectively.

Table 22  
Center Line Thermocouple Temperatures (K) for Methane Air and  
Methane Air Coal Dust Flames (30 mg/min)<sup>a</sup>

Height (mm) / $\phi$	1.0	1.0+Coal	1.1	1.1+Coal	0.77	0.77+Coal
2	1987	1790	1939	1755	1589	1270
1	1940	1686	1865	1703	1433	1139
0	1838	1658	1763	1659		
-1	1266	1222	1270	1087		
-2	1078	1097	1196	946		
-3	950	889	950	840		
-4	890	810	870	750		

<sup>a</sup> Zero height = burner head surface

In the observations in the methane-air flame the limiting noise, which determined the lower limit of detectability, was detector noise, for all the species, while in the methane-air-coal dust flames, the limiting noise source was flame background emission due to particle incandescence for the two species in the visible region  $C_2^*$  and  $CH^*$  with detector noise as the limiting noise for the 2 ultraviolet emitters,  $OH^*$  and  $CO^*$ . This is why in the flames with coal the same detection limits could not be obtained for  $C_2^*$  and  $CH^*$  as in the normal methane-air flames.

From the temperature profiles, Tables 17 and 21 it becomes apparent that the addition of coal to a flame reduces the temperature. Before the coal can begin to burn it must reach an ignition temperature and this heat is provided by the flame, which is cooled in the process. Upon the addition of coal to a stoichiometric flame the temperature drops by a large amount initially until the coal particle can begin to heat up whereupon the flame temperature is within 1% of its gas flame value at a height of 6 mm.

From Figure 41, change in concentrations upon addition of coal, we can see several interesting features. Initially at a height of 1 mm all species in the coal-gas-air flame are decreased relative to a methane air flame with the exception of  $C_2^*$  which shows an increase of 280% over that of a normal methane air flame. As we progress to a height of 2mm we see a decrease in  $C_2^*$  over the previous value but still much greater than a methane-air flame by 238%. As this is occurring  $OH^*$  increases to a +12% value and both  $CH^*$  and  $CO^*$  show increases from their 1 mm values with gains of 11 and 26% respectively although they are still below normal methane-air values. At a flame height of 3 mm



the  $C_2^*$  drops to its lowest value but still retains a positive value and at this height  $OH^*$  experiences a local minimum and  $CO^*$  a local maximum. Here also  $CH^*$  has increased to a +30% value, a 42% increase from the 2mm concentration.

After 3 mm the concentrations of  $C_2^*$  and  $CH^*$  rapidly increase obtaining values of +1780% at 8 mm for  $C_2^*$  and +1840% at 9 mm for  $CH^*$ .  $CO^*$  declines after 3 mm and then rises to obtain a + 5% value at 8 mm which is also where  $OH^*$  obtains its maximum value of +15%. The  $CO^*$  then dips down to -3% at 9 mm returning to -6% at 10 mm while the  $OH^*$  drops to 0% at 9 mm and oscillates around this value.

These observations can be explained with the aid of Figure 60. As the coal particles enter the burner through the bottom they first pass through a preheating and devolatilization zone where the coal particle undergoes heating at large heating rates as shown in Table 23. When the particle exists the burner it enters a region of high temperature ( $>1600$  K) which also possess a high heating rate ( $1.20 \times 10^4$  K/s) although not as large as under the burner where the velocities are greater. This preheating zone and its high heating rate promotes the production of volatiles from the coal particle. As a result when the coal particle enters into the flame it is surrounded by a cloud of volatiles produced in the pre-heating zone which causes the original stoichiometric equivalence ratio to become rich.

At a burner height of 0 mm the coal particle and its accompanying volatiles enter into the flame where the volatile can immediately start to burn. Once this volatile cloud starts to burn the coal particle will be open to attack from flame gas species or combusted

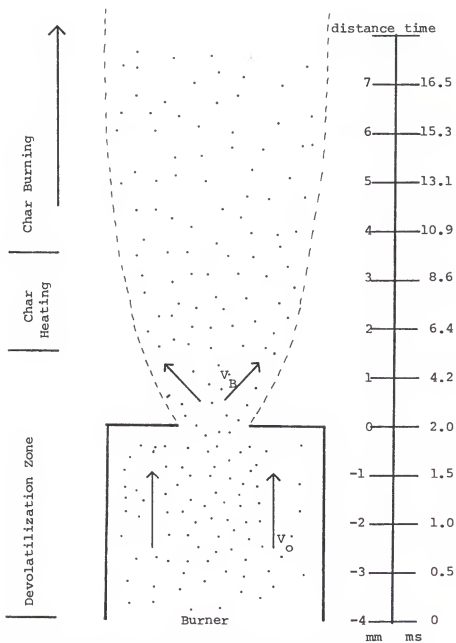


Figure 60. Proposed Coal Burning Model for  $\phi=1.0$  Flame.

Table 23  
 Devolatilization, Char Heating and Char Ignition Times for  
 Coal Particles (30 mg/min) in Methane Air Flames

	<u><math>\phi=0.77</math></u>	<u><math>\phi=1.00</math></u>	<u><math>\phi=1.10</math></u>
Devolatilization (ms)	8.0	5.5	8.6
Char Heating	2.9	3.1	6.7
Char Ignition	10.9	8.6	15.3

Table 24  
Heating Rates for 1mm Travel in Methane Air Coal Dust Flames (K/s)<sup>a</sup>

Height interval (mm)	$\phi=1.0+\text{Coal}$ (30mg/min)	$\phi=1.1+\text{Coal}$ (30mg/min)
0, +1	$1.20 \times 10^4$	$1.98 \times 10^4$
-1, 0	$8.72 \times 10^5$	$1.14 \times 10^6$
-2, -1	$2.50 \times 10^5$	$2.82 \times 10^5$
-3, -2	$4.16 \times 10^5$	$2.12 \times 10^5$
-4, -3	$1.58 \times 10^5$	$1.80 \times 10^5$

<sup>a</sup>Zero height = burner head surface

Table 25  
Analysis of Coal and Natural Gas Used for Study

Coal - Proximate Analysis

% Fixed carbon	52.7
% Volatile matter	32.8
% Ash	8.0
% Moisture	6.5
Btu/lb	13200

Natural Gas Analysis

Component	Mole %
O <sub>2</sub>	.008
N <sub>2</sub>	0.514
CO <sub>2</sub>	0.718
CH <sub>4</sub>	95.757
C <sub>2</sub> H <sub>6</sub>	2.664
C <sub>3</sub> H <sub>8</sub>	0.293
i-Butane	0.009
n-Butane	0.006
i-Pentane	0.007
n-Pentane	0.001
Hexane +	0.023

volatile species to further promote devolatilization. As the volatiles are produced the flame gases surrounding the particles will become extremely fuel rich and possess characteristics of a fuel rich flame. After all the possible volatiles are produced the coal char particle must heat up in order to begin combustion. This region is designated as the char heating zone in Figure 60 and during this time period the released volatiles should burn and be destroyed.

Once the particle leaves this char heating zone, which is defined as when the particle starts burning, it will once again produce local fuel rich conditions as combustion takes place with attack of the coal particle by the various species present in the flame. This char combustion zone is where the char is finally consumed and has the largest length of the 3 zones discussed. The length of time the particle spends in these zones will be dependent upon flame conditions such as temperature and equivalence ratio, which governs the species available to attack the coal, as well as coal characteristics such as particle size and rank.

Looking at Figure 41 and Figure 60 in more detail we can explain the observations in this flame as follows. Before the coal particles enter the flame zone they have undergone high rates of heating for a period of 2 ms, with a resultant production of a substantial amount of volatiles. As the particle volatile mixture enters the flame the volatiles immediately begin to burn, resulting in a fuel rich mixture, which produces an increased amount of  $C_2^*$  emission, similar to the case of a fuel rich methane air flame. Therefore we observe greatly increased  $C_2^*$  emissions at a height of 1 mm which is 4.2 ms after the

beginning of heating in the pre-heating and devolatilization zone.

At a height of 2 mm we still see very elevated levels of  $C_2^*$  indicating that more volatiles were produced in the flame from the coal particle during the 2 ms spent in the flame gases at very high temperatures ( $>1900$  K). At this point it should be remembered that the observations of the emissions from the flame will have a slight time lag from the actual physical and chemical processes actually occurring to the coal.

At this point in the flame (2 mm) we also observe an increase in  $OH^*$ ,  $CH^*$  and  $CO^*$  concentrations from the initially observed values. The large excess of  $C_2^*$  will start to decay, forming ground state  $C_2$ , which will promote the reaction



which will enhance the likelihood of



occurring. The increase in  $CO^*$  could be caused by the reactions



Due to the larger amount of  $C_2^*$  produced in this flame the following reactions may become possible



Heats of reaction for reactions involving excited states were calculated using the JANAF (289) tables to obtain heats of formation for the ground state species at a typical combustion temperature (1900 K)

in a stoichiometric flame. To obtain heats of formation for excited states the energy of the respective transitions (erg/molecule) were calculated using molecular constants obtained from Huber and Herzberg (290) and then converted to a value in kcal/mole using relations given by Fischbeck and Fischbeck (291). The JANAF value for the ground state molecule was then added to this value to obtain the heat of formation for an excited species. The total heat of reaction was then calculated by summing the heats of formation of the products and subtracting the sum of the heats of formation of the reactants. These values calculated for over all heats of reaction should be considered as an upper limit as it does not account for adiabatic reactions.

A possible explanation for the increase in  $C_2^*$  other than just the effect of a locally rich flame can be given due to interaction of the volatiles under the burner head. It may be possible that, when the volatiles are released underneath the burner head, they will be constrained from diffusing great distances, and a high density vapor will be formed. In the hot region under the head, the volatiles may react and condense with themselves to produce molecules containing more than one carbon and possibly large molecules such as  $C_8H_2$ . These large molecules would be highly susceptible to attack by the radical species in the flame with the possibility of forming  $C_3$  or even  $C_2^*$  due to the strongly exothermic nature of radical reactions. If  $C_3$  is produced in the combustion of these large molecules, the most likely process to occur would be





or possibly



From its minimum value of + 4% at a height of 3 mm, the  $C_2^*$  concentration shows a rapid increase to values of + 28%, + 152% and + 433% at heights of 4, 5 and 6 mm. A rapid increase in the concentration of  $CH^*$  is also seen to occur, but at a slightly later time than the  $C_2^*$  rise, which is to be expected if  $CH^*$  is formed from  $C_2^*$ . This very large increase in the emissions of  $C_2^*$  and  $CH^*$  indicate the ignition of the coal char particle and its continued combustion. As the coal char particle burns, the reaction products will be rich in carbon type molecules indicating a rich combustion zone around the particle which favors the production of  $C_2^*$  and  $CH^*$ . The coal particle begins to burn 8.6 ms from the time of initial heating under the burner and 3.2 ms from the end of volatile evolution. Possible chemical reaction mechanisms for coal char combustion will be discussed in a later section.

Figure 60 shows a diagram for the processes occurring to a coal particle in a stoichiometric flame, along with a time scale for the various zones and heating rates present in these zones. It should be noticed that gas flow rates are faster before combustion takes place with a velocity of 200 cm/s before ignition and a velocity of 45 cm/s in the flame. This variance in gas flow rates has been studied in great depth in the work of Lewis and Von Elbe (9) and the two velocities are related by the equation  $S_u = V_o \sin \alpha$  as given in Chapter II, where  $S_u$  is the velocity in a burning flame and  $V_o$  is the velocity of the input gases before ignition and  $\alpha$  is the cone half-angle.

Table 22 gives times for the various processes of devolatilization and char heating in flames of different  $\phi$  values and the percentage changes for flames with  $\phi = 0.77$  and 1.1 upon the addition of coal are shown in Tables 15 and 17. Table 34 compares the heating rates between two methane-air-coal dust flames with different  $\phi$  values.

#### Lean ( $\phi = 0.77$ ) and Rich ( $\phi = 1.1$ ) Flames

Figures 40 and 42 shows changes for a lean and rich flame upon the addition of coal dust. The general shape of these curves is similar in form to the one for stoichiometric flame, i.e. initial increase in  $C_2^*$  emissions followed by a reduction in emission with large increase in both  $C_2^*$  and  $CH^*$  at later times. However there are several distinct differences in each flame which could be accounted for by the physical and chemical composition of these flames. Table 17 shows percentage temperature change upon addition of coal while temperatures beneath the burner head are given in Table 21 for a methane-air flame and methane-air-coal dust flame with equivalence ratios of 1.0 and 1.1.

In the case of the lean methane-air-coal dust flame we see once again a large increase (+54%) in  $C_2^*$  early in the flame with a reduction to +22% at 4 mm which later increases to +202% and +288% at heights of 5 and 7 mm respectively. These increases in  $C_2^*$  show the same general trend as was seen in the  $\phi = 1.0$  methane-air-coal dust flame but with an overall reduction in percentage increases when compared to a methane-air flame with  $\phi = 1.0$ . Once again we observe that the concentrations of all other species are decreased relative to the gas flame. In this flame the coal char particle takes a longer time to start burning as compared to the stoichiometric flame. Coal char ignition times

are given in Table 33 along with pre-heat devolatilization and char heating times for the three coal flames studied. From the Table we observe that the coal particle takes a longer time to devolatilize in a lean flame (8 ms vs 5.5 ms) which results in a later start for char combustion (10.8 ms vs 8.6 ms) after a char heating time of 2.9 ms, very close to the stoichiometric value of 3.1 ms.

Comparing temperature values for a  $\phi = 1.0$  flame with coal and a  $\phi = 0.77$  flame with coal we find that the lean flame containing coal is greater than 500 K cooler than the stoichiometric flame at 1 mm above the burner head and approximately 400 K cooler at a height of 2 mm. Comparing temperature values for flames of  $\phi = 1.0$  and 1.1 with and without coal we see that temperature difference between 1 mm below the burner head and just above it is approximately 520 K. Therefore at 1 mm below the burner in a lean coal dust flame, the temperature is probably ~620 K, whereas in a  $\phi = 1.0$  coal dust flame the temperature at 1 mm below the burner head was 1266 K, and even at -4 mm a temperature of 890 K was present. These low temperatures under the head in a lean coal dust flame will result in much lower heating rates, resulting in a smaller amount of volatiles being produced when compared to a stoichiometric coal dust flame.

The smaller amount of volatiles produced in the pre-heating devolatilization zone would therefore yield a smaller percentage increase in  $C_2^*$  emissions than a large amount of volatiles. Another reason for the small observed increase in  $C_2^*$  emissions, when compared to the increase in the  $\phi = 1.0$  flame, is that because the lean flame has an

excess of oxygen it may be able to absorb more excess volatiles than the stoichiometric flame before forming a fuel rich region surrounding the coal particle. But the low level in  $C_2^*$  is most likely due to the low heating rates and low temperatures found in the methane-air coal dust flame.

An interesting feature in this flame is although it takes longer to generate volatiles in this flame the heating time for a char particle is about the same as that in the stoichiometric coal dust flame. Also in the other two flames with coal dust ( $\phi = 1.0, 1.1$ ) there is not much of a change in the  $OH^*$  concentrations with the largest increase being +23% in the rich flame and the largest decrease being -6% in the stoichiometric flame, but in the lean flame however we observe a 55% decrease initially at 1 mm which slowly rises to a 0% increase value at 7 mm which then rapidly rises to a value of +397% at 12 mm. This large rise in  $OH^*$  occurs after the char has started to burn, which may indicate a different char combustion mechanism in a lean flame compared to rich and stoichiometric flames.

When coal is introduced into a rich flame we observe the lowest increase in the initial  $C_2^*$  concentration of all the methane-air-coal dust flames. Figure 42 shows a small increase (37%) at 1 mm with a slight rise to 51% at 2 mm with higher values declining until a low of 20% is reached at 5 mm whereupon the coal char ignites and rises to a value of +44% at a height of 8 mm. In this flame the initial value for  $OH^*$  and  $CH^*$  shows small increases of +6 and +3% respectively at a height of 1 mm. The  $CH^*$  concentration then drops to a -40%

value and gradually returns to 0 by the height of 4 mm. Between heights of 5 and 6 mm the  $\text{CH}^*$  concentration shows a greater value than the  $\text{C}_2^*$  concentration but  $\text{C}_2^*$  easily passes the  $\text{CH}^*$  gain when the char particle starts to combust and  $\text{C}_2^*$  concentrations increase to a +109% value at 7 mm and a -449% value at 8 mm. The concentration of  $\text{OH}^*$  stays near a value of +10% except for a region between the heights of 7 and 9 mm where percentage increases greater than 20% are located.

In this flame the coal char takes 15.3 ms to reach the ignition point, the longest time of any in this study. Volatile production is found to end after 8.6 ms while the char heating zone is 6.7 ms long. The calculation of values for the end of devolatilization and beginning of char heating time was rather difficult due to the lack of a clear separation between the devolatilization zone and the char heating zone as is present in the stoichiometric flame. The devolatilization was thought to have ended at a height of 3 mm in the flame due to the drop in percentage of  $\text{C}_2^*$  when compared to the value at 2 mm (32% vs 52%) in analogy with the stoichiometric  $\text{C}_2^*$  concentrations at 1 and 2 mm used to determine the end of devolatilization in that flame.

As can be seen from Tables 17 and 21, the temperature in this flame is less than the coal flame with  $\phi = 1.0$  both above and below the burner head. Even though the heating rate (Table 23) is comparable to the heating rate in a  $\phi = 1.0$  flame, the difference in final temperatures (200 K less 1 mm below burner head, 100 K less 1 mm above

burner head) causes a resultant decrease in the devolatilization rate. The char heating time until ignition is also affected by this difference and also possibly by the oxygen deficient atmosphere of this flame.

#### Chemical and Physical Processes in Methane-Air-Coal Dust Flames

The methane-air-coal dust flames observed in this study can be broken down into 3 distinct zones in which different chemical and physical processes are occurring. In the first of these zones, the pre-heating and devolatilization region the coal particle encounters two completely different environments. The first zone extends from beneath the burner head to a certain distance into the flame depending upon flame  $\phi$  value. In this zone the particle undergoes at first just a heating effect under the burner which promotes the generation of volatiles. Upon entering the flame the particles are still affected by the temperature but are now also surrounded by a highly reactive combusting environment. The previously generated volatiles will immediately begin to burn upon entering the flame and these reaction products may further affect the coal particle subsequent volatile production.

After the coal particle has lost all of its available volatiles it enters into the char heating zone where the particle heats up to a temperature sufficiently high for combustion to commence, upon which point it enters into the char combustion zone. Both of these zones are totally surrounded by burning or burnt flame gases at high temperatures. In these zones the rates of heating are relatively small due to the relatively uniform temperature of the hot reaction products and their constant drop in temperature as they rise in the flame.

The combustion of the whole char particle will take the longest time of these three processes and the end of this zone was not observable in the flames in these studies.

In the stoichiometric methane-air-coal dust flame a devolatilization time of 5.5 ms was calculated from the experimental data for bituminous coal particles of 75  $\mu\text{m}$  diameter with 32.8% volatile matter as determined by proximate analysis. The complete proximate analysis is given in Table 24. The heating rate in this flame varied between  $1.2 \times 10^4$  and  $8.7 \times 10^5$  K/s with 2 ms of total time spent beneath the burner and the rest in the flame (3.5 ms). The temperature of the particles environment at the beginning of devolatilization was 890 K and at the end was about 1960 K.

This value for devolatilization time can be compared to the values obtained by other researchers to check the correctness of our calculations. Kobayashi et al. (151) studied the devolatilization of a lignite and a bituminous coal at high temperatures and rapid heating conditions in the presence of an inert atmosphere (Argon) in a laminar flow furnace. Heating rates of  $10^4 - 2 \times 10^5$  K/s were used with final temperatures between 1000 and 2100 K with time resolution down to a few milliseconds. The proximate analysis of the coal types used show the bituminous coal had a volatile matter content of 40.7% with the lignite containing 36.2%. Volatile yields of both coals was found to increase significantly with temperature and these yields were significantly in excess of the 46% value given by proximate analysis with a maximum value of 63% VM obtained on rapid heating to a high temperature (2100 K). Lower VM values were obtained at lower temperatures with

a value of 60% at 1940 K and 45% at 1740 K. At a temperature of 2100 K, after 10 ms 71% of the maximum total volatiles was released, with 100% volatile production after 20 ms. Coal particles in this study were size graded through a +400-325 Tyler Mesh for an average particle sizes between 45-55  $\mu\text{m}$ .

Ubhayakar et al. (152) studied the rapid devolatilization of pulverized bituminous coal particles in the size region around 75  $\mu\text{m}$ . In this study the coal particles were injected into a constant cross-section gasifier, which was heated by hot combustion products produced by an oil burner using #2 fuel oil having a hydrogen to carbon atom ratio (H/C) of 1.72, burned in stoichiometry with oxygen-enriched air. The coal in the study, received from a supplier as 70% passage through a 200 mesh screen, was divided into two groups, the fine fraction which passed through a 200 mesh screen and the coarse fraction which remained on the screen. When these coal particles were input to the gasifier at a temperature of 1970 K it was found that most of the devolatilization of the fine fraction occurred within the first 10 ms with the coarse fraction requiring  $\sim 25$  ms for complete devolatilization. The heating rate for these particles was  $1.3 \times 10^5$  K/s which is similar to heating rates found in this study. This time for devolatilization was faster than the times observed by Kobayshi et al. (151) which may be due to their smaller particle size or due to their use of an active oxygen containing medium (burnt fuel oil) for heating of the particles.

McLean et al. (292) made direct observations on the early stages of combustion of 65  $\mu\text{m}$  bituminous coal particles. These particles were



introduced into a high temperature transparent, laminar flow reactor fed by a pre-mixed gas flame using mixtures of methane, hydrogen and air. These were used to produce uniform reactor carrier gases at temperatures, from 1100 K to 1800 K with oxygen mole fractions of 0 to  $10^5$  K/s. In this study high speed photographs of particle emission, high magnification shadowgraphs of burning particles and micrographs of partially burnt captured material were obtained.

The ignition of bituminous coal particles were characterized by a bright diffuse emission, attributed to burning of ejected volatile matter, which ceased after approximately 5 ms which was replaced by incandescence attributed to heterogeneous char oxidation. Shadowgraphs of burning coal particles indicated that upon ignition, volatile matter ejected from the particle formed a condensed phase surrounding the particle. This condensed phase was thought to be a soot-like material resulting from pyrolytic cracking of hydrocarbons in the volatile matter. Under oxidizing conditions (fuel lean) the condensed volatile matter was oxidized during the early stages of char burning, while under reducing conditions (fuel rich) the matter persisted throughout the flow reactor.

Fu and Blaustein (293) studied the reactions of bituminous coal in a microwave discharge in the presence of hydrogen, water vapor and argon. In the microwave-generated discharges in  $H_2$ ,  $H_2O$  and Ar, coal was gasified to give gaseous hydrocarbons and carbon oxides plus tar and residual char.  $H_2$  was also produced either by dissociation of the water vapor or by devolatilization of the coal in the  $H_2O$  and/or Ar discharges. In the  $H_2$ -Ar discharge a net increase of  $H_2$  in the gas phase is observed only for high volatile bituminous coal.

The yield of hydrocarbons was highest in the  $H_2$ -Ar discharge and that of carbon oxides was highest in the  $H_2O$ -Ar discharge. Both the  $H_2$ -Ar and the  $H_2O$ -Ar discharge gave greater extents of gasification and produced more hydrocarbon products than the Ar discharge, indicating the occurrence of gas phase reactions of H, OH and active O species with the active carbon sites in the coal. In a  $H_2O$ -Ar discharge the extent of gasification and hydrocarbon production varied with initial  $H_2O$  concentration, increasing until a level was reached whereupon greater amounts of  $H_2O$  decreased the production of hydrocarbons due to gasification.

These four studies indicate fast devolatilization times at high temperatures and heating rates, and reactions that are influenced by the molecules contained in a flame, especially radical type reactions. We have seen in Chapter III, the accepted mechanisms for combustion of coal and char particles. What new reactions could be occurring in the methane-air-coal dust flame to explain the observed devolatilization time of 5.5 ms which is about a factor of 2 faster than the values obtained by Ubhayakar et al. (152) in a somewhat reactive medium.

In the studies by Ubhayakar et al. and McLean et al. (292) coal particles were heated up in the reaction products from a gaseous fuel similar to the fuel in the present study. The difference in the above two studies compared to the current study is that the gases used in the early studies were completely reacted and were quite some distance away from the primary reaction zone, therefore allowing a substantial amount of radical recombination reactions to occur thereby reducing the concentration of O, H, OH, etc. In the present study the coal is injected

the same time as the primary heating gases thereby allowing the coal particle to be present when the radicals are first formed in the primary reaction zone.

The reduction in devolatilization time seen in this study can be attributed to attack of the coal particle by free radicals formed in the primary combustion zone. Experimental evidence (294) has shown that at 1100 K to 2000 K oxygen atoms oxidize carbon from 5 to 80 times faster than oxygen molecules and, although direct evidence is lacking, it is likely that OH radicals have similar reactivity (295). The reactions



and



are both highly exothermic.

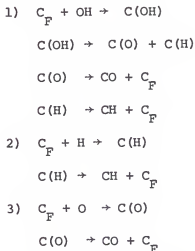
The high reactivity of OH towards carbon containing species is also indicated by the work of Fenimore and Jones (296) who studied the combustion of soot in flame gases. These authors burned a fuel rich ethylene-oxygen-argon mixture on a porous burner to give a gas containing soot equal to about 1% of the carbon fed as ethylene. Sixteen percent of the fuel remained in the gaseous products as hydrocarbons, mostly as acetylene and the rest as carbon oxides, steam, and hydrogen. The products were cooled, mixed with  $\text{H}_2$  and  $\text{O}_2$  to obtain various different  $\phi$ 's and then burnt on a second burner.

The rate of combustion of soot, measured by solids sampling at different heights above the second burner, was found to be little affected by changing the partial pressure of oxygen in the flame gases

from 0.04 to 0.30 atm. A good correlation was found however with the calculated equilibrium concentration of OH radicals and a somewhat better one with the measured OH concentrations (the measured concentrations being 4 to 8 times the calculated). Even in a fuel rich flame with the partial pressure of  $O_2$  about  $10^{-5}$  atm the soot disappeared only 2 to 3 times less rapidly than in the oxygen rich mixtures. From this evidence, along with the fact that dry oxygen-nitrogen mixtures (no OH) consumed the soot at a notably lower rate than that expected on the basis of the oxidation by the flame gases, Fenimore and Jones postulated that the soot is mainly oxidized by OH radicals. A calculated value shows that a carbon atom is removed from the soot particle by about every tenth collision of an OH radical with the surface.

From data obtained in this study and the above mentioned results of others it is most likely that the radicals produced in a methane-air flame greatly assist the combustion of the coal particle in many ways. During devolatilization the flame gas radicals may help stabilize the free radical species formed in a coal particle due to thermal cracking of the linkages forming the aromatic clusters (143). Attack of the coal molecule by radicals such as OH, O and H may also induce the production of more volatiles by increasing the susceptibility of carbon bonds. not normally reactive, or by reducing the amount of secondary reactions occurring which normally produce carbon deposition or polymerize into large soot type particles therefore reducing combustion efficiency.

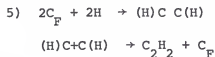
The reaction of gas phase free radicals with coal may proceed via the following mechanisms



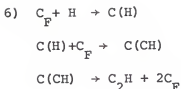
The attack by O and H atom should proceed faster than the similar reactions with molecular species as experimental data has indicated (293). Hydrogen atom could also attack lone methyl groups present as substituents upon coal ring structures or produced in pyrolysis by the following mechanism



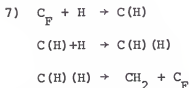
The work of Fu and Blaustein (293) shows that in the presence of H atoms the majority of the products are hydrocarbons which may be due to hydrogen attack in a localized area on more than one carbon. A typical reaction mechanism would be



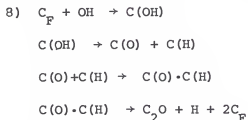
Many H atoms depositing at once at structurally weak points on the coal molecule could enhance production of higher hydrocarbons such as  $\text{C}_2\text{H}_4$  and  $\text{C}_3\text{H}_8$  which have been observed in devolatilization studies (146, 157, 293). Other small hydrocarbon species may be formed via the following:



or



In the case of OH radical attack (293) the reaction products contain more carbon oxides than hydrocarbons as reaction scheme 1 would indicate. OH could also form  $\text{C}_2\text{O}$  via



where  $\text{C(O)} \cdot \text{C(H)}$  is a mutually attracted pair which react together.

#### Comparison with Computer Kinetic Code Simulation Data

A computer code to simulate the kinetic processes occurring when coal is combusted in a methane-air flame has been developed, independent from this study, by Green and Pamidimukkala (297) in the laboratory where this study was accomplished. This computer code has been adapted from the type of kinetics used in atmospheric studies, suitably modified to simulate the combustion chemistry. The kinetic simulation of methane-air combustion uses a reaction set of 52 reactions with a total of 17 molecular and atomic species derived from Smoot et al. (61) with additional reactions from Jachimowski and Wilson (69).

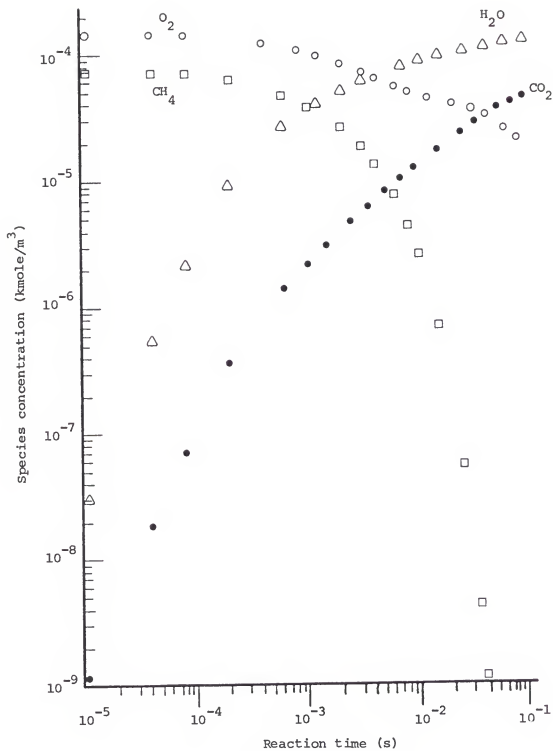


Figure 61. Kinetic model for  $\text{CH}_4/\text{Air}$  flame.

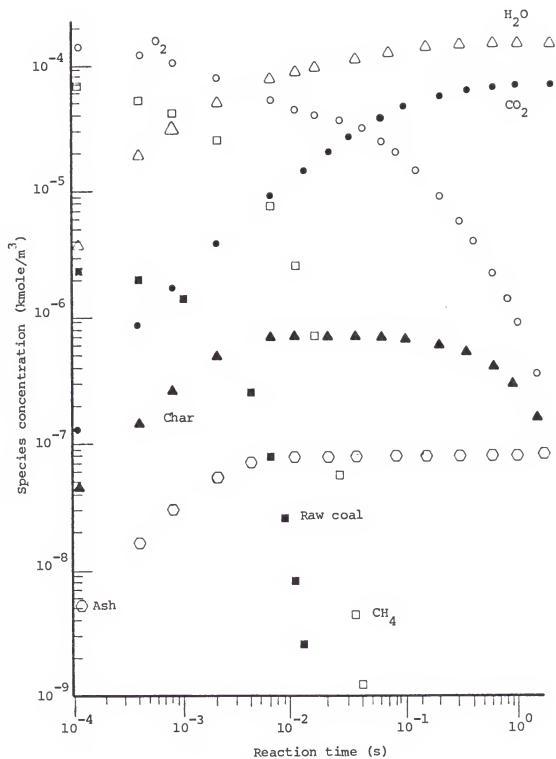


Figure 62. Kinetic model for  $\text{CH}_4/\text{Air}/\text{Coal}$  flame.



The model used to describe the combustion of the coal is that of Kobayashi et al. (151). In this model, described in Chapter III, the coal is devolatilized by 2 routes, a fast reaction which leads to char and the volatiles  $\text{CO}$ ,  $\text{H}_2$  and  $\text{CH}_4$ , and a slow reaction which yields the same products but at a much slower rate. The slow reaction will dominate at low temperature with the fast one dominating at high temperatures. Thus the net rate of disappearance of raw coal is the negative of the sum of the rate of char and volatile formation according to the 2 reactions. The net concentration of char depends upon the fast devolatilization reactions and the slow oxidation reactions of char with  $\text{O}_2$ ,  $\text{CO}_2$  and  $\text{H}_2\text{O}$ . The total reaction scheme to model the combustion of a methane-air-coal dust flame contains 57 reactions and 21 species, with the coal related species being raw coal, total volatiles, char, and ash.

Figure 61 shows the results of a kinetic run of a methane-air flame using experimental flow rates, while Figure 62 shows the same flame with the addition of 30 mg/min of bituminous coal. From Figure 62 one can see that the char is completely formed (all possible volatiles removed) at  $\sim 7$  ms which is in quite good agreement with the experimental value of 5.5 ms for devolatilization in a stoichiometric flame.

#### Conclusions

This study reports the first use of high resolution spectroscopic techniques in the ultraviolet and visible regions of the spectrum, to obtain absolute number densities of radical species in a methane-air-coal dust stationary flame. The only other previous investigation of

a methane-air coal dust flame (298) involved propagating methane-coal dust inhibitor flames. The majority of the spectral work in this earlier study was in the infrared region although spectra of OH (0,0) were obtained. However, no quantitative measurements of the band were made due to the poor resolution of the rapid scanning spectrometer used (approximately 25 Å). Blackbody coal dust temperature profiles were calculated from spectral radiance values at 435 and 436 nm.

The present study has demonstrated that a laboratory size burner can be used to perform spectroscopic observations on the simultaneous combustion of gas and coal. By observing the spectral emissions of the species OH, CH, C<sub>2</sub>, and CO some understanding of the coal burning processes occurring in the presence of gas can be obtained. This study has pointed out the complex relationships between flame composition and the enhanced combustion of coal. We have seen in this study how the devolatilization time is a function of both flame fuel-air ratio and temperature with the flame optimum value found in a stoichiometric flame.

The fast devolatilization and char ignition times found in this study indicate the feasibility of replacing oil boilers with a mixture of gas and coal. These fast times would cause a gas-coal flame to require less of a distance than a coal flame, enabling a higher power density to be developed in the boiler.

Evidence has been given which indicates a major role for radical species, OH, O and H in the attack and combustion of a coal particle and various reaction schemes were postulated to account for experimental observations.

The advantages gained when burning coal in the presence of a methane-air flame can be given as follows:

1. High temperature of the methane-air flame causes a rapid heating effect, thereby producing more volatiles from a coal particle than would normally be expected from proximate analysis.
2. A large production of volatiles will result in a smaller amount of char which will react faster, therefore decreasing the length of flame needed for complete combustion.
3. The high concentration of radicals in the methane-air flame gases help promote faster devolatilization and possibly help produce a greater amount of volatiles.
4. Stoichiometric and lean flame conditions promote the ignition of the devolatilized char particle resulting in a much shorter char heating time ( $\sim 3$  ms) when compared to a rich flame ( $\sim 7$  ms). This is probably due to the higher concentrations of O atoms found in a lean and stoichiometric flame when compared to a rich flame.

#### Future Work

The most intriguing aspects of the present study involve the presence of the flame radicals OH, O and H and the effect of these species. Evidence has been put forth in this study for a major role for these radicals in the devolatilization and combustion of the coal particle. One way to study these effects in greater depth is to increase the concentrations of these radicals in the flame. By spiking the flame with suitable gases one should be able to increase the concentrations of a specific radical and observe its action.

Hydrogen and oxygen radicals could be increased by adding the respective molecular species and OH and H atom could be generated by the aspiration of water into the flame. To make sure the effects of radicals, and not molecular species, were being observed the respective gases could be passed through a flowing microwave discharge and then to the flame, insuring a large concentration of radicals in the flame.

One problem with the present study is how to distinguish between the effect of temperature and the effect of radical species as the flame stoichiometry was changed. One way to separate the temperature effect from the chemical one is to run flames using methane, oxygen, nitrogen and argon mixtures. By varying the argon to nitrogen ratio the flame temperature could be varied over a sufficient range to determine the effect of temperature. As long as the methane-oxygen ratio was kept constant the population of radicals would be fairly constant. Another possible variation would be to vary all four gases in order to obtain different  $\phi$  values at a constant temperature.

Another question which could be addressed is the effect of particle size on the devolatilization and char ignition times. It would be interesting to see how the amount of volatiles produced (as measured by CH and C<sub>2</sub> emissions) varied with particle size and at what size the reaction went from a chemical controlled reaction to a mass transfer controlled reaction. The effect of  $\phi$  could also be studied with respect to particle size and devolatilization times. A certain size particle may produce one amount of volatiles in a flame with  $\phi=1.0$  and may produce more or less in flames with different  $\phi$ 's. The coupling of particle size to flame stoichiometry should be optimized in order to maximize the amount of char burned.

The C<sub>3</sub> emissions observed in some studies might be an indicator of how complete the combustion of the coal particles. C<sub>3</sub> emission could be monitored as a function of coal mass flow and particle size. Further work is needed to understand the significance of the C<sub>3</sub> emission when coal is introduced to the flame.

An important series of measurements would measure the ground state concentrations of the species observed in these studies. Absorption data would give information on ground state concentrations, the predominate reaction species, and the changes observed with the addition of coal should further elucidate the chemical reactions occurring in coal combustion. Ground state concentrations could also be used, with the temperature measurements, to determine what percentage of the excited state is thermally produced as opposed to the amount chemically produced.

Another useful study would involve observations of the complete char burning region. This would probably require a large burner to insure a tall enough flame to provide uniformly hot surroundings for the particles. Emission measurements would probably not be of any use in the upper regions due to the noise of the coal dust flame. Particle densities could possibly be measured by a scattering technique using a He-Ne or He-Cd laser to monitor densities at different heights and therefore the burnout rate. Another way to accomplish the same experiment would be to contain the flame in an oven and sample the flame at several different heights in order to determine burn out rate under different flame equivalence ratios or with different additives (i.e.  $H_2$ ,  $O_2$ ).

APPENDIX  
COMPUTER PROGRAMS

```

C      THIS PROGRAM ACCEPTS RAW DATA FROM FILES. CONVERTS
C      Y INTO NAIOAMPS, AXES THE EDGES, FLIPS THE DATA
C      AND MAKES THE DATA INTO 100 EQUALLY SPACED POINTS.
C      THE FILE CREATED BY THIS PROGRAM MAY BE USED
C      ALSO SCALES THE X-AXIS
C      IN INVER.FOR PROGRAM.
C*****
C      SETJEF.FOR
C      THIS IS THE MODIFIED VERSION OF SETUP.FOR
C*****
      REAL* 4 MM,IN(200),IN1(200)
      LOGICAL*1 ICH,ICJ,ICK
      DIMENSION ICH(14),X(200),X1(200)
      TYPE 1
      FORMAT ( '  WHAT IS THE DATA FILE  ' )
      ACCEPT 2,J,(ICH(I),I=1,J)
      TYPE 2
      FORMAT(Q,14A1)
      CALL ASSIGN (2,ICH,J,'RDO')
      TYPE 3
      FORMAT ( '  WHAT IS THE FILE TO BE CREATED  ' )
      ACCEPT 2,J,(ICH(I),I=1,J)
      CALL ASSIGN (3,ICH,J,'NEW')
      TYPE 10
      FORMAT ( '  ENTER X0 AND X-END' )
      ACCEPT 997,X0,XE
      TYPE 9
      FORMAT ( '  ENTER THE SCALING FACTOR ' )
      ACCEPT 20,SF
      TYPE 5
      FORMAT( '  ENTER THE X SCALING FACTOR(FOR CHART SPEED',/, '
      1 2 INS/MIN) MOTOR 2/1 RATIO XF=0.25,IF 5/1 RATIO ',/, '
      1 XF=0.01, FOR NO SCALING XF=0.1 ' )
      ACCEPT 20,XF
      TYPE 35
      FORMAT( '  DO YOU WISH TO FLIP THE DATA ?',/
      1,' ENTER 1<CR> FOR YES AND <CR> FOR NO.' )
      ACCEPT 40,IA
      TYPE 40
      FORMAT(I1)
      TYPE 20
      FORMAT (F10.5)
      N=0
      TYPE 100
      READ(2,997,END=110) XP,XI
      TYPE 997
      FORMAT(2F10.5)
      TYPE 102
      IF(XP.LT.X0) GOTO 101
      IF(XP.GT.XE) GOTO 111
      I=N+1
      X(I)=XP*XF*10.0
      IN(I)=XI*SF/19.85
      N=N+1
      IF(IF.EQ.1) GOTO 111
      TYPE 101
      GOTO 100
      TYPE 110
      IF=1

```

\*

```

      GOTO 102
111  R=X(I)-X(1)
      DELTA=R/100.0

      DO 900 I=0,99
      XP=I*DELTA
      J=1
650  XL=X(J)
      IF(XL.GT.XP+X(1)) GOTO 800
      J=J+1
      GO TO 650
800  J=J-1
      YP=IN(J)+((IN(J+1)-IN(J))/(X(J+1)-X(J)))*(XP+X(1)-X(J))
      IN1(I)=YP
      X1(I)=XP
900  CONTINUE
      WRITE(3,30) DELTA
30   FORMAT(F10.5)
      N1=1-2*IA
      XE=X1(99)
      DO 700 I=0,99
      X2=XE*IA +N1*X1(99*IA +N1*I)
      XI=IN1(99**IA+N1*I)
      WRITE(3,25) X2,XI

25   FORMAT(1X,2F10.5)
700  CONTINUE
      CALL CLOSE (2)
      CALL CLOSE (3)
      STOP
      END

```

\*



```

C      *****
C      THIS PROGRAM SMOOTHS DATA IN A .JEF DATA FILE BY THE
C      SAVITZKY - GOLAY METHOD(ANAL.CHEM.36,1627(1964)
C      USING 5 POINTS
C      *****
C      DIMENSION X1(200)
C      LOGICAL *1 NAME(14)
C      REAL *4 NDATA(1000),MDATA(1000),NP(9),NSUM
C      TYPE 110
C      ACCEPT 220,J,(NAME(I),I=1,J)
C      CALL ASSIGN (2,NAME,J,'RDO')
C      TYPE 120
C      ACCEPT 220,J,(NAME(I),I=1,J)
C      CALL ASSIGN(3,NAME,J,'NEW')
C      N=100
C      READ(2,400) DELTA
C      WRITE(3,400) DELTA
C      DO 50 J=1,100
C      READ(2,400)X1(J),NDATA(J)
50      CONTINUE
110     FORMAT(' ENTER NAME OF FILE TO BE SMOOTHED ' )
120     FORMAT(' ENTER NAME OF SMOOTH DATA FILE ' )
220     FORMAT(Q,14A1)
400     FORMAT(1X,2F10.5)
C      M=N-4
C      DO 10 I=2,5
C      J=I-1
10      NP(I)=NDATA(J)
C
C      DO 200 I=1,M
C      J=I+4
C      DO 11 K=1,4
C      KA=K+1
11      NP(K)=NP(KA)
C      NP(5)=NDATA(J)
C      NSUM=17.*NP(3)+12.*(NP(2)+NP(4))-3.*(NP(1)+NP(5))
C      MDATA(I)=NSUM/35
401     FORMAT(1X,2F10.5)
200     CONTINUE
C      WRITE(3,401)X1(1),0.0,X1(2),MDATA(1)/2.0
C      DO 900 I=1,M
C      WRITE(3,401) X1(I+2),MDATA(I)
900     WRITE(3,401) X1(99),MDATA(96)*0.5,X1(100),MDATA(96)*0.0
C      CALL CLOSE (2)
C      CALL CLOSE(3)
C      STOP
C      END
C      *

```

```

C*****
C
C      ABEL INVERSION PROGRAM
C
C      THIS PROGRAM WILL EVALUATE THE ABEL INVERSION INTEGRAL
C      USING THE BARR METHODE (JOSA; VOL.52,NO. 8,PAGE 885)
C      THIS PROGRAM ALSO AVERAGES (SYMETERIZES!◇)AFTER INVERTING
C
C*****
C      INPUT DATA FOR THIS PROGRAM IS READ IN FROM FORTRAN
C      CHANNEL TWO.
C
C      THE OUT PUT WILL BE OUT PUT TO FORTRAN CHANNEL THREE.
C
C*****
C      LOGICAL*1 NAME,FORM
C      REAL*4  IN,IN1
C      DIMENSION FORM(72),NAME(14),A(5),T(3),R(3,5),IN(100),FK(100)
C      1,X1(100),Y(3),X(100),IN1(100)
C      TYPE 110
C      ACCEPT 220,J,(NAME(I),I=1,J)
C      CALL ASSIGN (2,NAME,J,'RDO')
C      TYPE 120
C      ACCEPT 220,J,(NAME(I),I=1,J)
C      CALL ASSIGN(3,NAME,J,'NEW')
C      READ(2,400) DELTA
C      DO 50 J=1,100
C      READ(2,400)X1(J),IN1(J)
50  CONTINUE
C      GOTO 600
C
C*****
C*****      CALCULATE FK(K)      *****
C*****
C      85  DO 60K=0,49
C          FK(K)=0.0
C          DO 60 J=K,49
C              XJ=J
C              XK=K
C              IF(K.EQ.J) GOTO 70
C              A1=((XJ+1)**2)-(XK**2))**1.5
C              A1=A1/(2*XJ+1)
C              A2=4*XJ*((XJ**2)-(XK**2))**1.5
C              A2=A2/(4*XJ**2-1)
C              A3=((XJ-1)**2-(XK**2))**1.5
C              A3=A3/(2*XJ-1)
C              ALPHA=4*(A1-A2+A3)/3
C              GOTO 60
70  ALPHA=(4*(2*K+1.))**5)/3.
60  FK(K)=FK(K)+ALPHA*IN(J)
C
C
C      *

```

§

C\*\*\*\*\* FIT FK(K) TO  $A+BK^{-2}+CK^{-4}$  \*\*\*\*\*  
 C\*\*\*\*\*  
 C

DO 5 K=0,49  
 DO 20 I=1,3  
 DO 20 J=1,3  
 Y(I)=0.0  
 R(I,J)=0.0

R(1,1)=5  
 IF (K.LE.2) GOTO 8  
 KN=K

DO 30 I=KN-2,KN+2  
 XI=I  
 R(1,2)=R(1,2)+XI\*\*2  
 R(1,3)=R(1,3)+XI\*\*4  
 R(2,3)=R(2,3)+XI\*\*6  
 R(3,3)=R(3,3)+XI\*\*8  
 Y(1)=Y(1)+FK(I)  
 Y(2)=Y(2)+FK(I)\*XI\*\*2  
 Y(3)=Y(3)+FK(I)\*XI\*\*4

CONTINUE  
 R(2,1)=R(1,2)  
 R(3,1)=R(1,3)  
 R(2,2)=R(1,3)  
 R(3,2)=R(2,3)

DO 2 I1=1,3  
 DO 2 J1=1,3  
 TYPE 400,R(I1,J1)  
 DO 40 I=1,3  
 Y(I)=Y(I)/5.  
 DO 40 J=1,3  
 R(I,J)=R(I,J)/5

CONTINUE  
 F1=R(2,1)  
 F2=R(3,1)  
 DO 45 J=1,3  
 R(2,J)=R(2,J)-R(1,J)\*F1  
 R(3,J)=R(3,J)-R(1,J)\*F2  
 Y(2)=Y(2)-Y(1)\*F1  
 Y(3)=Y(3)-Y(1)\*F2  
 R(2,3)=R(2,3)/R(2,2)  
 Y(2)=Y(2)/R(2,2)  
 R(3,3)=R(3,3)-R(2,3)\*R(3,2)  
 Y(3)=Y(3)-Y(2)\*R(3,2)  
 Y(3)=Y(3)/R(3,3)  
 Y(2)=Y(2)-(Y(3)\*R(2,3))  
 B=Y(2)  
 C=Y(3)  
 F=- (B+2\*C\*K\*\*2)/(3.14159\*DELTA)

IN(K)=F  
 CONTINUE  
 GOTO 901

5  
 D  
 \*

```

903   IF(FLAG.EQ.1.0) GOTO 900
      GOTO 500
8     KN=2
      GOTO 35
600   DO 700 I=0.99
      RA=100*DELTA
      X1(I)=X1(I) -RA/2.
700   CONTINUE
      DO 800 I=0.49
      IN(I)=IN1(50-I)
800   CONTINUE
      FLAG=1.0
      GOTO 85
900   DO 925 I=0.49
      IN1(50-I)=IN(I)
925   CONTINUE
      DO 950 I=0.49
      IN(I-1)=IN1(50+I)
950   CONTINUE
      FLAG=0.0
      GOTO 85
100   FORMAT(' PLEASE ENTER THE NUMBER OF POINTS AND STEP SIZE')
110   FORMAT(' PLEASE ENTER THE NAME OF THE INPUT DATA FILE')
120   FORMAT(' PLEASE ENTER THE NAME OF THE OUTPUT DATA FILE')
200   FORMAT(I3,F5.3)
220   FORMAT(Q,14A1)
1000  FORMAT(Q,80A1)
400   FORMAT(1X,2F10.5)
550   FORMAT('(1X,2F10.5)')
500   DO 540 I=1.50
      IN1(50+I)=IN(I-1)
540   CONTINUE
      WRITE(3,550)
      DO 675 I=1.99
      WRITE(3,400) X1(I),(IN1(I)+IN1(99-I))/2.
675   CONTINUE
      CALL CLOSE(2)
      CALL CLOSE (3)
D 901  DO 902 I=1.50
D      TYPE 400 ,IN(I)
D 902  CONTINUE
D      GOTO 903
      STOP
      END

```

★

# REFERENCES

1. A. E. S. Green, Ed., "An Alternative to Oil: Burning Coal with Gas" (University Presses of Florida, Gainesville, 1982).
2. G. J. Minkoff, C. F. H. Tipper, "Chemistry of Combustion Reactions" (Butterworths, London, 1962).
3. R. M. Fristrom, A. A. Westerberg, "Flame Structure" (McGraw-Hill, New York, 1965).
4. A. G. Gaydon, "The Spectroscopy of Flames" (Chapman and Hall, London, 1974).
5. A. G. Gaydon, H. G. Wolfhard, "Flames: Their Structure, Radiation and Temperature " (Chapman and Hall, London, 1979).
6. M. W. Thring, "The Science of Flames and Furnaces" (Chapman and Hall, London, 1962).
7. B. Lewis, J. Grumer, Indust. Eng. Chem. 40, 1123 (1948).
8. B. Lewis, G. von Elbe, "Combustion, Flames and Explosions of Gases" (Academic Press, New York, 1961).
9. B. Lewis, G. von Elbe, J. Chem. Phys. 11, 75 (1943).
10. G. M. Hieftje, Appl. Spectrosc. 25, 653 (1971).
11. M. S. Uberoi, A. M. Kuethe, H. R. Menkes, Phys. Fluids 1, 150 (1958).
12. F. W. Ruegg, W. W. Dorsey, Combust. Flame 10, 1 (1966).
13. T. L. Cottrell, J. C. McCoubrey, "Molecular Energy Transfer in Gases" (Butterworths, London, 1961).
14. W. R. Kane, H. P. Broida, J. Chem. Phys. 21, 347 (1953).
15. R. Mavrodineanu, H. Boileux, "Flame Spectroscopy" (Wiley, New York, 1965).
16. E. Mallard, H. L. Le Chatelier, Ann. Mines 4, 274 (1883).
17. W. Nusselt, Z. Ver. Deut. Ing. 59, 872 (1915).

18. E. Jouguet, L. Crussard, *Compt. Rend.* 168, 820 (1919).
19. P. J. Daniell, *Proc. Roy. Soc.* A126, 393 (1930).
20. G. Damkohler, *Z. Elektrochem.* 46, 601 (1940).
21. Y. B. Zeldovich, D. A. Frank-Kamenetsky, *J. Phys. Chem. U.S.S.R.* 12, 100 (1938).
22. Y. B. Zeldovich, D. A. Frank-Kamenetsky, *Acta Physiochim. U.S.S.R.* 9, 341 (1938).
23. Y. B. Zeldovich, N. Semenov, *J. Exp. Theor. Phys. U.S.S.R.* 10, 1116 (1940).
24. Y. B. Zeldovich, N. Semenov, *J. Exp. Theor. Phys. U.S.S.R.* 10, 1427 (1940).
25. N. Semenov, *Progr. Phys. Sci. U.S.S.R.* 24, 433 (1940).
26. Y. B. Zeldovich, *Z. Tech. Phys. U.S.S.R.* 17, 3 (1947).
27. A. Th. Belayev, *Acta Physicochim. U.S.S.R.* 8, 763 (1938).
28. E. Bartholomé, *Naturwissenschaften*, 36, 171 (1949).
29. E. Bartholomé, *Naturwissenschaften* 36, 206 (1949).
30. S. F. Boys, J. Corner, *Proc. Roy. Soc.* A197, 90 (1949).
31. R. C. Murray, A. R. Hall, *Trans. Faraday Soc.* 47, 743 (1951).
32. D. B. Spalding, *Fuel* 33, 255 (1954).
33. C. Tanford, R. N. Pease, *J. Chem. Phys.* 15, 431 (1947).
34. C. Tanford, *J. Chem. Phys.* 15, 433 (1947).
35. C. Tanford, R. N. Pease, *J. Chem. Phys.* 15, 861 (1947).
36. A. Van Tiggelen, *Bull. Soc. Chim. Belg.* 55, 202 (1947).
37. A. Van Tiggelen, *Bull. Soc. Chim. Belg.* 58, 259 (1949).
38. N. Semenov, "Chemical Kinetics and Chain Reactions" (Clarendon Press, Oxford, 1935).
39. M. V. Smoluchowski, *Ann. Physik* 21, 756 (1906).
40. H. F. Coward, F. J. Hartwell, *J. Chem. Soc.* P401, 2676 (1932).
41. D. B. Spalding, *Phil. Trans.* A249, 1 (1956).
42. A. G. Gaydon, *Proc. Roy. Soc.* A196, 105 (1949).

43. N. Manson, *Compt. Rend* 226, 230 (1948).
44. J. O. Hirschfelder, C. F. Curtiss, *Adv. Chem. Phys.* 3, 59 (1961).
45. J. O. Hirschfelder, C. F. Curtiss, R. B. Bird, "Molecular Theory of Gases and Liquids" (John Wiley, New York, 1954).
46. S. Chapman, T. G. Cowling, "The Mathematical Theory of Non-Uniform Gases" (Cambridge University Press, London, 1970).
47. J. O. Hirschfelder, C. F. Curtiss, *J. Chem. Phys.* 17, 1076 (1949).
48. J. O. Hirschfelder, C. F. Curtiss, R. B. Bird, E. L. Spotz, "The Properties of Gases" (John Wiley and Sons, New York, 1953).
49. G. K. Adams, G. W. Stocks, Fourth Symposium (International) on Combustion, The Combustion Institute, Pittsburgh, 1953, p. 239.
50. D. B. Spalding, P. L. Stephenson, *Proc. Roy. Soc.* A324, 315 (1971).
51. D. B. Spalding, P. L. Stephenson, R. G. Taylor, *Combust. Flame* 17, 55 (1971).
52. S. V. Patankar, D. B. Spalding, "Heat and Mass Transfer in Boundary-Layers" (International Textbook Co., London, 1970).
53. G. Dixon-Lewis, *Proc. Roy. Soc.* A298, 495 (1967).
54. G. Dixon-Lewis, *Proc. Roy. Soc.*, A307, 111 (1968).
55. C. S. Wang Chang, G. E. Uhlenbeck, J. de Boer, "Studies in Statistical Mechanics, Vol. II" J. de Boer, G. E. Uhlenbeck Eds. (John Wiley and Sons, New York, 1964).
56. E. A. Mason, L. Monchick, *J. Chem. Phys.* 36, 1622 (1962).
57. E. A. Mason, J. T. Vanderslice, J. M. Yos, *Phys. Fluids* 2, 688 (1959).
58. L. Monchick, E. A. Mason, *J. Chem. Phys.* 35, 1676 (1961).
59. L. Monchick, A. N. G. Pereira, E. A. Mason, *J. Chem. Phys.* 42, 3241 (1965).
60. L. Monchick, R. J. Munn, E. A. Mason, *J. Chem. Phys.* 45, 3051 (1966).
61. L. D. Smoot, W. C. Hecker, G. A. Williams, *Combust. Flame* 26, 323 (1976).
62. G. Tsatsaronis, *Combust. Flame* 33, 217 (1978).
63. R. M. Fristrom, C. Grunfelder, S. Favin, *J. Phys. Chem.* 64, 1386 (1960).

64. G. E. Andrews, D. Bradley, Combust. Flame 19, 275 (1972).
65. J. Peeters, G. Mahnen, The 14th Symposium (International) on Combustion, The Combustion Institute, Pittsburgh, 1973, p. 133.
66. C. T. Bowman, Fourteenth Symposium (International) on Combustion, The Combustion Institute, Pittsburgh, 1973, p. 729.
67. D. B. Olson, W. C. Gardiner, Jr., Combust. Flame 32, 15 (1978).
68. C. K. Westbrook, J. Creighton, C. Lund, F. L. Dryer, J. Phys. Chem. 81, 2542 (1977).
69. C. J. Jachimowski, C. H. Wilson, NASA Tech. Paper, 1974 (1980).
70. A. A. Westenberg, R. M. Fristrom, J. Phys. Chem. 65, 591 (1961).
71. K. J. Laidler, "The Chemical Kinetics of Excited States" (Clarendon, Oxford, 1955).
72. P. L. Lijnse, "Electronic-Excitation Transfer Collisions in Flames" (Diss. Utrecht, 1974).
73. J. C. Polanyi, Appl. Opt. 10, 1717 (1971).
74. J. C. Polanyi, Diss. Faraday Soc. 44, 293 (1967).
75. J. C. Polanyi, J. J. Sloan, J. Wanner, Chem. Phys. 13, 1 (1976).
76. A. G. Gaydon, H. G. Wolfhard, Proc. Roy. Soc. 213, 366 (1952).
77. H. P. Broida, A. G. Gaydon, Proc. Roy. Soc. 218, 60 (1953).
78. S. L. N. G. Krishnamachari, H. P. Broida, J. Chem. Phys. 34, 1709 (1961).
79. R. P. Porter, A. H. Clark, W. E. Kaskan, W. E. Browne, Eleventh Symposium (International) on Combustion, The Combustion Institute, Pittsburgh, 1967, p. 907.
80. F. E. Belles, M. R. Lauver, J. Chem. Phys. 40, 415 (1964).
81. Y. Hidaka, S. Takahashi, H. Kawano, M. Suga, W. C. Gardiner, Jr., J. Phys. Chem. 86, 1429 (1982).
82. C. W. Hand, G. B. Kistiakowsky, J. Chem. Phys. 37, 1239 (1962).
83. E. M. Bulewicz, P. J. Padley, R. E. Smith, Proc. Roy. Soc. A315, 129 (1970).
84. T. Kinbara, K. Noda, Thirteenth Symposium (International) on Combustion, The Combustion Institute, Pittsburgh, 1971, p. 993.



85. K. H. Becker, D. Kley, Chem. Phys. Lett. 4, 62 (1969).
86. K. A. Quickert, J. Phys. Chem. 76, 825 (1972).
87. R. E. Ferguson, J. Chem. Phys. 23, 2085 (1955).
88. A. R. Fairbairn, Proc. Roy. Soc. 267, 88 (1962).
89. R. Bleekrode, W. C. Nieuwport, J. Chem. Phys. 43, 3680 (1965).
90. J. Peeters, J. F. Lambert, P. Hertoghe, A. Van Tiggelen, Thirteenth Symposium (International) on Combustion, The Combustion Institute, Pittsburgh, 1971, p. 321.
91. M. I. Savadatti, H. P. Broida, J. Chem. Phys. 45, 2390 (1966).
92. D. M. Mann, Chem. Phys. Lett. 47, 106 (1977).
93. P. H. Kydd, W. I. Foss, Eleventh Symposium (International) on Combustion, The Combustion Institute, Pittsburgh, 1967, p. 1179.
94. K. H. Becker, K. D. Bayes, J. Chem. Phys. 48, 653 (1968).
95. The American Society for Testing and Materials, "1976 Annual Book of ASTM Standards" Part 26, D388-77, Philadelphia, 1976.
96. E. A. Hattman, W. E. McKinstry, H. Schultz, Anal. Chem. 51, 135R (1979).
97. H. Schultz, A. W. Wells, T. W. Bergstresser, Anal. Chem. 53, 233R (1981).
98. A. H. Edwards, Fuel, 37, 415 (1958).
99. G. Ingram, "Methods of Organic Elemental Microanalysis" (Chapman and Hall, London, 1962).
100. O. I. Milner, R. J. Zahner, Anal. Chem. 32, 294 (1960).
101. P. J. Jackson, Fuel 35, 212 (1956).
102. A. C. Fielding, W. A. Selvig, U. S. Bureau Mines Bull. 492, 16 (1951).
103. W. R. Kirner, Ind. Eng. Chem. 8, 57 (1936).
104. M. Z. Schutze, Anal. Chem. 118, 245 (1939).
105. J. Unterzaucher, Ber. Dtsch. Chem. Ges. 73B, 391 (1940).
106. L. C. Bate, Nucleonics 21, 72 (1963).
107. O. U. Anders, D. W. Briden, Anal. Chem. 36, 287 (1964).
108. M. C. Stopes, Proc. Roy. Soc. 90B, 470 (1919).

109. M. C. Stopes, Fuel 14, 4 (1935).
110. H. R. Brown, A. C. Cook, G. H. Taylor, Fuel 43, 111 (1964).
111. L. G. Benedict, R. R. Thompson, J. J. Shigo, R. P. Aikman, Fuel 47, 125 (1968).
112. A. Davis, W. Spackman, P. H. Given, Energy Sources 3, 55 (1976).
113. P. H. Given, M. E. Peover, W. F. Wyss, Fuel 44, 425 (1965).
114. D. G. Murchison, J. M. Jones, Fuel 42, 141 (1963).
115. R. Millais, D. G. Murchison, Fuel 47, 247 (1969).
116. M. F. Kessler, Fuel 52, 191 (1973).
117. D. W. Van Kreuelen, "Coal" (Elsevier, New York, 1961).
118. B. N. Nandi, T. D. Brown, G. K. Lee, Fuel 56, 125 (1977).
119. H. H. Lowry, "Chemistry of Coal Utilication" Suppl. Vol. (John Wiley and Sons, New York, 1963).
120. M. Menser, H. O'Donnell, S. Ergun, Proc. 5th Carbon Conf. Vol. 2, Pergamon Press, London, 1962, p. 493.
121. H. Brusset, J. Devaux, A. Guinier, Compt. Rend. 216, 152 (1943).
122. S. Ergun, I. Wender, J. Appl. Chem. 10, 189 (1960).
123. L. Cartz, P. B. Hirsch, Philos. Trans. R. Soc. London A252, 557 (1960).
124. R. E. Franklin, Acta Crystallog. 3, 107 (1950).
125. J. B. Nelson, Fuel 32, 153 (1954).
126. P. B. Hirsch, Proc. Roy. Soc. London A226, 143 (1954).
127. M. M. Roy, Fuel 36, 249 (1957).
128. C. G. Cannon, Nature 171, 308 (1953).
129. R. A. Friedal, J. A. Queiser, Anal. Chem. 28, 22 (1956).
130. J. K. Brown, P. B. Hirsch, Nature 175, 229 (1955).
131. H. S. Rao, P. L. Gupta, F. Kaiser, A. Lahiri, Fuel 41, 417 (1962).
132. L. Czuchajowski, G. J. Lawson, Fuel 42, 131 (1963).
133. S. Fujii, Y. Osawa, H. Sugimura, Fuel 49, 68 (1970).

134. L. Czuchajowski, Arch. Gorn. 6, 257 (1961).
135. S. Fujii, H. Tsuboi, Fuel 45, 369 (1966).
136. R. M. Elofson, Can. J. Chem. 35, 926 (1957).
137. J. K. Brown, J. Chem. Soc. (London) 744 (1955).
138. A. G. Sharkey, J. T. McCartney in "Chem. of Coal Utilization" 2nd Suppl. Vol., M. A. Elliott, Ed. (John Wiley and Sons, New York, 1981).
139. I. Wender, L. A. Heredy, M. B. Neuworth, I. G. C. Dryden in "Chem. of Coal Utilization" 2nd Suppl. Vol., M. A. Elliott, Ed. (John Wiley and Sons, New York, 1981).
140. L. A. Heredy, A. E. Kostyo, M. B. Neuworth, Fuel 44, 125 (1965).
141. H. L. Retcofsky, Appl. Spectrosc. 31, 116 (1977).
142. P. H. Given, Fuel 39, 147 (1960).
143. W. H. Wiser, G. R. Hill, N. J. Kertamus, Ind. Eng. Chem. Process. Des. Dev. 6, 133 (1967).
144. W. Peters, H. Bertling, Fuel 44, 317 (1965).
145. J. F. Jones, M. R. Schmid, R. T. Eddinger, Chem. Eng. Prog. 60, 69 (1964).
146. D. B. Anthony, J. B. Howard, H. C. Hottel, H. P. Meissner, Fifteenth Symposium (International) on Combustion, The Combustion Institute, Pittsburgh, 1975, p. 1303.
147. S. Badzoich, P. G. W. Hawksley, Ind. Eng. Chem. Process. Des. Dev. 9, 521 (1970).
148. G. M. Kimber, M. D. Gray, Combust. Flame 11, 360 (1967).
149. R. T. Eddinger, L. D. Friedman, E. Rau, Fuel 45, 245 (1966).
150. H. N. Stone, J. D. Batchelor, H. F. Johnstone, Ind. Eng. Chem. 46, 274 (1954).
151. H. Kobayashi, J. B. Howard, A. F. Sarofim, Sixteenth Symposium (International) on Combustion, The Combustion Institute, Pittsburgh, 1977, p. 411.
152. S. K. Ubhayaker, D. B. Stickler, C. W. von Rosenberg, Jr., R. E. Gannon, Sixteenth Symposium (International) on Combustion, The Combustion Institute, Pittsburgh, 1977, p. 427.
153. M. G. Skyler, V. I. Shustikov, I. V. Virozub, Intern. Chem. Eng. 9, 595 (1969).

154. G. J. Pitt, Fuel 41, 267 (1962).
155. R. Rennhack, Brennstoff-Chemie 45, 300 (1964).
156. V. Vand, Proc. Phys. Soc. (London) A55, 222 (1943).
157. E. M. Suuberg, W. A. Peters, J. B. Howard, Ind. Eng. Chem., Process. Des. Dev. 17, 37 (1978).
158. B. K. Mazumdar, N. N. Chatterjee, Fuel 52, 11 (1973).
159. P. C. Lewellen, Ph.D. Thesis, MIT, 1975.
160. D. B. Anthony, J. B. Howard, H. C. Hottel, H. P. Meissner, Fuel 55, 121 (1976).
161. J. B. Howard, R. H. Essenhigh, Ind. Eng. Chem. Process. Des. Div. 6, 74 (1967).
162. D. Bhaduri, S. Bandyopadhyay, Combust. Flame 17, 15 (1971).
163. L. D. Smoot, M. D. Horton, G. A. Williams, Sixteenth Symposium (International) on Combustion, The Combustion Institute, Pittsburgh, 1978, p. 375.
164. J. B. Howard, R. H. Essenhigh, Eleventh Symposium (International) on Combustion, The Combustion Institute, Pittsburgh, 1967, p. 399.
165. W. Nusselt, Z. Ver. Deut. Ing. 68, 124 (1924).
166. S. P. Burke, T. E. W. Schuman, Porc. 3rd Int. Conf. Bituminous Coal 2, 484 (1931).
167. R. H. Essenhigh, Sixteenth Symposium (International) on Combustion, The Combustion Institute, Pittsburgh, 1977, p. 353.
168. H. Gan, S. P. Nandi, P. L. Walker, Jr., Fuel 51, 272 (1972).
169. J. M. Thomas, W. J. Thomas, "Introduction to the Principles of Heterogeneous Catalysis" (Academic Press, New York, 1967).
170. D. O. Hayward, B. M. W. Trapnell, "Chemisorption" (Butterworths Scientific Publications, London, 1964).
171. F. Bonner, J. Turkewich, J. Am. Chem. Soc. 73, 561 (1951).
172. S. Ergun, J. Phys. Chem. 60, 480 (1956).
173. M. A. Kanter, Phys. Rev. 107, 655 (1957).
174. R. Phillips, F. J. Vastola, P. L. Walker, Jr., Proc. 3rd Industrial Carbon Graphite Conf. 257 (1971).

175. F. J. Vastola, P. J. Hart, P. L. Walker, Jr., Carbon (Oxford) 2, 65 (1964).
176. P. J. Hart, F. J. Vastola, P. L. Walker, Jr., Carbon (Oxford) 5, 363 (1967).
177. P. L. Walker, Jr., F. J. Vastola, P. J. Hart, "Fundamentals of Gas-Surface Interactions" (Academic Press, New York, 1967).
178. L. Bonnetain, X. Duval, M. Letort, Proc. 4th Conf. Carbon (1960) p. 107.
179. F. J. Long, K. W. Sykes, Proc. Roy. Soc. (London) A193, 377 (1948).
180. P. L. Walker, Jr., F. Rusinko, L. G. Autin, Adv. Catal. 11, 133 (1959).
181. I. Langmuir, J. Am. Chem. Soc. 40, 1361 (1918).
182. G. S. Rushbrooke, Trans. Faraday Soc. 36, 1055 (1940).
183. J. E. Lennard-Jones, A. F. Devonshire, Proc. Roy. Soc. A156, 6 (1936).
184. S. Glasstone, K. J. Laidler, H. Eyring, "The Theory of Rate Processes" (McGraw-Hill, New York, 1941).
185. C. Kemball, Adv. Catalysis 2, 233 (1950).
186. J. Gadsby, F. J. Long, P. Sleightholm, K. W. Sykes, Proc. Roy. Soc. A193, 357 (1948).
187. A. E. Reif, J. Phys. Chem. 56, 785 (1952).
188. S. Ergun, U. S. Bureau of Mines Bulletin 598 (1961).
189. M. Mentser, S. Ergun, U. S. Bureau of Mines Bulletin 664 (1973).
190. J. F. Strange, P. L. Walker, Jr., Carbon 14, 345 (1976).
191. S. Ergun, M. Mentser, in the "Chemistry and Physics of Carbon", P. L. Walker, Jr. Ed. Vol. 1 p. 203 (Marcel Dekker, Inc., New York, 1965).
192. J. Gadsby, C. N. Hinshelwood, K. W. Sykes, Proc. Roy. Soc. A187, 129 (1946).
193. J. P. Blakely, L. G. Overholser, Carbon 3, 269 (1955).
194. R. F. Strickland-Constable, J. Chim. Phys. 47, 356 (1950).
195. J. F. Johnstone, C. Y. Chen, D. S. Scott, Ind. Eng. Chem. 44, 1564 (1952).
196. J. D. Blackwood, F. K. McTaggart, Aust. J. Chem. 12, 533 (1959).

197. G. O. Ingles, Trans. Faraday Soc. 48, 706 (1952).
198. J. D. Blackwood, Aust. J. Chem. 12, 14 (1959).
199. J. D. Blackwood, Aust. J. Chem. 15, 397 (1962).
200. C. W. Zielke, E. Gorin, Ind. Eng. Chem. 47, 820 (1955).
201. F. Moseley, D. Paterson, J. Inst. Fuel 38, 13 (1965).
202. J. L. Johnson in Coal Gasification, Advances in Chemistry Series No. 131, p. 145, (American Chemical Society, Washington, DC, 1974).
203. J. D. Blackwood, B. D. Cullis, D. J. McCarthy, Aust. J. Chem. 20, 1561 (1967).
204. C. W. Zielke, E. Gorin, Ind. Eng. Chem. 49, 396 (1957).
205. M. F. R. Mulcahy, I. W. Smith, Rev. Pure Appl. Chem. 19, 81 (1969).
206. C. G. Von Fredersdorff, M. A. Elliott in "Chemistry of Coal Utilization", H. H. Lowry, Ed., Supplementary Volume, p. 754 (John Wiley and Sons, New York, 1963).
207. A. B. Ayling, I. W. Smith, Combust. Flame 18, 173 (1972).
208. J. ARTHUR, Trans. Faraday Soc. 47, 164 (1956).
209. R. Phillips, F. J. Vastola, P. L. Walker, Jr., Carbon 8, 205 (1970).
210. N. R. Laine, F. J. Vastola, P. L. Walker, Jr., J. Phys. Chem. 67, 2030 (1963).
211. M. Rossberg, Z. Electrochem. 60, 952 (1956).
212. G. Blyholder, H. Eyring, J. Phys. Chem. 63, 1004 (1959).
213. F. Rodrigues-Reinoso, P. A. Thrower, P. L. Walker, Jr., Carbon 12, 63 (1974).
214. I. W. Smith, R. J. Tyler, Comb. Sci. Tech. 9, 87 (1974).
215. E. A. Gulbransen, K. F. Andrew, Ind. Eng. Chem. 44, 1034 (1952).
216. M. Faraday, C. Lydell, Phil Mag. 26, 16 (1845).
217. W. Galloway, Proc. Roy. Soc. 24, 34 (1876).
218. W. Galloway, Proc. Roy. Soc. 28, 410 (1878).
219. F. Abel, Proc. Roy. Inst. 10, 88 (1882).

220. Bedson and McConnel, Trans. Inst. Min. Engrs. 7, 27 (1894).
221. Bedson and Widdas, Trans. Inst. Engrs. 32, 529 (1906).
222. H. M. Cassel, A. K. Das Gupta, S. Gurreswarny, Third Symposium (International) on Combustion, The Combustion Institute, Baltimore, 1949, p. 185.
223. H. M. Cassel, I. Liehman, W. K. Mock, Sixth Symposium (International) on Combustion, The Combustion Institute, New York, 1957, p. 602.
224. R. H. Essenhigh, J. Csaba, Ninth Symposium (International) on Combustion, The Combustion Institute, Pittsburgh, 1963, p. 111.
225. W. F. Marshall, H. B. Palmer, D. H. Seery, J. Inst. Fuel 37, 342 (1964).
226. D. Bhaduri, S. Bandyopadhyay, Combust. Flame 17, 15 (1971).
227. L. D. Smoot, M. D. Horton, Prog. Energy Combust. Sci. 3, 235 (1977).
228. L. D. Smoot, D. T. Pratt, Eds. "Pulverized-Coal Combustion and Gasification" (Plenum Pres, New York 1979).
229. M. D. Horton, F. P. Goodson, L. D. Smoot, Combust. Flame 28, 187 (1977).
230. L. D. Smoot, M. D. Horton, G. A. Williams, Sixteenth Symposium (International) on Combustion, The Combustion Institute, Pittsburgh 1976, p. 375.
231. C. T. Crowe, L. D. Smoot, Ch. 2 in "Pulverized-Coal Combustion and Gasification", L. D. Smoot, D. T. Pratt, Eds. (Plenum Press, New York, 1979).
232. R. Edelman, O. Fortune, G. Weilerstein, Symposium on Emissions from Continuous Combustion Systems, (Plenum Press, New York, 1972).
233. C. Veillon, J. Y. Park, Anal. Chem. 42, 684 (1970).
234. J. J. Horvath, J. D. Bradshaw, J. N. Bower, M. S. Epstein, J. D. Winefordner, Anal. Chem. 53, 6 (1981).
235. C. Th. J. Alkemade, R. Herrmann, "Fundamentals of Analytical Flame Spectroscopy" (John Wiley, New York, 1965).
236. G. Cadle, R. D. Magill, Ind. Eng. Chem. 43, 1331 (1951).
237. W. A. Roach, J. Soc. Chem. Ind. London 65, 33 (1946).
238. V. A. Fassel, G. W. Dickinson, Anal. Chem. 40, 247 (1968).
239. N. Omenetto, J. D. Winefordner, Prog. Analyt. Atom. Spectrosc. 2, 1 (1979).

240. C. Th. J. Alkemade, W. Snellman, G. D. Boutilier, B. D. Pollard, J. D. Winefordner, T. L. Chester, N. Omenetto, *Spectrochim. Acta.* 33B, 3831 (1978).
241. C. L. Wyatt, "Radiometric Calibration: Theory and Methods" (Academic Press, New York, 1978).
242. W. Snelleman, Ph.D. Thesis, Utrecht, 1965.
243. J. J. Ball, *Rev. Sci. Instrum.* 44, 1141 (1973).
244. D. B. Vaidya, J. J. Horvath, A. E. S. Green, *Appl. Opt.* 21, 3357 (1982).
245. G. H. Dieke, H. M. Crosswhite, *J. Quant. Spectrosc. Radiat. Transfer*, 2, 97 (1962).
246. H. J. Kostowski "Self-Study Manual on Optical Radiation Measurements, Chap. 7, The Relative Responsivity and Slit-Scattering Function on a Spectroradiometer" (Nat. Bur. Stand. Tech. Note 910-4 1979).
247. J. F. James, R. S. Steinberg, "The Design of Optical Spectrometers" (Chapman and Hall, London, 1969).
248. L. M. Garrison, D. D. Doda, A. E. S. Green, *Appl. Opt.* 18, 850 (1979).
249. D. B. Yaidya, J. Samuels, A. E. S. Green, *J. Opt. Soc. Am.* 71, 1584 (1981).
250. K. M. Pamidimukkala, Private Communication.
251. R. W. B. Pearse, A. G. Gaydon, "The Identification of Molecular Spectra" John Wiley and Sons, New York, 1976).
252. G. Herzberg, "Molecular Spectra and Molecular Structure I. Spectra of Diatomic Molecules" (Van Nostrand Reinhold Co., New York, 1950).
253. W. L. Dimpel, J. L. Kinsey, *J. Quant. Spectrosc. Radiat. Transfer* 21, 233 (1979).
254. A. M. Bass, H. P. Broida, *Nat. Bur. Stand. Circ.* 541 (1953).
255. E. E. Whiting, A. Schadee, J. B. Tatum, J. T. Hougen, R. W. Nicholls, *J. Mol. Spec.* 80, 249 (1980).
256. J. B. Tatum, *Astrophys. J. Suppl.* 14, 21 (1967).
257. H. Honl, F. London, *Zr. F. Phys.* 33, 803 (1925).
258. R. S. Mulliken, *Rev. Mod. Phys.* 3, 89 (1931).
259. I. Kovacs "Rotational Structure in the Spectra of Diatomic Molecules" (American Elsevier Pub. Co. Inc., New York, 1969).



260. A. Schadee, B. A. N. 17, 341 (1964).
261. J. Hinze, G. C. Lie, B. Liu, *Astrophys. J.* 196, 621 (1975).
262. G. C. Lie, J. Hinze, B. Liu, *J. Chem. Phys.* 59, 1872 (1973).
263. C. E. Moore, H. P. Broida, *J. Res. NBS.* 63A, 19 (1959).
264. A. M. Bass, H. P. Broida, *NBS Monog.* 24 (1961).
265. D. M. Cooper, *J. Q. S. R. T.* 26, 113 (1981).
266. J. O. Arnold, S. R. Langhoff, *J. Q. S. R. T.* 19, 461 (1978).
267. J. G. Phillips, S. P. Davis, "The Swan System of the C<sub>2</sub> Molecule" (Univ. of Calif. Press, Berkeley, CA 1968).
268. M. J. Mumma, E. J. Stone, E. C. Zipf, *J. Chem. Phys.* 54, 2627 (1971).
269. P. H. Krupenie, "The Band Spectrum of Carbon Monoxide", NSRDS-NBS5, (U. S. Govt. Printing Office, Washington, DC 1966).
270. G. A. Hornbeck, R. C. Herman, *Ind. Eng. Chem.* 43, 2739 (1951).
271. L. B. Headrich, G. W. Fox, *Phys. Rev.* 35, 1033 (1930).
272. K. M. Pamidimukkala, A. E. S. Green, Unpublished work.
273. R. M. Fristrom, A. A. Westenberg, "Flame Structure", (McGraw-Hill, New York, 1965).
274. R. H. Tourin, "Spectroscopic Gas Temperature Measurement" (Elsevier, Amsterdam, 1966).
275. A. Savitzky, M. J. E. Golay, *Anal. Chem.* 36, 1627 (1964).
276. W. L. Barr, *J. Opt. Soc. Am.* 52, 885 (1962).
277. W. Magnus, F. Oberhettinger, "Special Functions of Mathematical Physics" (Chelsea Publishing Co., New York, 1949).
278. R. N. Bracewell, *Aust. J. Phys.* 9, 198 (1956).
279. M. P. Freeman, S. Katz, *J. Opt. Soc. Am.* 53, 1172 (1963).
280. J. B. Tatum, *Pub. Dom. Obs.* 13, 1 (1966).
281. R. J. Cattolica, *Combust. Flame* 44, 43 (1982).
282. W. M. Heffington, G. E. Parks, K. G. P. Sulzmann, S. S. Penner, Sixteenth Symposium (International) on Combustion, The Combustion Institute, Pittsburgh, 1977; p. 729.

283. J. Warnatz, Eighteenth Symposium (International) on Combustion, The Combustion Institute, Pittsburgh, 1981, p. 369.
284. D. S. Coe, B. S. Haynes, J. I. Steinfeld, Combust. Flame 43, 211 (1981).
285. A. D'Alessio, A. Di Lorenzo, A. F. Sarofim, F. Beretta, S. Masi, C. Venitozzi, Fifteenth Symposium (International) on Combustion, The Combustion Institute, Pittsburgh, 1975, p. 1427.
286. G. E. Andrews, D. Bradley, Combust Flame 18, 133 (1972).
287. D. M. Cooper, R. W. Nicholls, Spectros. Lett. 9, 139 (1976).
288. J. Carozza, R. Anderson, J. Opt. Soc. Am. 67, 118 (1977).
289. D. R. Stull, H. Prophet, JANAF Thermochemical Tables, 2nd ed. NSRDS-NBS-37, U.S. Government Printing Office, Washington, DC 1970.
290. K. P. Huber, G. Herzberg, "Molecular Spectra and Molecular Structure IV. Constants of Diatomic Molecules" (Van Nostrand Reinhold Co., New York, 1980).
291. H. J. Fischbeck, K. H. Fischbeck, "Formulas, Facts and Constants" (Springer-Verlag, Berlin, 1982).
292. W. J. Mclean, D. R. Hardesty, J. H. Pohl, Eighteenth Symposium (International) on Combustion, The Combustion Institute, Pittsburgh, 1981, p. 1239.
293. Y. C. Fu, B. D. Blaustein, Fuel 47, 463 (1968).
294. D. E. Rosner, H. D. Allendorf, Carbon 3, 153 (1965).
295. J. A. Graham, A. R. G. Brown, A. R. Hall, W. Watt, Conf. on Industrial Carbon and Graphite, 1957, Society of Chemical Industry, London 1958.
296. C. P. Fenimore, G. W. Jones, J. Phys. Chem. 71, 593 (1967).
297. A. E. S. Green, K. M. Pamidimukkala, "Proceedings of International Conference on the Combined Combustion of Coal and Gas", Cleveland, Ohio, 1982.
298. Z. J. Fink, L. E. Dalverny, J. Grumer, U. S. Bureau of Mines, Report of Investigations, 1956.

#### BIOGRAPHICAL SKETCH

John Joseph Horvath was born on March 24, 1954, at Bridgeport, Connecticut. He received his elementary and junior high school education in the public school system of Fairfield, Connecticut. Upon graduation from the Fairfield College Preparatory School in May, 1972, he received a scholarship from Windham College in Putney, Vermont, where he attended until May, 1973. In September, 1973, he transferred to the University of South Carolina in Columbia, South Carolina, and obtained his Bachelor of Science in chemistry (ACS certified) in May, 1976. In September, 1976, entered the University of Florida, receiving the Master of Science in analytical chemistry in 1980. Since that time he has pursued the Ph.D. in chemistry under the guidance of Drs. A. E. S. Green and W. B. Person. Presently he has six publications on studies of flames. He has been awarded a National Research Council Fellowship at the National Bureau of Standards.

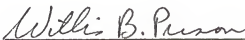
John J. Horvath is a member of the American Chemical Society, Optical Society of America, and the Astronomical Society of the Pacific.

I certify that I have read this study and that in my opinion it conforms to acceptable standards of scholarly presentation and is fully adequate, in scope and quality, as a dissertation for the degree of Doctor of Philosophy.



A. E. S. Green, Chairman  
Graduate Research Professor of Physics  
and Nuclear Engineering Sciences

I certify that I have read this study and that in my opinion it conforms to acceptable standards of scholarly presentation and is fully adequate, in scope and quality, as a dissertation for the degree of Doctor of Philosophy.



Willis B. Person, Co-chairman  
Professor of Chemistry

I certify that I have read this study and that in my opinion it conforms to acceptable standards of scholarly presentation and is fully adequate, in scope and quality, as a dissertation for the degree of Doctor of Philosophy.



Martin Vala  
Professor of Chemistry

I certify that I have read this study and that in my opinion it conforms to acceptable standards of scholarly presentation and is fully adequate, in scope and quality, as a dissertation for the degree of Doctor of Philosophy.



John G. Dorsey  
Assistant Professor of Chemistry

I certify that I have read this study and that in my opinion it conforms to acceptable standards of scholarly presentation and is fully adequate, in scope and quality, as a dissertation for the degree of Doctor of Philosophy.



Richard A. Yost  
Assistant Professor of Chemistry

This dissertation was submitted to the Graduate Faculty of the Department of Chemistry in the College of Liberal Arts and Sciences and to the Graduate School, and was accepted as partial fulfillment of the requirements for the degree of Doctor of Philosophy.

April, 1983

---

Dean for Graduate Studies and  
Research